Ground Vehicle Engineering Series

Dynamics of Wheel–Soil Systems

A Soil Stress and Deformation-Based Approach

Jaroslaw A. Pytka

CRC Press
Taylor & Francis Group

Dynamics of Wheel–Soil Systems

A Soil Stress and Deformation-Based Approach

Ground Vehicle Engineering Series

Series Editor:
Dr. Vladimir V. Vantsevich
Professor and Director
Program of Master of Science in Mechatronic Systems Engineering
Lawrence Technological University, Michigan

Dynamics of Wheel–Soil Systems: A Soil Stress and Deformation-Based Approach
Jaroslaw A. Pytka

Road Vehicle Dynamics: Fundamentals and Modeling
Georg Rill

Driveline Systems of Ground Vehicles: Theory and Design
Alexandr F. Andreev, Viachaslau Kabanau, Vladimir Vantsevich

Ground Vehicle Engineering Series

Dynamics of Wheel–Soil Systems

A Soil Stress and Deformation-Based Approach

Jaroslaw A. Pytka

CRC Press
Taylor & Francis Group
Boca Raton London New York

CRC Press is an imprint of the
Taylor & Francis Group, an **informa** business

CRC Press
Taylor & Francis Group
6000 Broken Sound Parkway NW, Suite 300
Boca Raton, FL 33487-2742

Version Date: 20120726

International Standard Book Number-13: 978-1-4665-1528-4 (eBook - PDF)

To my wife, Agnes, and our children, John, Alice, Frank, Joanna
And the youngest one who's coming soon
For their love and understanding

Contents

Series Preface

Ground vehicle engineering took shape as an engineering discipline in the 20th century and formed the foundation for significant advancements and achievements—from personal transportation and agriculture machinery to lunar and planetary exploration. As we move through the 21st century and face global economic challenges, we must develop fundamentally novel vehicle engineering technologies and effectively train future generations of engineers.

The *Ground Vehicle Engineering Series* will unite high-caliber professionals from the industry and academia to produce top-quality professional reference books and graduate-level texts on the engineering of various types of vehicles, including conventional and autonomous mobile machines, terrain and highway vehicles, and ground vehicles utilizing novel concepts of motion. The series concentrates on conceptually new methodologies of vehicle dynamics and operation performance analysis and control, advanced vehicle and system design, experimental research and testing, and manufacturing technologies. Applications include heavy-duty, multi-link, and pick-up trucks; farm tractors and other agriculture machinery; earth-moving machines; passenger cars; human-assist robotic vehicles; planetary rovers; and conventional and unmanned wheeled and track vehicles and reconnaissance vehicles for military uses.

Vladimir V. Vantsevich
Series Editor

Preface

This book was written as a reference for anyone involved in terramechanics who is studying wheel–soil mechanics, specifically soil responses quantified as soil stresses and deformations. I collected, analysed, and present results from my 15 years of experience in field experimentation on wheel–soil dynamics to create a single-source reference. Readers—automotive and agricultural engineers, instrumentation design engineers, researchers, and graduate students—will find descriptions of methods and devices for soil stress and deformation measurements along with numerical data from field experiments.

The methods and procedures can provide practical solutions to numerous methodological problems that may arise during the design and preparation of field experiments. I have omitted or minimised theoretical considerations as they are well addressed in the cited literature. Instead, wheel–soil dynamics are based on experimental data obtained from full-scale field settings. I tried to keep the text simple and concise throughout and assumed that potential readers have background knowledge of automotive and agricultural engineering, elementary soil mechanics, electronics, and metrology.

I express gratitude to several people, whose help was substantial: Professor Reiner Horn, under whose supervision I developed a passion for soil stress and deformation measurements; Professors Krystyna Konstankiewicz and Adam Pukos, who nurtured that passion during my doctoral studies at the Institute of Agrophysics in Lublin; Col. Dr. Jarosław Dąbrowski, a great partner and friend through many years of research and field work that produced many unforgettable moments and optimistic conclusions; and Professor Piotr Tarkowski for his spiritual care, continued tolerance, and encouragement. Also, many thanks to Susan Hardy, who agreed to read the entire manuscript. Her helpful comments, corrections, and editing improved the quality of the text.

About the Author

Jaroslaw Alexander Pytka was born in Wroclaw, Poland. He is presently a research engineer and instructor of undergraduate and graduate students of automotive technology at the Lublin University of Technology, Poland.

Dr. Pytka earned an MS in automotive technology from the Lublin University of Technology in 1992, and a PhD in soil physics from the Institute of Agrophysics in Lublin. His major research interest is wheel–soil interaction analysis with a focus on experimental studies.

1

Introduction to Wheel–Soil Systems

1.1 Ground Vehicles and Their Running Gears

We define ground vehicles as those designed for off-highway use, although some can also travel on public roads. A typical passenger car that is intentionally driven off road is not a ground vehicle. A ground vehicle must have special equipment or features that enable it to ride over natural, unimproved terrain. Examples of such features are

- Four-wheel or all-wheel drive system
- Reinforced tyres with special treads
- Power unit, typically based on a diesel engine, with an effective cooling system, dust filters, and high positioning of air intake and exhaust equipment
- Suspension that ensures stability on slopes and axle twisting capability for crossing obstacles and rough terrain
- Additional equipment such as a winch and pulling rope
- Water-resistant sealing

Historically, before roads were paved smoothly, all vehicles functioned as ground vehicles. Problems with poor traction, especially after rains, significantly slowed ground transportation. Vehicles could carry only limited numbers of passengers or amounts of freight, mainly due to wheel flotation. Railroads revolutionized ground transportation, but trains were always less mobile than cars.

Goodyear's rubber pneumatic tyre was a "milestone" invention that greatly improved vehicle performance. Wheels with tyres performed much better than rigid, wooden wheels with steel rings. Ride velocity increased and comfort and safety improved. For a typical ground vehicle, however, the introduction of tracked suspension was much more important. It allowed the vehicles to be very heavy with no loss of mobility on poor terrain. Tracked running gears dominated the design of military

vehicles. Today, ground vehicles with tyres are capable of traversing significant terrain obstacles and operate with satisfactory ride dynamics.

Ground vehicles are designed to go off highway, where traction on natural soft terrain is much less than on paved roads. Consequently, a well-engineered ground vehicle should be able to generate a surplus of driving power to be used in extreme situations. On the other hand, ground vehicles can destroy arable soils and natural ground. They create sudden and irreversible changes in soil structure and cause ecological degradation of the soil environment. Additionally, the increased speed of sport utility vehicles creates problems with lateral dynamics and handling. The loss of ride stability at high speed on a rough terrain can lead to rollover—one of the most frequent causes of fatal accidents in rural areas. These and other aspects of wheel–soil interactions are presented in this introductory chapter.

1.1.1 Agricultural Vehicles

Agricultural vehicles include tractors, combine harvesters, and all other towed or self-propelled field machinery. All are typical ground vehicles since they operate on soft soil surfaces or grass lands.

Tractors are the major multipurpose "work horses" in agriculture all over the world. Most tractors are wheeled vehicles although some use tracked suspension. They operate on a wide variety of surfaces, from typical paved roads to very poor, soft and wet, highly deformable soils. Although the basic concept has remained unchanged (Figure 1.1), modern tractors are high-technology machines, equipped with the newest systems

FIGURE 1.1
In contrast to their traditional appearance, modern agricultural tractors feature almost all the newest automotive technologies.

and accessories such as global positioning systems (GPSs), on-board diagnostics (OBDs), computer-assisted traction controllers, and continuously variable transmissions (CVTs). The highly accurate positioning made possible by GPS led to precision agriculture, defined as a complex method of managing within-paddock (or within-field) variability to optimise inputs to produce the best potential output. Precision agriculture increases profitability while minimizing environmental impact (Whitlock 2006).

Two of the newest innovations in this field are raised-bed farming (RFB)—a method of forcing tractor wheels to drive along furrows—and controlled field traffic (CFT)—limiting paddock traffic to well-defined permanent tracks. An important advantage of precision agriculture is better comfort for drivers and operators, especially on large-area farms. Maintaining speed is also an important concern in tractor engineering. Slow, controllable speeds are necessary during field operation. Travelling on public roads, however, requires faster speeds to avoid traffic delays. The CVTs on modern tractors allow a wide range of precisely controllable speeds within 0.1 to 80 km/h.

The second most important agricultural vehicle is a combine harvester. It is usually a wheeled, self-propelled machine used for harvesting grain crops. The name derives from the capability of the vehicle to combine three separate operations (reaping, threshing, and winnowing) into a single process, significantly saving human labor. Combines are usually big and heavy and produce great ground pressure. They usually have large-diameter, driven wheels, similar to those used on tractors.

A typical agricultural tractor has four wheels, with 2×4 or 4×4 drive. Older types had small, steered front wheels and large, driven rear wheels, but based on the current popularity of 4×4 drive, all four wheels have large diameters. This feature is important for traction as a large-diameter wheel generates a high driving force and most operations performed with a tractor require large drawbar pull forces. The tread pattern of tractor tyres is recognizable. Tractor tyre treads have long, high lugs that create a typical "spruce-shaped" pattern. This feature also adds to off-road performance, but the non-symmetrical tread does not perform well in reverse.

1.1.1.1 Tractor Tyre Modelling

*C*ompared to standard automobiles, tractors tyres have larger diameters, tread bars, and sections, and they operate at lower rotational speeds with larger deflections. Schlotter and Keen (2003) discussed off-road tyre characteristics and modelling with a special regard for ride comfort. To obtain tyre stiffness and damping characteristics, several researchers have taken into account non-linear dynamic effects. Factors such as inflation pressure, tyre age, road or ground surface, rolling speed, load, torque, ply

rating, and lug length were considered significant, although some authors obtained different results.

Wheel testers are typically used to test tractor tyres. The sizes of tractor tyres make it difficult to conduct tests of drum rigs. Consequently, mobile or stationary single wheel testers are commonly used (Armbruster 1986, Ferhadbegovic et al. 2006, Plesser 1997). Different methods and procedures are used including determination of static load–deflection relationship and dynamic excitation by rolling a test wheel over a square bumpy track with fixed wavelength and amplitude at a constant speed. With lateral dynamics, sinusoidal or ramp-change excitation modes determine tyre lateral force characteristics with final results in a form of Bode plot (Schlotter and Keen 2003). Based on such tests, tyre lateral behaviour is described by means of cornering frequency and relaxation time (or relaxation length), but quantitative results differ due to calculation method (amplitude ratio or phase shift). Experimental data obtained with wheel testers are used for evaluating tyre models.

Ferhadbegovic et al. (2006) developed a fully non-linear dynamic tyre model that can be linked with multi-body system (MBS) software to create software for vehicle dynamics. Their Hohenheim model uses only physical parameters and it has reduced the number of parameters as much as possible. The parameters for the model are easily obtained with a single wheel tester. The model uses velocities as inputs to calculate tyre deflection velocities, deflection amount, and forces. Modelling of tyre body behaviours in the three directions—longitudinal, lateral, and vertical—has been done with non-linear Voight–Kelvin elements. The model is significantly different from models commonly used to simulate smaller automobile tyres; those models rely on numerous parameters with no physical meanings.

1.1.2 Military Vehicles

Military vehicles fulfill various missions on a battlefield, but their primary function is to carry crew or infantry, protect them, transport and fire weapons, and perform engineering duties. One important design purpose is to find optimum parameters for vehicle weight, mobility over a wide variety of terrains, and crew protection. Because of obvious tactical requirements, military vehicles must be capable of travelling over the most difficult terrain that presents every possible obstacle. The main design criteria for military vehicles are (1) armour, protection, surveillance, and fire control; (2) power plant, transmission, steering, and suspension; (3) structure; and (4) mobility.

Research and development in this area started before World War II and pronounced improvements were made in the 1960s and 1970s (Ogorkiewicz 1968). Today's military vehicles incorporate the newest

technology developments including new materials, sensor and electronic technology, power plant, and mechanical design novelties.

Military ground vehicles can be divided into two major groups: (1) wheeled vehicles and (2) tracked vehicles. Another classification distinguishes unarmoured and armoured designs. Military vehicles include the following:

- Fighting tanks
- Infantry fighting vehicles
- Command and control vehicles
- Military utility and transport vehicles
- Military engineering vehicles
- Light utility vehicles
- Unmanned ground vehicles

1.1.2.1 Fighting Vehicles: Tanks and Infantry Fighting Vehicles

Military tanks are also called main battle tanks (MBTs) and are similar to armoured personnel carriers (APCs). They are heavy (up to 80 tonnes) tracked and armoured vehicles. Tracked undercarriages are very popular for military use, in contrast to civilian ground vehicles. A tracked suspension system allows tanks to be well armoured and carry lots of weaponry—two important features for fighting purposes. The tradeoff between mobility and protection is pronounced. A high level of protection leads to heavy weight, resulting in poor cross-country performance. A key consideration is survivability. A light vehicle with poor protection and less chance of surviving an attack would have a greater chance to avoid an attack due to its high mobility. On the other hand, a well-protected, heavy vehicle would be an easy target due to its poor mobility, but its armour could withstand an attack. Hetherington and Littleton (1987) developed a quantitative relationship between the mobility requirement and the resultant survivability of armoured fighting vehicles running on soft soils.

Tanks must travel over most types of terrain, including soils with low bearing capacity and strength. Tracks fulfill this requirement by distributing the weight of the vehicle over a large area, resulting in lower ground pressure. The ground pressure for a wheeled vehicle may exceed 300 kPa, while that for a tracked vehicle is well under 100 kPa.

Two tracks types have been used in tank and personnel carrier designs: (1) one- or two-pin tracks and (2) band tracks. Pin tracks are built of steel or aluminum alloys. In one- or two-pin tracks, a sprocket drives the track through the end connectors. A significant problem is track durability, which is relatively short (hundreds of kilometres). Band tracks are used for small machines such as unmanned ground vehicles and they

FIGURE 1.2
Based on the Finnish Patria, the Polish-built Rosomak as an armoured ambulance vehicle.

are the best choices for bigger and heavier vehicles. The advantages of band tracks include smoother ride, less weight, and ease of maintenance. A typical band-track design uses rubber and composite materials, so its durability is significantly longer than that of a pin track.

Infantry fighting vehicles (IFVs) may be wheeled or tracked. A typical tracked IFV weighs 10 to 15 tonnes; a wheeled IFV may weigh up to 22 tonnes. One of the newest IFV designs is the Polish-built Rosomak (Figure 1.2), based on the Finnish Patria; it uses armour composed of interchangeable modules of various thicknesses. This allows the vehicle to be tailored for particular missions such as decreasing vehicle weight for air transportation or strengthening the protection for engagement in dangerous missions. Rosomaks have been used extensively in Afghanistan for reconnaissance, proving their good design that provides both protection and mobility.

1.1.2.2 Logistic and Engineering Vehicles

Successful operations on the battlefield depend on the supply chain; armed forces need regular supplies of ammunition, fuel, and all the life-supporting goods. Logistic vehicles fill this role; they are sometimes called "unsung heroes" (Hohl 2003). These vehicles must be capable of constantly operating at full load under extreme environmental and terrain conditions. They also must be reliable and remain in serviceable condition for extended periods. One philosophy for obtaining a good military

logistic vehicle is modifying an existing commercial truck of a proven design by

- Installing bigger fuel reservoirs
- Redesigning to achieve four- or all-wheel drive configuration
- Adding differential locks
- Changing the tyre inflation system
- Equipping it with electronic communication and warfare systems

Logistic vehicles can be divided into light, medium, and heavy trucks. The payload of a typical heavy truck reaches 6 tonnes or more. This results in a gross weight of 12 to 14 tonnes, which requires a suspension with six or more road wheels. Adding an all-wheel drive system results in a significantly complex design. Traditionally, suspension of logistic trucks consisted of rigid axles, but independent suspensions introduced into this group of ground vehicles provide an important advantage with a significantly increased wheel stroke. In any configuration, the suspension of military trucks must be able to twist. The use of all-terrain, aggressively treaded tyres is also essential.

Military trucks, due to their gross weight, exert high pressure over their contact paths. This creates serious mobility problems and may lead to no-go situations during travel on soft and wet terrains. Twin (double) wheels or reduced tyre inflation pressure may help in such situations.

Military engineering vehicles, also known as combat engineering vehicles (CEVs), are used for construction work or for transporting combat engineers on battlefields. Engineering vehicles can be divided into two major groups: militarized civilian vehicles and purpose-built military engineering vehicles. Militarized civilian vehicles may also be modified, typically by adding armour for protection from battlefield hazards by installation of armour plates and steel jackets.

Purpose-built military vehicles are usually based on main battle tank platforms. A typical tank-based engineering vehicle includes a large dozer blade or mine plough, a large-caliber demolition cannon, augers, winches, excavator arms, and cranes or lifting booms. This equipment is installed to conduct obstacle breaching operations and other earth-moving and engineering work on battlefields. Some specialized types of military engineering vehicles are not as versatile and operate as typical multifunction vehicles.

1.1.2.3 Light Utility Vehicles and Unmanned Robots

Historically, light utility vehicles have been identified with the well-known Willys–Overland Motor Company's Jeep used in great numbers

during World War II. Light utility vehicles are now produced on a large scale and used by armed forces of most countries. The design features light weight and a short, unarmoured body with four-wheel drive that can carry at least four passengers. Civilian adaptations of proven military light utility vehicles became the prototypes of the sport utility vehicles that are very popular around the world today.

An unmanned ground vehicle (UGV) is a wheeled or tracked robot designed to operate under off-road conditions, capable of running at low or moderate speeds. Its primary task is to replace human forces in hazardous operations such as disabling explosives, maintaining checkpoints, and providing street presence in urban areas. UGVs are now used extensively in the current conflicts and for stabilizing and peacekeeping missions.

1.1.3 Engineering Vehicles and Heavy Construction Equipment

Engineering and construction vehicles are used for numerous tasks including earth moving (Haycraft 2011). These vehicles must develop large drawbar pulls. The need for large pulls along with the ability to operate over poor surfaces at construction sites requires optimum off-road performance for engineering vehicles (Figure 1.3).

Engineering vehicles have both wheeled and tracked suspension systems. Wheeled vehicles are commonly used for transportation outside construction sites. Trucks and dumps are capable of running at higher speeds. For stationary work or where ultimate off-road traction is required

FIGURE 1.3
Tracked or wheeled, engineering vehicles often operate on poor traction conditions, here on a highway construction site in southeast Poland.

(i.e. earth moving), tracked construction machines (bulldozers, diggers) are used. Tyre selection for engineering vehicles is different from typical on-road commercial vehicles. There are six categories of service—compactor (C), earthmover (E), grader (G), loader (L), log-skidder (LS), and mining and logging (ML)—and each requires a specific tyre.

1.1.4 Sport and Leisure Vehicles

Ground vehicles for personal use are called sport utility vehicles (SUVs), sports activity vehicles (SAVs), and all-terrain vehicles (ATVs). A typical, SUV is a light, four-or-five-passenger vehicle with all-wheel drive and a strong suspension on a light-truck chassis. Since 1990, SUVs have become more popular with the increased demand for a passenger car capable of travelling over rough terrain. Significant technology innovations in SUVs and SAVs include new concepts of transmissions, viscotic clutches, computer-based drive power distribution, and ride stability control.

One important application of SUVs is in motorsports. In addition to well-known international competitions and rallies, local contests are very popular. For example, every 2 years, the Lublin University of Technology supervises a 4×4 trial. The event is an open competition for high-mobility, modified SUVs and their drivers (Figures 1.4 and 1.5). Two-person crews (without the help of winches and other devices) must travel a race course containing a number of obstacles in a given time. Rally competitions are

FIGURE 1.4
The 4×4 trial, held every 2 years under the supervision of the Lublin University of Technology, always has a large audience.

FIGURE 1.5
A modified SUV trying to pass on muddy and sloped terrain during the 2011 4 × 4 trial in Lublin.

useful for testing new design concepts under harsh and demanding conditions (Gardyński 2011).

SUVs are not only popular for sport and leisure, they are important transportation systems in remote areas and serve as adjunct vehicles for forestry, fire, and paramilitary services. Current technology issues for SUVs include improvements in ride comfort and dynamics through application of active suspension and traction controlling systems (Cronje and Els 2010). A primary goal of such improvements is safety, especially in avoiding roll-overs that constitute the most frequent causes of fatal accidents with SUVs.

1.1.5 Planetary Rovers

A rover vehicle is designed to provide surface transportation on the moon or other astronomical body. Special requirements for engineering planetary rovers include

- Ability to withstand shocks and vibrations from extreme acceleration and deceleration during launch and landing
- Construction materials capable of operating at extreme temperatures, for example, ranging from –120°C to +220°C on Mars
- Operation with sufficient mobility on unknown (rough or unstable) surfaces
- Responsiveness to long-distance control

The first vehicle to travel on the lunar surface was developed by the U.S. National Aeronautics & Space Administration (NASA). Its Apollo Lunar Roving Vehicle provided transport in support of a mission to the moon in 1971. Although the first space exploration rover was a typical personnel carrier, all its successors were unmanned. The Russian Lunochod 2 was launched in 1973 to perform the first remote surface exploration of the moon. The vehicle had eight-wheel suspension.

The current planetary rovers are typically autonomous, self-operated vehicles with artificial intelligence engineered to fulfill the planned mission scenarios. The first Mars exploration rover, launched in 1996, was the Sojourner that had a six-wheeled undercarriage. The Sojourner was followed by the Mars exploration rovers (MERs) named Spirit and Opportunity that started their missions in 2003. The newest Curiosity rover uses a novel method to reach the Martian surface. After entering the Martian atmosphere, the lander with the rover performs a rocket-powered hover and lowers the rover to the surface on nylon cords. This landing technique was chosen because of the relatively high (850 kg) mass of the rover. Like previous rovers, Curiosity is equipped with six wheels in a rocker-bogie suspension that also serves as the landing gear.

1.1.5.1 Wheel Designs for Planetary Rovers

Several design concepts for planetary rover running gears have been examined, but multi-wheel, independent suspension, and tracked suspension are the most common. Wheels for exploration rovers can be rigid, smooth, or lugged as well as elastic. Lugged rigid wheels have proven more advantageous than smooth wheels, mainly because they provide enhanced traction on powdered Martian and lunar soils (Michaud et al. 2006 and Richter et al. 2006).

A small robotic rover designed for the Japanese Selene-2 lunar mission utilises lugged wheels for movement on sloped terrain. Their performance was tested in an inclined soil bin, filled with lunar soil simulant (Nakashima et al. 2010). The ExoMars rover developed for the European Space Agency's exobiology mission to Mars is designed to search for traces of past and present carbon-based life forms on the red planet. This rover has a six-wheel undercarriage that features flexible metallic wheels, mass-efficient passive suspension, a wheel-walking body phase adjustment capability, and all-wheel steering to permit crabbing motion. The flexible metallic wheels have been analysed for mobility in a soil bin with an instrumented rig for driving or towing wheel function modes (Patel et al. 2010).

Other interesting concepts are included in NASA's Curiosity rover that is intended to explore the Martian surface and atmosphere and carry a laboratory with a palette of research instruments. Each wheel is made of aluminum and is 26 cm in diameter (Figure 1.6). An inner hub contains

FIGURE 1.6
A comparison of Mars rover wheels, from left to right: the Sojourner, the Spirit, and the Curiosity. (NASA/courtesy of nasaimages.org.)

drive and steering actuators and is connected to the outer ring by means of five C-shaped spring elements. A rocker arm suspension similar to that used on previous Mars rovers was chosen as a good solution to conform to obstacles such as stones and rocks. The design optimises traction, mobility, and agility by maximizing wheel surface grip. One of the important concerns was ensuring the mechanical strength of the undercarriage for a new landing technique in which the rover touches the surface with wheels, not with cushioning airbags.

1.1.5.2 Track Designs for Planetary Rovers

As an alternative to wheeled suspension, Wakabayashi et al. (2009) developed and tested a tracked exploration rover for a lunar mission. This design used mesh crawler links to reduce contact pressure and to enhance mobility on slopes. This light crawler accommodates four mesh crawlers, each driven and steered independently for better mobility and agility. Full-scale tests of the rover have been conducted on a lunar regolith soil surface and on a rock-scattered field.

1.1.5.3 Planetary Soil Simulation

In addition to advances in guidance and control, power supplies, and remote operation systems, the latest technologies for planetary rovers involve advanced studies of mobility to meet planetary surface characteristics. Studies in wheel–surface interactions use simulated planetary or lunar soils known as simulants—composite materials based on Earth's volcanic ashes and soils that are very similar to Martian and lunar regoliths.

The Johnson Space Center's JSC Mars-1 Martian regolith simulant fragments are smaller than 1 mm—a fraction of the size of palagonitic tephra (glassy volcanic ash altered at low temperatures). The material for the stimulant was collected from the Pu'u Nene cinder cone located in the saddle between the Mauna Loa and Mauna Kea volcanoes on the Island of Hawaii. Palagonitic tephra from this cone has been repeatedly cited as a close spectral analogue to the bright regions of Mars (Allen et al. 1997).

The JSC-1AF lunar mare regolith simulant is another material produced to support NASA's future exploration of the lunar surface. The JSC-1AF was mined from a commercial cinder quarry at Merriam Crater (35°20′ N, 111°17′ W), a volcanic cinder cone located in the San Francisco volcano field near Flagstaff, Arizona, in the United States. Both JSC simulants are available for research (Zeng et al. 2010, Oravec et al. 2010 and Owens 2006).

1.1.6 Bush Planes

Bush planes are designed to operate on rough, unprepared airfields or from casual terrain. They feature high wings, conventional landing gear (two main wheels and a tail wheel), wing flaps and slots for short take-off and landing (STOL) performance, and very large, low-pressure tundra tyres (Figure 1.7) to allow take-offs and landings on poor surfaces. Two

FIGURE 1.7
Although not typical tundra tyres, the Antonov An 2 tyres are wide and low pressure for better performance in off-field flying. The aeroplane is considered one of the safest, thanks to its undercarriage and ability to land everywhere.

critical points in off-field flying related to wheel–soil interactions are (1) touchdowns and landings and (2) take-off rollouts.

At the moment of touchdown, the wheels hit the surface with high contact forces. This may lead to longitudinal or lateral instability that can cause the aircraft to crash. During a landing roll, motion resistance due to surface deformation is very high and it helps to stop the aircraft in a short distance. On the other hand, this resistance slows an aircraft on take-off so more distance is needed for it to become airborne. These issues are important for performance and are critical for safety. Large-diameter tundra tyres may solve the problem of high contact forces at touchdown and also help reduce rolling resistance due to surface deformation but they also generate high rolling resistance from tyre deflection and hysteresis effects. Consequently, the use of tundra tyres on paved aerodromes is safe, but not as energy efficient as normally inflated, standard aircraft tyres.

A number of aircraft are designed for both off-field and normal airport operations. Some general aviation aircraft such as sport, leisure, light transport, or training aircraft are equipped with wide, low-pressure tyres that represent a good compromise for use on both paved and grassy airfields. An important feature of such aircraft is their landing gear, with shock absorbers of long vertical stroke that minimise the effects of surface roughness and provide high mechanical strength. Bush aeroplanes can also be equipped with removable or adjustable skis or floats to allow operations on deep snow and water.

A recent advance for improved aviation running gear is a new aircraft tyre that uses an unpressurized system with a carbon fiber band embedded in the circumference to retain shape. The new tyre provides improved performance in all measurable areas of wear, traction, and rolling resistance, but the most pronounced feature is flat resistance. Applications include use in light and medium general aviation aircraft.

1.2 Major Research Problems

Although wheel–soil interactions involve numerous important and interesting topics, we define two problems of prime importance: (1) off-road traction and (2) vehicle impact and soil compaction. The next sections introduce those concerns and include a survey of significant achievements.

1.2.1 Off-Road Traction

Off-road traction is defined as all effects of wheel–soil interactions that influence vehicle dynamics, handling, and comfort. First, wheel forces

generated at a contact interface are responsible for vehicle behaviour. Wheel forces—as distinguished from forces generated by the vehicle and its aggregates—are the driving forces from the engine torque, steering force applied to wheels, and vertical load. For vehicle motion to begin and continue as intended by the driver, these forces must be transferred to the surface over which a vehicle is driven; then reaction forces should be generated. Vehicle traction depends on these reaction forces. This means that even a powerful vehicle can be motionless on a poor, highly deformable surface. In other words, we should pay more attention to wheel–soil system performance than to vehicle catalogue performance.

Reaction forces on a hard, non-deformable surface are generated mainly via surface friction (this is valid for longitudinal and lateral forces). A major difference between a paved road and a soil surface is that reaction forces on a soil surface are generated at dynamic soil deformations (or deflections). We distinguish these dynamic deformations from volumetric deformations caused mainly by vertical loads and shearing deformations that occur during driving or steering.

Soil volume changes during deformation create stresses that grow until a state of equilibrium is reached. Generally speaking, forces applied to a wheel by a vehicle are equal to reaction forces generated at the wheel–soil interface. This means we can obtain as much traction as the actual stresses generated in the soil medium. Or we can "wait" until the soil is stressed (and consequently deformed) so that the resulting reactions are equal to external forces. The more a soil surface is deformed, the more energy is lost (consumed for soil deformation). Thus we can speak of traction efficiency, which is considerably worse for off-road conditions than it is on paved roads.

1.2.1.1 Off-Road Traction Modelling and Prediction

A traditional approach to off-road traction modelling lies in the Coulomb-Mohr hypothesis. This oldest model of soil mechanics assumes that soil is a material with internal friction. A sudden breakdown of soil structure occurs when a certain level of stress is reached. The limiting level (shearing stress) is expressed by two basic parameters: soil cohesion and angle of internal friction. Based on this approach, the driving force (traction) on a wheel can be predicted; a number of models have used it as a basic relationship (Jakliński 2006).

The simplicity of the Coulomb-Mohr model, however, is accompanied by substantial drawbacks such as the lack of information about its stress–strain behaviour and its failure to consider time. A relationship between net traction (driving force divided by wheel load) and longitudinal wheel slip is used for off-road vehicle performance modelling. This relationship, graphically represented by a traction curve, can be obtained using a

modification of the Coulomb-Mohr theory by Janosi and Hanamoto (1961). They express a slip-dependent function describing shear stress in the contact path using the shear displacement modulus. Another basic theory for off-road performance prediction is Bekker's (1969) model of pressure sinkage behaviour. This model calculates rolling resistance and drawbar pull for both wheeled and tracked vehicles over different soils and uses a sinkage coefficient and two sinkage moduli determined with a specific device called a bevameter (Bekker's value meter).

For military vehicles, it is often necessary to predict conditions at which a vehicle becomes immobilized. Single-number synthetic indexes are used for such predictions. The oldest and probably most used is the vehicle cone index (VCI) that has been incorporated into the NATO Reference Mobility Model (NRMM). A comparatively simple and quick-to-use instrument, a cone penetrometer, determines the cone index (CI) that correlates well with the cohesive strengths of saturated clay soils. The VCI is then derived from cone index measurements during multi-pass trials as a minimum soil strength required for a single pass. The mobility index (MI) has been developed from various vehicle parameters (weight, running gear dimensions, etc.). Equations for predicting the MI are different for tracked and wheeled vehicles and are empirical. The rule is that the smaller the MI, the better the performance of a vehicle (Maclaurin 2007).

Mean maximum pressure (MMP) measurement is more realistic and simpler. Based on actual measurements of pressure under a tracked vehicle, it was found that the ground was loaded unevenly under the track, with peaks of pressure under each road wheel. The mean values of all these peaks constitute a measure that correlates well with actual performance and can be derived from a simple relationship of vehicle weight, track width and link pitch, and the number of wheels and their diameters. The MMP values are expressed in kilopascals (kPa).

An equivalent MMP expression was also derived for wheeled vehicles. Calculated MMP values for vehicles can be compared with soil strength, determined on the basis of cone penetration tests. The values of the MMP for military tanks are within 210 to 290 kPa, while for wheeled vehicles they range from 250 to well over 500 kPa. The desired ground pressure for wet clay soil in a temperate climate is 150 to 200 kPa, with 300 kPa as the maximum acceptable (Larmine 1992).

1.2.1.2 Terrain Modelling and Simulation

The above-described methods of wheel–soil modelling and simulations give satisfactory results only when we assume a flat and level soil surface. In fact, natural terrain is always rough. Unevenness of surface affects ride comfort through severe vibrations and also influences vehicle performance because of changes in contact forces between tyres and terrain.

Therefore, to incorporate wheel–soil models into a complete simulation tool for off-road vehicle dynamics analysis, a terrain profile must also be modelled.

One approach uses statistical methods. A terrain profile is described by means of two-dimensional statistical processes. Several solutions have been examined and presented in the literature. They can be Gaussian stationary and linear processes such as uniformity undulated methods and empirical mode decompositions for non-stationary, non-linear processes. Creating a complete model requires that experimental data obtained on an original terrain be applied for parameterisation; examples of such model terrain are Belgian pavement and Perryman 3 test tracks (Sun et al. 2007).

Another concept is to represent a terrain profile by a different stochastic modelling technique. Here, a profile is considered a two-dimensional stochastic process with variables described by probability distribution. Stochastic partial differential equations have been solved using the finite difference method. The model can create as many terrain profiles as needed for off-road vehicle dynamics simulations. The virtual terrain is created to preserve the stochastic properties of the original terrain (Lee and Sandu 2009).

A useful strategy is to define surface undulations by means of a single-number descriptor called the root mean square (RMS) method. Knowing the actual values of the RMS for a given terrain makes it possible to predict vehicle speed to ensure ride comfort and safety. Consequently, if the need is to assign RMS values to large areas of terrain, remote sensing is a practical method for obtaining calibration data.

An airborne LIDAR can create virtual charts of terrain with detailed topographic information by high-speed scanning from altitude. One disadvantage is that terrain profiles obtained for large areas are of relatively low resolution (5.0 m raster). A technique incorporating a combination of fractal dimensions and spectral analysis has been used to infer high-resolution RMS using low-resolution terrain mapping from LIDAR. It utilises a power spectrum analysis (PSD) computed on downscaled profiles using raw (non-detrended) data (Durst et al. 2011).

The Vehicle Dynamics and Mobility Server (VDMS) is a sample synthesis of terrain vehicle simulation. This multi-purpose platform performs real-time, high-fidelity simulations of unmanned ground vehicles (UGVs) to evaluate their mobility performance in simulated battlefield scenarios. VDMS includes real-time ground-vehicle models operating over high-resolution digital terrain. The models cover three-dimensional multi-body vehicle dynamics, off-road vehicle–soil interactions, collision detection and obstacle negotiation code, and autonomous control algorithms (Brudnak et al. 2002 and Brudnak et al. 2007).

1.2.1.3 Winter Traction and Snow Modelling

Snow is a natural material that exhibits greatly varying mechanical properties mainly due to metamorphism. We can distinguish constructive and destructive metamorphism although both are changes in snow structure dependent on air and snow temperatures, wind, sun radiation, and other meteorological factors. The dynamic nature of snow properties makes prediction of wheel and track performance and winter traction difficult.

Snow mechanical strength is a function of density and depth and may vary greatly. Fresh snow can carry very light vehicles (contact pressure ~5 to 30 kPa). Settled or frozen snow, with a bearing capacity reaching 200 kPa, can be used by SUVs, tracked vehicles, and even light trucks. In wheel–snow interaction analysis, we distinguish two cases: (1) shallow snow, where a rigid interface (frozen soil or road) affects snow stress distribution, and (2) deep snow. Shallow snow is dense; deep snow is usually not. Tracked vehicles of low contact pressure are best suited for travelling over deep snow. Snow grooming machines, for example, have wide, flexible rubber tracks that generate only a few kilopascals of pressure on a snow surface.

Snow hardness is an important parameter in wheel–snow interaction studies. It can be determined by various methods including simply observing whether a fist, finger, pencil, or knife blade can penetrate the snow. Instrumented methods use a Rammsonde or special micropenetrometer to measure snow stratigraphy. Snow density is strictly correlated with snow hardness and the resulting wheel performance; therefore, it is practical to obtain information about the geometry and microstructure of snow settlement. Ground penetrating radar (GPR) can determine geometric electromagnetic properties of terrain including snow. The dielectric constant of snow is a function of density and microstructure, so GPR probing has the potential of providing data for vehicle traction as well (Lee and Wang 2009). The time domain reflectometry (TDR) technique is a similar method that assumes the electromagnetic characteristic of snow is a key parameter. A hand-held meter is used to determine snow dielectric constant (Stacheder 2005).

Wheel–snow interaction models are most frequently based on the Drucker–Prager plasticity theory, and simulations have been performed with the finite element method (FEM; Shoop 2001, Fervers 2004, Aubel 2005). Measurements obtained for rigid or pneumatic deformable wheels include snow stress distribution, snow deflection, and wheel motion resistance. Lee (2011) performed a high-fidelity FEM simulation of the interactions between a deformable tyre and low-strength snow. Measurements including traction, motion resistance, tyre sinkage, tyre deflection, snow density, contact pressure, and contact shear stress were obtained for braked, towed, driven, and self-propelled wheel states. As an alternative

for time-consuming FEM simulations, an indentation model has been proposed for plate–snow or wheel–snow interaction analysis. The model defines three deformation zones and is described by algebraic equations. For calibration, it requires only a limited number of physical parameters that can be determined by indentation tests (Lee 2009).

Full-scale winter traction research involves two general objectives. One is analysis of vehicle handling dynamics on snow-covered roads. For this purpose, standard dynamics tests are not suitable, mainly because of much lower grip between tyre treads and slippery winter surfaces. Modified procedures based on sine-wave steering wheel excitation have been used to determine the effects of wheel chain application on lateral dynamics of a passenger car (Deppermann 1988). One significant weakness was the impossibility of reaching a vehicle speed higher than 40 km/h. Industrial testing is often performed on winter proving grounds, but such tests focus on examination of prototypes; they do not constitute research for scientific purposes.

The second objective of full-scale testing is performing traction tests on prepared proving grounds with special attention to various snow conditions. Probably the most research of winter traction tests and vehicle dynamics on slippery surfaces has been performed at the Engineer Research and Development Center's Cold Regions Research Engineering Laboratory (ERDC-CRREL) at Hanover, New Hampshire, in the United States. An instrumented vehicle equipped with advanced measurement systems has been used for traction, motion resistance, tyre lateral force, slalom, circle, and other test measurements. The tests are conducted on a level 1000×1000 m test pad under various surface conditions (ice, densely packed snow, partially packed snow, fresh snow). One important purpose of testing was to validate winter traction systems such as the Vehicle Terrain Interaction (VTI) model (Coutermarsh and Shoop 2009, Parker el al. 2009).

1.2.2 Vehicle Impact and Soil Compaction

1.2.2.1 Military Vehicle Impacts on Training Grounds

Since the late 1970s, the environmental community has debated the effects of off-road military and recreational vehicles in natural areas. Most research on the effects of military vehicle training on soils, vegetation, and wildlife has been observational (Anderson et al. 2005a,b). For a more quantitative assessment of vehicle impact and better management of training lands, the United States Army implemented the Range and Training Land Assessment (RTLA) program, originally called the Land Condition Trend Analysis (LCTA) program. Under RTLA, a training vehicle load is characterised by measures such as tracked vehicle equivalents (TVEs)—a numerical rating of each piece of tactical equipment as compared to a

standard vehicle. A TVE accounts for the relative environmental damages caused by different types of vehicles.

Other measures include tracked vehicle days (TVDs) and manoeuvre impact miles (MIMs); see Anderson et al. (2005). The C factor or vegetative cover factor is a function of ground cover, aerial cover, and minimum dip height. The C factor is used mainly to quantify vehicle impact on soil erosion. For a specific manoeuvre analysis and its correlation with field impact, the disturbed width (DW) parameter defines the width of disturbance caused by an off-road vehicle. The impact severity (IS) quantifies the severity of disturbance of an area by a single pass of a vehicle (Li et al. 2007a,b).

These indices, while simple and practical to use, are general and lack deep insight into microscopic changes in soil and vegetation. Althoff and Thien (2005) performed a detailed experimental study to assess the impacts of a M1A1 main battle tank on physical, chemical, and biotic indicators of soil and on total vegetative biomass. They sampled soil subjected to three treatments (no traffic, tank traffic under wet soil conditions, and tank traffic under dry soil conditions). The test vehicle performed figure-eight patterns on three sampling area types: crossing, straight, and curving. Results showed significant effects of vehicle loads on soil compaction, penetration resistance, rut depth, soil bulk density, texture, chemical composition, plant biomass, soil microbial diversity, and nematode and earthworm taxa. The tank disturbance significantly reduced the total vegetative biomass compared with biomass in non-trafficked areas. The effects of vehicle loads, however, depended on soil type and moisture conditions (Althoff and Thien 2005).

1.2.2.2 Soil Compaction by Agricultural Vehicles

Soil compaction is a physical process that modifies soil pore volume and pore structure. Intensive mechanization of tillage disturbs natural soil sustainability and initiates a number of physical, chemical, and biological processes that change soil environment. In agricultural work, soil—a vital ecosphere for plant vegetation—also becomes a running surface for the tractors and other machines used on the fields. Every agricultural vehicle running over soil causes volumetric and shear strain. Volumetric strain is characterised by an increase of soil density, while shear strain involves relative displacement of soil layers. Volumetric strain is dominant and may constitute up to 90% of the total mechanical strain. It changes the packing of the solid phase of the soil, thereby changing the volumes of soil pores and slowing air filtration and water movement within the soil volume. Shear strain may change the aggregate structure of the solid phase of the soil.

Soil compaction represents the relationship of changes in density and stress, taking moisture content into account. Stress caused by running wheels of tractors or machines depends on vertical loads and contact

surface. It is obvious that the use of wide low-pressure tyres may result in lower soil density, but an increase of forward speed also results in less compaction.

In general, the impact of soil compaction on plant growth and subsequent crop yield is negative. Diminished permeability of the soil–pore system to water and air in compacted soil may decrease soil aeration and infiltration rates, causing soil erosion and the loss of fertile layers (Wiermann et al. 1999).

Another important concern is the high cost of subsoiling or tillage below depths of 35 cm. This deep ripping is required to loosen upper soil horizons and it consumes a tremendous amount of machinery power (Konstankiewicz and Pytka 2008).

Mitigating soil compaction is a priority research problem in agricultural engineering. Negative effects of wheel or track loads on arable soils and crop yield have been the topics of many research projects, conferences, papers, and books. The International Soil and Tillage Research Organization is a world community with the goal of improving land use in a manner that mitigates environmental degradation (Horn 2006). Raper (2005) presented a summary of good practices for minimizing soil compaction. It is assumed that soil compaction, although it may not be eliminated, can be controlled and reduced through intelligent management of field traffic.

Recommendations to reduce negative effects of vehicle traffic on soils include reducing axle loads; reducing ground pressure by using radial tyres, dual wheels, or tracks; conducting field work only when the soil moisture is less than 60% of field capacity; using conservation tillage and controlled traffic; and subsoiling to eliminate compacted soil profiles. Raper discussed these recommendations in light of previous research results. For example, using tracks instead of tyres may not be effective; similar soil pressures have been measured under rubber tracks and under tyres of vehicles with similar mass. Peak pressures exerted under rollers were similar in magnitude to those under tyres. Moreover, the use of dual wheels doubled the area of impacted soil (Raper 2005).

1.2.2.3 Modelling Soil Compaction

A variety of methods have been used to model soil compaction. A classical compression theory assumes the packing state of soil (void ratio) is related to the log of the effective stress. A simplified version of this approach uses compressive pressure instead of the effective stress. Models in critical state soil mechanics describe soil response to the widest possible range of stress states. This method, developed by civil engineers for saturated soils, has also been applied to unsaturated agricultural soils. This approach requires separation of compression stresses from shear stresses. Empirical methods in soil compaction studies depend mainly

on deriving relationships between final bulk density of compacted soil and factors affecting it, including weight, wheel dimensions, number of passes, speed, initial bulk density, initial thickness of soil layer, water content, and other parameters.

One of the simplest methods is weighing soil samples of 100 cm^3 volume before and after wheeling events. More sophisticated methods include determination of bulk density by means of x-ray radiation. Results from authors worldwide show that the variety of methods, units, and expressions applied to innumerable combinations of wheel types, field conditions, and soil characteristics is confusing. Soil scientists have a strong need for a coherent and general theory for predicting soil compaction (Soane 1983).

The above-mentioned studies of soil compaction assume continuity and homogeneity of soil media. However, there is need for a theory that can employ a stress–strain relationship to soil investigation that considers time factors and immediate strains at the high rates that occur in loose agricultural soils impacted by running wheels. Rheology can account for the time factor but is insufficient for the response of loose agricultural soil. Rheological models are expressed in terms of differential equations and the mechanical analogues of three fundamental properties of matter: elasticity, viscosity, and plasticity. Soil, as a three-phase medium, possesses all three properties.

The variables in rheological models are stress and strain, while the parameters describing the body properties are coefficients of elasticity and viscosity. A particular model is created by parallel or serial combinations of mechanical analogues. One of the simplest rheology models for soil is the three-element type developed by Poyting-Thomson. However, Konstankiewicz and Pytka (2008) showed that, based on the experimental verification, rheology models are insufficient for describing loose agricultural soil responses to wheel loads. Experimental results differed substantially among model stress–strain relationships obtained for several soils with an assumption of constant coefficients of viscosity and elasticity.

The weakness of classical rheology lies in its assumption of linear characteristics of equations formulated phenomenologically. A modification based on statistical thermodynamics obtained coefficients of elasticity and viscosity as functions of time and applied stress. This approach significantly improved the resulting stress–strain relationship for soil analysis (Konstankiewicz and Pytka 2008).

Pukos (1994) presented an unorthodox approach to the problem of soil compaction modelling. This method assumes that soil consists of a great number of elements (particles, pores, aggregates) that differ in size and shape. The interactions among them are complex and it is impossible to describe all the interactions with a limited number of equations. Thus, the model considers the parameters influencing soil deformation as random

variables. The random variables introduced to describe soil structure were (1) diameters of soil skeleton particles (aggregates), (2) pore diameters, (3) pore volumes, and (4) contact forces. The probabilistic theory expresses the process of soil compaction in terms of the probability of a solid particle entering a pore. The probabilistic equation derived for a single pore was integrated over all sizes of pores, aggregates, particles, and contact forces to yield soil deformation as a function of soil structure and its initial conditions. Macroscopic verification experiments were performed using typical soil mechanics methods (triaxial apparatus), but lack of appropriate measuring methods led to problems identifying particular model parameters.

1.2.2.4 Stress Analysis in Soil Compaction Studies

Stress measurement and analysis play important roles in soil compaction studies. Under both laboratory and in situ conditions, pressure sensors of various designs have been used for years, but strain gage and hydraulic sensors are now more common. Horn and Lebert (1994) discussed the most important methodological aspects of soil–stress measurements, including problems with introducing transducers into soil and the effects on measurements, effects of transducer-to-soil stiffness ratio, effects of transducer design (plastic or rigid bodies), and other factors.

Nichols et al. (1987) were the first to describe stress state transducers (SSTs) in soil compaction studies. Their device, consisting of six pressure sensors, can determine the complete stress state in soil under loading. Measurements of soil stress with the SST were performed with differing factors, such as reduced inflation pressure, wheel load, and succeeding passes of a wheel (Bailey et al. 1996, Horn et al. 2003, Raper et al. 1995, Way et al. 1996, Wiermann et al. 1999 and 2000).

References

Allen C.C., Morris R.V., Lindstrom D.J. et al. 1997. JSC MARS-1: Martian regolith simulant. *Lunar and Planetary Science XXVIII*, Document 1797.

Althoff P.S. and Thien S.J. 2005. Impact of M1A1 main battle tank disturbance on soil quality, invertebrates, and vegetation characteristics. *J. Terramech.* 42: 159–176.

Anderson A.B., Palazzo A.J., Ayers P.D. et al. 2005a. Assessing the impacts of military vehicle traffic on natural areas: Introduction to special issue and review of relevant military vehicle impact literature. *J. Terramech.* 42: 143–158.

Anderson A.B., Wang G., Fang S. et al. 2005b. Assessing and predicting changes in vegetation cover associated with military land use activities using field monitoring data at Fort Hood, Texas. *J. Terramech.* 42: 207–229.

Armbruster K. 1986. Development of a single wheel tester for measurements on driven angled wheels. *Proc. 4th ISTVS European Conference*, Wageningen.

Aubel T. 2005. FEM simulation of the interaction between elastic tyre and soft soil. *Proc. 11th ISTVS Conference,* Lake Tahoe, NV.

Bailey A.C., Raper R.L., Way T.R. et al. 1996. Soil stresses under a tractor tire at various loads and inflation pressures. *J. Terramech.* 33: 1–11

Bekker M.G. 1969. *Introduction to Terrain Vehicle Systems.* Ann Arbor, MI: University of Michigan Press.

Brudnak, M., Nuñez, P., and Reid, A. 2002. *Real-Time, Distributed, Unmanned Ground Vehicle Dynamics and Mobility Simulation*. SAE Technical Paper 2002-01-1178.

Brudnak M.J., Gunter D.D., and Bylsma W. 2007. Modeling of moguls on an endurance test course. *Proc. ISTVS Conference,* Fairbanks, AK.

Coutermarsh G. and Shoop S.A. 2009. Tire slip-angle force measurements on winter surfaces. *J. Terramech.* 46: 157–163.

Cronje P.H. and Els P.S. 2010. Improving off-road vehicle handling using an active antiroll bar. *J. Terramech.* 47: 179–189.

Depperman K.-H. 1988. Einfluss von Schneeketten auf die Fahrdynamik allradgetriebener Personen Kraftwagen. *ATZ (Automobiltechnische Zeitschrift)* 90(4):209–11.

Durst P.J., Mason G.L., McKinley B. et al. 2011. Predicting RMS surface roughness using fractal dimension and PSD parameters. *J. Terramech.* 48: 105–111.

Ferhadbegovic B., Brinkmann Ch., Kutzbach H.D. et al. 2006. Hohenheim tyre model: A transient model for driving dynamics simulation. *Proc. ISTVS Conference*, Budapest.

Fervers C.W. 2004. Improved FEM simulation model for tire–soil interaction. *J. Terramech.* 41: 87–100.

Haycraft, W.R. 2011. History of construction equipment. *J. Constr. Eng. Mgt.* 137: 10.

Hetherington J.G. and Littleton I. 1987. The role of mean maximum pressure in specifying cross-country mobility for armoured fighting vehicle design. *J. Terramech.* 24: 263–280.

Hohl G.H. 2003. Military terrain vehicles. *Proc. 9th ISTVS European Conference.*

Horn R., Fleige H., Peth S., and Xinhu P. (eds.). 2006. *Soil Management for Sustainability: Advances in Geoecology.* Reiskirchen, Germany: Catena Verlag.

Horn R. and Lebert M. 1994. Soil compactability and compressibility. In *Soil Compaction in Crop Production.* Amsterdam: Elsevier.

Horn R., Way T., and Rostek J. 2003. Effects of repeated tractor wheeling on stress–strain properties and consequences on physical properties in structured arable soils. *Soil Till. Res.* 73: 101–106.

Jakliński L. 2006. *Mechanika układu pojazd-teren w teorii i badaniach. Wybrane zagadnienia* (in Polish). Warsaw: Warsaw University of Technology Press.

Janosi J. And Hanamoto B. 1961. The analytical determination of drawbar pull as a function of slip for tracked vehicles in deformable soils. *Proc. First ISTVS Conference,* Torino.

Kiernicki, Z. and Gardyński L. 2011. VIII Trial 4x4 Politechnika Lubelska. Biuletyn Informacyjny Politechniki Lubelskiej, pp. 39–40 (http://www.pollub.pl/files/4/attachment/BIPL-26.pdf)

Konstankiewicz K. and Pytka J. 2008. Soil engineering. In *Encyclopedia of Soil Science.* Dordrecht: Springer.

Larmine J.C. 1992. Modification to the mean maximum pressure system. *J. Terramech.* 29: 239–255.

Lee J.H. 2009. A new indentation model for snow. *J. Terramech.* 46: 1–13.

Lee J.H. and Wang W. 2009. Characterization of snow cover using ground penetrating radar for vehicle trafficability: Experiments and modeling. *J. Terramech.* 46: 189–202.

Lee J.H. 2011. Finite element modeling of interfacial forces and contact stresses of pneumatic tires on fresh snow for combined longitudinal and lateral slips. *J. Terramech.* 48: 171–197.

Lee R. and Sandu C. 2009. Terrain profile modeling using stochastic partial differential equations. *Int. J. Vehicle Systems Model. Test.* 4: 318–356.

Li L., Sandu C., Lee J. et al. 2007a. Development of tire-on-stochastic snow models using a polynomial chaos approach. *Proc. ISTVS Conference,* Fairbanks, AK.

Li Q., Ayers P.D., and Anderson A.B. 2007. Modeling of terrain impact caused by tracked vehicles. *J. Terramech.* 44: 395–410.

Maclaurin B. 2007. Comparing the NRMM (VCI), MMP and VLCI traction models. *J. Terramech.* 44: 43–51.

Michaud S., Richter L., Thueer T. et al. 2006. Rover chassis evaluation and design optimisation using the RCET. *Proc. 9th ESA ASTRA Conference*, Noordwijk.

Nakashima H., Furii H., Oida A. et al. 2010. Discrete element method analysis of single wheel performance for a small lunar rover on sloped terrain. *J. Terramech.* 47: 301–327.

Nichols T.A., Bailey A.C., Johnson C.E. et al. 1987. A stress state transducer for soil. *Trans. ASAE*, 30: 1237–1241.

Ogorkiewicz R. 1968. *Design and Development of Fighting Vehicles*. London: Macdonald Publishing.

Oravec H.A., Zeng X., and Asnani V.M. 2010. Design and characterization of GRC-1: A soil for lunar terramechanics testing in Earth-ambient conditions *J. Terramech.* 47: 361–377.

Owens C. 2006. Characterization summary of JSC-1AF lunar mare regolith simulant. Marshall Space Flight Center. Document Version 1.6.2.

Patel N., Slade R., and Clemmet J. 2010. The ExoMars rover locomotion subsystem. *J. Terramech.* 47: 227–242.

Parker M.W., Shoop S.A., Coutermarsh B.A. et al. 2009. Verification and validation of a winter driving simulator. *J. Terramech.* 46: 127–139.

Plesser J. 1997. Dynamisches Verhalten von Ackerschlepperreifen in Vertikal- und Längsrichtung auf fester Fahrbahn. Doctoral thesis, University of Stuttgart.

Pukos A. 1994. Quantitative description of structural changes in soil and plant material during deformation. *Int. Agrophysics,* 8: 103–112.

Raper R., Bailey A., Burt E. et al. 1995. The effect of reduced inflation pressure on soil–tire interface stresses and soil strength. *J. Terramech.* 32: 43–51.

Raper R. 2005. Agricultural traffic impacts on soil. *J. Terramech*. 42: 259–280.

Richter L., Ellery A., Gao Y. et al. 2006. A predictive wheel–soil interaction model for planetary rovers validated in test beds and against MER Mars rover performance data. *Proc. 10th ISTVS European Conference,* Budapest.

Schlotter V. and Keen A. 2003. The dynamic characteristic of off-road tyres. *Proc. 9th ISTVS European Conference.*

Shoop S.A. 2001. *Finite Element Modeling of Tire-Terrain Interaction*. ERDC/CRREL TR-01-16.

Soane B.D., Ed. 1983. *Compaction by Agricultural Vehicles: A Review*. Scottish Institute of Agricultural Engineering. Technical Report 5.

Stacheder M. 2005. TDR and low-frequency measurements for continuous monitoring of moisture and density in a snow pack. *Int. Agrophys.* 19: 75–78.

Sun T.C., Chaika M., Gorsich D. et al. 2007. Methods of simulation of terrain profiles. *Proc. ISTVS Conference,* Fairbanks, AK.

Wakabayashi S., Sato H., and Nishida S.I. 2009. Design and mobility evaluation of tracked lunar vehicle. *J. Terramech.* 46: 105–114.

Way T., Johnson C., Bailey A. et al. 1996. Soil stress state orientation beneath a tire at various loads and inflation pressures. *J. Terramech.* 33: 185–194.

Whitlock A. 2006. Precision farming: Supporting innovations. In *Soil Management for Sustainability*. Reiskirchen: Catena.

Wiermann C., Way T.R., Horn R. et al. 1999. Effects of various dynamic loads on stress and strain behavior of a Norfolk sandy loam. *Soil Till. Res.* 50: 127–135.

Wiermann C., Werner D., Horn R. et al. 2000. Stress–strain processes in a structured unsaturated silty loam luvisol under different tillage treatments in Germany. *Soil Till. Res*. 53: 117–128.

Zeng X., He C., Oravec H.A. et al. V.M. 2010. Geotechnical properties of JSC-1A lunar soil simulant. *ASCE J. Aerospace Eng.* 23: 111–116.

2

Measurement of Soil Stress and Deformation

In nature, we identify various stresses: mechanical, thermal, water and air, biological, and human. Generally, no matter what kind of stress is involved, it always follows an internal or external load. Internal loads result from the interactions among particles, elements, or subsystems of an object; external loads are generated by factors outside an object. One important difference between stresses and loads is that the stresses are always internal even if the loads are external. Thus, stress always occurs among the elements of a loaded object.

We consider that soil stresses are mechanical (although other stresses also occur in soil) and arise from external forces. The two types of external forces are (1) surface forces distributed over the surface area of a body, and (2) body forces derived from gravitational or inertia effects and transmitted over the volume of a body. Those forces are transmitted throughout a finite part of soil volume and finite surface areas of soil particles. Their values differ at any point, in contrast to metals or solids. This is because of the visco-elasto-plasticity nature of soil. The energy applied to soil is dissipated and the range of force transmission is narrowed. However, at any point within the active stressed volume of soil, we can define stress as a density of forces F acting on an infinite small area A (Figure 2.1):

$$Stress = \frac{Force}{Area} \tag{2.1}$$

The stress is a tensor and has direction. When a stress is compressing, it has positive values. Otherwise, tensile stress is negative. In general, the stress direction is other than the normal to the A plane and we therefore resolve the stress vector into two components: normal, designated σ, and tangential (shear) τ. They are defined as

$$\sigma = \lim \frac{\delta F_n}{\delta A}, \ \tau = \lim \frac{\delta F_s}{\delta A} \tag{2.2}$$

where F_n and F_s are the two components of the force F, normal to the plane and other than normal, respectively (Megson 2010).

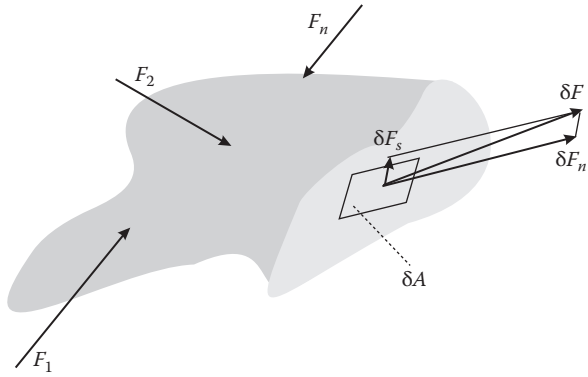

FIGURE 2.1
Illustration of the stress definition.

The determination of soil stress caused by machinery traffic requires the use of stress transducers properly installed at different depths and distances from the centre line of a wheel. In field experiments, natural undisturbed soil is subjected to excavation, penetration, and installation of a stress sensor whose mechanical properties are much different from those of the soil medium. The complexity of soil requires the use of non-standard sensor systems and experimental procedures that depend on soil mechanical (stiffness and strength), structural (soil particle distribution, material of soil medium), and physical properties. A specific sensor system must be designed for each investigated soil. The desired results determine the choice of sensor for a given soil type.

A typical arable soil is very deformable, and any mechanical input (by wheeling or tillage) changes the shape of the surface. Complete information on the mechanical behaviour of soil is provided by both the soil stress state and extent of deformation. This chapter covers techniques for measurement of both soil stress and deformation. It discusses factors to consider in the design of sensor systems and describes the instruments we built for the experiments described in subsequent chapters.

2.1 Soil Stress Measurements: Introduction

We determine soil stress by measuring the dynamic response of a transducer placed in the investigated soil. Transducers can be of various kinds; generally they change mechanical inputs (force or pressure) into electrical

outputs. Although we identify soil stress as these measured mechanical inputs, the soil pressure or forces in soil may vary from the actual soil stress. In other words, a transducer (sensor) measures soil pressure of greater or smaller value than actual soil stress. We can presume that these erroneous measurements are caused by stress redistribution on the sensor surface together with longitudinal stresses caused by many factors that are discussed below. However, the most significant factor seems to be the stiffness of the sensor body. If the sensor is stiffer than the soil, we obtain pressure values greater than real values (over-registration); when the sensor stiffness is less than soil stiffness, the measured pressure is smaller than the actual value (under-registration).

Additionally, we realize that placing a sensor into soil changes its structure. Placement procedures may damage the primary structure of a soil and change its porosity, bulk density, and other characteristics. As we determine stress states in the soil contacting the sensor, we may be investigating soil that displays different mechanical properties from the surrounding soil. It is therefore necessary to investigate the interactions between stress sensors and soil.

2.1.1 Significant Features of Sensors Affecting Stress Determination

2.1.1.1 Sensitivity

We define sensor sensitivity as the ratio of a maximum applied input value (force, pressure) to maximum indicated output value (response):

$$s = \frac{n_{IND\,\max}}{p_{\max}} \tag{2.3}$$

In other words, sensitivity is the smallest value of applied input value that is measured and yet quantified by the sensor as a whole unit (for example, 1 Pa, 1 mV, or 1 N). Sensitivity is dependent on sensor design and also on signal conditioning unit resolution. It is strongly recommended that the resolution be greater than the sensitivity. Resolution is quantified by bits; for example, in an 8-bit sensor, the resolution is the full measuring range divided by 2^8.

2.1.1.2 Non-Linearity

In most cases, sensors used for stress determination are linear and the relationship between applied input and measured output can be presented graphically as a line. Otherwise, a sensor's non-linearity can be expressed as follows (see also Figure 2.2 for notation):

$$l = \pm \frac{n_1}{n_{IND\max}} \tag{2.4}$$

Some non-linearity may be caused by sensor design. Others causes arise from interactions of the sensor and investigated material.

2.1.1.3 Hysteresis

When a sensor is first loaded and then relaxed, the relation between an applied impulse (force) and the response of the sensor may be graphically presented by the same curve (line). If the output consists of two semi-parallel lines instead of a single line, we expect the sensor to have hysteresis that can be expressed as

$$h = \frac{n}{n_{IND\max}} \tag{2.5}$$

The greater the distance between those two lines, the more significant is the hysteresis. Positive hysteresis exists when the loading line over-registers; otherwise, we have a negative hysteresis.

2.1.1.4 Dynamic Instability

The difference in a sensor's output over several cyclic repetitions of the same input value is called dynamic instability. It occurs mainly when we have chosen an improper type of sensor for a specific material or for specific measurement conditions.

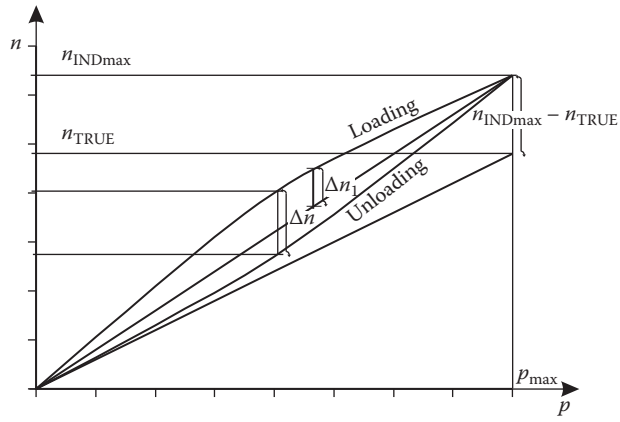

FIGURE 2.2
Factors affecting soil stress measurements.

2.1.1.5 Relative Error

The relative error is the over- or under-registration captured by a sensor divided by the real value:

$$e_R = \frac{n_{IND\max} - n_{TRUE}}{n_{TRUE}} \tag{2.6}$$

Those errors always occur because of numerous factors, including sensor design and the properties of the investigated material. It is important to be able to determine such factors and quantify errors with adequate precision.

2.1.1.6 Time Inertia

Time inertia of a sensor occurs when a measured output signal is phase shifted with an applied input. The causes for this lie in the sensor's design.

2.1.2 Factors Influencing Precision of Measurements

We can divide factors influencing determination of soil stress into three groups:

A. Factors related to the design and characterisation of a sensor
B. Factors related to the qualities of an investigated medium
C. Conditions of measuring practices

Factors A and B are partially interdependent. We can minimise the A factors when designing a sensor, but we should clearly understand the B factors. The A factors are classified as:

A1 (thickness-to-diameter ratio) — For the ideal sensor, the ratio should be 0 (zero). At 0, neither under- nor over-registrations occur because of minimal structure damage in the case of a thin sensor.

A2 (ratio of stiffness of investigated material to sensor) — This ratio should be about 1 to 10 for best results. Stiffness can be identified with a modulus of deformation.

A3 (deformation of sensor membrane related to membrane diameter) — If this ratio is more than 1 to 5000, we can expect a sensor to be significantly incorrect.

A4 (distribution of pressure on sensor surface) — This factor is related to the ratio of the active and passive surface areas of a sensor as well as to the shape of those surfaces. For the best exact measurements, the recommended ratio is around 0.4–0.5 and the surfaces should be rounded.

Certainly, the active part of the sensor should be in the centre with the passive part surrounding it.

A5 (forces acting parallel to membrane) — Sensors that use strain gages as transducers can measure forces in a horizontal plane (out of our interest) while no forces in a vertical (normal) direction occur.

2.2 Characterisation of Soil Stress Transducers

2.2.1 Choosing Sensor Type, Membrane Material, and Pressure Transducer

Pressure transducers are used for most soil stress sensing. Thus, a part of a sensor (or rarely all of it) is deformed when subjected to stresses generated in soil. Theoretically, the deformation of the sensitive area should be no smaller than the deformation of the soil structure. This would prevent the damage of soil structure caused by stresses **even if no stresses are registered**, as in a case of a rigid sensing element. On the other hand, the sensing element should not demonstrate elasticity with significant hysteresis. Otherwise, part of the stress energy would be dissipated and would not be registered by the transducer. The size and proportions of a sensor should be determined by two general factors: soil structure damage by the installation and soil aggregate (particle) size.

In general, three types of pressure transducers are used for soil stress determination: (1) electrical resistance strain gage with an elastic deforming sensing element (diaphragm), (2) hydraulic sensors that are also subjected to elastic deformations, and (3) pneumatic sensors—a diaphragm is deformed as the air (or other non-aggressive gas) is compacted (Figure 2.3). In strain gage pressure transducers, the sensing element is made of aluminum (steel is rarely used) and piezoelectric materials or semiconductors transmit the output. In hydraulic sensors, elements that stay in contact with soil are usually made of rubber or silicon (rarely steel) and fluids that transmit the pressure are silicon oils or even water. Deformable diaphragms of pneumatic sensors are usually made of thin rubber (Verma et al. 1976).

The material used for the deformable membrane influences sensor characteristics, particularly sensitivity, progressivity (or regressivity), and hysteresis. Rubber, silicon, or plastic membranes ensure the best sensitivity, whereas steel and aluminum membranes usually have higher sensitivity thresholds (they are less sensitive because of high elastic moduli). Softer membranes result in sensor regressivity; stiffer membranes cause progressivity. Hydraulic transducers tend to measure lower soil pressures than the real values; this is explained as the effect of membrane

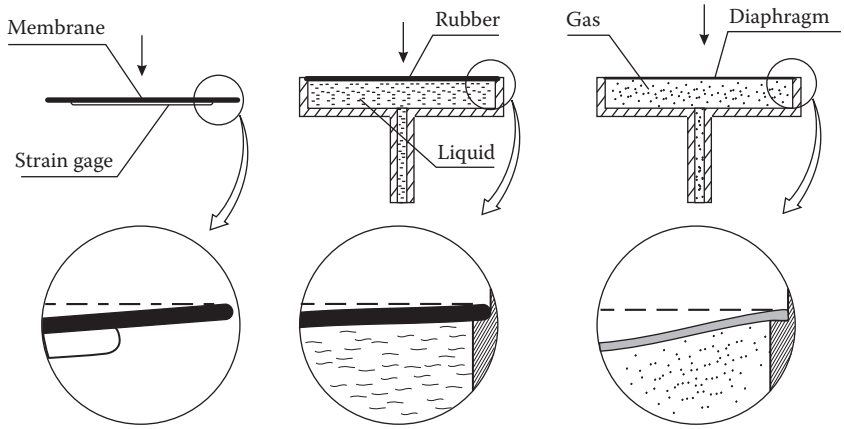

FIGURE 2.3
Three general types of transducers that are used for soil stress measurements.

deformation (membrane stiffness is lower than soil stiffness). Strain gage pressure transducers equipped with metal membranes, however, indicate greater pressures because of the greater stiffness of the elastic membrane.

Thus, we can speak of under-registration and over-registration for hydraulic and electrical resistance strain gage transducers, respectively. Figure 2.4 depicts the actions of the two types of transducers. Important disadvantages of the hydraulic transducer are possible hydraulic system problems; the hydraulic system must be liquid-tight and able to withstand the applied hydraulic pressure. In practice, a soft rubber membrane may not be able to withstand the applied loads. Further, it is difficult to fill a hydraulic system with oil or water while eliminating air from the system. Some measurement errors may depend on the membrane material hysteresis, which is higher for rubber, silicon, and plastics than for steel or aluminum.

Cooper et al. (1957) were the first to describe the development of an electrical resistance strain gage pressure sensor for use in soil investigation.

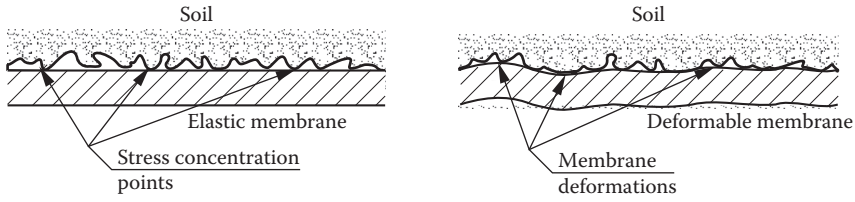

FIGURE 2.4
A principal action of two different types of soil stress transducers: strain gage (left) and hydraulic (right).

A relatively complex design utilised two electrical strain gages cemented to the lower side of a stainless steel disc soldered to a round brass box. Two additional gages used for temperature compensation and completion of a bridge circuit were cemented to the inside wall of the box; these gages were inactive in sensing the soil pressure. A slight deflection of the diaphragm caused by soil pressure was registered as a change in bridge resistance. The transducer was calibrated by placing the cells in a closed system filled with water and applying pressure to the liquid.

The use of commercially available strain gage pressure cells as transducers facilitated the design of small sensors with very stable outputs, suitable for long-term static or slowly varying measurements. (It should be noted that hydraulic sensor systems often suffer from the lack of hermeticity and do not perform long-term measurements.) Nichols et al. (1987) described 6.35-mm diameter thin diaphragm electrical resistance strain gage transducers. To keep the transducer stress–strain modulus greater than the soil modulus, aluminum was chosen for the discs to which the strain gages were mounted. Because the sensing elements were cemented on the outer surfaces of the aluminum discs (to minimise protrusion above the disc surface), the sensing gages were subjected to mechanical (vibrations, shocks) and chemical (corrosion) influences from surrounding soil. To minimise the influences of lateral forces on pressure measurements, the total contact (outer) area of the discs was covered with 0.1-mm thin Teflon tape. The sensitivity of the transducers ranged from 0.0016 to 0.0025 mV/kPa and the linearity was 0.5% to 1.0%.

2.2.2 Geometry of Soil Stress Sensor

Most soil pressure sensors are circular with the exception of some spherical hydraulic sensors (described above). A typical pressure sensor used for soil investigation is a circular plate with a diameter of 5 to 50 mm, although sensors of significantly greater dimensions are also used. The sensor height ranges from 3 to 20 mm. An important consideration is the aspect (height-to-diameter) ratio of the sensor. The investigated soil can arch onto or across the transducer, depending on the rigidity of the sensor body and the soil strength. The optimum aspect ratio is 0.1 or less; for greater ratios, pressure redistribution can significantly influence the measurements.

Because the sensor is a rigid body, pressure can concentrate on its edges and lead to uneven distribution of the pressure across the sensor. To avoid this source of error, Peattie and Sparrow (in Horn and Lebert 1994) suggested that the ratio of the sensitive area to the total contact area should be less than 0.45 for a sensor with a pressure-responsive diaphragm. The outline dimensions of a soil pressure sensor should be as small as possible to minimise errors that occur during installation and measurement. Small sensors cause smaller pressure concentration. Multiple sensors placed

close to each other can erroneously overestimate the total soil strength. It is also important to select the right shape for a soil pressure sensor. Smooth regular lines cause less damage to soil structures during installation.

2.2.3 Signal Conditioning and Data Acquisition

As mentioned earlier, pressure signals from strain gage transducers may suffer from external noise sources and connectors between the measuring system components. The noise levels may often be higher than the small voltage signals from strain gages. Such situations can be prevented with high-quality shielded-signal cables and zero-loss connectors (with golden contacts). The cable length should not exceed 2 m and the cables should have high mechanical strength.

Multi-channel measuring systems present challenges although commercially available acquisition and conversion (A/C) cards may considerably facilitate these functions. Factors to consider include the number of transducers (number of active channels), transducer output signal (uni- or bi-), required sampling rate (based on Nyquist criterion), resolution (8, 12, or 16 bits), computer type (portable PC or mobile notebook), and existing computer ports. Some software tools can help to design an optimum data acquisition system and to choose the right hardware and software for measurements.

2.2.4 Calibration of Pressure Sensors

The performance of a soil pressure sensor system depends on calibration methodology. It is best to calibrate such sensors under controlled laboratory conditions that will simulate in situ properties of the soil to be investigated. It has been assumed for some time that transducer response is influenced by the mechanical properties of the medium investigated. The best results are therefore obtained when calibration is performed in the soil that will be measured. Soil used for the calibration should also have the same or similar moisture content and compaction as the soil to be measured.

The in-soil calibration routines can also consider the effects of soil–aggregate damages on a rigid transducer body. A part of the loading energy is dissipated into shape or dilatational strain and this energy can be quantified when a pressure membrane does not deform.

Electrical signals registered by a sensor depend on forces acting on a sensing element, but the soil pressure required to determine stress depends on the contact area between a sensing element and soil particles. No information on the size of this area is available during a measurement; therefore, sensors calibrated in media other than an investigated soil can yield erroneous results. In some cases, calibrations are performed in both

air and soil. For in-air calibrations, a typical pressure chamber is used. Linear characteristics are obtained and compared with in-soil calibrations.

Harris and Bakker (1994) and Bakker and Harris (1995) developed a method for a stress state transducer (SST) calibration in soil. An SST is a grouping of six pressure transducers placed near each other so that the measured pressures can be recalculated into a complete stress state (principal stresses and their direction cosines; see Section 2.4). They installed an SST within a volume of soil that was then isotropically compressed by external air pressure with the assumption that the stresses at all points within the volume were equal. A rubber sleeve and O rings were used to prepare a soil sample with the SST inside. The cylindrical sample was placed in a triaxial chamber and subjected to air compression. Before in-soil calibration, adjustments were made to each sensor bridge supply at the values established in the air calibration. It was confirmed that each sensor over-estimated the applied stress for an investigated soil. However, the test also revealed an identical threshold value of moisture content of 55% for calibration of both in-soil and in-air tests. For a clay loam soil, the critical moisture content was 45%.

2.2.5 Installation of Transducers in Soil

Installation procedures always cause soil disturbances and soil structure damage; the extent depends on soil type and sensor size and shape. The smaller the transducer, the less significant are the influences on soil stress measurements. On the other hand, in non-aggregated or non-cohesive sandy soils, an extrinsic, rigid or deformable sensor body may cause only minor under- or over-registrations during measurements (Abu-Hamdeh and Reeder 2003).

The installation techniques must ensure that the whole sensing surface of a transducer contacts soil particles to prevent stress concentrations on a transducer (Kirby 1999). Many researchers have installed sensor systems in light-textured soil by excavating and then refilling with the already disturbed soil. Horn et al. (1992) developed an installation method using a drill in a tube that is equal to the SST in diameter. An additional tube with sharpened edges and the same cross section as the SST shaped the end of the horizontal hole in soil with precision. The SST was installed and the remaining space in the hole was refilled with disturbed soil. During the procedure, the contact between transducers and soil was continuously monitored. Even with this precise method, it was almost impossible not to disturb the investigated soil structure.

Moreover, such a procedure is not appropriate for high clay content soils. For such soils, Harris and Bakker (1994) developed a simple, efficient method of sensor system installation. An SST with six strain gage pressure transducers was inserted into a Perspex tube and kept in place at the front end with a closing disc and the tube was filled with soil of 55% moisture

content. The Perspex tube allowed visual monitoring of the filling process (that must be done carefully). After filling, the tube was inserted in a horizontal hole in the soil profile and the Perspex tube removed. The residual stresses caused by the installation procedures reached 20% of the maximum stresses measured.

2.3 Strain Gage Pressure Transducers for Soils

Strain gage pressure transducers are known as the most accurate and are suitable devices for both static and dynamic measurements (Kobielak 1991), although long-term static measurements may be affected by zero drift. Temperature changes and voltage fluctuations from a power supply can also influence the final results (output signals are functions of supply voltages). Output signals are low and usually require conditioning devices such as amplifiers or filters. These disadvantages, however, are technical and can be solved by proper instrumentation. Other problems of soil stress measurements resulting from soil–transducer interactions are

1. Design of the transducer (required measuring range, sensitivity, and accuracy)
2. Calibration of transducer that should take into account the effect of the soil (or other measured material) and its moisture content

The following sections examine design considerations for strain gage pressure transducers and describe our method of producing and calibrating these devices.

2.3.1 Design Considerations for Strain Gage Pressure Transducers

2.3.1.1 Choosing Membrane Material

The membrane material influences a transducer's characteristics, especially sensitivity (progressivity or regressivity) and hysteresis effects. Nichols et al. (1987) recommend that the ratio of transducer stress–strain modulus to soil stress–strain modulus should be 10 or greater. This recommendation, however, is difficult to fulfill because transducers are designed to be used in different soils.

Three materials are commonly used for construction of pressure transducers: steel, aluminum, and titanium. They are suitable because of their mechanical characteristics and the ability to mount the gages with glue. Steel is the easiest material for fabrication, but its Young's modulus is

TABLE 2.1

Material Properties of Basic Alloys Used as Membrane Materials

	Steel	DURAL PA9	Titanium
Young's modulus [GPa]	207	70	118
Poisson's ratio [–]	0.285	0.34	0.34

three times that of aluminum. The elasticity of the membrane affects the transducer's mechanical resistance and therefore the measurement of the applied loads (bearing capacity). From this view, steel membranes would be the best choices. Titanium is very good for dynamic measurement applications because of its high fatigue strength. This is very important in the case of dynamic multi-cyclic measurements involving heavy vehicles at wheel contact pressures over 500 kPa. Table 2.1 presents general data for three metals considered for membrane material. We used a hardened and anodized aluminum alloy (DURAL PA9).

2.3.1.2 Strain Analysis and Determination of Membrane Geometry

A strain gage transducer functions as a resistor whose resistance changes with changes in the length and cross-sectional area of the conductor as the membrane strains. To determine the basic geometrical properties of a membrane, it is therefore necessary to analyse the strains to which it is subjected. The strain state on a circular membrane is shown in Figure 2.5. The radial strain (along a radius of the membrane) and tangential strain (parallel to the plane of the membrane surface and perpendicular to its radius) at the centre of the membrane are identical (Vishay Precision Group 2011 and 2010):

$$\varepsilon_R = \varepsilon_T = \frac{3PR_0\left(1-\nu^2\right)}{8t^2E} \tag{2.7}$$

The radial strain is positive at the centre of the membrane. As you move out from the centre along a radius of the membrane, it decreases and becomes negative (Figure 2.5). The tangential strain decreases to 0 at the periphery of the membrane:

$$\varepsilon_{R0} = \frac{-3PR_0^2\left(1-\nu^2\right)}{4t^2E} \tag{2.8}$$

$$\varepsilon_{T0} = 0 \tag{2.9}$$

where $\varepsilon_{R0} = \varepsilon_R$ at the periphery of the membrane and $\varepsilon_{T0} = \varepsilon_T$ at the periphery of the membrane.

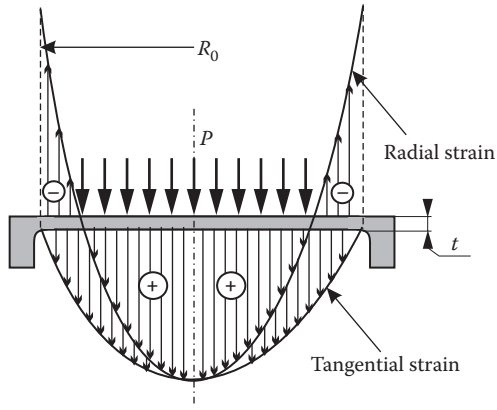

FIGURE 2.5
Strain state on a membrane of a pressure transducer subjected to applied pressure.

Equation (2.10) is the formula for membrane deflection at the centre of the transducer:

$$Y_c = \frac{3PR_0^4\left(1-\nu^2\right)}{16t^3E} \tag{2.10}$$

The total gage output, assuming a gage factor of 2.0 (product of strain and quotient of change in strain gage resistance and unstrained resistance of strain gage) and averaging the outputs of all sensing elements, is

$$e_0 = 0.75PR_0^2\frac{1-\nu^2}{4t^2E} \tag{2.11}$$

Solving Equation (2.11) for t, we obtain the thickness of the membrane for a given radius, membrane material, and pressure to be measured (Raper et al. 1995):

$$t = R_0\sqrt{0.75P\frac{1-\nu^2}{4e_0^2E}} \tag{2.12}$$

Pressure transducers with membrane outside diameters of 20 and 30 mm were fabricated. A typical membrane geometry is depicted in Figure 2.6. Sensing area diameters ($D_0 = 2R_0$) were 9.45 mm for the transducers intended to measure ranges from 0 to 30 kPa, 15 mm for higher ranges of 0 to 300 and 0 to 500 kPa, and 25 mm for 0 to 200 kPa. Those parameters were

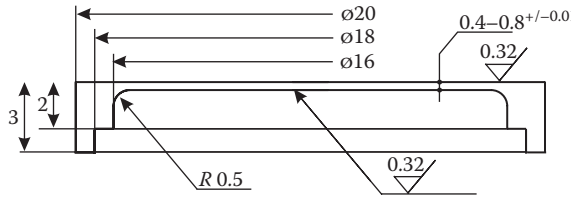

FIGURE 2.6
Geometry of a pressure transducer membrane.

set up for the diameters of available strain gages. The resulting thicknesses of the membranes are

1. For the lightest transducers, t = 0.3 mm, the required measuring range is 0 to 30 kPa, and maximum pressure of 100 kPa.
2. For the medium transducers, there are two values of thickness: t1 = 0.6 and t2 = 0.8 mm, and required measuring ranges are 300 and 500 kPa.
3. For the 30-mm transducers intended for use in silo measurements, the thickness was t = 0.6 mm while the required measuring capacity was 200 kPa.

2.3.1.3 Fabrication of Transducer

To ensure the required accuracy and repeatability of the measurements, membranes should be fabricated as precision elements based on technological requirements. First, the applied fabrication method should not introduce self-stresses into the membrane. Turning and polishing cause internal self-stresses that may influence the stability of the output signals. Moreover, those imposed stresses relax over time and initiate a zero drift effect. Those disadvantages may be minimised by postponing the final assembly of the transducer to let the stresses relax.

In the work reported in this book, we used a 3- to 6-month period of stress relaxation by keeping the rough membranes in a refrigerator. In prior fabrications, the transducers assembled with membranes without stress relaxation gave unstable signals (fluctuations of output signal from an unloaded transducer). Relaxation of a complete transducer (with a glued-on strain gage) was also possible, but caused a pronounced zero drift.

In the cases of very thick membranes (0.3 mm), traditional cutting methods for fabrication (Figure 2.7a) were not suitable, because it was not possible to fix the membrane for finishing. This caused the membrane to deform plastically. To avoid this, we used an electrical discharge machining (EDM) method to fabricate the membranes; its schematic is shown

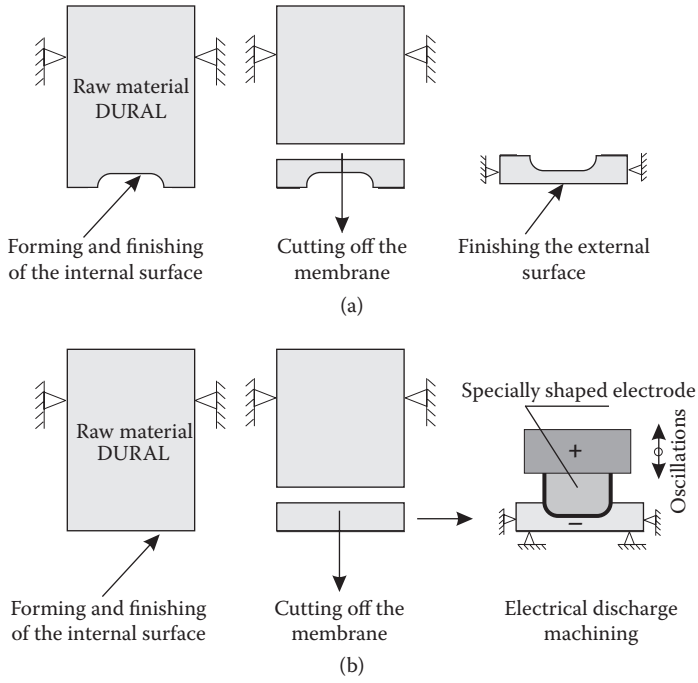

FIGURE 2.7
Two fabrication methods for transducer membranes.

in Figure 2.7b. In this method, fabricated membranes are ready for final assembly with no stress relaxation needed. The EDM method is especially well suited for cutting intricate contours or delicate cavities that would be difficult to produce with other cutting tools.

For an EDM operation, an electrode must be machined first; then the electrode is connected to the power source attached to a ram and slowly fed into the work piece. The repetitive electrical discharges that pass between the electrode and the work piece remove metal until a final shape is obtained. An EDM operation is performed during submersion in a fluid bath (usually petroleum). This fluid serves as a coolant and conductor for the current and flushes metal away. Figure 2.8 shows a membrane fabricated via the EDM method.

2.3.1.4 Final Assembly

We used circular strain gages for our transducers. The strain gages were full Wheatstone bridge types. External diameters were 9.45-mm for the lightest 20-mm transducers, 15-mm for the medium 20-mm types, and 25-mm for the 30-mm transducers. Sample strain gages used for transducer fabrication

FIGURE 2.8
A membrane of a low-pressure 10-mm transducer for snow stress measurements.

are shown in Figure 2.9. The resistance values of the strain gages were 400, 350, and 350 Ω, respectively. A proper technique of gluing the strain gage is essential for error-free operation of the transducer as well as for stability of its characteristics. Completed transducers are shown in Figure 2.10. About 50 transducers were fabricated: a series of 10 pieces of 20-mm low-range transducers, 30 pieces of 20-mm medium and high range transducers, and 10 pieces of 30-mm transducers.

FIGURE 2.9
Strain gages used for fabrication of soil pressure transducers.

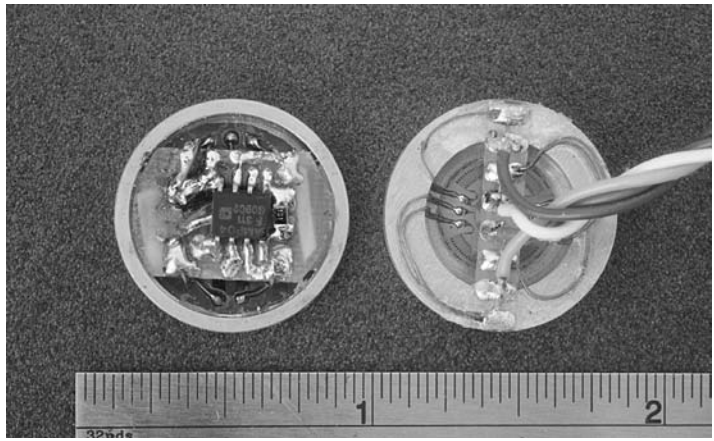

FIGURE 2.10
The actual sensors of 20-mm outer diameter: the integrated sensor with instrumentation amplifier (left) and the high-sensitivity sensor for snow.

2.3.1.5 First-Generation Signal Amplifier

Our first-generation signal amplifier system used a six-channel amplifier that operated with a DC bridge supply to minimise external electromagnetic field influences. This required additional subsystems such as a phase shifter, demodulator, and end filter to condition the signal. Measured six-pressure signals were digitalized and recorded in a high-performance data acquisition system based on a 64-channel A/D board performing 500 kS/s in 16-bit resolution. Figure 2.11 is a schematic of the electrical circuit. This system was used for laboratory measurements as described in Chapter 3.

2.3.1.6 Integrated Soil Pressure Transducer

Small signals from a strain gage require high amplification (Kitchin and Counts 1992). In most cases, the distance between a sensor and amplifier exceeds 1 m. This causes problems in signal disturbances even if high-quality shielded signal cables are used. An integration of a standard strain gage sensor with an instrumentation amplifier solves those problems. Electrical connections between a bridge and amplifier pins can be as short as millimetres and may be soldered; eliminating connectors minimises noises. Moreover, the transducer is characterised by high output signals of 1 to 5 V and good resistance to external electric and electromagnetic fields.

Our modified "mechatronic pressure transducer" consists of a typical membrane pressure transducer with a circular strain gage and a

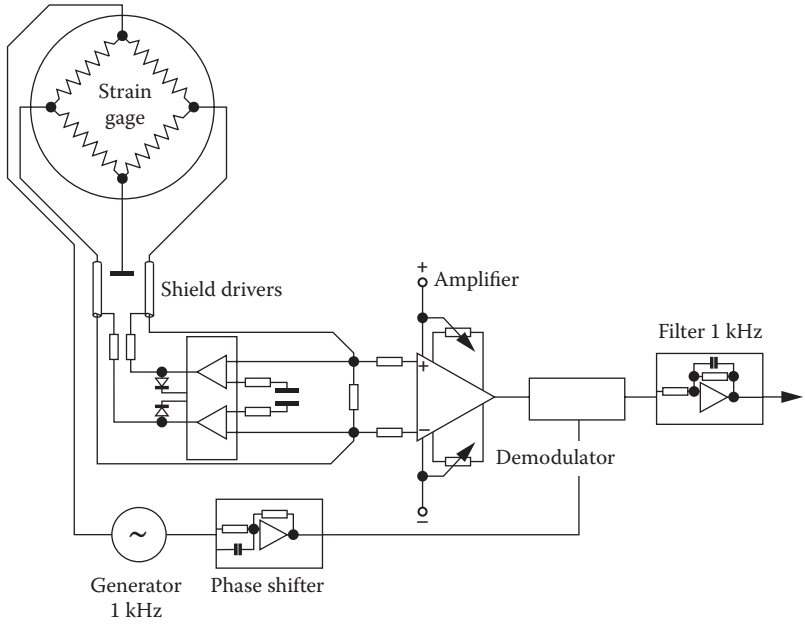

FIGURE 2.11
A schematic of the external signal amplifier.

subminiature precision instrumentation amplifier. The membrane is 20 mm in diameter and the total height of the transducer case is 3 mm; a complete bridge instrumentation amplifier must be placed and connected in that small space. Today's surface-mounted device (SMD) technology offers multi-function and specialized chips in small packages.

For the present project we used a SIM-8 package option; the only external part besides the integrated circuit is a miniature precision instrumentation amplifier with a gain ranging from 1 to 1000, set up by a single resistor. The unit works on single supply +5 V. Figure 2.12 is an electrical diagram of the signal amplifier. The gain is set at 1000 because of small input signals generated in the bridge. Figure 2.13 is a complete construction diagram of the integrated soil pressure transducer. The SMD amplifier and gain resistor were mounted on a small plate that was glued to the transducer housing. Next, electrical connections between bridge and amplifier were soldered. A standard three-wire shielded cable connected the unit with a data acquisition system.

One advantage of the integrated transducer is that the output signals range from 0 to +2.5 V and yield little noise. This is an advantage in comparison to transmitting weak signals from strain gages through several metres of cables to an external amplifier. In field experiments with fast, heavy vehicles, a portable data recorder is usually several metres away

from the measuring point because of safety considerations. Such long cables connecting with strain gages may be exposed to external electromagnetic sources that may affect the measurements.

Compact integrated transducers are easier to use, and 5-V batteries instead of the ±12-V supply in traditional strain gage applications are very helpful in field measurements. Integrated transducers in a stress state transducer (SST) were used to determine: (1) stress states of sandy, loess, and turf soils under loads of different vehicles; (2) snow stresses under loading of a snow grooming machine during preparation of ski routes; and (3) pressure distribution of organic seeds during filling and emptying of a silo.

One of the most frequent questions concerning results of these experiments relates to the precision of the measurements. During the experiments, we discovered that the type and the state of soil influence SSTs with strain gage transducers. It was assumed that a special method for calibration of the transducers may improve the accuracy of the measurements.

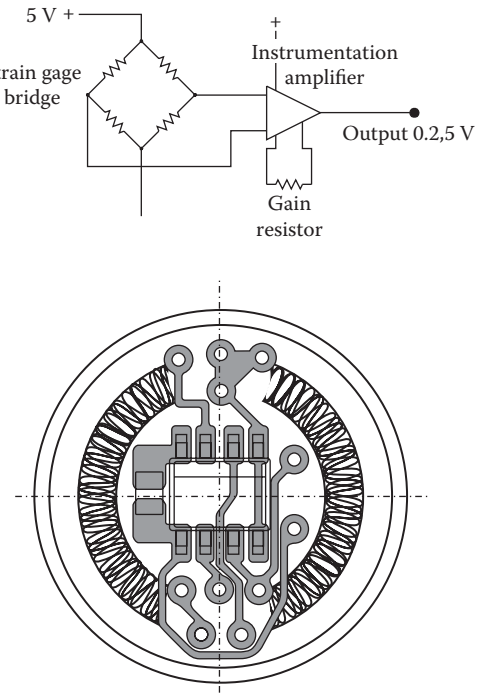

FIGURE 2.12
A schematic of the miniature signal amplifier.

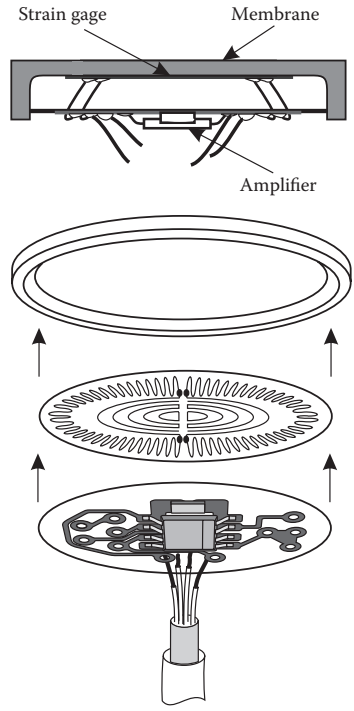

FIGURE 2.13
The concept of the integrated pressure transducer.

2.3.2 Calibration of Soil Pressure Transducers

During calibration, loading was applied to a transducer membrane through a thin layer of soil or cereal grain. In this manner, we hoped to obtain accurate data on the soil and grain effects of membrane–soil interactions (Pytka 2009). The intermediate soil layer (in contact with the transducer) should be as thin as possible (2 to 3 mm) to minimise the effects of energy dissipation (damping) in the soil. Moreover, we assumed that the soil moisture content is critical for soil mechanical properties and considered this parameter in calibration tests.

Harris and Bakker (1994) showed how soil moisture affected the calibration of their SST in soil and noted a critical soil moisture level at which in-soil calibrations equal in-air calibration. In our tests, we gradually increased gravimetric soil water content (W_{water}/W_{soil}) from 0 to ~20% for loess and sand and up to 37.5% for turf in increments (steps) of 2.5%. We used three different soils: loess, sand, and turf. Loess and sand possess opposite mechanical properties. Loess has low internal friction and high cohesion; typical sand has high internal friction and less cohesion. Turf

is an organic soil. The soils used for our tests were taken from the fields where soil stress measurements with running vehicles are performed. The sandy and loess soils are characterised in Table 2.2.

The experimental set-up for the calibration tests is depicted in Figures 2.14 and 2.15. External air pressure is applied to a rubber coat that covers the

TABLE 2.2

Material Properties of Soils Used in Calibration Tests

1	2	3
Sandy soil		
k_c = 39.31 [kN/n + 1]	S_{max} = 103 [kN/m^2]	C = 0.7 [kN/m^2]
$k\varphi$ = 105.1 [kN/n + 2]	K_w = 0.51 [cm]	φ = 29°
N = 1.2269		
Loess soil		
k_c = 56 [kN/n + 1]	S_{max} = 78 [kN/m^2]	C = 3,04 [kN/m^2]
$k\varphi$ = 64 [kN/n + 2]	K_w = 0.38 [cm]	φ = 33°
N = 0.68		

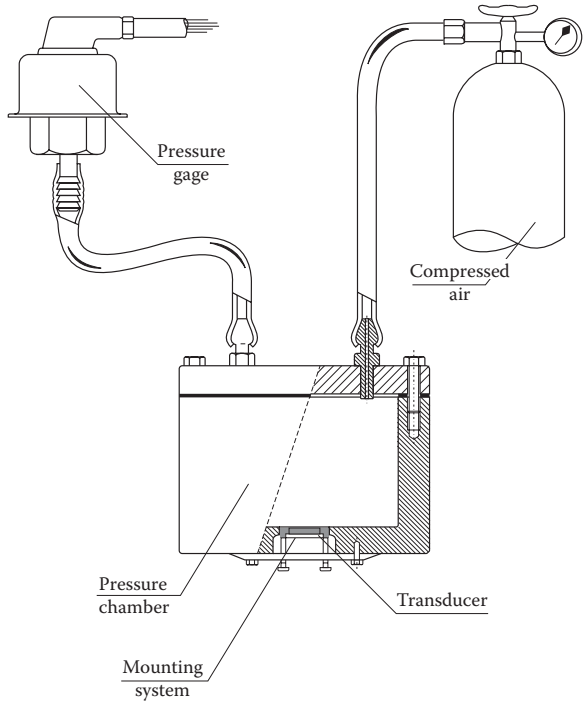

FIGURE 2.14
The experimental set-up for pressure transducer calibration in air.

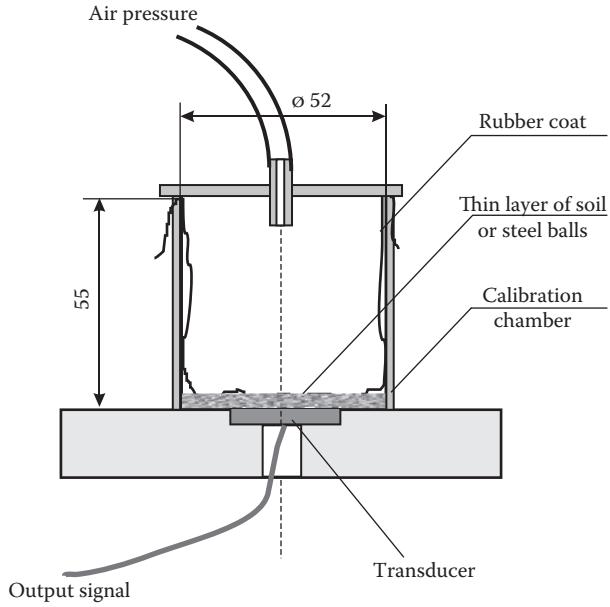

FIGURE 2.15
The experimental set-up for pressure transducer calibration in soil; units of dimensions are mm.

thin layer of soil on the membrane. The rubber coat should be as thin as possible so it will have a minimal effect on the calibration. The pressure applied ranged from 0 to 200 kPa, with a 10-kPa step in the 0 to 50-kPa range and a 25-kPa step in the 50- to 200-kPa range. The maximum value of calibration pressure was kept lower than the maximum capacity of the 20- and 30-mm transducers because of the limitations of the pneumatic system. The medium- and high-range transducers were additionally calibrated in a high-pressure chamber to obtain a full range of characteristics but as in-air calibrations without intermediate soil layers. For every combination of soil–moisture content, a minimum of five replications was performed.

Natural soils may contain aggregates or small stones that may cause stress concentrations and over-registration. Calibration was performed with steel (bearing grade) balls to counter those effects. Four diameters (2.5, 3.0, 4.0, and 5.0 mm) of balls were used. The steel balls were placed into the calibration chamber instead of the thin soil layer. Components of the calibration system are shown in Figure 2.16. The tests were performed at increasing numbers of layers (1 to 10). The lightest transducer was designed for snow stress measurements. It was calibrated in air, keeping the effects of temperature in mind: normal calibration was at +10°C and low temperature calibrations were at +2°C and –2°C.

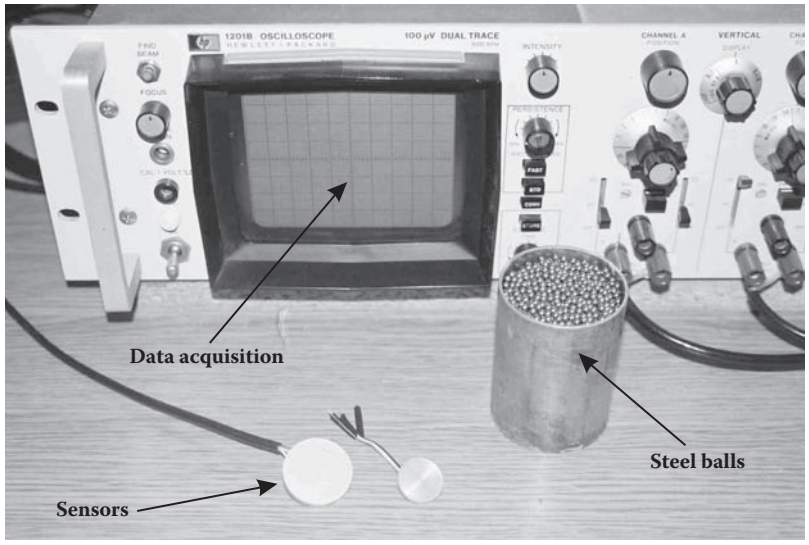

FIGURE 2.16
Components of the test stand (a cylinder with steel balls, a signal acquisition system) and two tested pressure transducers: 30-mm and 20-mm.

2.3.3 Results of Calibration Tests

2.3.3.1 In-Air Calibration

All the tested transducers showed linear voltage load responses within the design range. Typical calibration lines for the three transducers are shown in Figure 2.17. The effect of membrane thickness for the 20-mm transducers was significant for soils. The output scale factor (OSF) was about 0.6 mV/kPa for membrane thicknesses of 0.8 mm and 1.7 mV/kPa for thicknesses of 0.6 mm.

The OSF for the transducer with a 0.8-mm membrane was analysed for a "population" of 25 transducers; Figure 2.18 shows the results. A distribution of the OSF for all tested transducers is presented. The most frequent OSF is ~0.83 mV/kPa; two transducers yielded OSF results of 0.64 and 0.9. This can be explained by the effects of fabrication. The transducers for snow measurements were tested at lower temperatures. The output scale factor changed for different temperatures: ~2.700 at +10°C, 2.508 at +2°C, and 1.592 at –2°C.

2.3.3.2 In-Soil Calibration

Figure 2.19 depicts the effect of soil water content (WC) on the gage output for calibrations in the three investigated soils for the 20- and 30-mm

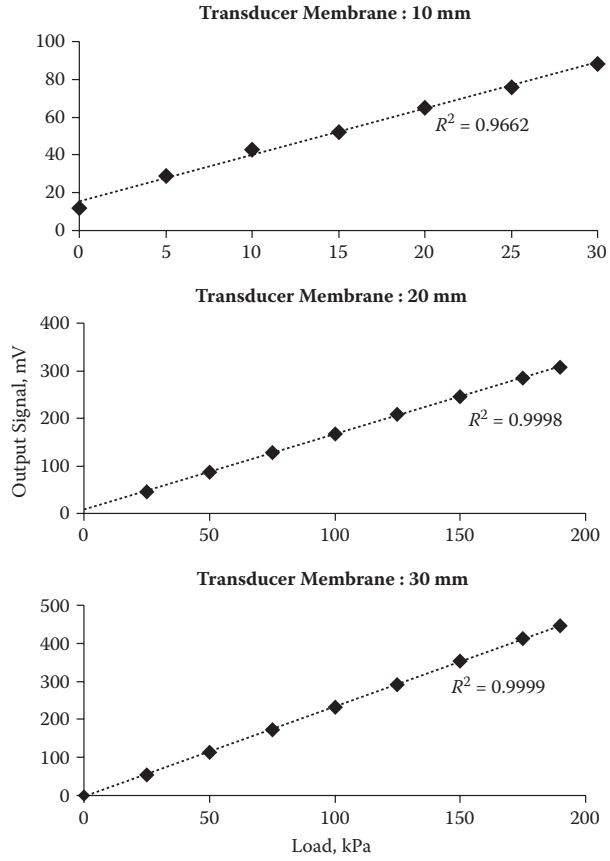

FIGURE 2.17
Typical calibration graphs for the different transducers.

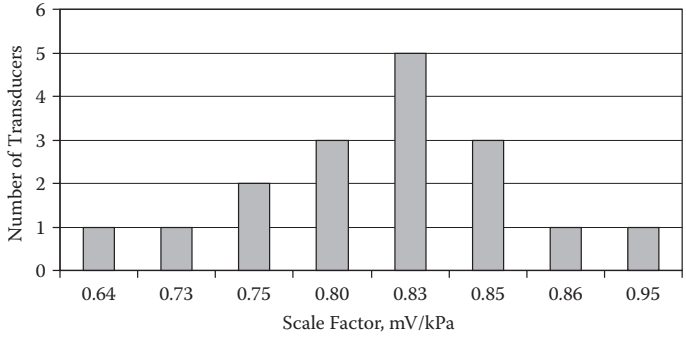

FIGURE 2.18
Distribution of the output scale factor for a "population" of 25 transducers.

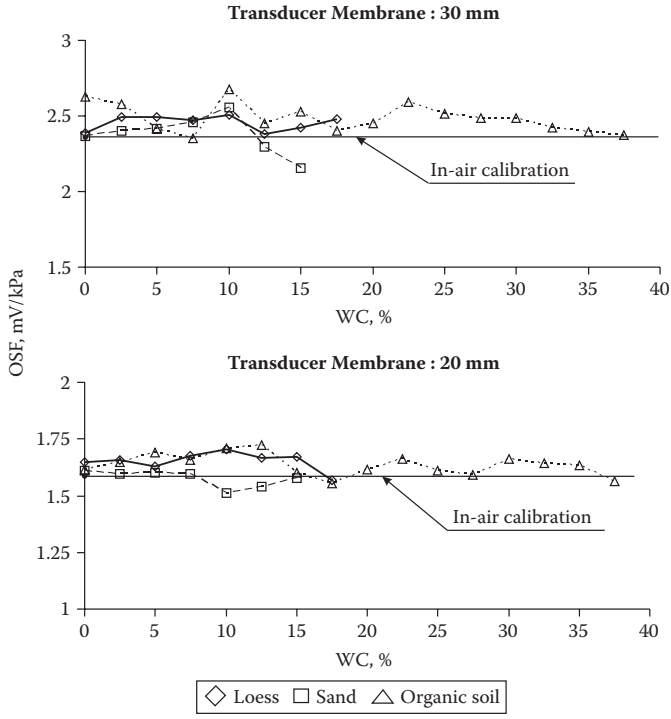

FIGURE 2.19
Effect of soil water content on the output scale factor for the two tested transducers.

transducers. At WC = 0%, the OSF is almost the same as for the in-air calibrations (with an exception of in-turf calibration of the 30-mm transducer). Water added to soils caused an increase in the OSF—the transducers became more sensitive. The effect of water in soil was the most significant in turf; it was less significant in loess and sand. Calibration in sand showed a transition between the increase and decrease of the OSFs for both transducers. This transition occurred at about 7.5% to 12.5% WC because of an "apparent cohesion" of sand at a certain WC due to the effect of suction. Finally, an apparently harder material makes the transducer–soil system less sensitive.

2.3.3.3 Calibration with Model Material (Steel Balls)

Figure 2.20 shows the relationships between the number of steel ball layers in the calibration chamber and gage output for the two transducers. The OSF values for increasing numbers of steel ball layers indicate a regressive relationship between the two transducers. This can be explained by the effect of friction between the balls and the cylinder walls or simply by the

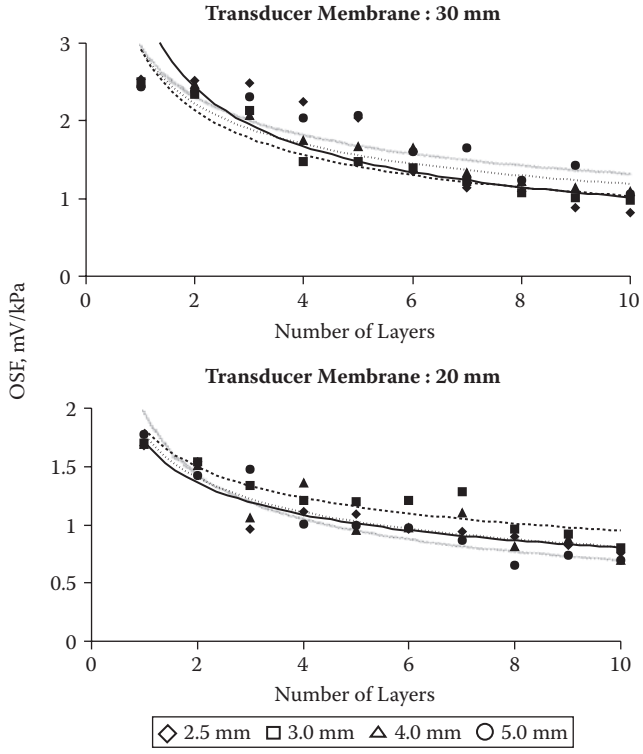

FIGURE 2.20
Effect of the number of steel balls layers on the output scale factor for the two tested transducers.

effect of the distance between the applied load and the measuring point. This is described by the Boussinesq equation:

$$p = \frac{3P}{2\pi r^2} \tag{2.13}$$

where p = pressure at the point of measurement, P = applied load, and r = distance between the measurement point and load application point.

In this case, the procedure was not a calibration; it was an investigation of stress distribution along the vertical axis. Of special interest, however, was the effect of steel balls on the standard deviations of the OSF values. For model materials such as steel balls, the fluctuations in gage output may depend on the geometry of the spatial system of the balls. According to Skibinski (1922), there are two possible spatial compositions of balls: (1) each ball touches three balls of a lower layer or (2) each ball touches two balls of a lower layer. System (2) is obviously unstable but required

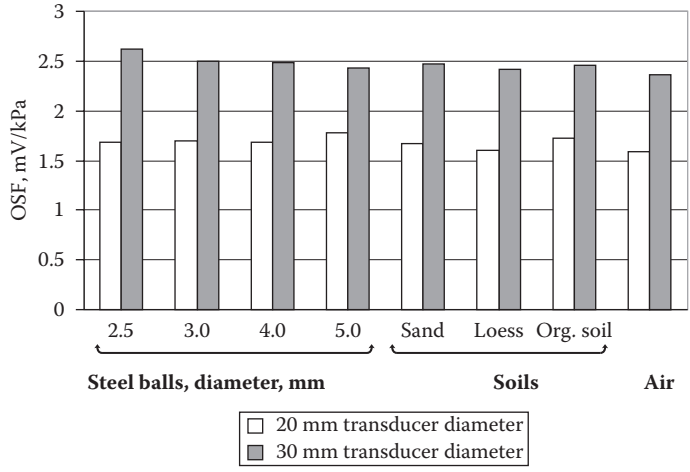

FIGURE 2.21
Effect of calibration material on the output scale factors for the tested transducers.

examination because this system becomes stable when only one of the balls in a given layer touches four balls of a lower layer. A more detailed analysis is included in the cited reference.

One conclusion of Skibinski's research was that a number of balls in any layer (also the lowest layer that contacts our transducer) can differ, so the actual number of contact points between the balls and transducer may vary. As more layers were added into the chamber, an accidental composition of the balls was created that resulted in higher deviations in gage signals.

The effects of all calibration materials on gage output are shown in Figure 2.21. Scale factors are presented for the three soils and for the steel balls in a single layer. The effect of calibration material is more pronounced for the larger transducer (30-mm); for the 20-mm transducer, the differences in gage signals are less than 10% of the full-scale output. This suggests that smaller transducers are influenced less by differences in soil gradation.

2.3.4 Summary

We designed, constructed, and calibrated strain gage pressure transducers for soil stress measurements using calibration methods encompassing the effects of the material intended to be measured. Based on the results obtained, the following conclusions can be made:

1. The method of design proposed by Nichols el al. (1987) was successfully applied to achieve the required measuring range of the transducers.
2. Of the two methods of membrane fabrication used (turning with polishing and electrical extrusion), electrical extrusion allows construction of thin-walled membranes with no residual stresses.
3. In the final assembly, signal amplifiers were integrated internally with the transducers. This simplified maintenance, especially under field conditions and minimised external noise in the output signals.
4. The calibration test stand was completed and calibrations were performed using various materials, including soils and cereal grains. The calibration material and its water content affected the output scale factor for transducer membrane diameters of 20- and 30-mm.

2.4 Stress State Transducer (SST)

As noted earlier in this chapter, the SST is a grouping of six pressure transducers placed near each other so that the measured pressures can be recalculated into a complete stress state including the principal stresses and their direction cosines. The previous section mainly covers the individual transducer types, especially strain gage transducers; this section describes theory, calculations, and construction of the grouped transducers into an SST.

2.4.1 General Theory of Operation

The SST designed by Nichols et al. (1987) allows measurement of the axial stress components σ_X, σ_Y, and σ_Z along with the normal stress components σ_{N1}, σ_{N2}, and σ_{N3}. This lets us quantify the shearing stress components and major stresses at a point. This stress state in the soil continuum, consisting of three principal stresses designated σ_1, σ_2, and σ_3 is responsible for volumetric changes in soil when loads exceed soil strength (Raper et al. 1995). Figure 2.22 shows SST geometry.

2.4.2 Calculation of Complete Soil Stress State

Figure 2.23 shows the equilibrium of a very small tetrahedron: OBCD. BCD is an arbitrary face, on which the contact force (or stress) is acting. If l, m, and n denote direction cosines at which the outward normal n is

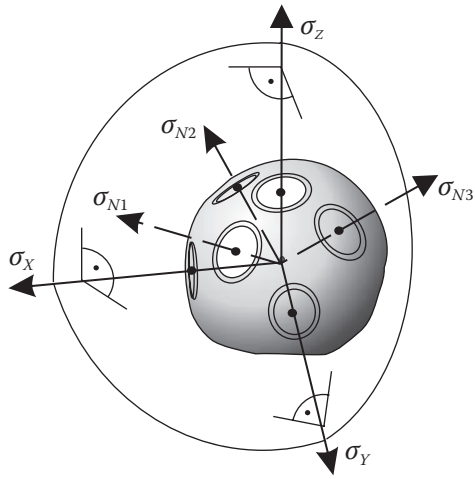

FIGURE 2.22
Geometry of the SST.

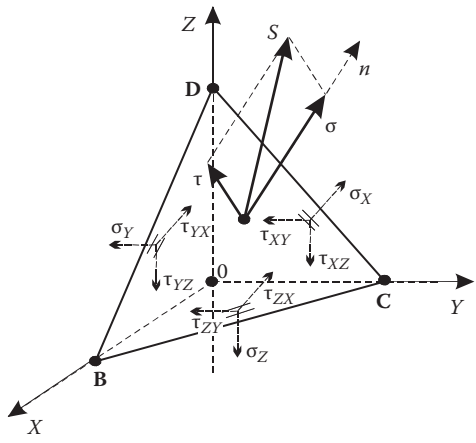

FIGURE 2.23
Equilibrium of a tetrahedron.

inclined to the co-ordinate axes X, Y, and Z, respectively, the equilibrium of the tetrahedron is described in the three following equations:

$$(S - \sigma_X)l - \tau_{XY}m - \tau_{XZ}n = 0 \tag{2.14}$$

$$-\tau_{XY}l + (S - \sigma_Y)m - \tau_{YZ}n = 0 \tag{2.15}$$

$$-\tau_{XZ}l - \tau_{YZ}m + (S - \sigma_Z)n = 0 \tag{2.16}$$

where σ_X, σ_Y, and σ_Z are stress components along the co-ordinate axes. Equations (2.14) through (2.16) will produce one non-zero solution when the determinant equals zero:

$$S^3 - (\sigma_X + \sigma_Y + \sigma_Z)S^2 + (\sigma_Y\sigma_Z + \sigma_Z\sigma_X + \sigma_X\sigma_Y - \tau_{XY}^2 - \tau_{ZX}^2 - \tau_{YZ}^2)S +$$
$$(\sigma_X\sigma_Y\sigma_Z + 2\tau_{YZ}\tau_{ZX}\tau_{XY} - \sigma_X\tau_{YZ}^2 - \sigma_Y\tau_{ZX}^2 - \sigma_Z\tau_{XY}^2) = 0 \quad (2.17)$$

The next equations introduce the stress invariants.

Normal stresses:

$$I_1 = \sigma_X + \sigma_Y + \sigma_Z = \sigma_1 + \sigma_2 + \sigma_3 \quad (2.18)$$

$$I_2 = -(\sigma_Y\sigma_Z + \sigma_Z\sigma_X + \sigma_X\sigma_Y) + \tau_{XY}^2 + \tau_{ZX}^2 + \tau_{YZ}^2 = -(\sigma_2\sigma_3 + \sigma_3\sigma_1 + \sigma_1\sigma_2) \quad (2.19)$$

$$I_3 = \sigma_X\sigma_Y\sigma_Z + 2\tau_{YZ}\tau_{ZX}\tau_{XY} - \sigma_X\tau_{YZ}^2 - \sigma_Y\tau_{ZX}^2 - \sigma_Z\tau_{XY}^2 = \sigma_1\sigma_2\sigma_3 \quad (2.20)$$

Shear stresses:

$$J_1 = \sigma_X + \sigma_Y + \sigma_Z \quad (2.21)$$

$$J_2 = \tfrac{1}{6}\left(\sigma_Y - \sigma_Z\right)^2 + \left(\sigma_Z - \sigma_X\right)^2 + \left(\sigma_X - \sigma_Y\right)^2 + \tau_{ZX}^2 + \tau_{XY}^2 + \tau_{YZ}^2 =$$
$$\tfrac{1}{6}\left(\sigma_2 - \sigma_3\right)^2 + \left(\sigma_3 - \sigma_1\right)^2 + \left(\sigma_1 - \sigma_2\right)^2 = \tfrac{1}{3}\left(I_1 + 3I_2\right) \quad (2.22)$$

$$J_3 = \sigma_X\sigma_Y\sigma_Z + 2\tau_{YZ}\tau_{ZX}\tau_{XY} - \sigma_X\tau_{YZ}^2 - \sigma_Y\tau_{ZX}^2 - \sigma_Z\tau_{XY}^2 =$$
$$\tfrac{1}{27}\left(2I_1^3 + 9I_1I_2 + 27I_3\right) \quad (2.23)$$

An SST is built with six sensors in two groupings: three sensors (σ_X, σ_Y, and σ_Z) are positioned as the arbitrary planes; the other three sensors (σ_{N1}, σ_{N2}, and σ_{N3}) act as mutually orthogonal planes. The direction cosines for these planes are given in Table 2.3. When the three arbitrary and mutually

TABLE 2.3

Direction Cosines for Arbitrary and Mutually Orthogonal Planes of SST

	σ_X	σ_Y	σ_Z
σ_{N1}	0.707	0.707	0.707
σ_{N2}	–0.707	0.707	0.707
σ_{N3}	0.707	–0.707	0.707

orthogonal pressures are determined with the SST, the shear stresses can be also calculated:

$$\tau_{XY} = -0.75\left(\sigma_{N2} - \sigma_{N3}\right) + \tfrac{1}{2}\left(\sigma_X + \sigma_Y + \sigma_Z\right) \tag{2.24}$$

$$\tau_{XZ} = -0.75\left(\sigma_{N1} - \sigma_{N3}\right) + \tfrac{1}{2}\left(\sigma_X + \sigma_Y + \sigma_Z\right) \tag{2.25}$$

$$\tau_{YZ} = -0.75\left(\sigma_{N1} - \sigma_{N2}\right) + \tfrac{1}{2}\left(\sigma_X + \sigma_Y + \sigma_Z\right) \tag{2.26}$$

The six normal stresses (σ_X, σ_Y, σ_Z, σ_{N1}, σ_{N2}, and σ_{N3}) along with the above shear stresses constitute the stress tensor that describes the stress state at a point. Substituting the stress tensor components into Equation (2.24), we can determine the principal stresses σ_1, σ_2, and σ_3. Since

$$l^2 + m^2 + n^2 = 1 \tag{2.27}$$

it is possible to determine direction cosines of the principal stresses too.

2.4.3 Fabrication of SST

The basic element of the SST is a rigid body for containing stress transducers. It was designed with the main objective of simplifying fabrication and optimising sensor exchange. Smaller and larger variants of the SST were fabricated. The body for the larger SST was milled from a piece of aluminium 70 mm in diameter. Mounting holes (nests) for the sensors were drilled in six directions and an access to the junction of the holes was drilled through the rear of the transducer. Figure 2.24 shows an exploding view of the SST assembly; construction details are included in Figure 2.25.

A second, smaller version of the SST body was milled from a 40-mm piece of aluminum. A removable cover screwed to the bottom of the SST body ensured access to the six pressure transducers. Another difference was the use of a multi-pin feature for connecting and disconnecting the signal cable.

2.5 Soil Deformation Determination

Forces acting on a body cause linear and angular displacements of particles. Those displacements may occur in three directions: *x*, *y*, and *z*. They are designated *u*, *v*, and *w*, respectively. Strain occurs when at least two particles have different displacements. Otherwise, we have only translation; the whole body

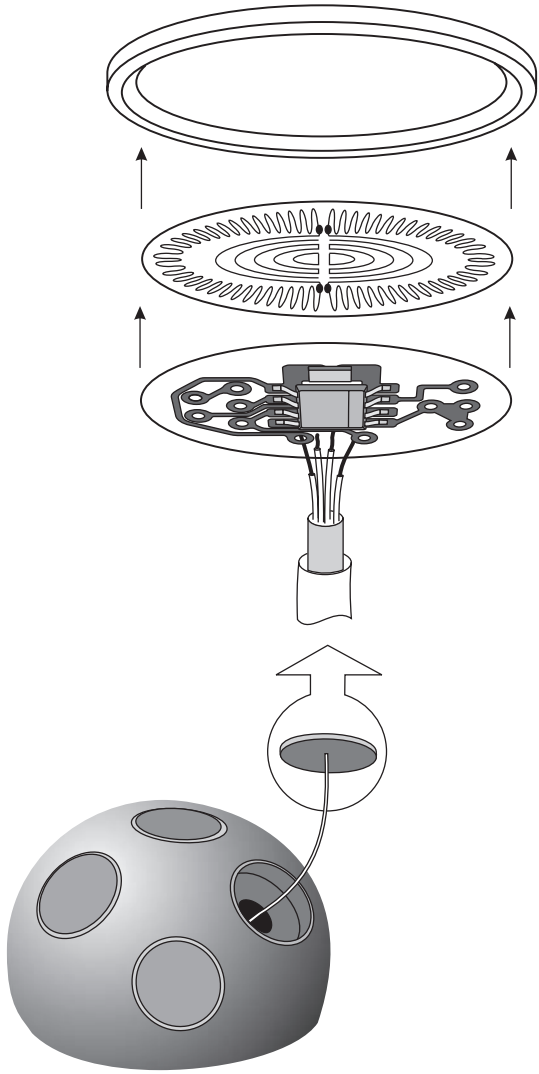

FIGURE 2.24
An exploding view of the SST.

is displaced (Cottrell 1964). As for stresses, we can distinguish direct and shear strains ε and γ. They are caused by normal and shear stresses, respectively. Direct strains are quantified by the change in length of a line element in a body. The direct strain for small displacements is defined as follows:

$$\varepsilon = \lim \frac{L}{L} \tag{2.28}$$

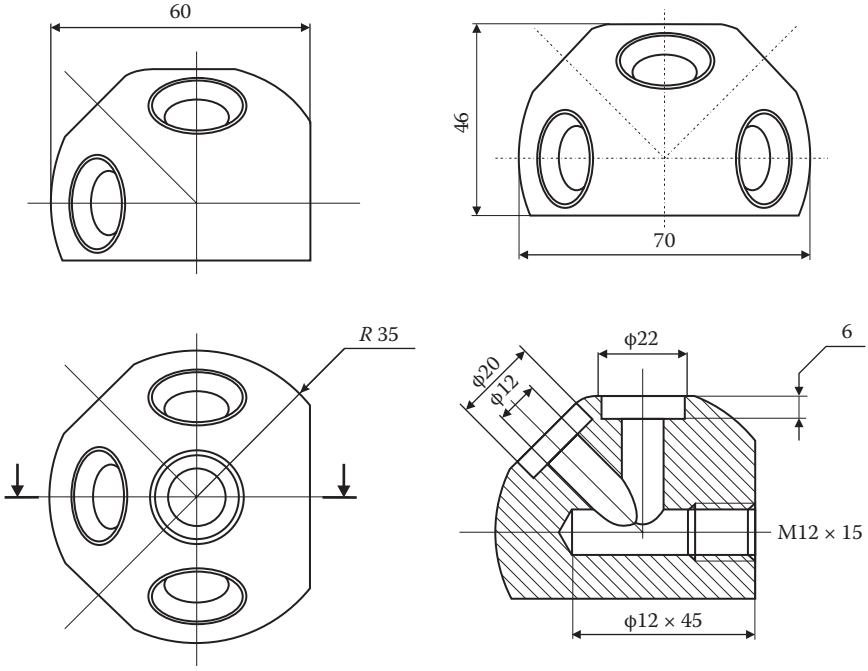

FIGURE 2.25
Construction details of the SST.

We can quantify direct strain by the terms of fraction differentials in three main directions:

$$\varepsilon_x = \frac{\partial u}{\partial x} \tag{2.29}$$

$$\varepsilon_y = \frac{\partial v}{\partial y} \tag{2.30}$$

$$\varepsilon_z = \frac{\partial w}{\partial z} \tag{2.31}$$

Shear strain is defined as the change in the angle between two mutually perpendicular lines at a point. From that we can derive equations on three shear strain components for small rotations:

$$\gamma_{xz} = \frac{\partial u}{\partial z} + \frac{\partial w}{\partial x} \tag{2.32}$$

$$\gamma_{xy} = \frac{\partial v}{\partial x} + \frac{\partial u}{\partial y} \tag{2.33}$$

$$\gamma_{yz} = \frac{\partial w}{\partial y} + \frac{\partial u}{\partial z} \tag{2.34}$$

In a soil medium, we can distinguish three kinds of strains: rotation, shearing, and distortion. Since a soil is a composition of numerous particles that may be subjected to very small strains, it is more practical to consider soil deformation—a sum of all the strains of the particles. Figure 2.26 shows these deformations as related to elementary strains. The most pronounced kind of soil deformation is shearing that leads to soil structure damage. Soil compaction is a product of elementary volumetric strains and in fact occurs when particles fill the pore spaces in a soil. An increase of soil bulk

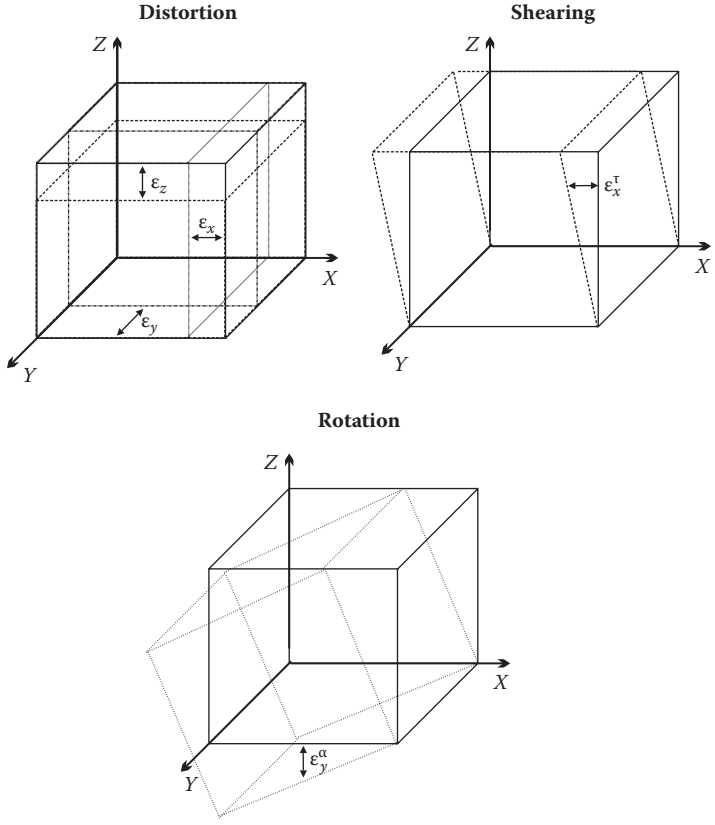

FIGURE 2.26
Three kinds of soil deformation.

density, often identified with soil compaction, is caused by direct strains and also by shearing of soil aggregates.

2.5.1 Review of Existing Experimental Methods

Soil deformation may be determined by macroscopic measurements of sample dimensions before and after compacting, but more interesting results may be obtained by continuous monitoring of soil particle movements. In practice, soil movements can be investigated by monitoring two or more soil points in which sensing elements are installed.

The two major types of methods to determine soil deformation under loads are (1) the non-contact method in which sensing elements are installed into soil, but the elements are not connected to a data logging system; and (2) the projection method in which a rigid arm connected with a sensor in the soil projects soil deformation or movement.

In non-contact methods, photo or video techniques track the motion of sensing elements (point grids) installed in soil. The movements of the sensors occur over a full six degrees of freedom and are not affected by the tracking system. In the projection method, the movement of the sensor is affected by both soil deformation and the mechanical suspension of the projection system. The system may allow movements in only one, two, or three directions, depending on the bearing used.

Van den Akker (1988) developed a marker photographic method to measure and visualise deformation in the subsoil due to traffic. A vertical point grid was positioned into the soil profile perpendicular to the direction of moving of the wheel. The point grid was photographed before and after a wheel pass. A photographic technique measured the positions of the grid points before and after a passage, and deformation was computed from the measurements. This method was used to validate the soil compaction model (SOCOMO).

A typical projection system for soil deformation measurement was developed by Kühner et al. (1993). Their soil displacement transducer system (DTS) consists of three potentiometers that act as position transducers. Soil movements can be determined in the three main directions: X, Y, and Z. The system can be connected to the SST (installed in the undisturbed soil prior to wheeling experiments) by a rigid arm. The arm is suspended in a spherical bearing that allows rotations in the X and Z directions and pushing in the Y direction. The movements of the SST induced by stresses in soil are projected by a mechanical system with rollers and potentiometers. The advantage of this system is the possibility of simultaneous measurements of soil stresses and displacements.

Arvidsson and Ristic (1996) proposed another method for measuring soil displacements. Vertical movement of soil was determined by measuring the hydrostatic pressure of liquid. The sensor system consisted of a

liquid-containing aluminum cylinder (29 mm in diameter and 60 mm in length) and a hose connecting the cylinder with a fixed pressure transducer. Vertical displacements of the cylinder during wheeling generated changes of the hydrostatic pressure of the column of liquid closed in the sensor system. The cylinder can be installed into the soil volume through a horizontal hole in the soil profile. Performance of this simple method depends on the pressure transducer characteristics: its measuring range is –1 to +1 kPa, resolution values are 1 Pa (–102 to +102 mm) and 0.1mm, respectively. The cylinder was also fitted with a soil pressure transducer for soil stress measurements. The major advantages of this simple method are low cost and easy handling but the method is limited to measurements of stresses and displacements only in the vertical direction.

2.5.2 Optical Non-Contact Measuring System

2.5.2.1 First-Generation Optical System

For the measurement soil deformation, we assumed that the SST moves with the deforming soil. Additionally, when movements of a point on the soil surface are simultaneously determined, the deformation of the soil volume between the SST and the surface can be determined. Deformations of the surface were determined by movements of a loading plate in laboratory experiments or a flat lintel (rut depth probe) placed on a soil surface in the field (Pytka and Dąbrowski 2001, Pytka and Konstankiewicz 2002).

A laser-based system was developed to project SST movements. It consisted of three major elements: laser projectors, a semi-transparent shield, and a video camera. The complete system is supported on a suspending frame with fixed points of rotation with uniball bearings. This allows free movements of the SST and the sinkage probe in the horizontal and vertical axes, within a rotation angle of ±30°. The connection between the SST and the optical system was rigid, but it is possible to use a homokinetic joint to allow the SST to rotate; in this manner, local movements of the SST can be determined. Figure 2.27 is a schematic view of the connection between SST and deformation system.

Both the SST and the sinkage probe move as soil is loaded and deforms. The movements are projected on the shield and the images are recorded by the camera. For laboratory experiments, a CCD monochromatic camera was connected to an image acquisition system. Soil stress and image data were recorded by the same computer. A computer program can process each video image by determining the co-ordinates of the two lighting points to develop a time-dependent soil deformation relationship. In our field investigations, we used a common video system and image analysis was performed by determining the locations of two light points (repre-

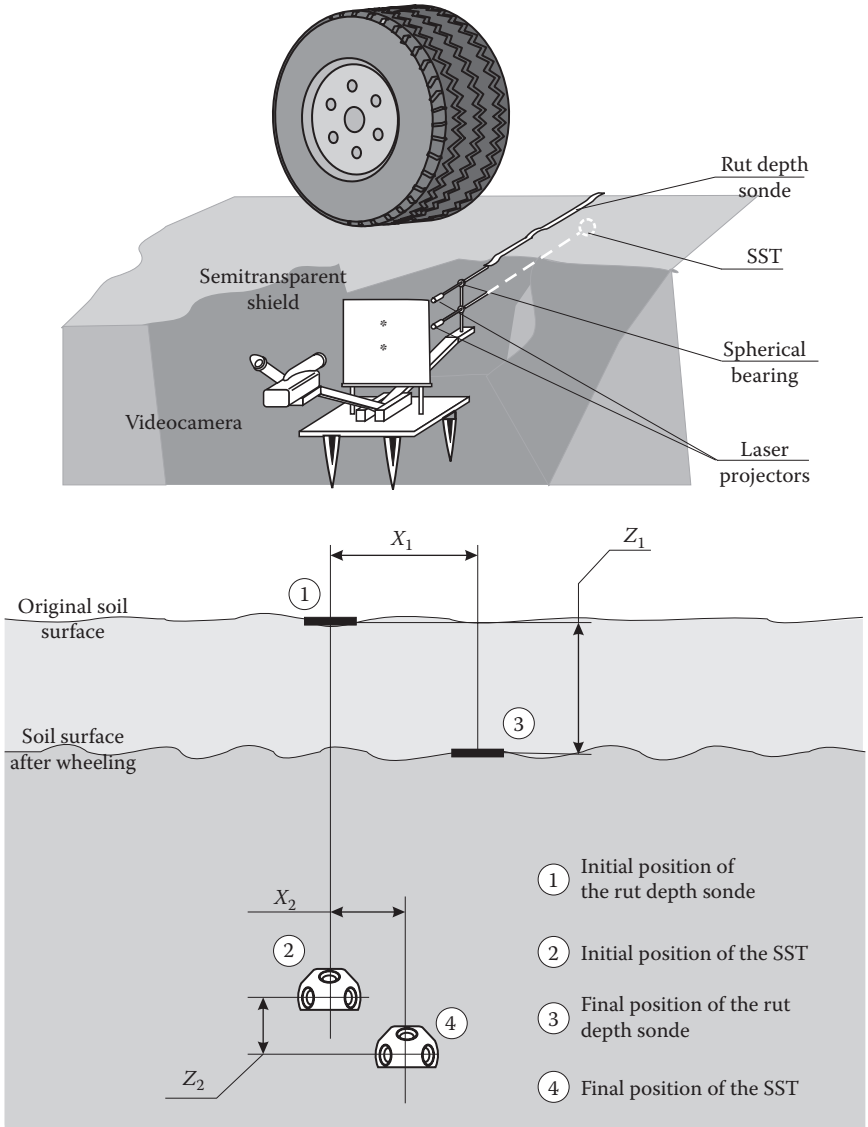

FIGURE 2.27
An optical method for soil deformation measurements.

senting the location of the SST and the rut depth probe) in two directions for each video grab.

Based on these data, an experimental relationship between major stress σ_1 and vertical deformation of soil can be derived. The relative deformation of soil volume ε_v (vertical soil strain) was calculated by dividing the difference

of the initial and final distance between the SST and rut depth probe (along the vertical axis) by the initial (after preparation and installation but before wheeling) value of this distance for each measuring time point:

$$\varepsilon_V = \frac{150 - X_1 + X_2}{150} \times 100\% \tag{2.35}$$

where X_1 and X_2 are the vertical movements of the rut depth probe and SST, respectively, in millimetres and 150 is the vertical initial distance between rut depth probe and the SST, also in millimetres.

2.5.2.2 Second-Generation System

The second-generation system consists of four probes installed in a test soil volume. Passing a load over the test soil displaces the probes that move together with the deforming soil. The probes can be displaced in vertical and horizontal directions. The probes are supported on four uniball spherical bearings. Four laser projectors are sited on the opposite ends of the probes.

When a wheel passes over, light points move on a semitransparent shield and the movements are recorded by a video camera. The lengths of the deformable probes and the projector arms were chosen to obtain an optical transmission of 4 to 1 so that 1 mm of soil deformation results in a 4-mm displacement of the light point. The advantage of this method is the ability to measure horizontal soil deformation. When both vertical and longitudinal soil deformations are known, it is possible to analyse shearing and rotations. An exploding, three-dimensional view of the measuring apparatus installed in soil is shown in Figure 2.28. Chapters 3 and 4 describe how this system can be used for measuring soil deformation in field experiments.

2.6 Conclusions

Measurements of soil stresses and deformations under loads may be highly important in soil mechanics studies. Knowing the actual soil stresses and the resulting deformation will help explain (1) the processes that occur in soil and (2) the interactions with tractive elements of vehicles running on soil surfaces as shown in subsequent chapters that examine soil stress and deformation measurements under loads of a variety of vehicles.

Strain gage pressure transducers are good choices for measurements of soil stresses under vehicle loads, as proven in numerous successful experiments. Calibration tests with various materials are significant steps

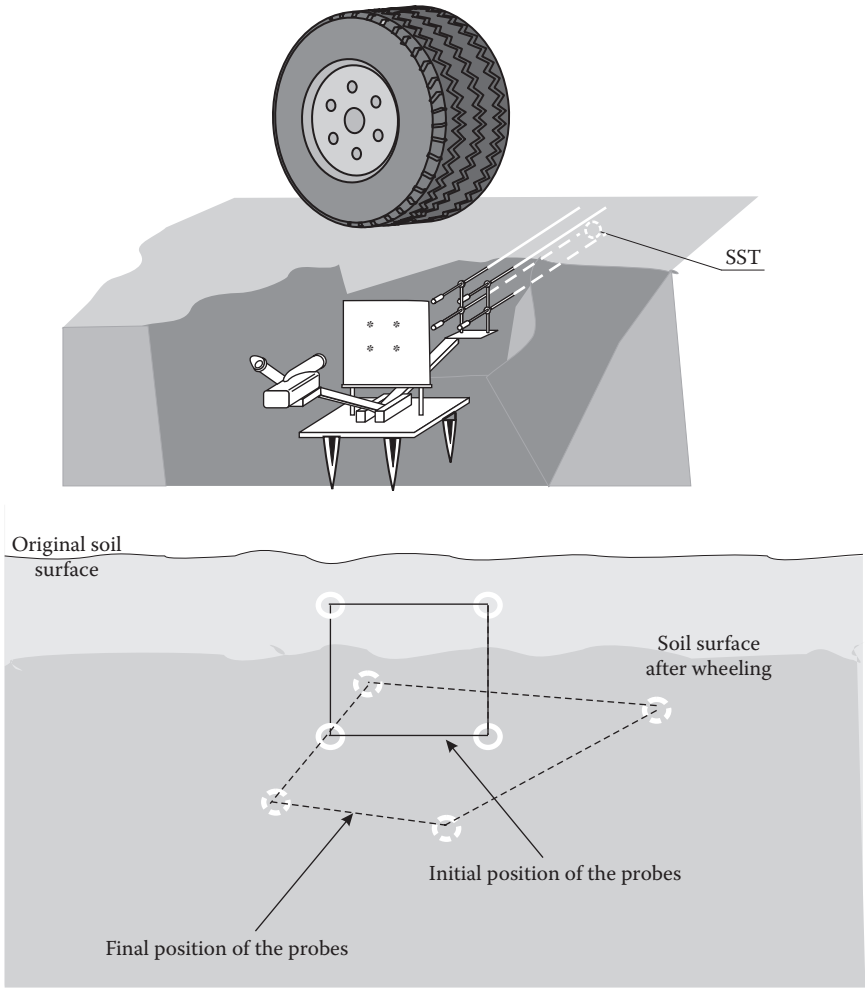

FIGURE 2.28
A schematic of the second-generation optical system.

forward. In the case of stress state determinations in different soils, pressure transducers should be calibrated with a given material at test conditions, especially with regard to material water content. Differences in output scale factor may have significant effects on measured values of soil stress; therefore the practices described in this chapter will become important as we aim to improve precision.

Subsequent chapters explain use of the methods described here in real experiments with trucks, tractors, SUVs, military tracked vehicles, and aeroplanes operating on unsurfaced airfields.

References

Akker van den J. 1988. Model computation of subsoil stress distribution and compaction due to field traffic. Wageningen: Institute of Land and Water Management Research, Report 23.

Abu-Hamdeh N.H. and Reeder R.C. 2003. Measuring and predicting stress distribution under tractive devices in undisturbed soils. *Biosyst. Eng.* 85: 493–502.

Arvidsson J. and Ristic S. 1996. Soil stress and compaction effects for four tractor types. *J. Terramech.* 33: 223–232.

Bakker D.M., Harris H.D., and Wong K.Y. 1995. Measurements of stress paths under agricultural vehicles and their interpretation in critical state space. *J. Agric. Eng. Res.* 61: 247–260.

Cooper A.W., Vanden Berg G.E., McColly H.F. et al. 1957. Strain gage cell measures soil stresses. *Agric. Eng.* April: 232–235.

Cottrell A.H. 1964. *The Mechanical Properties of Matter*. New York: John Wiley & Sons.

Harris H.D. and Bakker D.M. 1994. A soil stress transducer for measuring in situ soil stresses. *Soil Till. Res.* 29: 35–48.

Horn R., Johnson C., Semmel H. et al. 1992. Raumlische Spannungsmessungen mit dem Stress State Transducer (SST) in ungesattigten aggregierten Boden – theoretische Betrachtungen und erste Ergebnisse. *Z. Pflanzenren. Bodenkunde* 155: 269–274.

Horn R. and Lebert M.1994. Soil compactability and compressibility. In *Soil Compaction in Crop Production*, Soane B.D. and Van Ouwerkerk C., Eds. Amsterdam: Elsevier, pp. 41–96.

Kirby J.M. 1999a. Soil stress measurement I. *J. Agric. Eng. Res.* 72: 151–160.

Kirby J.M. 1999b. Soil stress measurement II. *J. Agric. Eng. Res.* 73: 141–150.

Kitchin C. and Counts L. 1992. *Instrumentation Amplifier Application Guide.* Norwood, MA: Analog Devices Inc.

Kobielak S. 1991. *Application of Pressure Cells in Civil Engineering*. Wroclaw University of Technology: Civil Engineering Series 63.

Kühner S., Horn R., Baumgartl T. et al. 1993. Stresses and particle displacement during wheeling. ASAE Meeting Presentation 93-1092.

Megson T.H.G. 2010. *An Introduction to Aircraft Structural Analysis*. Burlington, MA: Butterworth-Heinemann.

Nichols T.A., Bailey A.C., Johnson C.E. et al. 1987. A stress state transducer for soil. *Trans. ASAE* 30:1237–1241.

Pytka J.A. and Dąbrowski J. 2001. Determination of the stress–strain relationship for sandy soil in field experiments. *J. Terramech* 38: 185–200.

Pytka J.A. and Konstankiewicz K. 2002. A new optical method for soil stress and strain investigation. *Soil Till. Res.* 65: 243–251.

Pytka J.A. 2009. Design consideration and calibration of pressure transducer for soil stress measurements. *J. Terramech.* 46: 241–249.

Raper R.L., Bailey A.C., Burt E.C. et al. 1995. The effects of reduced inflation pressure on soil–tire interface stresses and soil strength. *J. Terramech.* 32: 43–51.

Skibiński K. 1922. *Equilibrium of Granular Materials* (in Polish). Warszawa: Księgarnia Naukowa Polsk. T-wa. Pedagog. Księgarnia M. Arcta.

Verma B.P., Bailey A.C., Schafer R.L. et al. 1976. A pressure transducer in soil compaction study. *Trans. ASAE*, 442 – 447

Vishay Precision Group. 2011. *Strain Gage-Based Transducers: Their Design and Construction*. Raleigh, NC.

Vishay Precision Group. 2010. Diaphragm Pressure Transducers Technical Note 510-1. Raleigh, NC.

3

Soil Stress and Deformation State: Investigations in Monolith Soil Samples

3.1 Introduction

One good engineering practice is to represent full-scale objects with models. This technique is valid for material models and for mathematical simulations. For example, experiments can be done with monolith soil samples rather than in actual wheel–soil conditions. Soil monoliths can measure up to $1 \times 0.6 \times 0.6$ m—much larger than practical for most soil samples. The main advantage of soil monoliths is that the volume is large enough for conducting loading tests without any boundary effects. And, of course, the tests can be performed under controlled laboratory conditions.

The samples can be conditioned and important parameters can be monitored easily to meet the test requirements. Monolith soil samples can be used for a variety of purposes: one is determination of soil stress and deformation under external loads applied to the surface by a circular plate.

The use of a circular plate to "load" a monolith soil sample is an idealization of wheel loading. When we set the plate pressure equal to tyre contact pressure, we simulate wheel loading on the soil surface under fully static conditions, as if we added mass to a stopped vehicle (truck or trailer). From a mechanic's view, deformation always occurs when a rigid body is subjected to stresses. Assuming that soil is a complex structure of small rigid bodies with water and air between them, strains in soil can be designated as normal strain components ε_x, ε_y, and ε_z and shear strain components ε_{xy}, ε_{xz}, and ε_{yz}. As with stress, it is possible to construct a coordinate system to reduce the strain tensor. Thus, soil strain is described by three main components: ε_1, ε_2, and ε_3.

The loads applied to soil during typical agricultural operations (tractor or machinery wheeling) are much higher than internal soil strength and usually cause immediate and irreversible deformations. The three types of deformations are compression rotation, and shearing. While rotation

has no effect on soil deformation and does not change soil properties, compression and shearing are responsible for soil deformation. External forces may cause compression—the increase of soil mass per unit volume—and shearing—a change of shape at constant volume. Compression of unsaturated soils is called compaction; it changes the mechanical characterisation and the soil's air–water relationship, and also influences the agricultural quality of arable soils (Horn and Lebert 1994). Deformations in soils are usually immediate and irreversible.

Others have studied the effects of applied loads on soil stress deformation (Arvidsson 1996, Bailey et al. 1996, Harris and Bakker 1994, Wiermann 1999 and Wong 1995), but the lack of experimental data led us to perform additional experiments and analyses. In this chapter, we describe experimental relationships between load and stress deformation state for structured and disturbed soils and for tillage variants.

3.2 Effect of Static Load and Soil Stress and Deformation in Loamy Luvisol

3.2.1 Experimental Set-Up and Procedures

The experiment was conducted at the Institute for Plant Nutrition and Soil Science in Kiel, Germany. The Ap horizon of a sandy loamy Luvisol derived from glacial till (at Hohenschulen near Kiel) was used in the form of large monoliths. Some properties of this horizon are presented in Table 3.1.

Monolith samples (600 × 400 × 300 mm, L × W × H) were taken from the topsoil down to 300-mm depth after tillage. First, a rigid steel frame was placed vertically into the soil and then the exterior soil was excavated. The bottom of the monolith frame was sliced under the soil sample to enclose the soil. Then, the sample was lifted and transported to the laboratory on an air mattress to minimise disturbances. Figure 3.1 shows this process.

Bulk density values were determined for initial conditions of each treatment as well as for the final compacted soil. The cylindrical samples for soil bulk density determination were taken at a depth of 100-mm. For each

TABLE 3.1

Characterisation of Investigated Soils

Soil	Specific Density	Sand	Silt	Clay	Organic Carbon
Loam	2.58 g/cm^3	58.5%	25.9%	15.6%	0.89%

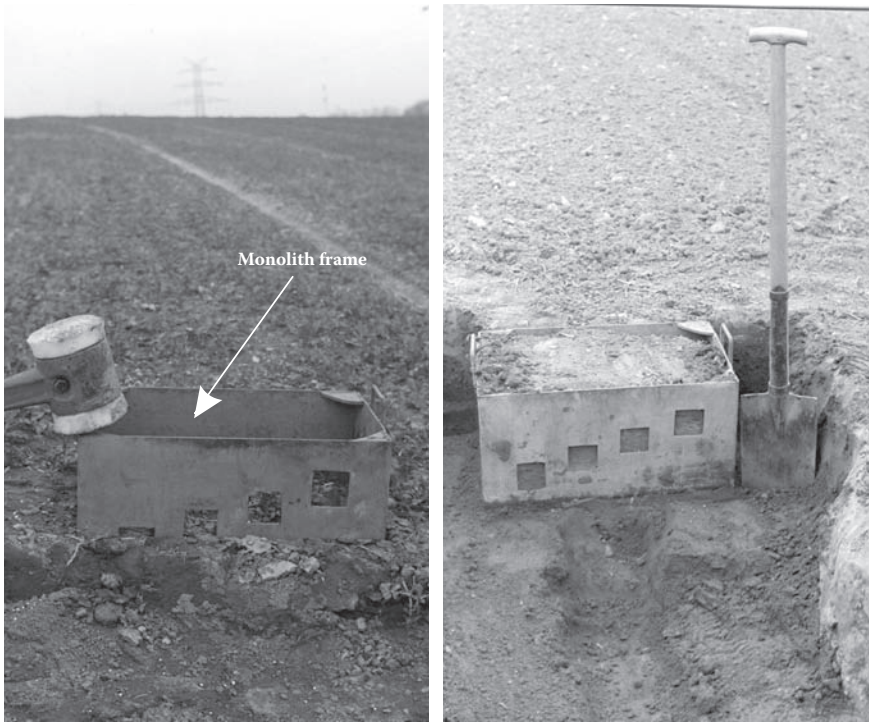

FIGURE 3.1
Taking the monoliths from the field:. Left photo—placing the frame into soil surface (rototilled soil); Right photo—removing the soil from around the frame (plowed soil).

of the investigated soil monoliths, five samples were taken from unloaded soil and one sample from under the loading plate.

3.2.1.1 Soil Variants Used in Experiment

We investigated two variants of soil tillage: conventional (plowed) and conservative (rototilled). The soil was loosened to a depth of approximately 350 mm for the plowed material and 80 to 100 mm for the rototiller treatment. The soils were tilled in autumn, and the monolith samples were taken between February and April. To equalize water conditions, each monolith was equilibrated and drained by several ceramic cells (each 300 mm long, 30 mm in diameter) until the pore water pressure reached –60 hPa.

For each of the two tillage treatments (conventional and conservative), we investigated two soil states: undisturbed (structured sample) and complete manual homogenisation (homogenised or repacked sample). The monoliths of homogenised soil were packed in separate layers, approximately 50 layers thick, to reproduce the initial bulk density of the full volume of the

TABLE 3.2

Soil Tillage and Structure Variants

Variant Index	A	B	C	D
Soil type	Loam	Loam	Loam	Loam
Tillage variant and depth	Rototilling 8 to 10 cm	Rototilling 8 to 10 cm	Plowing 35 cm	Plowing 35 cm
Structure	Undisturbed	Homogenised	Undisturbed	Homogenised

undisturbed sample. Table 3.2 contains complete information for the soil variants. Five replicates of each soil variant were investigated.

3.2.1.2 Measuring System

The instrumentation for the experiment consisted of the stress state transducer (SST), deformation transducer system (DTS), and a PC notebook computer. The SST (see Figure 3.2) was designed at the Institute for Plant Nutrition and Soil Science in Kiel by Horn (Horn and Lebert 1994). It uses strain gage type pressure transducers built with steel membranes.

The outer diameter of the SST is approximately 60 mm and the device has a rigid arm connected to the deformation transducer. This arm is a thin-wall tube that also contains the signal cables.

The stress transducers installed in the SST were calibrated in air using a triaxial chamber. A rubber diaphragm sealed the transducer to allow the application of constant pneumatic pressure during calibration. The air pressure was applied from a compressor with a valve and air pressure calibrator. The sensitivity of the pressure calibrator was 0.1 kPa; the calibration range was 50 to 400 kPa with a maximum deviation of ±1%. The DTS, shown as a separate device in Figure 3.3, was attached to the SST via the arm that was supported by a double-row spherical ball bearing.

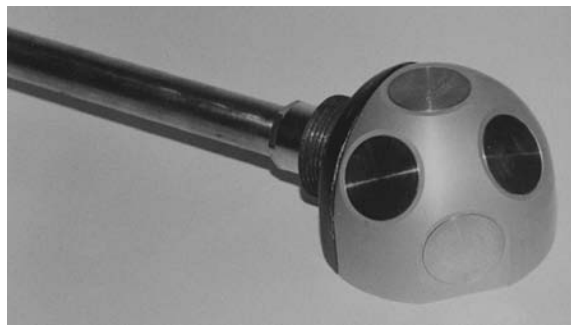

FIGURE 3.2
Stress state transducer (SST) used for the measurements.

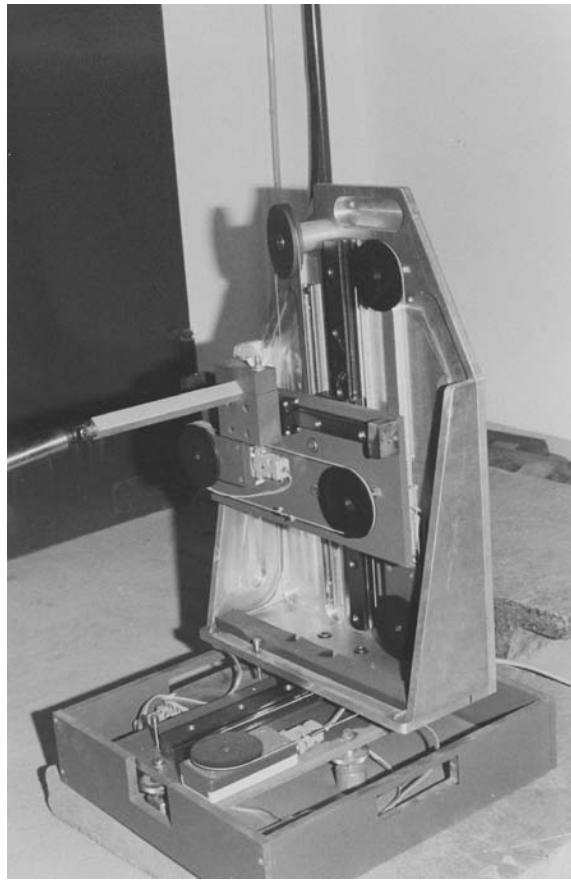

FIGURE 3.3
Deformation transducer system (DTS).

The bearing unit mounted to the side wall of the monolith frame and the arm are visible in Figure 3.4. The spherical bearing supporting the arm permitted the determination of horizontal and vertical displacements via highly sensitive round potentiometers. This system was calibrated using a clock-length sensor with a sensitivity of ±0.1 mm. The range of the calibration was ±100 mm. Both sensors (SST and DTS) were activated and registered the stress-induced changes of soil displacement simultaneously.

3.2.1.3 Installation of Measuring System in Monolith Samples

The SST transducer was installed at the depth of 100 mm in the monolith. After preparation of soil water conditions, a hole of approximately 60-mm diameter was drilled on the side of the monolith using a special

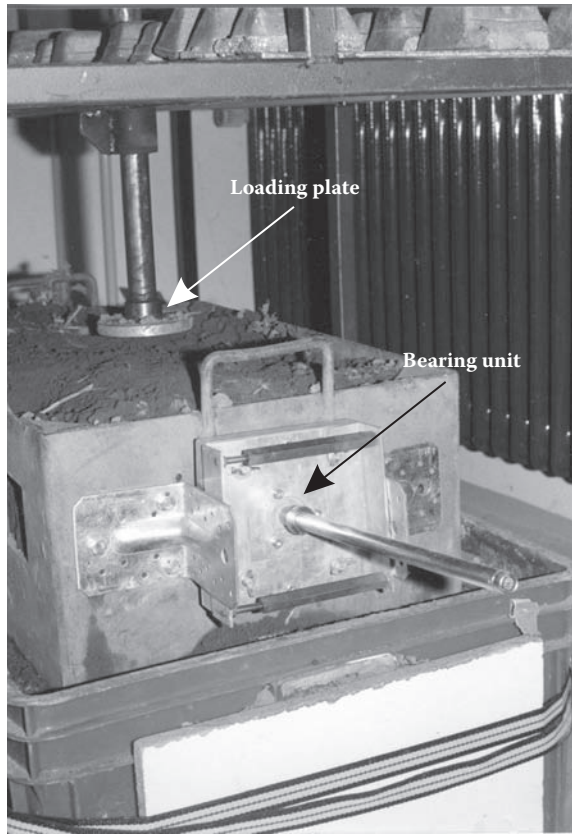

FIGURE 3.4
The monolith soil sample from the side: spherical bearing unit mounted to the monolith frame and the rigid arm, connecting the SST with the DTS.

tool. After the SST transducer was placed in the hole, the remaining soil was replaced into the hole.

To ensure contact between the sensors and soil, the transducer was placed in the hole under a certain pressure. The centre of a loading plate was approximately on top of the centre of the vertical stress sensor. The SST and DTS were connected, but only the vertical movement of the SST transducer was measured because of the vertical direction of loading. Figure 3.5 shows the complete installation of the measuring equipment in a soil monolith sample.

3.2.1.4 Loading Monolith Samples

The topsoil was compressed with a circular plate of 100-mm diameter that was loaded with weights of 40, 80, 120, 160, 200, 240, and 280 kg

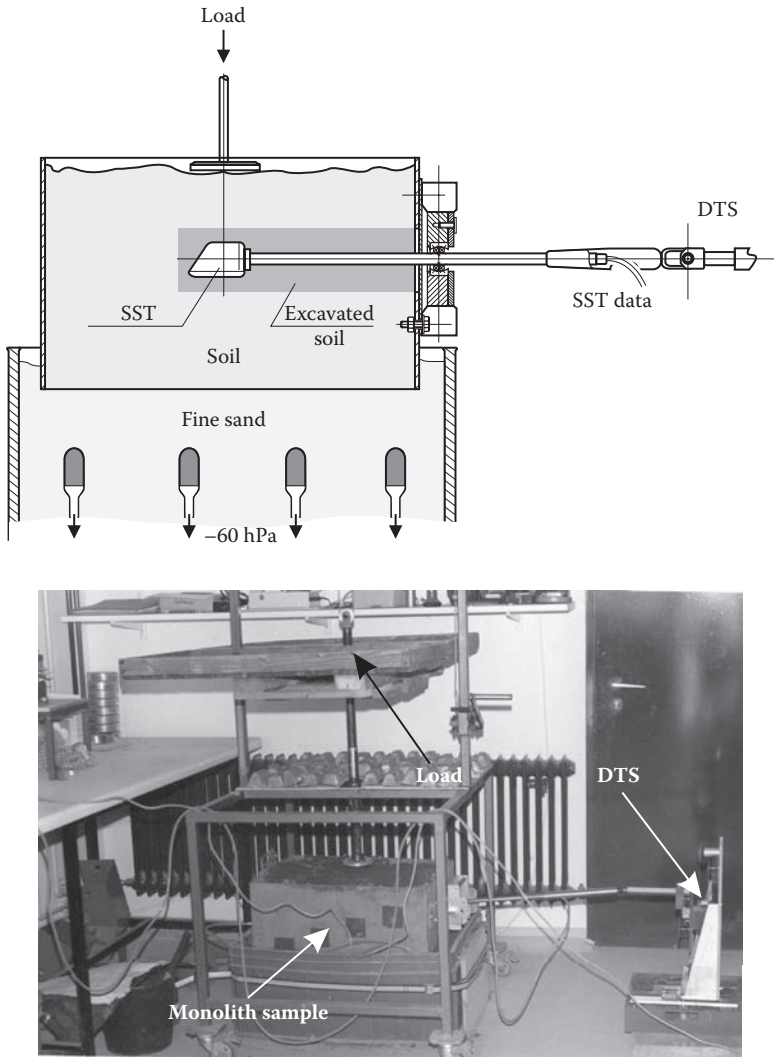

FIGURE 3.5
A complete experimental set-up for static load of loamy soil.

(pressures of 50, 100, 150, 200, 250, 300, and 350 kPa). This loading pattern simulated increasing loads caused by the tyres of an agricultural vehicle during transport and harvesting. During the 30-second loading periods, the stresses of the six sensors and the vertical movement of the SST were recorded at 10 Hz sampling frequency.

3.2.2 Results

A detailed statistical analysis of all calculated stress and deformation data was performed. The influences of load and soil variants—tillage treatments (plowed and rototilled) and soil state (undisturbed or homogenised)—were established by means of a one-way analysis of variance. The significant level was 0.05.

The major stresses σ_1, σ_2, and σ_3 and the mean normal stress along with the octahedral shear stress and its angle were calculated from the measured SST data. DTS data were used to calculate values of the deformation parameters: (1) SST displacements in two perpendicular directions; as noted earlier, only vertical displacement of the SST was analysed; and (2) rut depth determined at the final position of the loading plate.

All the replications in the first stage of the experiment were carried out for 30 seconds, but significant changes were observed only in the first 10 seconds. The peak values of stress state components were selected for further analyses. Table 3.3 presents the means of five replications for all loads and soil variants. Some significant and pronounced relationships and interactions of the data in Table 3.3 are discussed below.

3.2.2.1 Effects of Soil Variants

As stated earlier, the study examined two tillage variants: conventional (plowed) and conservative (rototilled) soils. Tillage always influences soil structure and decreases its strength. Different tillage operations exert varying effects on soil mechanical properties. Soil after conventional plowing exhibits a relatively loose structure within the tilled depth.

The soil samples were taken up to a depth of 30 cm within the loose soil layer. Therefore, soil variants C and D taken from soil plowed to 35 cm were looser and weaker in structure compared to the A and B variants in which soil was rototilled up to 8 to 10 cm. This may be observed in Figure 3.7. The major stress σ_1 always reaches greater peak values for soil variants after conventional tillage. Similar effects of soil tillage are seen when the deformation values for soil preparation variants are analysed (Figure 3.8): both rut depth and SST vertical displacement are greater for soil variants C and D.

An interesting observation was also made when comparing the soil variants within the two tillage operations. Although stresses for homogenised soil variants are significantly greater than for undisturbed (structured) soil samples, the same trend in soil deformation values was observed only for the soil samples after conventional plowing. The resulting deformations for the soil samples after conservative rototilling are significantly greater for repacked (homogenised) soil.

TABLE 3.3

Effects of Load on Soil Stress and Deformation State for A, B, C, and D Variants

		Soil Stress (kPa)					Soil Deformation (mm)	
Load (kPa)	**Stress**	**A**	**B**	**C**	**D**		**Rut Depth**	**SST Displacement**
50	σ_1	32.98*	31.53*	35.54	22.05	50 kPa		
	σ_2	1.46	–0.62	1.69	3.70	A	0.74	0.6
	σ_3	–15.92	–10.03	–12.91	–10.60	B	0.68	0.25
	σ_{OCT}	6.14	3.79	8.38	5.10	C	3.96	0.33
	τ_{OCT}	20.32***	13.65**	20.45***	13.93**	D	5.14	0.82
100	σ_1	83.71	64.63	76.92	122.80	100 kPa		
	σ_2	0.71	–0.61	0.65	3.14	A	7.12	1.97
	σ_3	–27.32	–16.54	–25.04	–36.65	B	8.08	1.12
	σ_{OCT}	20.08*	15.49	19.77*	31.35	C	10.28	1.66
	τ_{OCT}	46.88	35.15	50.38	70.08	D	11.56	4.32
150	σ_1	116.7	141.60	175.66	216.56	150 kPa		
	σ_2	1.57	–0.37	0.117	1.01	A	14.10*	5.36**
	σ_3	–37.43*	–36.37*	–52.84	–58.54	B	13.98*	3.09
	σ_{OCT}	27.18	34.66	37.11	55.41	C	29.82	5.18**
	τ_{OCT}	65.32	76.99	97.29	117.16	D	31.84	8.74
200	σ_1	201.26	174.93	227.03	246.6	200 kPa		
	σ_2	–1.39	0.42	–1.53	2.94	A	17.14	9.42*
	σ_3	–64.15*	–48.01	–65.09*	–71.98	B	15.80	4.94
	σ_{OCT}	45.59	42.45	53.33	68.73	C	34.46	9.54*
	τ_{OCT}	113.23	95.79	124.76	131.16	D	37.58	15.95
250	σ_1	281.40*	214.36	263.16	287.23*	250 kPa		
	σ_2	7.21	3.22	–4.19	6.37	A	21.08*	14.59
	σ_3	–85.24	–62.08	–70.35**	–70.77**	B	20.96*	7.65
	σ_{OCT}	68.84***	50.84	67.65***	101.03	C	31.56	17.49
	τ_{OCT}	154.93	117.23	148.36	161.33	D	35.66	23.98
300	σ_1	308.09	275.98	342.26*	357.11*	300 kPa		
	σ_2	3.56	1.23	–3.73	11.41	A	25.12	20.88
	σ_3	–86.54	–74.18***	–76.46***	–83.27	B	27.45	10.77
	σ_{OCT}	66.16	71.95	98.55	117.93	C	56.02	25.67
	τ_{OCT}	171.56	147.43	179.73**	178.33**	D	61.32	33.21
350	σ_1	323.65	298.23	366.63	399.60	350 kPa		
	σ_2	8.52	1.38	–1.76	11.47	A	34.80*	29.37
	σ_3	–97.36	–83.52	–91.35	–79.51	B	33.42*	14.11
	σ_{OCT}	94.96	72.12	104.06	128.26	C	68.62	34.48
	τ_{OCT}	185.43	176.78	204.86	195.62	D	81.63	44.96

Note: σ_1 = major normal stress. σ_2 and σ_3 = minor normal stresses. σ_{OCT} = octahedral normal stress. τ_{OCT} = octahedral shear stress. Values (means) followed by the same symbol (*, **, or ***) are not significantly different within the four soil variants.

3.2.2.2 Loading Effects

Figures 3.6 and 3.7 show the effects of load on soil stress and deformation state. For all treatment variants and each value of acting force, the effect of load on stresses and deformation parameters was significant (with the exception of σ_2). Generally, the greater the applied load, the higher are

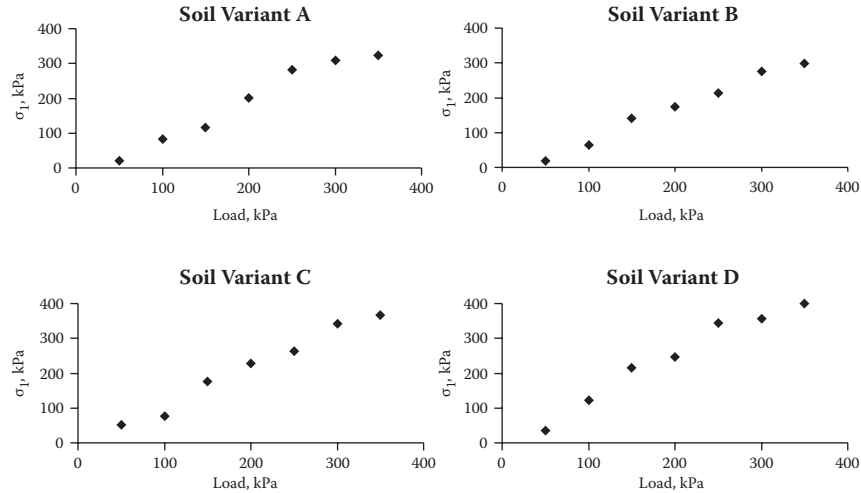

FIGURE 3.6
Soil stress σ_1 as a function of applied loads for four soil variants.

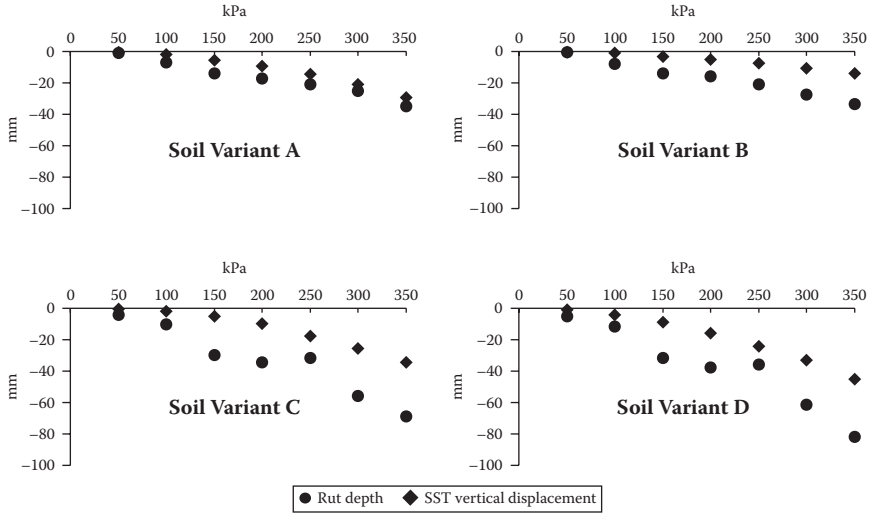

FIGURE 3.7
Deformations in soil under loads.

the peak values of stress components; the load is the most significant factor affecting the resulting stresses and deformations. This is true for all variants, although the intensity of stress increase with increasing load differed for the four variants. The major stress σ_1 slope is significantly affected by load in the full range of applied loads. Similar interactions can be observed for soil deformations.

3.2.2.3 Ratio of σ_{OCT} to τ_{OCT} as Factor in Soil Failure

The SST used in the experiment could determine the complete stress state at a given point of the investigated soil volume. Principal major σ_1 and minor σ_2 and σ_3 stresses, octahedral normal stress σ_{OCT}, and octahedral shear stress τ_{OCT} were determined. The two octahedral stresses represent two different behaviours (compaction and shearing) of a loaded soil (Figure 3.8). It is therefore practical to analyse σ_{OCT}-to-τ_{OCT} ratios for all the soil variants and for the load values.

This ratio, for which values are presented in Figure 3.9, indicates which factor—compression or shearing—has the most influence on soil failure. We can safely assume that in the investigated soil the two mechanical processes existed at the same time. The average values indicate that shearing is slightly more pronounced for all soil variants; this difference was most pronounced in the plowed soil. Tillage variants influenced the σ_{OCT}-to-τ_{OCT} ratio significantly (0.05 level), while the changed structure of soil samples was pronounced only for loose soil (variants C and D).

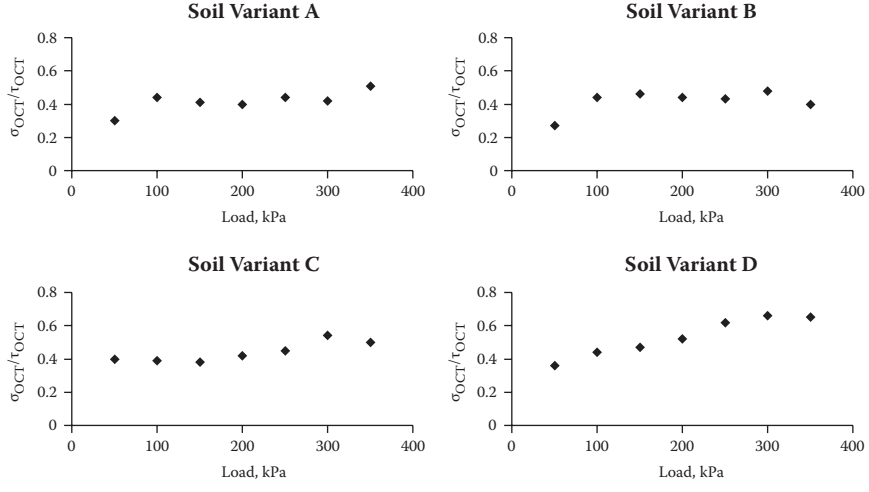

FIGURE 3.8
Mean normal to octahedral shear stress ratio for soil variants.

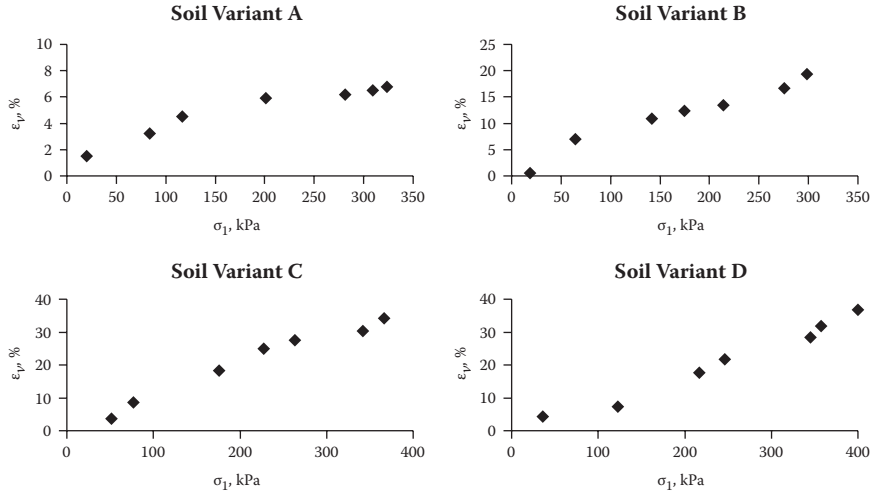

FIGURE 3.9
Relationships between the major stress σ_1 and the vertical strain ε_V.

3.2.2.4 Soil Stress–Strain Relationship

After further analysis of soil deformation data, we derived stress–strain relationships for all the investigated soil variants. The strain can be determined by assuming a one-dimensional compaction process in which the soil volume between the loading plate and the SST is vertically compressed and moved downward. The resulting vertical strain would be the relative decrease of the height of the soil volume. Hence, soil strain was calculated from the rut depth and SST movement.

As the major stress σ_1 is the greatest compressive stress, values of this parameter were selected to obtain the soil stress–strain interaction. Relationships between σ_1 and the vertical strain show increased strain for greater stress values, but the intensity of that increase varies. The most significant strain increase was observed for homogenised soil. However, the major stress σ_1 reached significantly different peak values for each of the treatment variants. We therefore analysed the ratios of σ_1 to vertical strain for the soil variants (Figure 3.10).

For a typical elastic body, this ratio is constant and provides information about the elasticity of the body. The elasticity of soil depends on many factors including soil type, water content, porosity, and structure. Certainly the elasticity of soil may vary for applied load values. The ratios indicate that soil elasticity is markedly greater for rototilled soil, especially for the structured (undisturbed) variant. For both structured and homogenised variants after rototilling, soil elasticity rises with increased

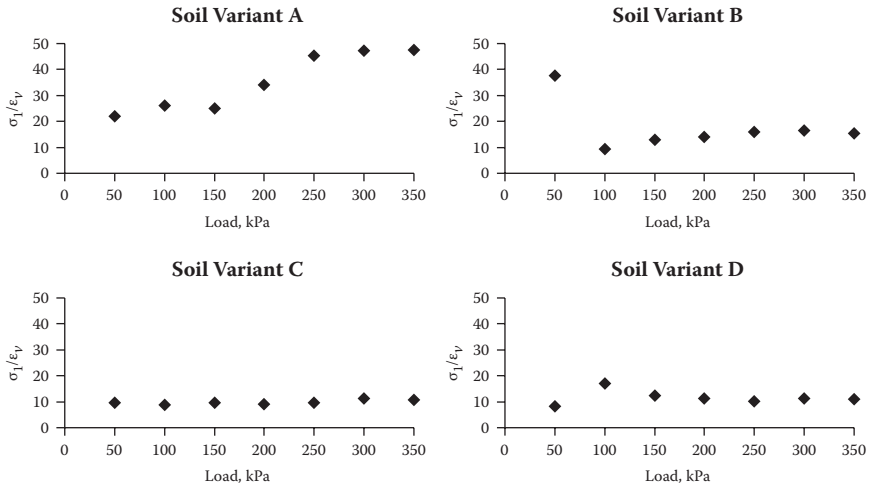

FIGURE 3.10
Major stress σ_1 to vertical strain ε_V ratio.

loads, but the values under the greatest load are significantly different. The conventional plowed variants do not show such dynamic changes in soil elasticity and oscillate around a value of 10.

3.2.2.5 Stresses, Deformations, and Changes in Bulk Density

Table 3.4 shows bulk density values for all treatment variants. The relative increases of bulk density differ for the structured and homogenised plowed variants by 7% and 12%, and by 7% and 9% for the structured and homogenised rototilled variants, respectively. The relatively greater compactability of the plowed soil is caused by its loose weaker structure and lower strength. This is a logical continuation of the results for stress and deformation. We can assume that the greater the soil stress and deformation, the greater its compactability. Figure 3.11 shows the trends for all variants. We found that the σ_{OCT} trends similarly to the major principal

TABLE 3.4

Changes in Soil Bulk Density and Compaction for Variants A, B, C, and D.

Variant	A	B	C	D
Initial bulk density (g/cm^3)	1.483/0.013	1.431/0.065	1.471/0.034	1.448/0.072
Final bulk density (g/cm^3)	1.586/0.082	1.587/0.023	1.575/0.009	1.600/0.011
Compaction (%)	6.94	10.91	7.07	10.49
Measured vertical strain (%)	6.8	19.4	34.2	36.7

Note: Bulk density values were determined for the soil samples taken from 10-cm depth.

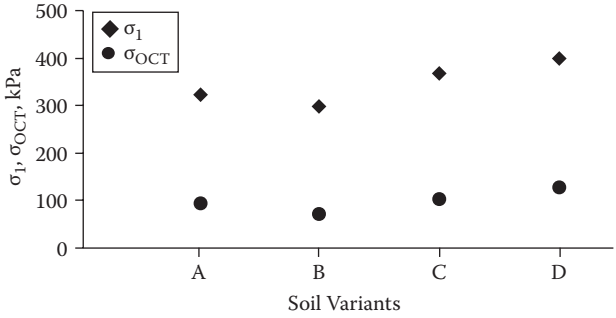

FIGURE 3.11
Trends in stresses for the four soil variants.

stress—the greatest measured stress component. Bailey et al. (1996) demonstrated similar stress behaviour for a Norfolk loam loaded by a demonstrator tyre in a soil bin.

3.2.3 Discussion

Based on these results, we can predict some mechanical behaviour of the investigated soil material, but we cannot yet make quantitative determinations of soil compactability, compressibility, or trafficability. We found that soil tilled to a greater depth and soil with a weakened structure tend to fail with ease when compared to a structured soil at given pore water pressure of –60 hPa at the Ap horizon. Consequently, stress state components reach greater peak values for conventionally plowed or disturbed soil. It is obvious that stress distribution in this soil can reach much deeper, until the potential energy of volumetric and non-dilatational strain equals the energy of the applied load.

In general, stress distribution in soils always occurs anisotropically. For unconfined conditions, the vertical stress component is greater and the two horizontal components are relatively small and, in theory, more or less identical. The proportion of these main stress components σ_1:σ_2:σ_3, however, as measured for all variants, was about 25:5:1, suggesting that continued investigation of these phenomena is reasonable, even if a slight effect may be created by the soil of the plate.

The general trends in soil stresses, deformations, and resulting soil compaction are correlated for a greater stress; deformations are significantly higher and the final effect of soil loading as indicated by the relative change in bulk density is greater for the all variants. Thus, we assume that soil stress state created under a given load is a constitutive parameter for soil at a certain water content. Additionally, relations between normal stress and shear stress components provide information about the type or

predominance of deformation process at the macro scale—not for a single soil particle.

Stress and deformation measurement methodology should be further investigated and experiments continued for different soils with a wide range of parameters influencing stress and deformation state. Such measurements may suffer from instrumentation errors (pressure transducer configuration, shape, and size; methods for placing the transducer into soil) or soil-induced errors (physical properties, non-homogeneous character, presence of stones, roots, or other materials).

Detailed analysis of soil stress measurements shows that for variants after conventional plowing, stress values are significantly greater than the applied load, especially for higher loads. We believe there are two probable reasons for stress over-registration. The first is the presence of stones in the investigated soil. When a stone presses against a pressure transducer and the membrane–stone contact area is small, the stress concentration may result in high values.

The second reason may lie in the designs of pressure transducers that contain very stiff metal membranes. The SST is an extrinsic body of relatively large size that is likely to be subjected to stress concentration. Many researchers working with SSTs report similar problems. We have experienced intense over-registrations when measuring stresses in sand under a heavy tracked vehicle (described in Chapter 5). On the other hand, it is difficult to detect under-registrations in soil stress measurements.

Soil functions as a high damping medium and energy is always dissipated (Pytka and Konstankiewicz 2002). Thus, the resulting stresses measured at a particular depth may reach peak values significantly smaller than applied loads. However, we are not able to state whether the measured values are under-registered, as we do not know the real values or have sufficient theoretical models to predict stress distribution in soil under loads.

Kirby (1999) found numerous methodological factors that affect soil stress measurements. First, soil disturbance during emplacement of the stress sensors is pronounced, and it is important to keep the disturbed zones very thin or conduct stress measurements in totally disturbed soil (after tillage). In any case, the measured stress values should be treated with caution.

The determination of soil deformation performed with the DTS system may suffer from the DTS design. It is possible that the SST attached to the DTS is limited to a circular movement, as the rigid arm connecting the SST with the DTS is supported at one point and becomes a centre of rotation. Although the bearing allows the rigid arm to move forward and aft (a three-degree-of-freedom kinematics system), the mass inertia of the DTS may be too high to record every soil material deformation and flow, especially in the direction of the rigid arm axle.

The mass inertia of the DTS may also influence the representation of vertical SST displacement (Pytka et al. 1995); however, the resulting errors do not seem to be pronounced. The idea of simultaneous measurements of both stress and deformation at a point in a soil medium is valuable and should be further investigated. Continuous soil stress–strain curves can provide more precise and useful information on soil mechanical properties (Pytka and Konstankiewicz 2002).

3.2.4 Conclusions

The applied loads significantly affected soil stress and deformation state. The four investigated soil variants yielded different mean values of stress state components and deformation parameters—rut depth and vertical movement of the SST. For all the soil variants, distortional strain by shear stress components is probably relatively greater than volumetric strain, assuming that the energy of distortion is greater than the energy of compaction. That was quantified by means of the ratio of σ_{OCT} to τ_{OCT} (0.5 for all variants).

Tillage variants influence soil deformation significantly. We determined that both deformation parameters and vertical strain in soil after conventional plowing are markedly greater when compared to conservative rototilling. Soil state (undisturbed or homogenised) has a less significant effect on deformations under applied loads.

It is especially interesting that the two soil state variants for the plowed and rototilled soil do not show the same tendency as the tillage variants exhibited. The differences in soil strength for the two tillage systems and for the structure variants were quantified by means of a ratio of major stress σ_1 to vertical strain.

3.3 Effects Deformation Rate on Soil Stress and Deformation State in Loess

3.3.1 Experimental Set-Up and Procedures

The second experiment performed on monolith soil samples was performed at the Institute of Agrophysics of the Polish Academy of Science in Lublin (Pytka 1997). Monolith samples of loess soil were prepared in a laboratory using soil material taken from a field at depths up to 300 mm. Table 3.5 describes the soil horizon.

Soil was prepared by wetting to 11% water content (to replicate in situ conditions); soil portions were then placed into a monolith frame and manually

TABLE 3.5

Characterisation of Loess Used to Prepare Monolith Samples

Bulk Density (g/cm^3)	Sand (%)	Loess (%)	Loam (%)	Organic Matter (%)
2.64	18	68	14	1.53

compressed. A measuring system was installed in the frame before it was filled. The following sections describe the measuring systems.

3.3.1.1 Determination of Soil Deformation

Chapter 2 describes the optical system for measuring soil deformation. Here we discuss some technical aspects of applying this method to measure soil deformation in a monolith sample. A rigid arm connects the stress transducer with a laser projector on the opposite end and is suspended in a spherical bearing that allows rotations of the arm ±30°. Thus, each movement of the transducer caused by soil deformation is projected as a moving point on a semitransparent shield.

Figure 3.12 shows the complete experimental set-up. The movement of the light point is recorded by a CCD camera with an RGB (red–green–blue) image acquisition system. An upgraded portable computer serves both the camera and a multi-channel system that processes the soil stress data. Original software for both data acquisition systems enables simultaneous

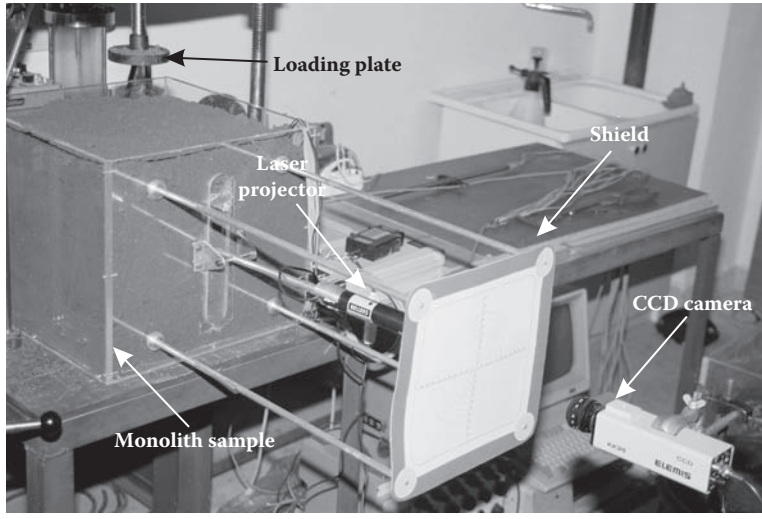

FIGURE 3.12
Optical system of soil deformation transducer installed in the monolith sample.

sampling of SST data and images from the camera and saves the data to hard discs.

3.3.1 2 Stress State Transducer (SST)

The SST used for the experiment was developed at the Institute of Agrophysics of the Polish Academy of Science in Lublin. The device uses six strain-gage pressure transducers; Chapter 2 describes the design and fabrication. The transducers are mounted in an aluminum body ~70 mm in diameter. Prior to installation in the SST body, each pressure transducer was calibrated by an in-air-method. The complete SST is presented in Figure 3.13.

3.3.1.3 Installation of Measuring System in Monolith

The SST was installed when the monoliths were prepared. Even the most advanced installation methods of milling and excavating can seriously damage soil and cause problems *from* contact between sensor membranes and soil. To mitigate those problems, we devised a simple method of placing the transducer after excavating the soil mass and then waiting until the soil strength reached initial values through age hardening.

When the monolith frame was filled to 15 cm below the top, the SST was placed in the middle and the monolith was carefully filled with the soil. Next, the monolith was coated to *deter* perspiration and left for 48 hours. After that, the instrumentation was installed and the set-up was ready for a test. Care was taken to fill the space of direct contact with the SST *thoroughly*. The *uniform* shape of the SST head was chosen to obtain optimum contact between soil and pressure transducers.

FIGURE 3.13
The SST used for the experiment.

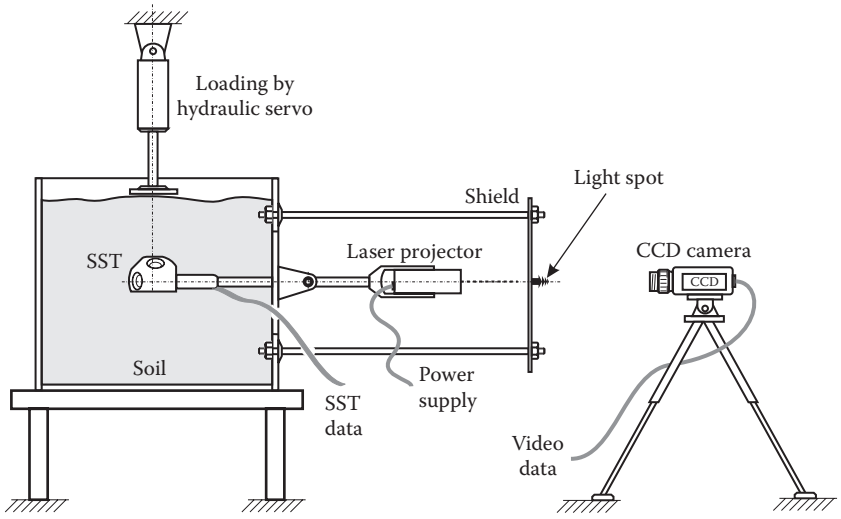

FIGURE 3.14
The complete experimental set-up for deformation rate ready for measurements.

3.3.1.4 Loading Soil

A 100-mm diameter circular plate was used to load the soil monolith surface. The loading plate was driven by a hydraulic servo with a control unit that allowed vertical movement at 0 to 0.04 m/s. The plate was driven into the soil monolith to a maximum of 65 mm. After it reached the lowest point, the plate was stopped for 2 to 3 seconds and then withdrawn. Figure 3.14 shows the complete system ready for measurements.

3.3.2 Results

The graphs in Figure 3.15 show deformation velocity effects on stress and deformation in soil. The soil was loaded vertically and horizontal SST displacements were not observed; therefore σ_1 and vertical displacement of the SST are shown together for five deformation velocities. It is obvious that loading velocity affects both soil stress σ_1 and soil deformation (identified here with SST vertical displacement). The shape of the stress curves for all velocities can be divided into three phases:

1. The loading process from the beginning to the point of maximum σ_1: the stress increases rapidly until the loading plate stops.
2. The loading plate is held in the lowest position: the stress decreases slowly.
3. The loading plate moves upward: soil stress decreases exponentially.

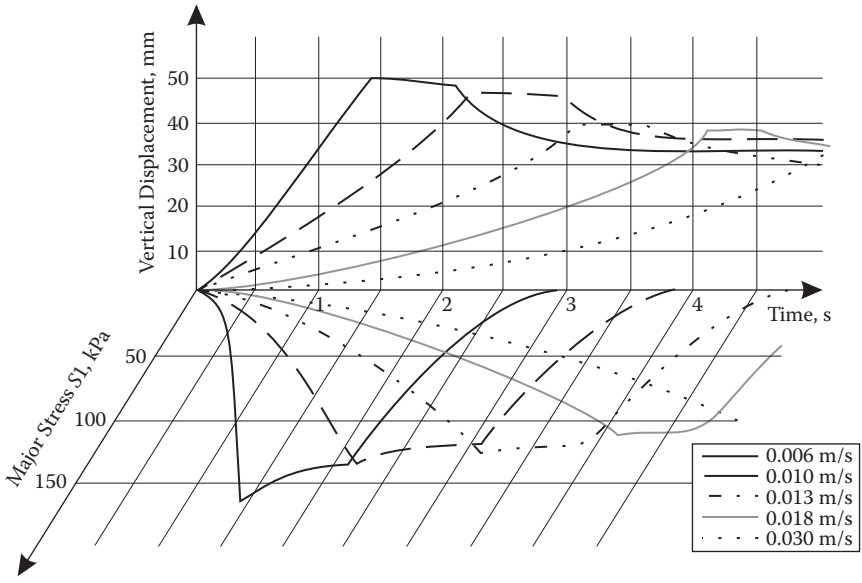

FIGURE 3.15
Effects of deformation rate on soil stress and deformation.

The increase of the soil stress σ_1 in the first phase is quasi-linear, and the loading velocity influences the intensity of the stress as quantified by the tangent of the angle between the time axis and the σ_1 curve. We would expect that amount of load applied to the soil would also influence the intensity of the stress. Both the loading velocity and the applied pressure should be investigated for their relationships with stress values and increased intensity.

After the soil was unloaded (the loading plate was lifted off), the stress decreased exponentially and reached asymptotically the value of about 0.6 to 0.7 σ_{1MAX}. This stress value can be called the residual stress in soil after loading.

3.3.3 Conclusions

The main purpose of the experiment was to examine a new optical method for measuring soil deformation combined with an SST to measure soil stress state. The results showed that the method is suitable for soil measurements and is promising for field experiments with running vehicles as described in the next chapters.

The soil monolith sample method is very useful in a laboratory. The soil can be carefully conditioned and environmental conditions such as weather do not affect procedures or results. On the other hand, even

such a large monolith sample cannot simulate full-scale wheel dynamics. Traditionally, laboratory experiments in wheel–soil dynamics were performed in soil bins and an instrumented wheel was driven over the surface of a soil in the bin. In our approach, however, we chose field experiments with running vehicles as the condition closest to reality.

References

Arvidsson J. and Ristic S. 1996. Soil stress and compaction effects for four tractor types. *J. Terramech.* 33: 223–232.

Bailey A.C., Raper R.L., Way T.R. et al. 1996. Soil stresses under a traction tire at various loads and inflation pressures. *J. Terramech.* 3: 1–11.

Bakker D.M., Harris H.D., and Wong K.Y. 1995. Measurements of stress paths under agricultural vehicles and their interpretation in critical state space. *J. Agric. Eng. Res.* 61: 247–260.

Harris H.D. and Baker D.M. 1994. A soil stress transducer for measuring in situ soil stresses. *Soil Till Res.* 29: 35–48.

Horn R. and Lebert M. 1994. Soil compactability and compressibility. In *Soil Compaction in Crop Production,* Soane B.D. and Van Ouwerkerk C., Eds. Amsterdam: Elsevier, pp. 41–96.

Kirby J.M. 1999a. Soil stress measurement I. *J. Agric. Eng. Res.* 72: 151–160.

Kirby J.M. 1999b. Soil stress measurement II. *J. Agric. Eng. Res.* 73: 141–150.

Pytka J., Horn R., Kuhner S. et al. 1995. Soil stress state determination under static load. *Int. Agrophys.* 9: 219–226.

Pytka J.A. 1997. Investigation of soil stresses and deformation with respect to loading process dynamics. PhD dissertation. Institute of Agrophysics, Lublin (in Polish with English summary).

Pytka J.A. and Konstankiewicz K. 2002. A new optical method for soil stress and strain investigation. *Soil Till. Res.* 65: 243–251.

Wiermann C., Way T.R., Horn R. et al. 1999. Effects of various dynamic loads on stress behaviour of a Norfolk sandy loam. *Soil Till. Res*. 50: 127–135.

4

Stress State under Wheeled Vehicle Loads

4.1 Introduction

In many approaches to the problem of off-road mobility, contact pressure is a main input parameter. A concrete surface acts something like a bridge that transfers and distributes wheel loads over a greater surface, while a soft surface deforms intensively because the loads are concentrated on a very small contact surface. Numerous papers have proven the importance and practical meaning of the stress state under wheels for measuring and predicting off-road traction (Dąbrowski et al. 2006, Foda 1991, Muro 1993, Hetherington and White 2002, Hetherington and Littleton 1987, Pytka 2007, Shibusawa and Sasao 1996, Shmulevich and Osetinsky 2003, Upadhyaya et al. 1997, Wanjii et al. 1997). In most models, tractive forces—driving force, rolling resistance, and vertical load—are determined based on an analysis of stress state or stress distribution on a contact surface. These forces are expressed in Bekker's equations:

$$F_{DR} = \int \tau(\alpha)\, d\alpha \tag{4.1}$$

$$F_{RR} = \int \sigma(\alpha)\, d\alpha \tag{4.2}$$

where $\tau(\alpha)$ is the shear stress component, $\sigma(\alpha)$ is normal stress, and α is a measure of a surface of volume over which the stresses accumulate.

Loads applied to a soft contact surface, however, are also distributed into the soil, and the character of this phenomenon depends on the kind of soil and its state as well as factors related to the vehicle such as speed, wheel slip, etc. Just as the load state under a wheel is complex, so is the soil stress state. The stress tensors change in value and orientation during the pass of a wheel. Knowledge of the dependencies between vehicle ride parameters and stresses may be advantageous for mastering the models of wheel–ground interactions.

This chapter describes our efforts to (1) develop procedures to measure soil stress state under moving vehicles in the field; (2) determine stresses under various vehicles on different soils at various ride parameters such as forward velocity, multiple passes, tyre inflation pressures, and wheel function modes (rolling and driving); and (3) determine and analyse octahedral stresses and their correlations with drawbar pull force generated by an additional braking vehicle.

4.2 Field Experiment Preparation

This section describes the experimental set-up used in all the tests described in this chapter. We used several types of wheeled vehicles including military trucks, a light utility vehicle, and agricultural tractors. These vehicles represented various weight categories and were equipped with different tyres. Table 4.1 summarises experimental conditions, variants, and test manoeuvres.

4.2.1 Stress State Determination

We used stress state transducers (SSTs) to capture soil pressures that we then recalculated into stress state components: principal stresses σ_1, σ_2, and σ_3; octahedral mean normal stress σ_{OCT}; and octahedral shear stress τ_{OCT}. The method is described in Chapter 2 and in the cited literature (Bailey et al. 1996, Horn et al. 2000, Horn and Rostek 2000, Pytka 1997, 2005, 2007, Raper et al. 1995, Way et al. 1996, Wiermann et al. 1999).

The SSTs were 35 mm in diameter, and the strain gage pressure transducers were 20 mm in diameter. Figure 4.1 is a photograph of one of the SSTs used in the experiment. Normally, one SST was installed at 10 to

TABLE 4.1

Technical Data for Test Vehicles

			Wheel Loads (kN)		
Vehicle	**Tyres**	**Mass (kg)**	**Front**	**Rear 1**	**Rear 2**
6 × 6 truck	14.00 × 20	Empty: 8180	20.55	10.25	11.08
		Mid: 11,780	21.92	18.14	19.08
		Full: 14,180	23.93	23.44	24.42
4 × 4 truck	12.00 × 20	5560	16.90	10.10	—
4 × 4 agriculture tractor	7.50 × 20	3100	5.15	10.80	—
	15.00 × 30				

FIGURE 4.1
The stress state transducer (SST) used in the experiment.

15 cm depth, but in some tests, two or even three SSTs were used at 15, 35, and 50 cm depths. In these experiments, the SSTs were always placed beneath the centre lines of the right wheels of the vehicles.

Various installation methods were used to place the SSTs at the required depths in the three different soils—loess, sand, and turf. We used simple excavation in the sandy and loess soils and in snow. In the loess soil containing structural bonds between particles, the SST was installed 3 to 6 hours before testing to let the aging effect rebuild the damaged soil structure. In the snow cover and sandy soil samples that had no structural bonds, tests were performed immediately after the SSTs were put in place. In turf, we drilled a round hole in the soil profile, pushed the SST into place, and then backfilled the excavated turf. Figure 4.2 presents the three techniques and Figure 4.3 shows a sample installation of the SSTs at depths.

4.2.2 Soil Surface Deformation Determination

The deformation of the soil volume was determined by an optical system consisting of four laser projectors, a semitransparent shield, and a video camera. This system let us measure vertical and longitudinal (volumetric) deformations and structural (shape) deformations of the soil. Figure 4.4 is a schematic of the system. The soil deformation transducer system was installed along with the SST. Figures 4.5 and 4.6 show soil deformation probe rods during installation and the completed experimental set-up.

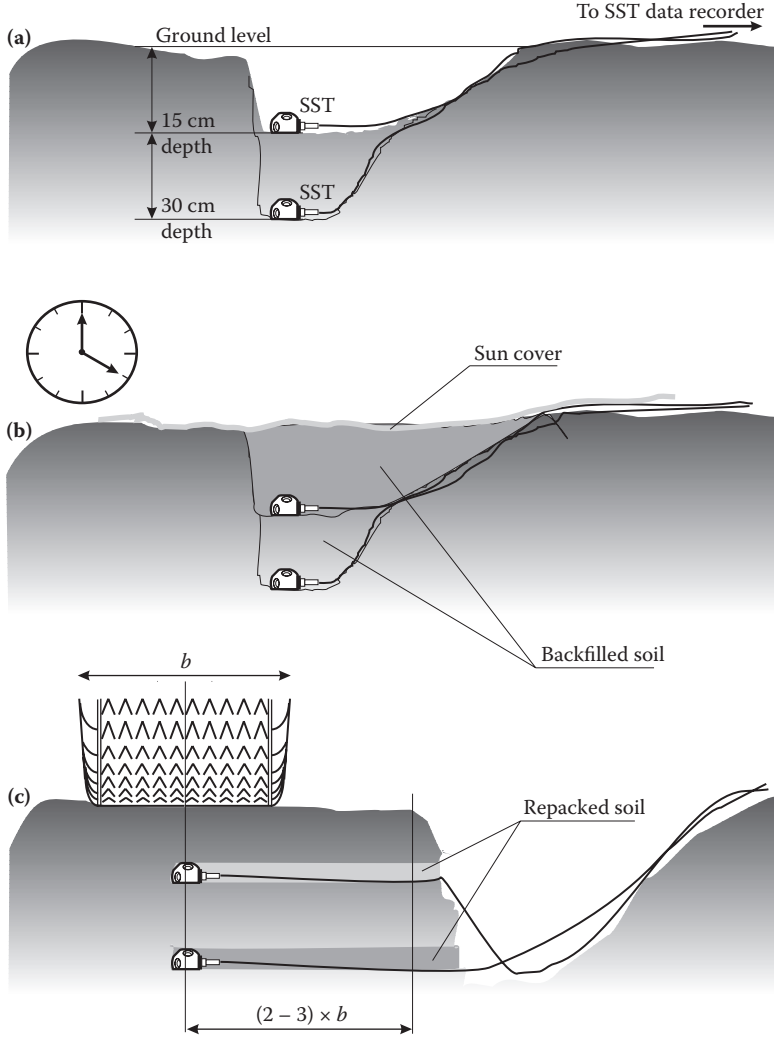

FIGURE 4.2
Installation of the SST in soil profiles (a) sandy soil, (b) loess soil, (c) turf.

4.2.3 Pulling Force Determination

A pulling force was generated to investigate the influence of wheel slip on stresses and create correlations between octahedral stresses and drawbar pull. The pulling force was created by a vehicle connected to the test vehicle by an elastic rope. In other tests, we investigated wheel loading and repeated rolling over the SSTs. Stress states in the three different soils

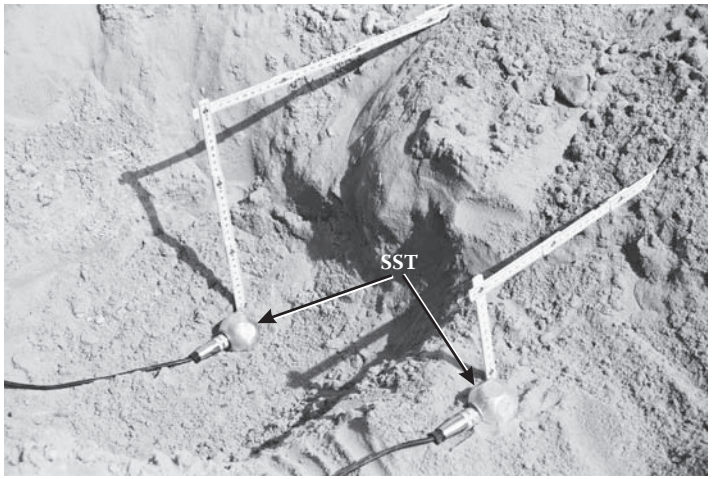

FIGURE 4.3
Installation of the SSTs at depths.

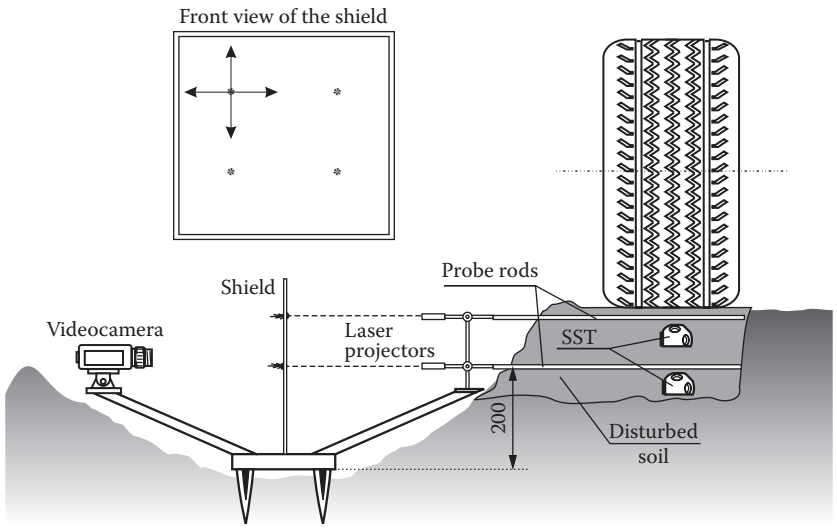

FIGURE 4.4
A schematic of the soil surface deformation transducer system.

were determined and analysed. Related vehicle measures were determined as follows:

- Drawbar pull F_{DBP} was measured with a strain gage dynamometer connected to the rear of the test vehicle.

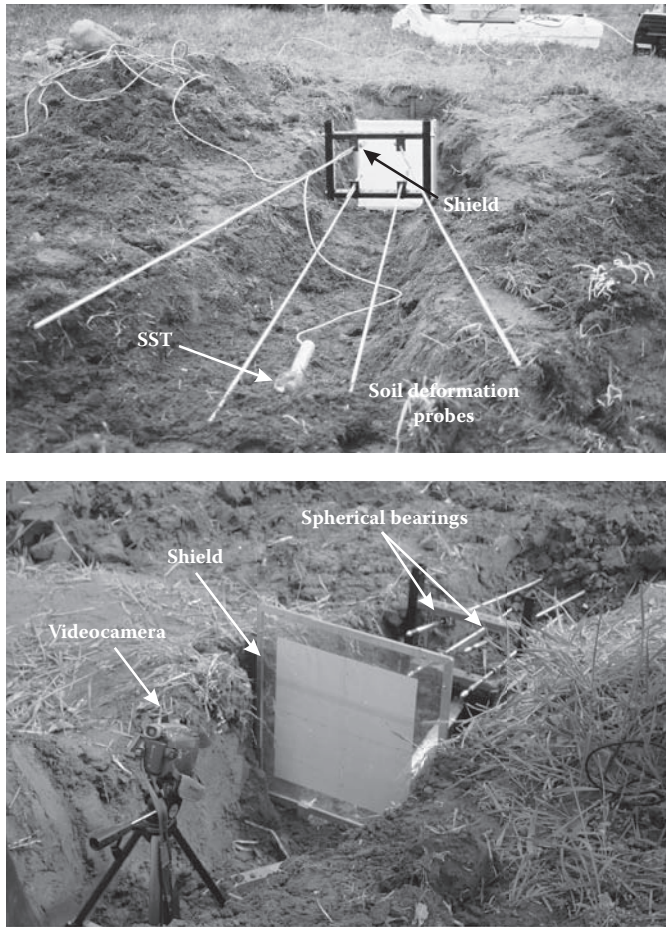

FIGURE 4.5
Installation of the soil surface deformation probe rods (a) and a video camera together with the projector shield (b).

- Wheel slip was determined from measured forward velocity obtained with an optical sensor and from wheel rotation speed measured by a tachometer attached to a driven wheel.
- Data acquisition was performed on a portable computer with an external data acquisition system; a digital data recorder DAT was used in parallel to save the data.

More detailed descriptions of the experimental set-up are given by Dąbrowski et al. (2006) and in Chapter 8 where we present a method for obtaining traction curves.

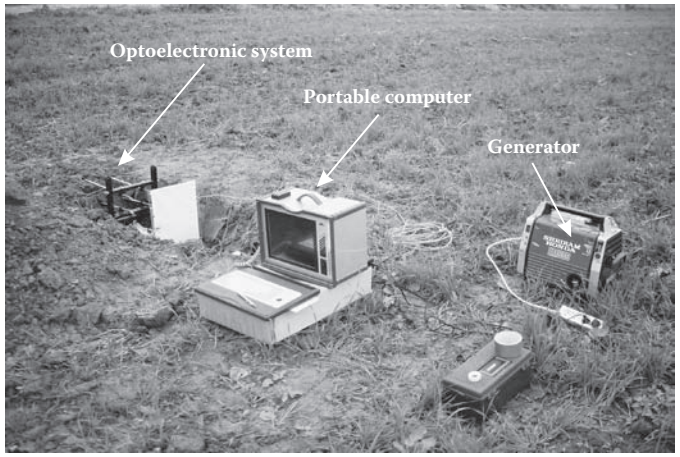

FIGURE 4.6
The complete experimental set-up ready for the measurements.

4.2.4 Test Vehicles, Field Procedures, and Soil Surfaces

Three wheeled vehicles were used in the tests (Figure 4.7). Basic technical data for the vehicles and details of their use for particular tests are presented in Tables 4.1 and 4.2, respectively. Normally, vehicles were driven at 5 to 8 km/h with little or no wheel slip. The tests investigated wheel loading, reduced inflation pressure, rolling velocity, and multiple and repeated rolling over the SSTs.

As cited above, the field tests were performed on three soil surfaces and on snow cover. The soils were chosen to investigate the effects of the differences in internal friction and cohesion in sand and loess.

A typical sand exhibits compactive failure, and vehicle traction increases with increasing wheel slip. This is caused by high internal friction and low cohesion when sand is dry. Cohesion occurs in loess or loamy soils, especially in moist conditions, resulting in an early peak in the traction curve (net traction, μ-wheel slip, *s* curve) and a decrease in traction at high slip.

The values of bulk density were 1.72 and 1.64 g/cm^3 for the sand and the loess, respectively. The turf was chosen as a typical forest surface. Its amorphic structure and high sensitivity to changes in water content (WC) created a wide range of mechanical properties. The snow cover was shallow, 40 cm deep, and had a density of ~0.55 g/cm^3. Snow temperature during the tests was 0.3°C.

(a)

(b)

(c)

FIGURE 4.7
The vehicles used in the experiments: (a) 14-T 6 × 6 and, (b) 5.6-T 4 × 4 trucks, and (c) 3.1-T agricultural tractor.

TABLE 4.2

Summary of Experimental Conditions

Soil Type	WC	Depth (cm)	Wheel Mode	Load	Tyre Pressure (kPa)	Passes	Velocity (km/h)
5.6 Tonne 4 × 4 Military Truck							
Loess	Dry	15 and 30	Driving	Max	390	1	5 to 8
	Dry	15 and 30	Rolling	Max	390	1	5 to 8
	Wet	15	Rolling	Max	390	1	5 to 8
Sand	Dry	15 and 30	Driving	Max	390	1	5 to 8
	Dry	15 and 30	Rolling	Max	390	1	5 to 8
	Wet	15	Rolling	Max	390	1	5 to 8
Turf	Dry	15 and 30	Driving	Max	390	1	5 to 8
	Dry	15 and 30	Rolling	Max	390	1	5 to 8
	Wet	15	Rolling	Max	390	1	5 to 8
Snow	—	15	Driving	Max	390	1	5 to 8
	—	15	Rolling	Max	390	1, 2, 3, 4, 5	5 to 8
14 Tonne 6 × 6 Military Truck							
Loess	Dry	15 and 30	Driving	8/11, 6/14 tonnes	200 and 390	1	5 to 8
	Dry	15 and 30	Rolling	8/11, 6/14 tonnes	200 and 390	1	5 to 8
Sand	Dry	15 and 30	Driving	8/11, 6/14 tonnes	200 and 390	1	5 to 8
	Dry	15 and 30	Rolling	8/11, 6/14 tonnes	200 and 390	1	5, 10, 15
3.1 Tonne Agricultural Tractor							
Loess	Dry	15 and 30	Rolling	Max		1, 2, 3, 4, 5, 6	3 to 5
Sand	Dry	15 and 30	Rolling	Max		1, 2, 3, 4, 5, 6	3 to 5

4.2.5 Data Reduction Methods

Soil pressure data were calculated into stress state components using software that determines three principal stresses—σ_1, σ_2, and σ_3—and their direction cosines. The algorithm for the stress state calculation is based on a theory of elasticity presented in Chapter 2. The complete set of data was searched for peak maximum stresses. Normally, stresses from the road wheels were averaged from a minimum of five replications, so the presented results represent arithmetic average values.

Video data were analysed by reading the Z and X co-ordinates of the light spots from video images before and after each pass of a vehicle. In this manner, the initial and final states of soil deformation were determined. To avoid or minimise the erroneous effects of the shapes of the light spots (ellipsoid, ~2 × 4 mm), a representative point was positioned as a geometrical centre of each spot. To visualise soil deformations after each vehicle pass, changes in shape and dimensions of a basic soil volume were recorded.

Only the final positions of the deformed soil volume after each of the vehicle passes are drawn for better clarity of the graphs. In further analyses, total surface area of the quadrilaterals was determined with a surface integrator. Values of percentage decrease of area were determined as functions of increased pass numbers for two soils. Finally, strain ε was determined as the specific decrease of the surface area of the quadrilaterals for each pair of two succeeding passes:

$$\varepsilon = \frac{S_{n+1}}{S_n},\ n = 1, 2, 3, 4, 5, 6 \tag{4.3}$$

where S = surface area of the measured quadrilaterals. The angle of shearing was determined graphically from the obtained data.

4.3 Analysis of Principal Stresses

4.3.1 Introduction

A stress state must be defined when we consider stresses in a body. For this purpose, we place the investigated body in an orthogonal set of axes; the zero point is the point in the body at which we want to determine stresses. Introducing a notation for stresses, we allocate a single subscript to direct stresses to denote the plane on which they act and two subscripts to shear stresses: the first for the plane, the second for direction (Megson 2010).

Now we describe the complete stress state at a point in a body by specifying components of shear and normal stresses on the faces of an elemental cube. Assuming that the stresses are uniformly distributed over the surface of each face, the sides of the cube are infinitesimally small. By dividing the forces by the surface of each face, we calculate nine stress components:

$$\begin{matrix} \sigma_x & \tau_{xy} & \tau_{yz} \\ \tau_{yx} & \sigma_y & \tau_{yz} \\ \tau_{zx} & \tau_{zy} & \sigma_z \end{matrix} \tag{4.4}$$

This is a stress tensor and the components σ_x, σ_y, and σ_z are normal tangential (positive) or compression (negative) stresses acting on three orthogonal axes. The resting components are shear stresses.

The complete stress state was derived for a situation in which actual loads act on a body and the state of stress is determined for an arbitrary system of axes. It is necessary to investigate the state of stress on other than arbitrary planes on which the direct and shear stresses may be greater. When we want to determine stresses acting on a plane inclined at an angle θ to the vertical axis, we can resolve direct stress as below:

$$\sigma_n = \sigma_x \cos^2 \theta + \sigma_y \sin^2 \theta + \tau_{xy} \sin 2\theta \tag{4.5}$$

and shear stress:

$$\tau = \frac{\sigma_x - \sigma_y}{2} \sin 2\theta - \tau_{xy} \cos 2\theta \tag{4.6}$$

At any point of our investigated body, we can separate a basic cube with sides parallel to the major planes. In other words, three axis stresses σ_x, σ_y, σ_z attain a maximum or minimum value when

$$\frac{d\sigma}{d\theta} = 0 .$$

By resolving Equation (4.5) with respect to this, we get the condition for the extremum σ_n: θ and $\theta + \pi/2$. Further, by resolving Equation (4.6), we discover the values of shear stresses are 0. They are called principal stresses and are designated σ_1, σ_2, and σ_3. For the principal stresses we have

$$\sigma_1 > \sigma_2 > \sigma_3 \tag{4.7}$$

For a two-dimensional state of stress we have only two principal stresses—σ_1 and σ_2—that are called major principal and minor principal stresses, respectively.

4.3.2 Experimental Details

To analyse principal stresses, we used soil pressure data obtained with the 14-tonne and 5.6-tonne military trucks driven over loess, sand, and turf under the following conditions:

Zero slip conditions at ~5 to 8 km/h
High slip conditions (pull tests utilizing an additional braking vehicle)
Varying speeds (5, 10, and 15 km/h

We used only two SSTs without optoelectronic systems for soil deformation determination. The SSTs were placed at depths of 15 and 30 cm, in line beneath the right wheels of the test vehicles. Details of SST installation are included in the Section 4.2 and a summary of the test conditions can be found in Table 4.1.

4.3.3 General Analysis of Principal Stresses

Values of principal stresses under the wheels of the test vehicles are shown in Table 4.3. Figure 4.8 shows a sample graph of the soil stress state components with principal stresses σ_1, σ_2, and σ_3 plotted versus time. Although

TABLE 4.3

Peak Maximum Values of Principal Stresses under Wheels of Test Vehicles[a]

A. 5.6-tonne 4 × 4 truck driven on loess, sand, and turf

Depth	Wheel	σ_1 (kPa)	σ_2 (kPa)	σ_3 (kPa)
Loess				
15 cm	Front	647.2 (8.65)	194.0 (6.69)	–234.4 (7.12)
	Rear	460.2 (25.03)	128.6 (15.23)	–165.6 (23.30)
30 cm	Front	294.15 (4.25)	95.1 (4.90)	–117.45 (4.52)
	Rear	210.0 (11.70)	64.35 (2.33)	–80.1 (3.57)
Sand				
15 cm	Front	653.8 (12.84)	93.4 (28.17)	–393.8 (14.56)
	Rear	435.8 (14.64)	74.6 (43.02)	–323.06 (7.48)
30 cm	Front	372.97 (5.50)	107.43 (33.48)	–77.02 (19.63)
	Rear	223.83 (8.74)	62.4 (23.87)	–56.85 (23.07)
Turf				
15 cm	Front	117.8 (38.30)	33.2 (31.60)	–108.8 (34.84)
	Rear	77.2 (20.57)	24.6 (22.23)	–48.6 (12.33)
30 cm	Front	60.7 (34.99)	1.5 (57.73)	–104.5 (31.02)
	Rear	62.4 (20.31)	4.5 (10.87)	–112.95 (10.9)

(continued)

TABLE 4.3 (continued)

Peak Maximum Values of Principal Stresses under Wheels of Test Vehicles[a]

B. Major principal stress σ_1 only for 14-tonne 6 × 6 truck driven on loess and sand at three loads

Depth	Wheel	8.18-T	11.78-T	14.18-T
Loess				
15 cm	Front	399.8 (16.9)	473.6 (7.4)	353.9 (11.6)
	Rear I	216.6 (23.1)	340.6 (8.4)	464.75 (6.0)
	Rear II	283.2 (18.1)	287.0 (1.7)	462.4 (5.0)
30 cm	Front	174.45 (8.9)	270.9 (0.7)	245.73 (9.3)
	Rear I	73.95 (20.0)	210.6 (2.0)	308.79 (5.4)
	Rear II	80.85 (4.3)	170.7 (5.1)	283.23 (7.9)
Sand				
15 cm	Front	244.0 (8.6)	263.3 (17.4)	265.75 (13.3)
	Rear I	94.0 (23.7)	126.5 (18.0)	194.66 (14.2)
	Rear II	190.0 (17.2)	190.5 (26.7)	259.06 (10.2)
30 cm	Front	84.07 (8.8)	80.2 (22.3)	62.57 (8.8)
	Rear I	24.24 (26.3)	18.83 (22.7)	31.30 (25.7)
	Rear II	53.22 (22.3)	49.53 (10.0)	54.96 (15.4)

[a] Percentage values of standard deviation shown in brackets.

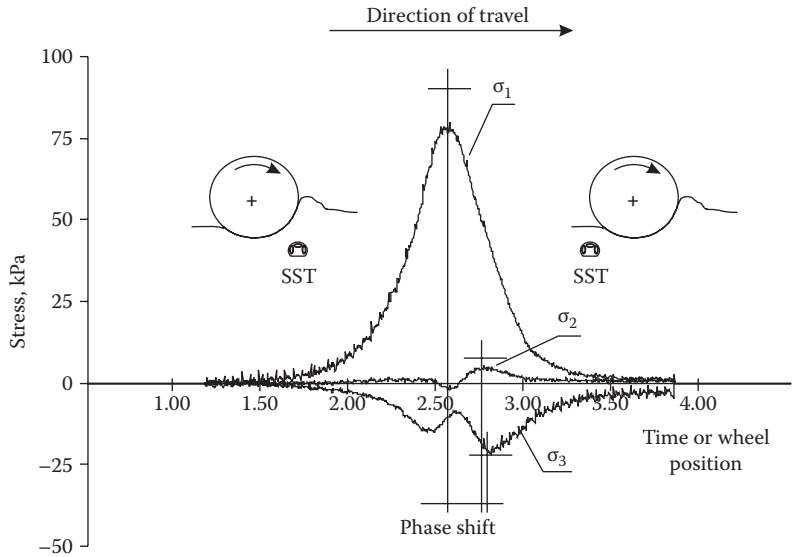

FIGURE 4.8
An example graph of soil principal stress state components.

values of the stress state components vary over a wide range, the relationship among them is stable. The major principal stress σ_1 is always the greatest compressive stress, while σ_2 in some tests was very low or close to 0, suggesting a two-dimensional stress state.

The minor principal stress σ_3 reached negative values in many tests. In such cases, the soil was under tension, not compression. It is interesting to note where the peak maximum stresses are located on the time axis. There is a phase shift between σ_1, σ_2, and σ_3. The σ_3 stress increases and reaches its local maximum (a negative value) just before the maximum of σ_1.

At the point of σ_1 maximum, σ_3 reaches its local minimum and then increases to the second local maximum. After that, σ_3 tends to zero. The major stress σ_2 follows a similar trend but at much lower positive values. These changes in the major stresses were observed for most of the measurements and are caused by the effect of the wheel; before the σ_1 stress reaches its maximum, the two other principal stresses increase; then at the maximum of σ_1, the other stresses decrease.

4.3.4 Effect of Soil Surface

The differences among the three soils are pronounced (Figure 4.9). The highest values of stresses were found in the loess; stresses were lower in the sand and lowest in the turf. Other researchers reported similar tendencies for loess and sand (Bailey et al. 1996). This effect, however, changes for different water content (WC) values. Figure 4.9 shows graphs for two WC conditions: A is for relative dry soils (WC of 3% to 8% for sand and loess and 12% for turf) and B is for moist soils (WC of 10% to 13% for sand and loess and about 28% for turf).

Increasing WC had noticeably different effects on sand and loess. The increase in stresses for moist soil conditions in sand can be explained by viscosity or increased cohesion as a result of additional interactions among grains. The decrease of stresses as WC increased in loess can be explained by plasticity caused by water added to the soil. Loess and loamy soils become plastic when water is added, so the indicated stresses under vehicle loads are lower. There was a significant difference between the two WC conditions for turf. This soil surface is very sensitive to WC changes; adding water causes significant changes in volume and weakens the mechanical properties.

4.3.5 Effects of Wheel Function Modes: Rolling and Driving

In wheel mechanics, the two general modes of wheel function are (1) rolling in which a wheel rotates as the result of an external source, and (2) driving or braking during which a wheel generates its driving or braking force. During rolling, the forces acting on a wheel are rolling resistance

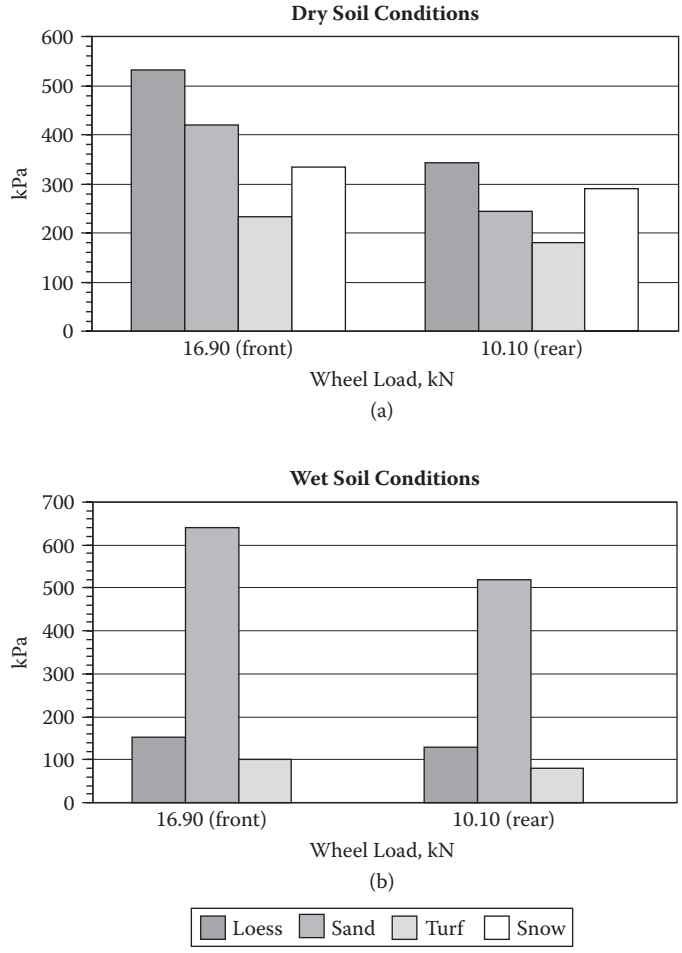

FIGURE 4.9
Effect of surface on stress under wheel loads of the 5.6-T 4 × 4 truck.

and vertical load. During driving or braking, another driving force is generated in the wheel surface contact area and inside a volume under this patch (Muro 1993, Wulfsohn and Upadhyaya 1992, Wanjii et al. 1997). This driving force depends on numerous factors—tyre dimensions, tread pattern, inflation pressure, type and state of surface, and other factors in addition to the engine power that determines the limits of driving action.

Conversely, the wheel function mode (driving versus rolling) can affect the response of a surface, especially for a deformable soil. Wheel slip becomes an important factor during driving on soft, easily deformed surfaces. In such situations, forward velocity decreases and wheel–surface interaction changes because of large longitudinal forces on the contact

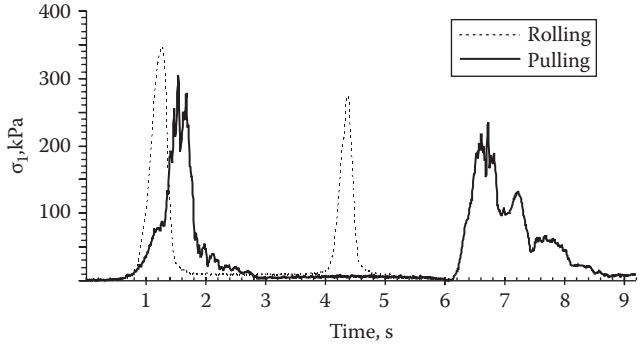

FIGURE 4.10
Effect of pull force and wheel slip on soil stress courses (5.6-T 4 × 4 truck).

patch (Wanji et al. 1997, Dąbrowski et al. 2006). We therefore chose the wheel function mode as one of the important factors affecting the stress states under wheel loads.

Figure 4.10 shows a general difference in stress curves between the two wheel function modes. The difference between rolling and driving was investigated for a 5.6-tonne 4 × 4 truck (on loess, sand, and turf) and a 14-tonne 6 × 6 truck (on loess and sand only). For the 14-tonne 6 × 6 truck at different loading levels, driving resulted in lower values of stresses, although a greater difference was observed on the loess soil surface.

As was expected for the sandy soil, at 15-cm depth, the stresses under the wheels were greater during driving than rolling. For the 5.6-tonne 4 × 4 truck, the effect of driving was much more significant and occurred in all three soils (see Table 4.4). Note that this truck was driven at a high slip (almost enough to stop the vehicle, 100% slip), while the 14-tonne vehicle passed the SST at moderate to high slip (40% to 80%). Moreover, the vehicles were equipped with different tyres (universal and terrain treads, respectively). This suggests significant and complex effects of driving and wheel slip on soil stress.

This conclusion is in opposition to that of Bakker et al. (1995) and Block et al. (1994), who concluded that slip exerted little or no effect (of similar tendency) on soil stresses. However, the wheel slip values used by Block et al. were 10% and 18.5%, and the experiment was conducted with a rigid wheel. Bakker et al. did not determine wheel slip. They used a cultivator to apply pull force to the vehicle and the results are only qualitative.

4.3.6 Orientation of Principal Stress σ_1

The method we used allowed us to determine stress values and their orientation. The stress state consists of a 3 × 3 matrix. Its components are

TABLE 4.4

Peak Maximum Values of Major Principal Stress σ_1 in Rolling and Driving Modes

	Rolling	Driving
5.6-Tonne 4 × 4 Truck		
Loess	647.2 (8.65)	148.13 (31.30)
	460.2 (25.03)	235.53 (7.92)
Sand	653.8 (12.84)	246.56 (25.30)
	435.8 (14.64)	268.25 (23.16)
Turf	117.81 (38.30)	140.95 (23.67)
	77.2 (20.57)	259.6 (22.14)
8.18-Tonne 6 × 6 Truck		
Loess	399.8 (16.9)	171.59 (14.3)
	216.63 (23.1)	260.35 (12.0)
	283.22 (18.1)	276.8 (12.2)
Sand	244.05 (8.6)	255.5 (13.5)
	94.21 (23.7)	158.0 (41.7)
	190.32 (17.2)	295.43 (27.2)
11.78-Tonne 6 × 6 Truck		
Loess	473.64 (7.4)	157.34 (12.7)
	340.62 (8.4)	220.65 (15.8)
	287.44 (1.7)	330.41 (8.1)
Sand	263.32 (17.4)	205.41 (21.6)
	126.5 (18.0)	108.05 (8.3)
	190.5 (26.7)	214.67 (30.7)
14.18-Tonne 6 × 6 Truck		
Loess	353.94 (11.6)	67.5 (39.8)
	465.07 (6.0)	253.42 (20.8)
	462.4 (5.0)	334.65 (21.0)
Sand	265.75 (13.3)	248.61 (8.5)
	194.68 (14.2)	311.22 (8.4)
	269.06 (10.2)	330.51 (8.7)

[a] Measured depth = 15 cm. Percentage values of standard deviation shown in brackets.

three eigenvalues and three eigenvectors. The eigenvalues are the magnitudes of the principal stresses σ_1, σ_2, and σ_3. Each eigenvector consists of three direction cosines, which are cosines of the included angles between the direction of the principal stresses and the three orthogonal axes *x*, *y*, and *z* (Way et al. 1996). The orientation of stresses is given by the direction cosines and is determined for each time (or location) point during the pass of a tyre.

The orientation of principal stress σ_1 is shown in Figure 4.11. The vectors of σ_1 are in side views, so only the angles between stress direction and the vertical axis are presented. The figure is shown to scale, but the relationship between the stress and length scale is arbitrary. The stress vectors are given for three different soil surfaces at two depths, and for

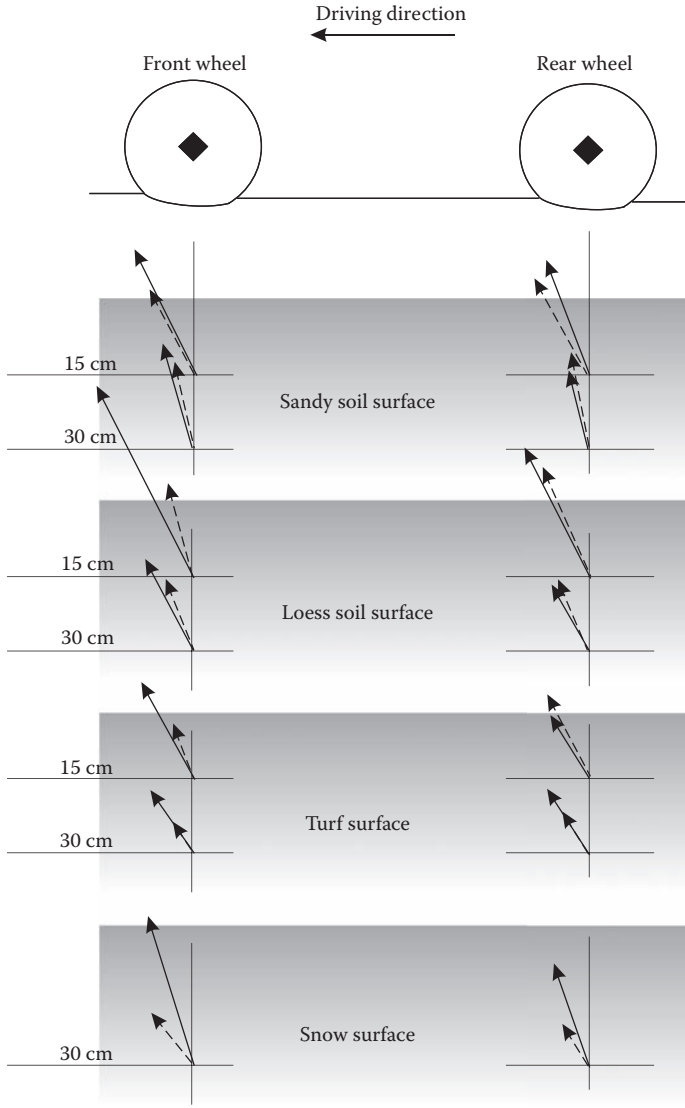

FIGURE 4.11
Orientation of the principal stress σ_1 at two driving modes in three soil surfaces under loading of the wheels of the 5.6-T 4 × 4 truck.

driving and rolling for the front and rear wheels of the 5.6-tonne 4×4 truck. Note the vectors are shown for the σ_1 directly beneath the centre line of a wheel. Determining the vectors outside the centre line is unreliable due to the small magnitude of σ_1.

Generally, the major principal stress was tilted forward under the tyres for all cases. In sandy soil, the orientation of the principal stress σ_1 changed with the stress measuring depth: the deeper the measurement, the smaller the angle. There was no significant difference between the two wheel-function modes.

In loess soil, the angle of the σ_1 was almost unchanged for two depths, but there was an effect under the front wheels at driving mode: the σ_1 vector at driving was less tilted than at rolling (the front wheels were much more loaded than the rear wheels). Moreover, the magnitude of the σ_1 stress was higher at rolling than at driving. We found no pronounced effects of depth and driving mode on the σ_1 stress on a turf surface.

The effect of depth on stress orientation in sandy soil can be explained by the internal friction of the sandy soil. The driving force is a sum of frictional forces between sand particles and tyre tread and among the particles themselves. The interactions within the sand volume were weakened for deeper points. Therefore, the horizontal (shearing) component of stress state decreases and the tilt angle of the resulting stress decreases with greater depth.

The investigated soil surfaces were at relatively low WC (dry soil condition). A dry loess soil surface rebuilds a strong structure similar to a solid. Wheel loads helped compress and strengthen this structure even more. Therefore, the stress orientation in loess probably was not influenced by depth (at least up to 30 cm). Also, the relatively strong structure of dry loess soil surface does not explain why driving resulted in less tilt to the stress orientation than rolling. An adverse mechanism would be expected because of the high shear (horizontal) stresses during driving. This difference in the effect of loess and sand soil surfaces at the two wheel-function modes underlines the difference between the two investigated surfaces for off-road traction.

4.3.7 Effect of Increasing Vehicle Speed

The effect of speed was investigated for the 6×6 truck on the sandy soil. The vehicle was driven at three loads—empty, mid, and full loads—at normal inflation pressure (390 kPa; Figure 4.12). Generally, stress values decreased as velocity increased; this effect was greatest with the full load. Moreover, the effect of velocity was always greater for the front wheel. This wheel deforms the soil and the primary stress distribution occurs under it. The rear wheels follow the rut formed by the front wheel and,

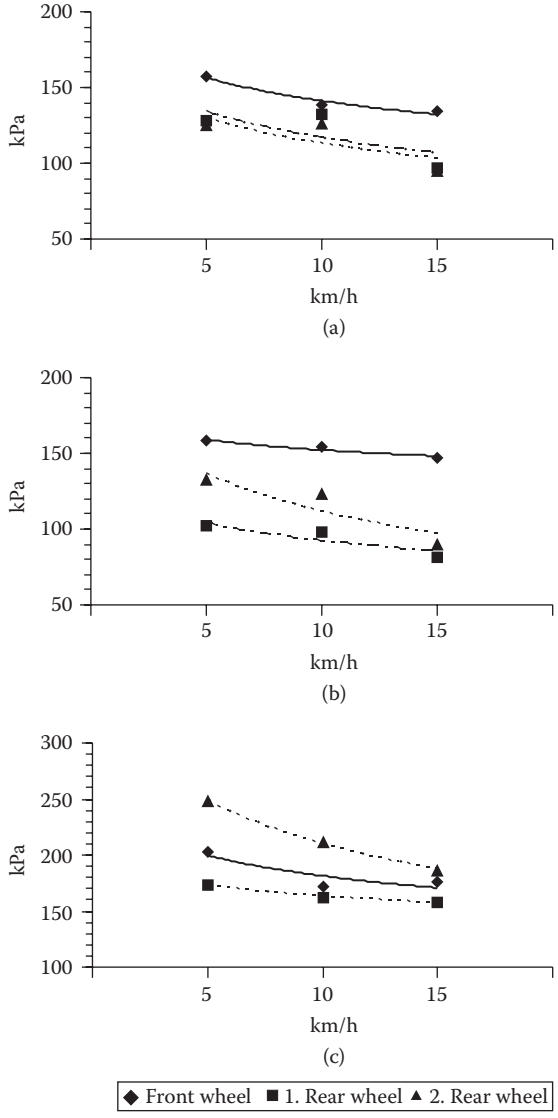

FIGURE 4.12
Effect of forward velocity on the major stress σ_1 in the sandy soil under wheels of a 14-T 6 × 6 truck. A – empty weight, B – mid load, C – full load.

because the soil is already compacted, the stresses do not change (decrease) greatly. This suggests that when vehicles are driven in a column, the first vehicle should be driven at higher velocity to ensure better traction for succeeding vehicles.

4.4 Effect of Vehicle Loading and Reduced Inflation Pressure

4.4.1 Introduction

Vehicle performance on soft surfaces depends on two major factors: (1) its design features such as power unit, transmission, suspension, tyres, etc., and (2) the type and state of the soil surface—type, WC, compaction, and structure. In some cases, vehicle-related parameters can be improved, and traction depends on the strength of the soil surface. Heavy vehicles running on soft, moist soils cause huge deflections of the surface that are irreversible and immediate after the first pass.

A soil deforms under vehicle loading because of the soil's strength or weakness and its bearing capacity. The total amount of soil deformation can be related to soil compaction that should be minimised for agricultural tractors and machinery. This can be achieved by wide, low-pressure tyres; by parallel wheels; or by reducing vehicle mass. Rolling resistance and fuel consumption increase as more soil is deformed, because more traction energy is consumed through soil deformation. Unfortunately, wide, low-pressure tyres are not practical on paved roads because of poor performance. Another solution must be found for vehicles that must travel on and off paved roads.

One efficient method for improving off-road traction is reducing inflation pressure to enlarge the wheel–soil contact area and improve positive friction between the tyre and the soil. This method is limited, however, by the increased rolling resistance of under-inflated tyres.

On the other hand, an increase in wheel load may have positive influence on traction. Higher loads compact the soil surface and increase soil strength. Also, high contact pressure creates more intensive friction between the tyre and the soil surface, leading to higher shear stresses.

Shear stress or shear resistance of soil surface is a generic measure for drawbar pull force. It is obvious that increasing the wheel (or vehicle) load requires more power and affects fuel consumption, but for required mobility, as in military operations, this is not a concern.

We assume that reduced inflation pressure and increased wheel load may increase drawbar pull and decrease soil deformation. Small or moderate reductions in inflation pressure for off-road operations may be achieved easily and should not affect tread wear and hardpan traction. It is interesting to see how increasing the wheel load affects traction, especially on different soil surfaces. To obtain a deeper understanding of the phenomena of interest here, we investigated soil deformations and soil stress at different depths. These measures can be related to obtained traction.

4.4.2 Experimental Details

The 14-tonne 6 × 6 truck was used in this experiment. The tyres were inflated at normal (390 kPa) and reduced (200 kPa) pressures. Wheel loading was changed by adding masses of 3.6 and 6.0 tonnes, and the vehicle was tested without external load. Table 4.1 cites masses and wheel loading; Figure 4.13 is a schematic of loading.

Test rides were made with tyres inflated to normal pressure (390 kPa) carrying three loads (empty weight, +3.6 tonnes, and +6.0 tonnes) and with tyres at reduced pressure (200 kPa) at empty weight only. Field tests

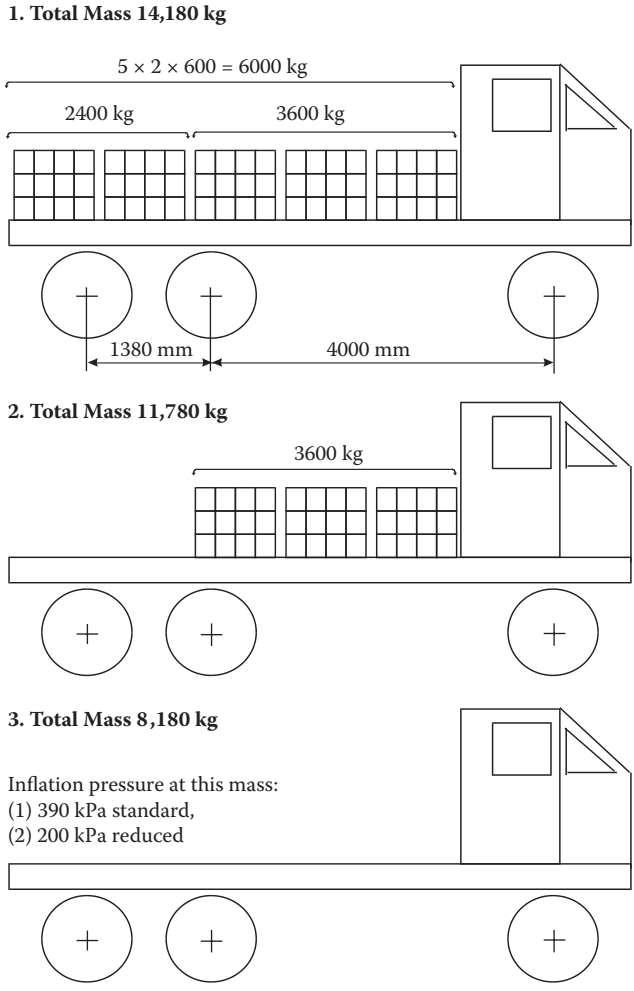

FIGURE 4.13
A schematic of the 14-T 6 × 6 truck loading.

FIGURE 4.14
A typical test ride.

were carried out on sand and loess. Soil surfaces were prepared by manual homogenisation, up to 30 cm. Moisture content of both soils was low (5% to 8% w/w). No rainfall occurred for 5 days before the tests. After each test ride, the soil surface was manually homogenised up to a depth of 30 cm and the ruts were levelled. A typical test ride is shown in Figure 4.14.

4.4.3 Effects of Loads on Soil Stresses

The effect of dynamic loads on the wheels is interesting. Figure 4.15 shows the relationships of dynamic wheel loads and peak maximum values of the major stress σ_1 in the sandy and loess soils during passes by the 14-tonne 6×6 truck. The vehicle was run empty (8.18 tonnes gross weight), half loaded (11.78 tonnes gross weight), and fully loaded (14.18 tonnes gross weight). Points on the graphs represent pairs of wheel dynamic loads and their respective stresses. The graphs are plotted for two measuring depths: 15 and 30 cm.

Although the absolute values of the principal major stress σ_1 are greater for the loess soil, the stress increase is stronger for the sandy soil. There is also a significant difference between the two measuring depths for the sandy soil; for the 15-cm depth, the σ_1 increased much more intensively. The reason may be that the sandy soil deformed to a greater degree and depth than the loess, and the deformation is not uniform along the soil profile. Moreover, the loess soil, with a more stable structure, makes a quasi-elastic body with a linear load–stress relationship within the whole volume.

The values of the three major stresses show that the stress state under the wheel loadings at high wheel slip is not homogeneous. The highest

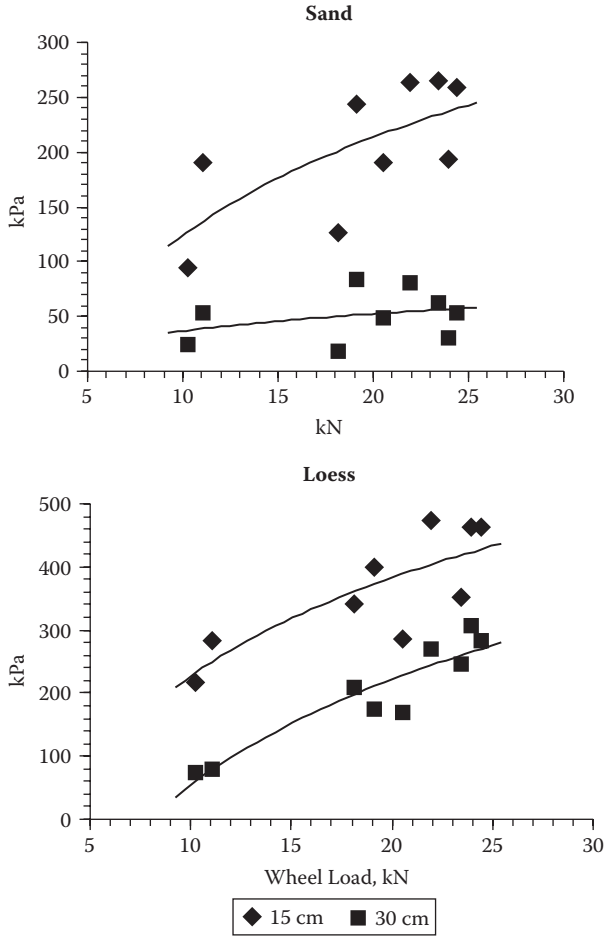

FIGURE 4.15
Effect of dynamic wheel loads on the major stress σ_1 for the 14-T 6 × 6 truck.

major stress σ_1 that acts almost vertically is clearly greater than the two remaining major stresses σ_2 and σ_3. The σ_2 is almost 0, and σ_3 has negative values of about 1/3 of σ_1. Octahedral shear stress is higher than mean normal stress, especially for higher vehicle loading. This suggests a dominance of shearing over compression in the test soils.

The two stress components in the octahedral stress system, σ_{OCT} and τ_{OCT}, quantify two general mechanical behaviours of the soil surface materials. Mean normal stress describes dynamic response on compressive external loads, while shear stress has its origin in tangential forces in wheel–soil systems. Of great importance is the fact that those stresses are accommodated in a soil volume as well as on a contact surface.

4.4.4 Effects of Reduced Inflation Pressure on Soil Stresses

The effect of reduced tyre inflation was examined on the empty 14-tonne 6 × 6 truck at two drive modes: rolling (wheel rotates as the result of an external source) and driving (wheel generates the driving or braking force). The measurements were performed on sandy and loess soil surfaces at depths of 15 and 30 cm. Both soil surfaces were dry. Soil stresses were determined with (1) normally inflated tyres at 390 kPa and (b) tyres with inflation pressure reduced to 200 kPa. The reduced inflation pressure was chosen based on the tyre manufacturer's recommendations for the lowest possible value to avoid spinning (rotating) of the tyre around the rim. A snow tread tyre was used.

The effect of reduced inflation pressure was unexpected. Although rolling over loess soil and driving over sandy soil decreased peak stress values at the lower inflation pressure, the effect was the opposite for the two other cases. Soil stresses were higher at lower inflation pressure for rolling on sandy soil and for driving on loess soil (Figure 4.16). The differences for all cases were in the range of 10% to 20%. Note that these results were

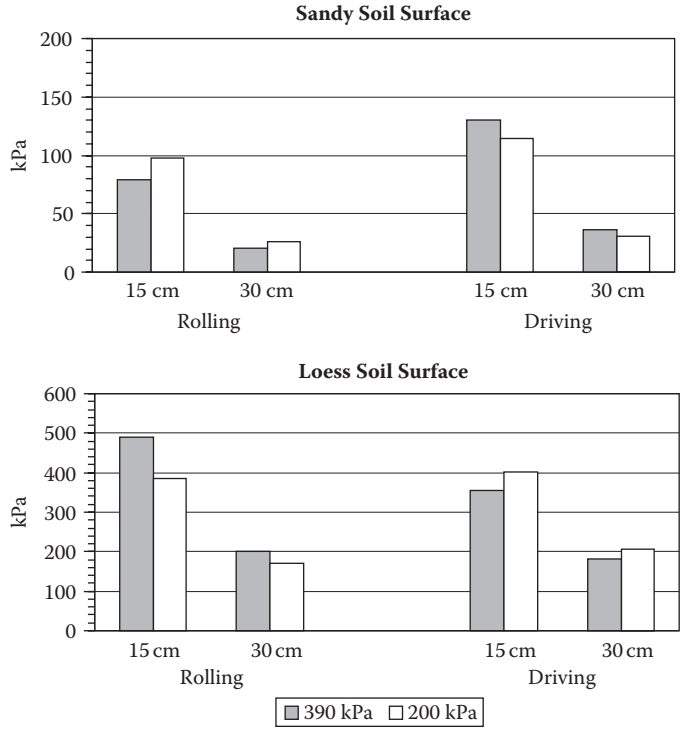

FIGURE 4.16
Effect of reduced inflation pressure on soil stresses under the wheels of the 14-T 6 × 6.

obtained at dry soil conditions. This behaviour may be explained (1) by the effect of soil type and its conditions and (2) by the effect of drive mode.

A dry sandy soil surface is easily deformed and the deformations are multi-directional. These deformations of dry sand can be especially pronounced when tyres are driven rather than rolled over a surface. The reduced inflation pressure of 200 kPa may not have influenced the resulting load distribution on the tyre–soil interface since the stiffness of the tyre was still high compared to soil stiffness.

On the other hand, dry loess soil builds a relatively strong structure that deforms in two ways: the topsoil is sheared and subsoil is compacted. The shearing of the topsoil reaches a depth approximately equal to the depth of as tyre tread (~5 cm). Under this sheared layer, the soil is compacted and can withstand the loading of the tyre, especially when the tyre is deflated to 200 kPa. This may be the reason the two soils reacted differently to the reduced inflation pressure.

Some explanations of the unexpected soil behaviours can be seen in Figure 4.17. It shows sample stress curves under a single wheel of the 5.6-tonne 4 × 4 truck at 500 and 200 kPa. The vehicle was driven over the loess soil surface at high moisture content (~20%). Mechanically, such a surface is similar to soft sandy soil with its high deformability. For the lower pressure, the sidewalls carried part of the load, resulting in a two-peak stress distribution.

4.4.5 Effects on Soil Deformation

To determine soil surface deformation, video data were analysed. Primary locations of four light points were determined first (their co-ordinates were described in Z–X directions). After each pass of the test vehicle (usually five or six repetitions for a given combination), final locations were sought and became the initial locations for the next pass. After the light-point displacements were determined, a simple geometrical transformation was made. The graphs were symmetrically rotated (movements of light points

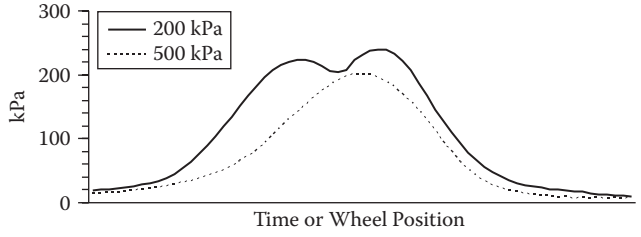

FIGURE 4.17
Stress curves in a wet loess surface under loading of an over-inflated tyre (500 kPa), and at reduced inflation pressure (200 kPa). Results were obtained with the 5.6-T 4 × 4 truck.

are transverse to probe displacements) and linearly multiplied by the factor of 4 (optical transmission of the measuring system).

Figures 4.18 and 4.19 depict soil surface deformations under the wheels of the test vehicle for various weights and inflation pressures on the two test soil surfaces. Generally, surface deformations are different for rolling

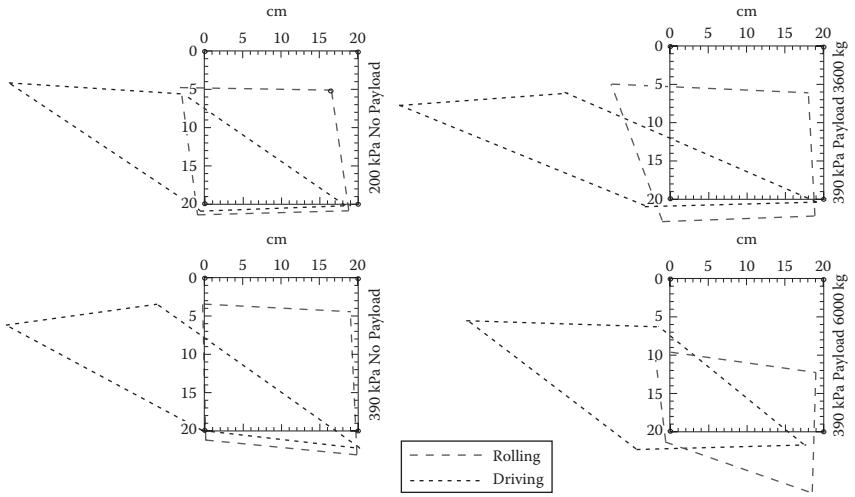

FIGURE 4.18
Deformations of sandy soil surface.

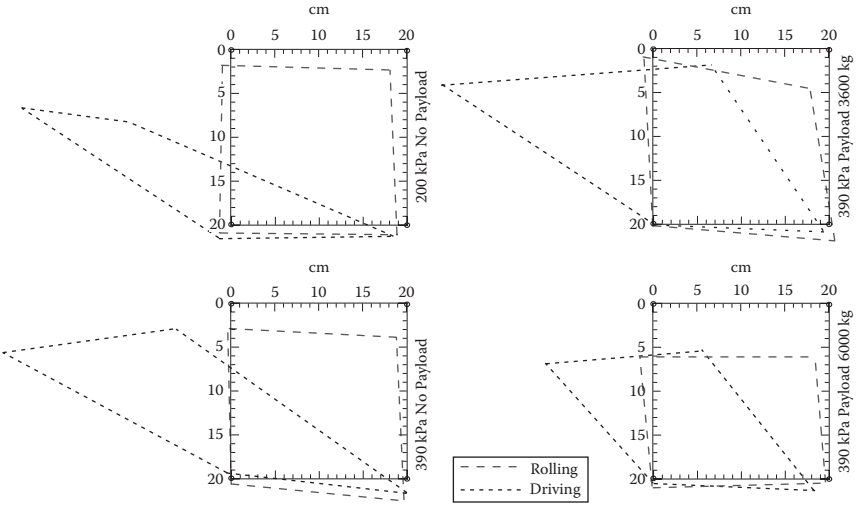

FIGURE 4.19
Deformations of loess soil surface.

and driving tests. Soil surface deformed vertically in tests without slip (at rolling), while significant shearing occurred in driving tests. Under a complex state of loading present under wheels at high slip, deformations of soil surface are generated in vertical and longitudinal directions.

Longitudinal soil deformations caused mainly by wheel slip and shearing are higher for greater vehicle loading. Values of longitudinal deformations are significantly lower at rolling. There is obviously a difference between the two soils. Sand deforms more strongly than loess in the longitudinal direction. Vertical deformations are natural effects of gravity distributed on wheels. These deformations are also greater for sand. Further analysis shows that a complete soil deformation state consists of

- Volumetric strain that may be quantified by the surface of a quadrilateral; final versus initial surface yields strain value.
- Shape deformations involving both rotation and translation.

4.5 Effects of Repeated Rolling

4.5.1 Introduction

Agricultural tractors and machinery run on arable soils and excessive traffic occurs frequently. The first and second passes of a wheel generate stresses in a soil that can exceed its elastic limit and leads to significant deformation of the soil surface along with changes in soil volume and structure. Deformations of soft soils are rapid and irreversible; even advanced tillage practices cannot restore a compacted soil's initial bulk density, air, and water properties. Such a situation is detrimental to the ecological quality and yield capability of a soil.

Numerous research publications address repeated driving of agricultural vehicles over soil (Arvidsson and Ristic 1996, Bakker et al. 1995, Gliński et al. 1991, Hakansson 1994, Horn et al. 1989, Piechnik 1986, Schwanghart 1991, Skwarek et al. 1986 and Schjonning et al. 2006). Repeated passes on the same track contribute to a high degree of soil pulverization in ruts with the action of wheel slip. When soil was tracked six times by a tractor, the increase of rut depth was from 7.5 to 12.7 cm after the first three passes and to 13.2 cm after the next three passes (Piechnik 1986).

Vertical deformation in the plow layer of a silty loam soil at two moisture levels was observed to be a function of the number of tractor passes. Residual vertical deformation is a logarithmic function of the number of passes and is two times greater for moist than for dry soil (Horn and Rostek 2000). Two tractor passes increased the density from

1.46 to 1.603 Mg/m^3, and the next two to 1.637 Mg/m^3 for the 0 to 15 cm soil layer. For the deeper 15 to 30 cm layer, the increases were from 1.561 to 1.650 and 1.670 Mg/m^3, respectively. The greater increase in density of a sandy soil occurred after the two first passes, and further passes resulted in smaller changes of density. The penetration resistance was greater when the tractor was run over higher density soil (Gliński et al. 1991).

Horn and others (Horn et al. 1989, Horn et al. 2000, Horn and Rostek 2000) investigated the effects of repeated wheeling on the soil stress and deformation state. An increasing number of wheeling events influenced both the major principal and octahedral stresses. Shear stress increased at a given mean normal stress in dry Hinwassee clay. A volumetric displacement of the soil occurred laterally and vertically, with a significant domination of vertical deformations. Why all the stress components decreased for the second wheeling while each succeeding pass resulted in an increase of all components remains unexplained. These authors also investigated the effects of various tillage treatments on stress and deformation behaviour of Luvisol derived from loess for a number of repeated wheelings.

Because of increasing vehicle loading and its negative effects on soils, it is important to investigate the effects of repeated wheeling on soil mechanical, physical, and ecological properties. Experimental data would help us learn more about the complex processes of soil compaction, especially by modelling soil deformation under loading with respect to actual stress states. The next sections describe our investigations of the effects of repeated traffic on soil stress, deformation, and stress–strain behaviour.

4.5.2 Experimental Details

In the experiments on repeated passes, we used an agricultural tractor of 3100-kg mass as a test vehicle. It was driven at low speed (~3 to 5 km/h with the centres of the right wheels exactly over the SST in the investigated soil volume. Experiments were conducted on arable sandy and loess soils under natural field conditions. The air temperature was 15 to 17°C, air pressure was 998 to 1010 hPa, clouds were 7/8, and no rain was observed for 3 days before the tests. The experiments were conducted in autumn, after crop harvesting. The experimental sites were located in Paulinów for the loess soil and Marcinów and Kłoda for the sandy soils; all sites are in southeast Poland. The soils had been plowed and harrowed. No special preparations or conditioning were applied before the experimental passes and measurements.

We used the SST with pressure sensors of 0 to 300 kPa measuring range. The SST was installed at depths of 15 and 30 cm. The tests covered two soils, six passes, and two depths ($2 \times 6 \times 2$), and they were replicated five

or six times. The deformation of soil volume was determined by an optoelectronic system with four laser projectors, a semi-transparent shield, and a video camera (see Chapter 2 for details). The system let us determine vertical and longitudinal deformations of soil (volumetric deformations) and structural (shape) deformations of the soil volume enclosed by the deformation probes.

4.5.3 Effects of Repeated Rolling on Soil Stress

The peak maximum stresses under the front and rear wheels of the tractor were found; Tables 4.5 and 4.6 show the averaged values from the repetitions. In general, the higher the number of tractor passes, the greater the stress values for both soils (Figures 4.20 and 4.21). The greatest increase was observed for the major stress σ_1 between the first two passes. The stress values increased three times for loess and three and one-half times for sandy soil. The increase of stress after further passes was smaller, probably because of soil consolidation and compaction during the first passes that increased the soil strength. The increase of stress for the fourth, fifth, and sixth passes was no greater than 20% total. This suggests that only the first two or three passes have a significant effect on changes in soil stress state.

The effect of repeated wheeling was significantly greater for the 15-cm depth than for the 30-cm depth. Stress distribution in the soil is a function of depth, so the obtained results are logical and predictable. Generally, the soil stress at 30 cm was about 25% to 50% of the stress at 15 cm after the last passes. However, after the first passes, the difference was small.

We conclude that the effect of depth causes only small differences in stress values for the first pass. This is obvious when you consider the mechanics of soft soil deformation. Soil strength in the plow layer (0 to 30 cm) is relatively low and approximately the same throughout the layer after tillage. Soil deformations during the first pass are the greatest, and the stress causing the deformation cannot be significantly different throughout the volume. Analysis of peak maximum stress values showed that the greatest values were reached by the major stress σ_1, which is the greatest compressive stress.

Shear stress in the octahedral stress system is always higher than mean normal stress, suggesting the dominance of shearing resulting in structural damage rather than compaction and volumetric changes in the soil. This effect was more intensive for loess soil: the absolute values of octahedral shear and normal stresses were higher than for sandy soil. We can assume that shearing is more intensive in loess than in sand. An aggregate structure of cohesive loess soil is more susceptible to shear and consequently poorly structured sandy soil of low cohesion would not transmit high shearing stresses.

TABLE 4.5

Soil Stresses Affected by Repeated Wheeling in Sandy Soil

		15-cm Depth		30-cm Depth	
Pass #	**Stress**	**Front Wheel**	**Rear Wheel**	**Front Wheel**	**Rear Wheel**
I	σ_1	30.41	109.43	10.24	24.13
II		119.35	100.84	39.01	41.98
III		81.99	136.21	37.03	66.45
IV		93.23625	139.8544	54.88375	58.85
V		98.52	154.40	52.90	69.76
VI		120.67	162.99	40.66	86.29
I	σ_2	11.24	13.88	3.30	13.55
II		17.19	14.21	22.48	22.15
III		43.64	37.03	4.62875	10.24
IV		39.34	32.73	20.16	22.15
V		37.69	16.53	3.63	2.645
VI		41.98	19.50	2.64	2.31
I	σ_3	–8.59	–28.76	–4.95	–20.49
II		–41.39	–25.78	–34.05	–24.13
III		–52.56	–45.95	–20.49	–19.50
IV		–11.57	–21.82	–19.17	–22.81
V		–18.8456	–22.48	–14.21	–11.57
VI		–44.63	–49.92	–9.58	–14.21
I	σ_{OCT}	9.58	36.03	2.97	7.93
II		32.07	33.06	8.92	13.22
III		25.45	42.32	10.24	21.16
IV		27.11	41.32	18.84	19.83
V		28.10	49.26	14.54	20.49
VI		39.34	43.97	11.57	24.79
I	τ_{OCT}	14.87	52.90	5.62	18.51
II		31.74	49.26	16.86	23.80
III		50.91	61.16	22.15	33.06
IV		49.26	62.81	27.44	29.42
V		34.71	35.04	26.78	34.71
VI		56.53	73.39	20.82	43.64

4.5.4 Effects of Repeated Rolling on Soil Deformation

The three general types of deformation to identify in soil mechanics are compression, shearing, and rotation. Figure 4.22 presents the relative deformations in the investigated soils after tractor passes. In the sandy soil, shearing was observed (first, second, and fifth passes) and it was relatively small. In the loess soil, all the three types of deformations occurred and the most intensive were compression and shearing. Thus, we can

TABLE 4.6

Soil Stresses Affected by Repeated Wheeling in Loess Soil

		15-cm Depth		30-cm Depth	
Pass #	**Stress**	**Front Wheel**	**Rear Wheel**	**Front Wheel**	**Rear Wheel**
I	σ_1	68.42	207.01	51.75	132.82
II		90.27	242.07	80.50	129.37
III		192.62	251.27	88.55	123.05
IV		217.35	268.52	76.47	99.47
V		219.65	258.17	82.22	134.55
VI		211.60	262.77	89.70	142.02
I	σ_2	12.07	77.05	10.35	28.75
II		4.025	103.50	10.92	31.62
III		32.20	109.82	10.35	37.95
IV		24.72	118.45	17.82	39.10
V		39.10	93.72	20.12	36.80
VI		42.55	113.85	20.70	41.97
I	σ_3	–51.17	–106.37	–14.37	–16.10
II		–40.82	–130.52	–12.07	–20.70
III		–73.60	–127.07	–16.10	–25.30
IV		–58.07	–122.47	–20.12	–30.47
V		–73.02	–80.50	–20.70	–31.62
VI		–77.05	–97.17	–23.00	–31.62
I	σ_{OCT}	19.55	58.07	18.97	49.45
II		26.45	71.30	25.87	47.15
III		50.02	77.62	28.17	46.90
IV		60.95	87.97	26.45	36.80
V		61.52	90.27	27.02	46.57
VI		58.65	93.15	28.75	51.17
I	τ_{OCT}	46.57	125.92	24.15	60.95
II		45.42	147.77	38.52	59.80
III		93.72	135.70	43.12	59.22
IV		91.42	129.37	36.80	48.30
V		90.85	101.20	40.82	64.97
VI		93.72	112.12	44.85	70.72

conclude that a two-dimensional deformation state occurs in loess soil and that the deformation state in loess is more complex than in sand. This may be the effect of cohesion and the aggregate structure of loess soil and also the stronger and multi-directional interactions between soil particles.

Relative strain as a function of increasing number of tractor passes is presented in Figure 4.23; the upper graph shows loess and the lower, sandy soil. We can observe a decrease of incremental strain for the succeeding

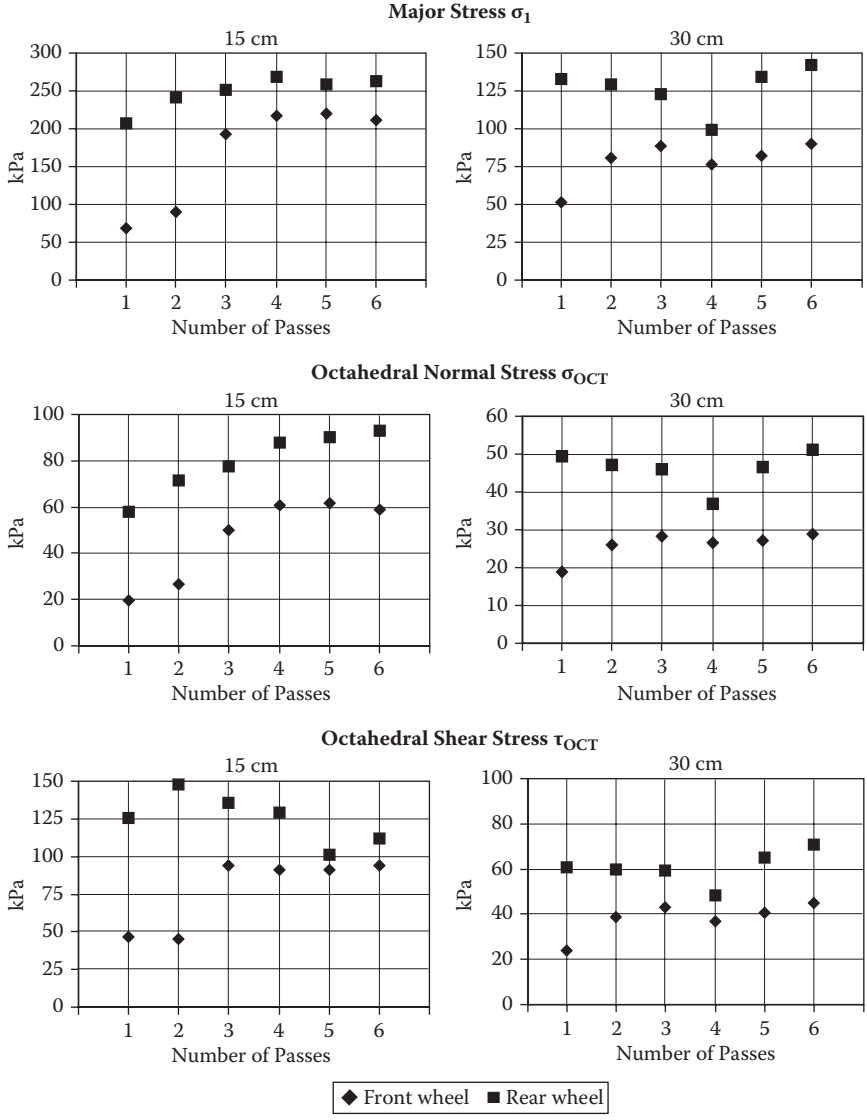

FIGURE 4.20
Effect of repeated wheeling of a tractor on peak maximum stresses in loess soil.

passes. That supports the thesis that sandy soil can be more highly compacted regardless of differences in tractor mass. What is remarkable is the highest increase of relative strain between the first and the second passes for both the investigated soils. In the case of sand, the third and the fourth passes also resulted in significant deformation.

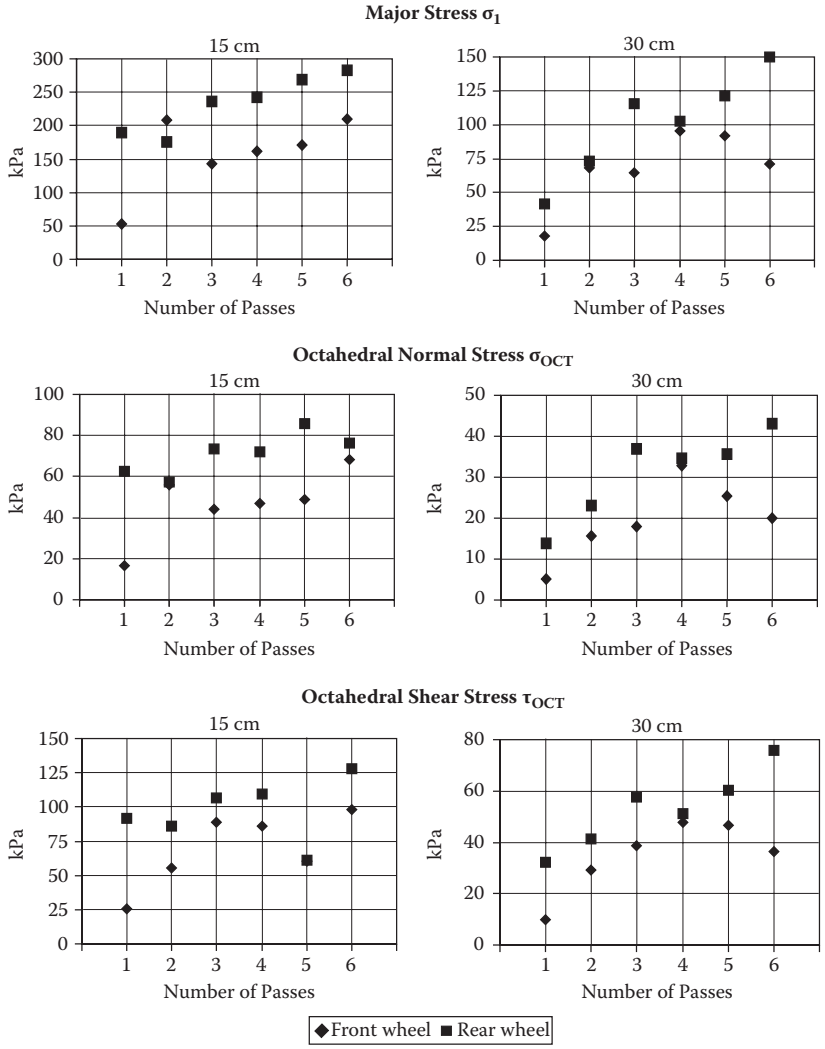

FIGURE 4.21
Effect of repeated wheeling of a tractor on peak maximum stresses in sandy soil.

4.5.5 Effects of Repeated Rolling on Stress–Strain Behaviour

For any material, a stress–strain relationship can reveal a lot of information about its mechanical behaviour. Such a relationship can also be determined for soil, but of greatest interest may be the changes in stress–strain behaviour after a series of tractor passes. The experimental data from this study included both stress and deformation state data. This let us create

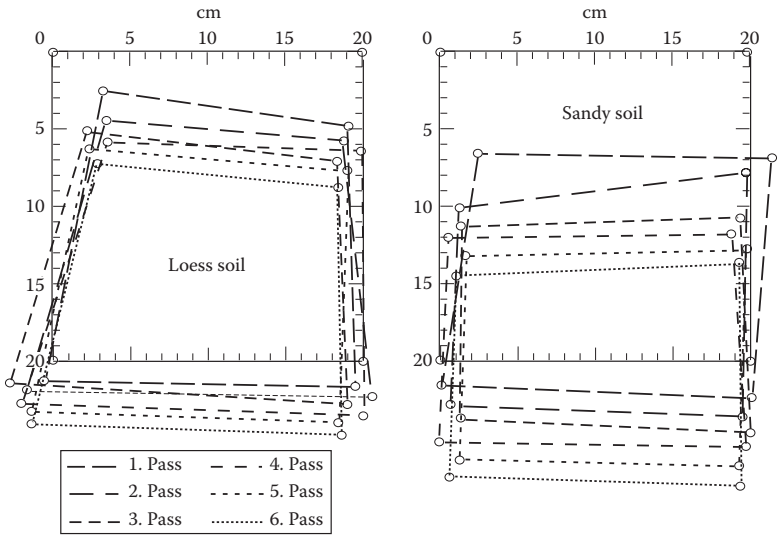

FIGURE 4.22
Deformations of soil volume under repeated rolling of the tractors.

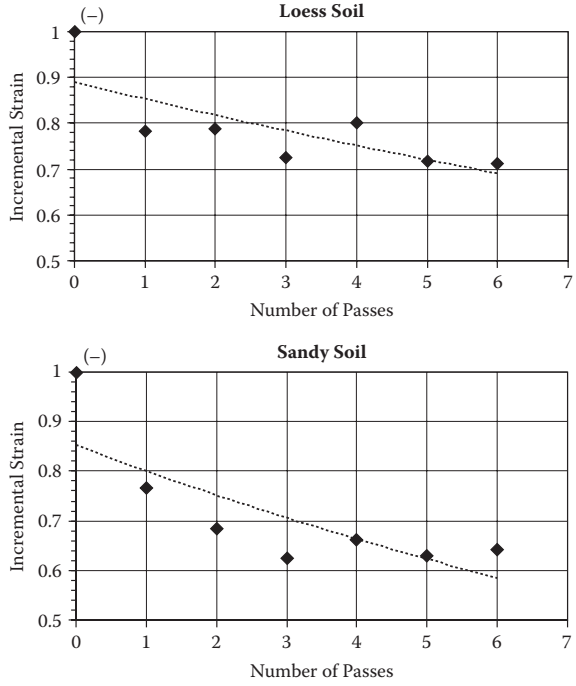

FIGURE 4.23
Relative volumetric strain in two investigated soils versus number of tractor passes.

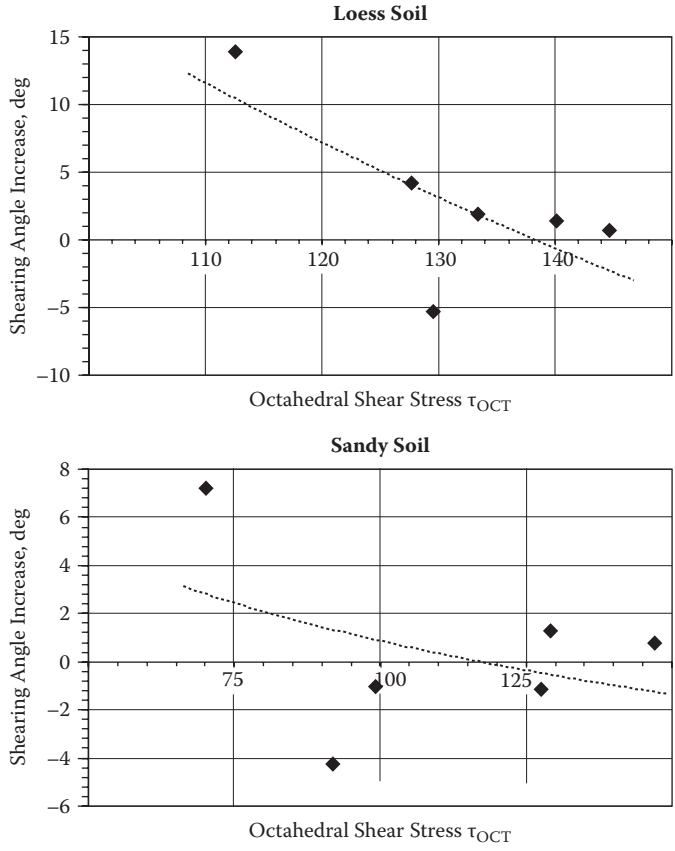

FIGURE 4.24
Relative incremental strain versus successive pressure applications at middle depth (15 to 30 cm).

two kinds of relationships: mean normal stress versus incremental volumetric strain (Figure 4.24) and octahedral shear stress versus shearing angle increase (Figure 4.25).

The first relationship describes the process of soil compaction, while the second gives information about shearing and structural deformation. In other words, changes in mean normal stress versus volumetric strain may be identified with the actual soil compactability, which decreased for the succeeding passes and pressure increments, but was more intensive for sandy soil. Similarly, the relationship of octahedral shear stress versus shear angle gives information about the soil shear strength and shear behaviour under a complex load state. It is obvious that the changes in shear stress versus shear angle data are more significant in loess soil. Pronounced shearing was not observed in the sandy soil.

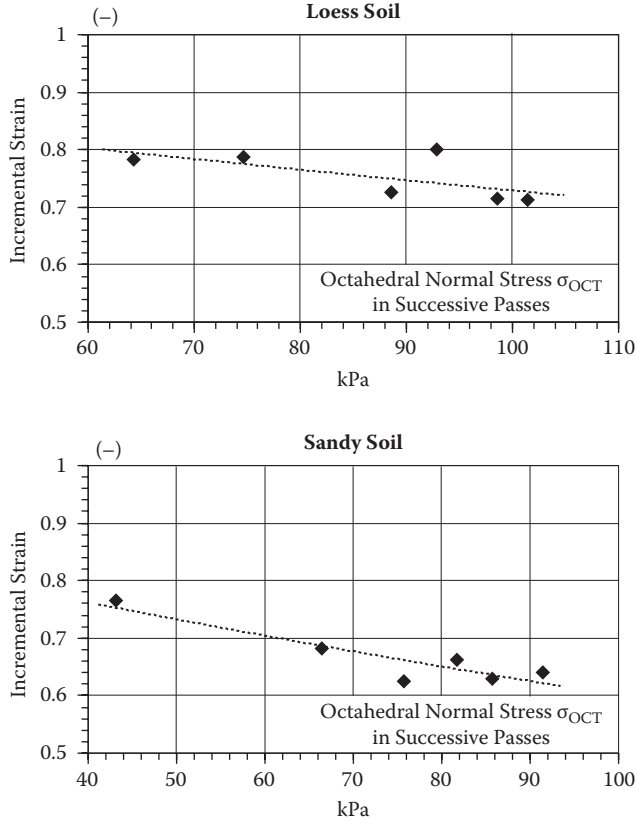

FIGURE 4.25
Incremental shear strain angle versus successive applications of octahedral shear stress at middle depth between 15 and 30 cm.

It is interesting, however, that the incremental shearability of the investigated soils changed significantly (decreased), and this was more pronounced for loess soil. The changes in compactability became less dependent on the number of passes. This is contrary to the conclusion about soil compressibility based only on soil stress. This contradiction illustrates the importance of analysing both soil stress and deformation states in soil mechanics investigations. An analysis of stress state alone provides incomplete information and leads to misunderstandings of soil mechanical behaviours.

4.5.6 Discussion

From a mechanics view, we consider three major properties of matter: elasticity, viscosity, and plasticity. Soil possesses all three properties to some

degree. Soil can accumulate the energy of elastic deformation to absorb and dissipate the equivalent energy of the work of internal friction force, and, finally, to deform when loaded to the point that the loads exceed a given value of strength. Hence, we can expect to see effects of these properties in mechanical behaviour of soils loaded in a series of multiple tractor passes. In the following sections, we discuss how repeated loading influences the mechanical properties of soil.

4.5.6.1 Elasticity

At microscale, soil can be treated as an elastic body only after major simplifications. In the elastic theory, we must respect the assumption of infinite small deformations of irreversible character. Moreover, in elastic bodies, mechanical behaviour is not a function of deformation rate. This excludes arable soils; only highly compacted ground and foundations may be described as quasi-elastic materials.

The two soils used in the experiment were exposed to repeated cyclic loading. They were compressed and the effects of this compression (from repeated wheeling) on stress–strain relationships should be recognized. In the analysis of these factors, we find differences between sandy and loess soil and also differences between model sand and loess and the model elastic body. The effects of repeated wheeling are clearer for loess soil, although this conclusion is based only on qualitative evidence. For the last wheeling, loess soil is more like an elastic body than sandy soil is. Each repetition of the same load caused the same (or almost the same) state of stress in loess soil.

4.5.6.2 Viscosity

This property exists purely in Newtonian fluids; only a very moist clay can be treated as a viscous body. We should expect viscous elasticity in soft, arable soils under normal field conditions. Water content in soil causes some viscous behaviour that results in time effects on the equilibrium of stress and strain. A hysteresis effect may be also observed. The effect of time appears in creeping or stress relaxation.

Popular rheological models for soils based on viscous elasticity theories have been devised recently. In such models, the mechanics properties of soils are described mathematically with elementary mechanical analogues: elasticity (Hooke), viscosity (Newton), and plasticity (St. Venant). By connecting these elements, complex soil models may be obtained and much research has been done on soil mechanics, compaction, and trafficability. However, we should realize that rheology is based on the assumption of the reversibility of sudden deformations.

This is not the case for soil properties: the first sudden deformations of loose soil are always irreversible.

Loading of soil causes infiltration of water contained within the pores. The effect of repeated wheeling on soil viscosity depends on the ride velocity of the vehicle and the strain rate. Both parameters are the highest for the first pass because the deformation of soft, unloaded soil is very intensive. For succeeding passes, this effect becomes less significant because the deformation and strains are significantly smaller. In conclusion, repeated wheeling causes a decrease of viscosity behaviour, and this effect is considerable stronger for loess soil.

4.5.6.3 Plasticity

When a stress state in a body exceeds a given limit of strength, plastic rupture of the body results. Such deformations take place in the whole volume of a body, and no elastic deformation occurs. We understand *plastic deformation* to indicate an irreversible change in volume or shape. The limit of strength to be exceeded is called the plasticity limit and certain criteria are required to determine the limit. Because of the Bauschinger effect (plasticity limit for compression ≠ plasticity limit for tension), we cannot describe soil simply as a plastic medium.

The plasticity limit is a value of shear yield stress. This stress causes plastic rupture and the material yields on a specific surface: a cylindrical surface for the von Mises criterion and a hexagonal cylindrical plane for the Tresca criterion.

A plasticity limit for soil depends on pressure and has been described as a friction resistance effect proportional to pressure (Coulomb plasticity criterion). A wet clay displays cohesion effects only; the internal friction is zero and the Coulomb equation becomes the Tresca criterion. The effect of multiple passes of a tractor on the plastic behaviour of soil is difficult to quantify. Loads by repeated wheeling cause increase of pressures that may result in higher plasticity limits. However, it is highly probable (as we noted during our experiments) that the first pass caused plastic yield of the material so we should consider cyclic plastic rupture with simultaneous changes of plasticity limit.

Another phenomenon to consider is shakedown. The self-stress remaining from the first loading superimposed on any of the elastic states between 0 and the maximum stress produces a total stress below the yield stress. A shakedown is a state of self-stress that, when added to a variable applied stress, yields a total stress that satisfies equilibrium conditions and does not exceed the yield stress value at any time. In this state, a body responds purely elastically to variations of applied stress, even though it may earlier have deformed plastically to get into the state.

The first or the second pass of a vehicle may lead to a quasi-shakedown state of soil, while the response of soil to succeeding passes is more elastic. This phenomenon clearly applies to loess soil. We observed shakedown-like behaviour of soil in an experiment on soil stress determination under a landing aeroplane (described in Chapter 7).

In traditional methods of soil mechanics, cohesion and angle of internal friction are determined from shear and sinkage tests. These measures are obtained with small soil samples that are subject to errors due to effects of fixing the samples. To avoid this issue, the best method is using a cylindrical, thin-walled soil sample. Promising results may be acquired with monolith samples. To eliminate boundary effects, investigations may be conducted in situ.

The philosophy of classic soil mechanics is based on laboratory experiments, and only simple methods developed for trafficability studies are suitable for field use (cone penetrometer, bevameter). Moreover, we should realize the limitations of the Coulomb model that serves as a basic statement for many models in classic soil mechanics: (1) it makes no statement about strains; (2) it implies that volume changes do not affect the shear strength, which is certainly untrue; and (3) it implies that the intermediate principal stress does not affect the shear stress. It is essentially illogical to separate considerations of displacements and strength, and such separate considerations may lead to serious misconceptions about structural behaviour, especially for such a deformable body as soil.

Local failure of part of a soil mass occurs at much smaller loads than those required to cause structural collapse. Under these conditions, the simple elastic models may give very poor estimates of displacement. Therefore, new methods have been incorporated. Soil stress and deformations state measurements in situ were begun 50 or more years ago, and a number of published papers provide valuable archival results and instrumentation details. Currently, we are still far from standardization; the subject requires a lot of research.

Methodological problems, unproven reliability of measurements with strain gage or hydraulic transducers, soil structure disturbance during installations of transducers, and effects of numerous factors influencing measured stress values make experimentation a veritable minefield, and each step should be taken with due caution. We believe a solution would be a comparison of experimental results obtained by classic methods and results from new methods. This would be preceded with a detailed study of mechanical similarity of the measuring methods and resulting data. We are searching for a general theory for soil mechanics that describes the behaviour of a particular material under any condition.

4.6 Analysis of Octahedral Stresses

4.6.1 Introduction

Stresses in the octahedral stress system consist of octahedral mean normal stress σ_{OCT} and octahedral shear stress τ_{OCT}. These two octahedral stresses give complete information on stress state, providing an alternative to the principal stress system. When we consider any complex three-dimensional stress system, we can create the octahedral planes that cut across the corners of the principal elements to produce an octahedron. The stresses acting on the octahedral planes have particular significance. The normal stresses acting on each of the eight octahedral planes are equal in value and tend to compress or enlarge the octahedron without distorting its shape. They are also called hydrostatic stresses and have values given by

$$\sigma_{OCT} = \tfrac{1}{3}\left(\sigma_1 + \sigma_2 + \sigma_3\right) \tag{4.8}$$

Similarly, the shear stresses acting on each of the octahedral planes are identical in value and tend to distort the shape of the octahedron without changing its volume. The value of the octahedral shear stress is:

$$\tau_{OCT} = \tfrac{1}{3}\ \left(\sigma_1 - \sigma_2\right)^2 + \left(\sigma_2 - \sigma_3\right)^2 + \left(\sigma_3 - \sigma_1\right)^2\ = \tfrac{1}{3}\left(\tau_{12}^2 + \tau_{23}^2 + \tau_{13}^2\right)^{\frac{1}{2}} \tag{4.9}$$

Octahedral stresses are important; their interpretation is adequate for the effects of wheel loading when loads are multi-directional.

4.6.2 Effects of Wheel Loads and Function Modes on Octahedral Stresses

In Table 4.7, the peak maximum values of the octahedral stresses were collected for the loess and sandy soil tracked by the 14-tonne 6×6 truck at three loading levels. The table shows results from both free-rolling and driving test runs. Octahedral shear stress τ_{OCT} is higher than mean normal stress σ_{OCT} at all times and cases. The difference between these stresses increased with higher vehicle load and was affected by the soil type. In the loess soil, the increase in the τ_{OCT} is significantly higher than in the sand.

The effect of pull force was also pronounced. Generally, stresses under wheels at driving are lower than those under rolling wheels. This was not true for the sandy soil in this experiment. When a pull force is applied to a point above the centre of gravity (CG) of a vehicle, a torque is generated and causes the rear wheels to overload and the front to unload.

TABLE 4.7

Peak Maximum Values of Octahedral Stresses (kPa) of 14-Tonne 6 × 6 Truck Driven on Loess and Sand[a]

		Sand		Loess	
Depth	**Wheel**	σ_{OCT}	τ_{OCT}	σ_{OCT}	τ_{OCT}
Rolling; vehicle weight = 8.18 tonnes					
15 cm	Front	90.0 (6.4)	94.0 (6.7)	123.8 (15.8)	217.8 (17.9)
	Rear I	48.0 (22.6)	32.0 (16.2)	60.6 (20.4)	118.6 (20.7)
	Rear II	70.0 (5.0)	58.0 (11.5)	72.8 (22.7)	154.2 (18.4)
30 cm	Front	22.35 (10.0)	48.6 (9.9)	57.15 (6.7)	96.75 (6.8)
	Rear I	7.5 (12.4)	14.64 (25.0)	19.8 (12.4)	42.9 (18.7)
	Rear II	14.85 (9.7)	30.96 (12.6)	22.35 (9.7)	46.65 (5.3)
Driving; vehicle weight = 8.18 tonnes					
15 cm	Front	100.2 (11.2)	108.1 (13.7)	39.5 (10.6)	119.35 (9.8)
	Rear I	69.33 (17.2)	86.66 (11.5)	62.85 (10.9)	164.07 (4.1)
	Rear II	111.8 (46.3)	138.0 (25.3)	72.0 (10.5)	195.85 (8.3)
30 cm	Front	15.45 (10.9)	33.99 (11.2)	37.42 (6.5)	75.39 (9.9)
	Rear I	8.325 (33.2)	17.68 (23.7)	35.28 (13.6)	71.58 (12.5)
	Rear II	19.023 (7.9)	37.57 (11.8)	48.11 (17.3)	93.37 (17.8)
Rolling; vehicle weight = 11.78 tonnes					
15 cm	Front	104.3 (13.1)	138.7 (24.6)	118.0 (7.0)	268.2 (7.7)
	Rear I	58.85 (21.7)	74.5 (8.6)	83.6 (7.5)	192.8 (6.5)
	Rear II	80.5 (15.1)	92.5 (9.5)	67.0 (3.7)	157.6 (3.2)
30 cm	Front	20.57 (16.1)	45.26 (21.7)	75.0 (1.4)	155.7 (0.3)
	Rear I	5.43 (25.7)	10.95 (23.2)	56.85 (1.3)	120.0 (1.2)
	Rear II	12.95 (12.7)	28.03 (10.0)	45.0 (4.6)	97.05 (7.6)
Driving; vehicle weight = 11.78 tonnes					
15 cm	Front	80.25 (13.8)	68.1 (26.4)	32.0 (33.1)	101.93 (8.3)
	Rear I	49.33 (3.0)	46.66 (26.3)	53.75 (30.3)	160.2 (8.8)
	Rear II	81.13 (28.2)	90.04 (19.9)	71.53 (23.0)	212.5 (15.7)
30 cm	Front	15.45 (16.2)	33.99 (15.2)	41.55 (2.6)	83.7 (2.7)
	Rear I	8.32 (8.0)	17.68 (7.1)	59.32 (8.8)	123.11 (5.4)
	Rear II	19.0 (25.6)	37.57 (13.5)	62.7 (6.2)	127.5 (7.1)
Rolling; vehicle weight = 14.18 tonnes					
15 cm	Front	103.5 (9.4)	121.0 (14.3)	87.1 (16.4)	197.2 (13.2)
	Rear I	69.66 (54.0)	89.06 (16.2)	123.4 (6.0)	257.95 (6.6)
	Rear II	95.33 (21.7)	123.3 (14.5)	121.05 (5.1)	255.65 (5.7)
30 cm	Front	19.81 (9.7)	37.71 (7.9)	66.51 (9.6)	139.9 (10.6)
	Rear I	9.45 (26.7)	18.87 (26.0)	84.61 (4.8)	175.98 (4.6)
	Rear II	16.85 (20.5)	33.46 (17.9)	76.35 (9.4)	187.88 (8.8)

(continued)

TABLE 4.7 (continued)

Peak Maximum Values of Octahedral Stresses (kPa) of 14-Tonne 6 × 6 Truck Driven on Loess and Sand[a]

		Sand		Loess	
Depth	**Wheel**	σ_{OCT}	τ_{OCT}	σ_{OCT}	τ_{OCT}
Driving; vehicle weight = 14.18 tonnes					
15 cm	Front	91.33 (3.2)	110.7 (16.3)	13.9 (20.7)	52.6 (23.8)
	Rear I	114.5 (9.0)	144.07 (8.1)	58.0 (33.1)	165.8 (21.9)
	Rear II	147.0 (5.3)	182.6 (13.9)	93.15 (35.7)	204.1 (25.2)
30 cm	Front	11.28 (19.4)	23.57 (16.4)	30.66 (16.3)	63.06 (16.2)
	Rear I	16.54 (8.0)	32.53 (8.4)	76.83 (4.1)	155.94 (3.6)
	Rear II	23.64 (11.5)	45.12 (7.1)	70.02 (1.8)	142.86 (3.4)

[a] Percentage values of standard deviation shown in brackets.

Logically, this causes the stress distribution under the road wheels to change. Moreover, the overloading of the rear wheels by the pull force is more pronounced for more deformable soil because greater rut depth intensifies the effect.

This is the most probable reason for the higher values of octahedral stresses at pulling in the sandy soil. To correct the load acting on each wheel according to pulling force F_{DBP}, we performed a simplified analysis of moments that acted (Figure 4.26). The pulling force F_{DBP} results in vertical reaction changes on the road wheels; the values of these changes, ΔF^{Front}, ΔF^{Rear1}, ΔF^{Rear2} are expressed in the following equations:

$$F_{DBP} \times h = F^{\text{Front}} \times (l_1 + l_2) \tag{4.10}$$

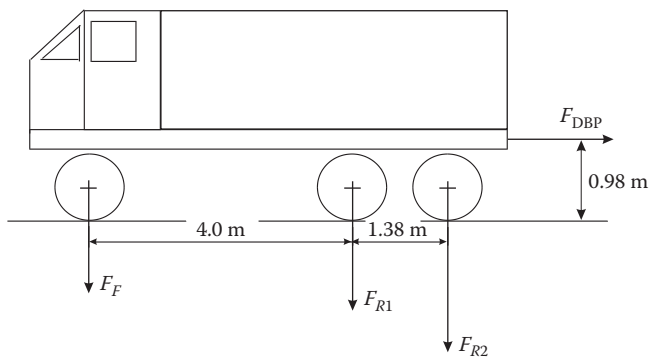

FIGURE 4.26
Correction of wheel load changes due to pulling force.

$$F_{DBP} \times h = F^{\text{Rear1}} \times l_1 \tag{4.11}$$

$$F^{\text{Front}} = - F^{\text{Rear1}} - F^{\text{Rear2}} \tag{4.12}$$

In addition, we calculated mean values of stresses under each of the three road wheels (Figures 4.27 and 28). For the loess soil, with the exception of stress values under empty vehicles at 30-cm depth, both stress values, σ_{OCT} and τ_{OCT}, were lower at wheel slip (pull runs or driving). The difference between stresses during free rolling and driving increased as

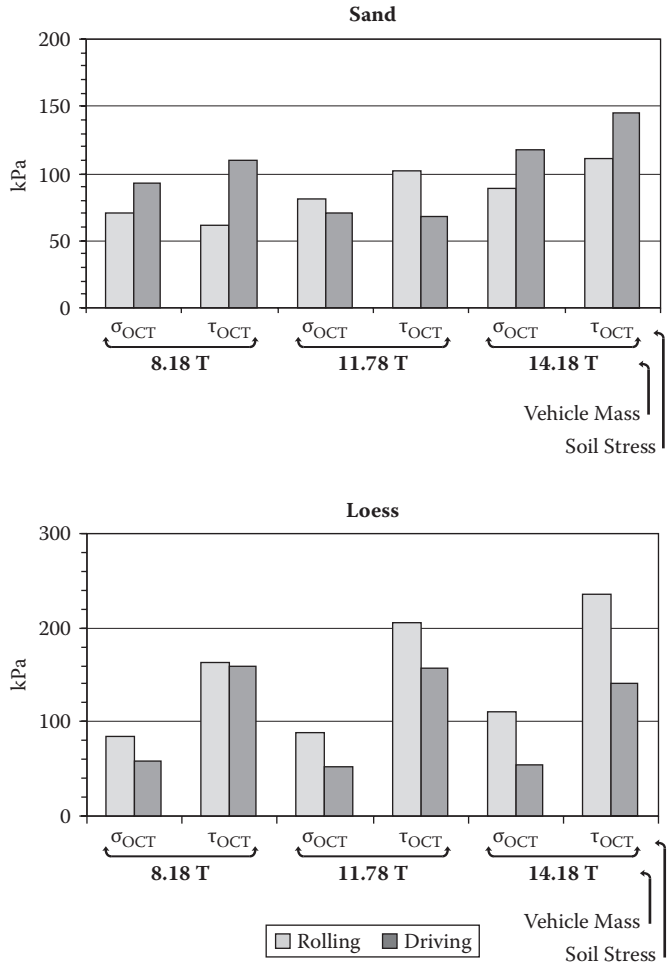

FIGURE 4.27
Effects of drive mode on octahedral stresses at 15-cm depth in loess and sand under loads of the 14-T 6 × 6 truck at different vehicle weights.

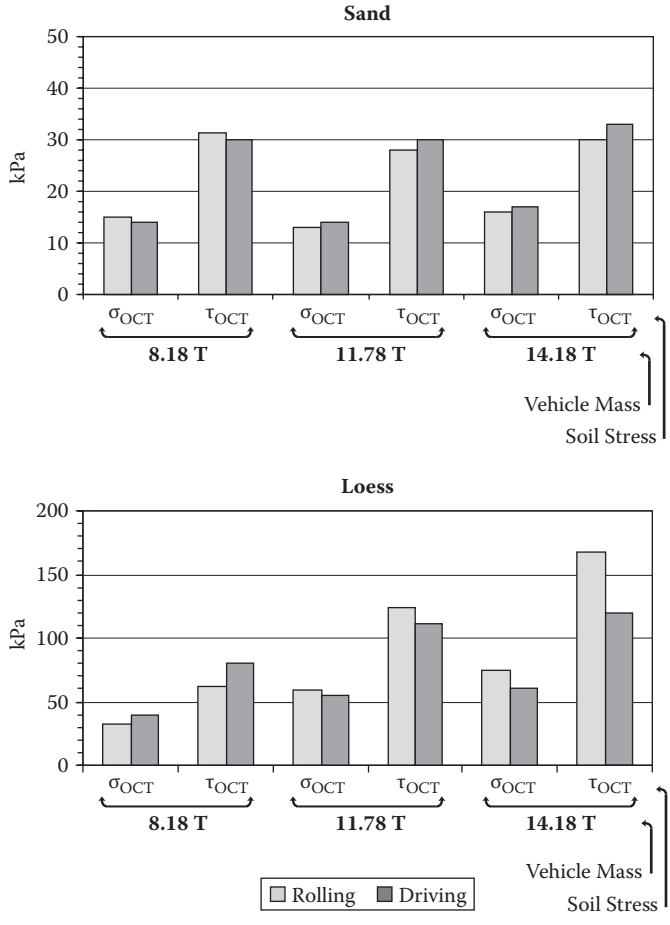

FIGURE 4.28
Effects of drive mode on octahedral stresses at 30-cm depth in loess and sand under loads of the 14-T 6 × 6 truck at different vehicle weights.

vehicle mass increased. Moreover, this difference was significantly higher at 15-cm depth.

In contrast, the effect of wheel function modes for the sandy soil was inverse (at 15-cm depth) or almost non-existent (at 30 cm). The differences between σ_{OCT} and τ_{OCT} were smaller for the sand than for the loess soil. Note the relations between both analysed octahedral stresses. Higher differences between σ_{OCT} and τ_{OCT} were accompanied by higher values of measured drawbar pull F_{DBP} in the vehicle driven over the loess than on the sandy soil surface. The next section discusses this further.

4.7 Relationships of Soil Stress and Drawbar Pull

In wheel–soil mechanics, driving forces are determined from contact stresses, and net traction is calculated from tangential stresses and rolling resistance from normal stresses on the contact profile (Wanjii et al. 1997). Because the wheel loads (vertical and longitudinal) are also carried by deeper layers of soil—as shown in the above section—it is reasonable to analyse how the mentioned forces depend on the soil stresses.

The main traction measure known as drawbar pull or FDBP can be represented in the octahedral stress system. The FDBP is a difference between horizontal driving force and a withstanding force. Therefore, we chose a difference between τ_{OCT} (shear stress) and σ_{OCT} (normal stress) for the relationships. In other words, shearing stress is expected to correlate with driving force, while the rolling resistance correlates with mean normal stress (Pytka 2005). To establish these correlations, two methods were used: (1) correlation of average values of stresses with average values of drawbar pull for the 14-tonne 6×6 truck data, and (2) correlation of peak values of soil stresses with respective real-time values of drawbar pull for the 5.6-tonne 4×4 truck (this method of correlation is depicted in Figure 4.29). The FDBP data used for correlations for both methods were fraction values calculated as follows:

$$F_{DBP}^{Front} = F_{DBP} * \frac{F_V^{Front}}{W} \tag{4.13}$$

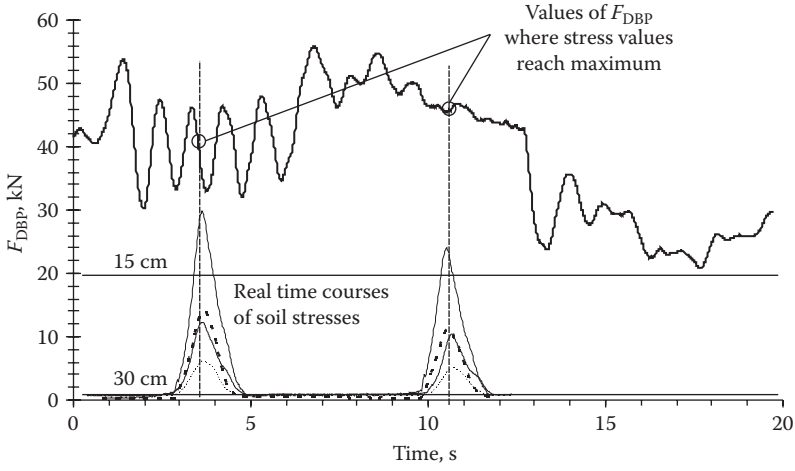

FIGURE 4.29
A method for obtaining the stress–drawbar pull relationships.

$$F_{DBP}^{\text{Rear1,2}} = F_{DBP} * \frac{F_V^{\text{Rear1,2}}}{W} \tag{4.14}$$

where F_{DBP}^{Front}, $F_{DBP}^{\text{Rear1,2}}$ are calculated fraction drawbar pull values (average or real-time) for the front, rear 1, and rear 2 wheels; F_V^{Front}, $F_V^{\text{Rear1,2}}$ are wheel loads; and W is the vehicle weight.

The results of the analysis are shown in Figures 4.30 and 4.31. Correlations of averaged values of F_{DBP} and octahedral stresses in soil are depicted for the 14-tonne 6 × 6 truck in Figure 4.30. The curves were different for the two investigated soils—increasing for the sand and decreasing for the loess. Also the stress measurement depth had an effect. The curves for sand at 15-cm depth were more progressive (or regressive for loess soil)

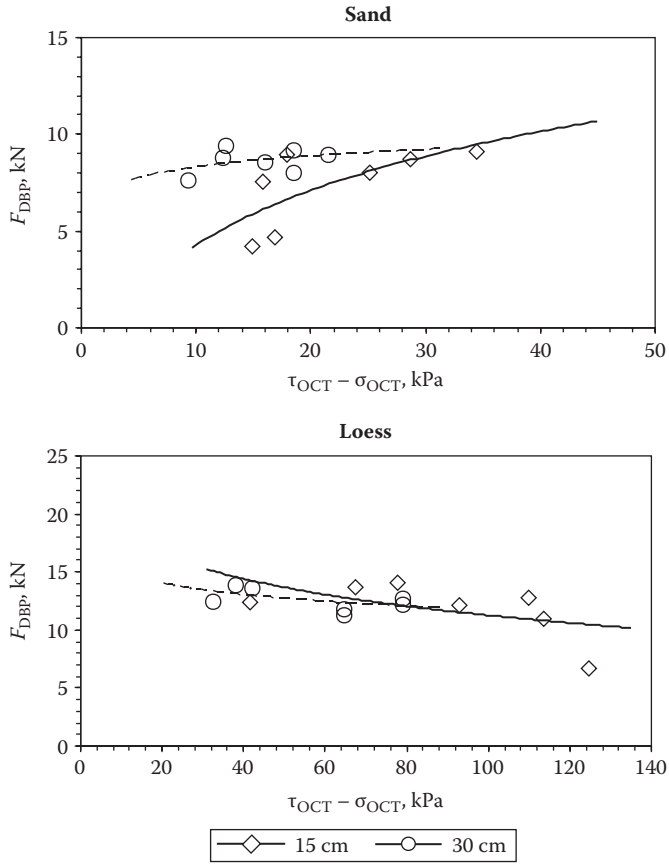

FIGURE 4.30
Correlations of averaged values of octahedral stresses with drawbar pull force for the 14-T 6 × 6 truck.

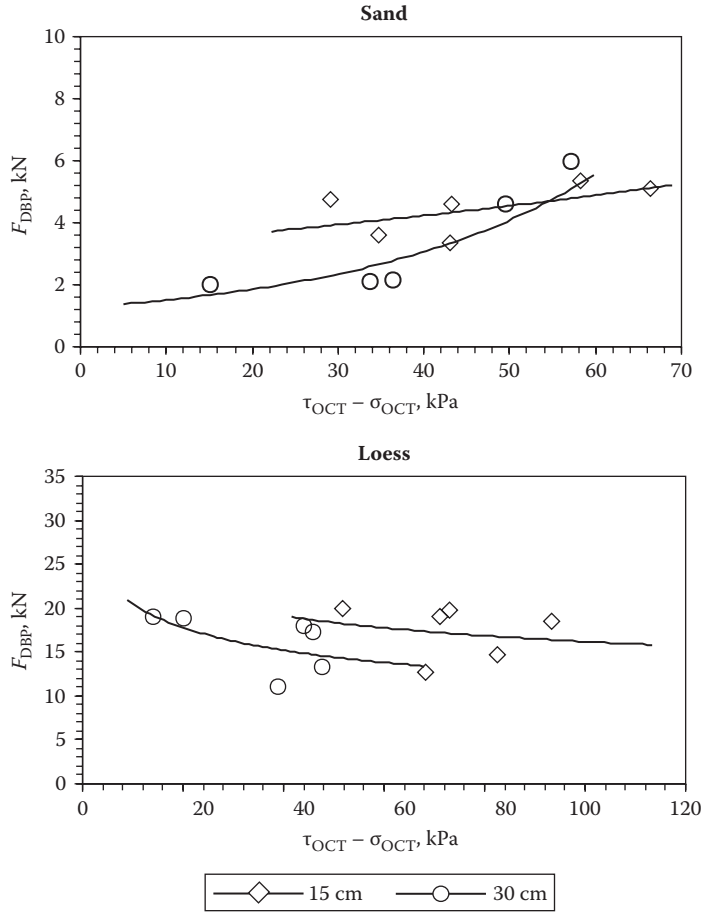

FIGURE 4.31
Correlations of simultaneous peak stress values with drawbar pull for the 5.6-T 4 × 4 truck.

than for 30-cm depth where the curves were almost flat. The mechanism of wheel force generation is stronger in upper layers. In general, these relationships are of experimental nature and fluctuations occur.

The parameter that determined the relations between the F_{DBP} and soil stresses was the wheel load because the experimental data were recorded at a quasi-constant level of wheel slip (80% to 100%). It was impossible to control the wheel slip because of the procedure used to generate the pull force by an additional vehicle. Figure 4.31 presents curves for the 5.6-tonne 4 × 4 truck obtained by simultaneous peak values of F_{DBP} and octahedral soil stresses; these show how wheel slip may affect the mechanics of driving force generation in a wheel–soil system.

4.8 Final Discussion and Concluding Remarks

Wheel and vehicle loading resulted in higher stresses in all cases; other researchers reported similar results. Of special interest would be an estimate of the type of relationship between wheel load and soil stresses. We believe it can be described by means of a logarithmic function, in which parameters depend upon the soil type and conditions, especially moisture content. The differences found here between the loess and the sand are good examples. Lower stresses in the sandy soil are probably the results of the lack of structure in this soil (Pytka et al. 2006).

On the other hand, the structure of the loess soil was damaged during the installation of the SST; the rebuilding process (age hardening) must be long enough to restore initial soil strength. It should be noted that the stress values may depend upon the time allowed after the installation of the SST in the loess soil.

The two investigated wheel function modes, driving and rolling, represent two different means of surface loading by wheels. The greatest shearing action is expected with driving, while rolling will generate a mostly vertical loading of the surface. The experiments described in this chapter confirmed this. Generally, stresses are lower at driving, because of shearing damage of the top layer of the surface and subsequent deformations. This agrees with the conclusions by Wanjii et al. (1997), who analysed normal and tangential stresses on the wheel–soil contact patch and their relationships with wheel slip for a loamy soil.

We expected the effect of rolling velocity to be significant, but these results showed only a small influence of vehicle speed upon soil stresses. Uncertainties caused by the effect of the measuring method may have played a role, especially the dynamic effects of running a vehicle at high speed on a rough, natural soil surface.

Tyre inflation pressure is often reduced to improve off-road traction by enlarging the contact surface area and minimizing the effect of surface loading on soil ecology. It is well known and documented in the literature that tyres at decreased inflation pressure perform significantly better in off-road conditions. Results from the literature prove that soil stresses decrease at lower inflation pressures, but this effect was observed for very low inflation pressures (~40 to 50 kPa). Such a low pressure is possible for large tractor tyres, according to tyre manufacturers' recommendations.

In our work, the reduced inflation pressure was 200 kPa—much greater than previously studied values but the lowest possible value for this tyre type to avoid spinning around the rim. This may help explain the unexpected effects of reduced tyre inflation seen in this study.

The relationships between soil stresses and drawbar pull force suggest a different interpretation of the results. Such a relationship is in fact a unique experimental model of a wheel-surface system; it seems to be reasonable to (1) compare this method with the results by other researchers and (2) continue research by adding other tyres, surfaces, and factors affecting both soil stresses and wheel–soil forces. Pacejka (2004) discusses the usefulness and advantages of empirical models, and the research presented in this book proves that, for wheel–soil systems, experimental-based models and predictions are valuable.

An examination of the literature shows that the use of soil stresses would be a completely new method for interpreting wheel–soil mechanics. Most authors (Muro 1993, Shibusawa and Sasao 1996, Shmulevich and Osetinsky 2003, Wanjii et al. 1997, Wulfsohn and Upadhyaya 1992) applied a modified Bekker's model based on the Coulomb equation on shear stress in a cohesive frictional body.

Foda (1991) applied a tribological theory to describe the mechanism of wheel–soil force generation. Those works, however, are based on an assumption that wheel forces are correlated with surface stresses acting at the wheel–soil interface. The method presented here is different, since wheel forces are correlated with in-soil stresses. Such an approach could provide a new interpretation of wheel–soil force mechanisms. It is necessary, however, to improve the experimental method used to define the model.

Some uncertainties in the stress results may suggest that the measuring method has some effect that is not yet known. The sensitivity and selectivity of the method used (stress determination under running vehicles in the field) is probably not precise enough to investigate some of the factors influencing soil stress. The effects of the test method should be further investigated as some of the differences obtained in this study are small and the relationships remain somewhat speculative. We suspect that the effect of the SST installation and the SST itself may have a significant influence on the indicated soil stresses.

On the other hand, a soil bin method also has limitations, mainly because of the inability to represent all the conditions of field tests. Moreover, it seems that experimental models of wheel–soil systems would be more accurate when soil stresses could be correlated with wheel forces, not the drawbar pull (DBP) divided by a number of road wheels. In conclusion,

1. Soil stress increases with higher wheel loads and this increase is different for the soil types. In the sandy soil, stresses increased the greatest amount; in all investigated soils, stress increases were smaller at the greater depth (30 cm).

2. The two wheel-function modes affected all three soils and stresses under driving wheels were generally lower than during free rolling.
3. Successive passes of the agricultural tractor caused increases of stress state components, especially the major stress σ_1, but the effect was greatest after the first two passes.
4. Generally, at dry conditions values of soil stress were highest in the loess soil, somewhat lower in the sandy soil, and lowest in the turf. At wet conditions the relationship is different. Indicated stresses reached the highest values in sand and stresses in wet loess and turf were much lower.
5. Stresses in the sandy soil decreased with higher rolling velocity.
6. The effect of reduced inflation pressure was unexpected and was different in sandy and loess soil surfaces and for the two drive modes.
7. The two drive modes exhibited a noticeable difference between sand and loess in octahedral stress. The octahedral stress increased little with driving and a lot with rolling in the sandy soil, while the opposite occurred in the loess soil, where stress values decreased significantly.
8. The relationships between octahedral stresses were affected by both soil type and the wheel-function mode. The dominance of the τ_{OCT} over σ_{OCT} was greater for loess than for sand.

The method and results presented here provide a background for a new analytical method for calculation of wheel performance. When compared to the existing methods (Foda 1991, Muro 1993, Shmulevich and Osetinsky 2003, Upadhyaya et al. 1997, Wanjii et al. 1997, Wulfsohn and Upadhyaya 1992), the use of soil stress analysis can be advantageous over the method based on wheel–soil contact stresses that are difficult to measure. In future research of wheel–soil systems, parameterisation and verification of existing models and the creation of new models are very important. The literature lacks experimental databases, and known solutions must be improved. Wheel–soil models are derived from experimental data in Chapter 8. Other ways to widen the applicability of the findings are

- Optimisation of vehicle undercarriage concepts and designs to achieve maximum performance and minimum soil degradation (compaction)
- Optimisation of off-road vehicle ride parameters (velocity, tyre inflation pressure, loading, etc.) for tractive performance and low soil compaction and degradation from off-road traffic

References

Arvidsson J. and Ristic S. 1996. Soil stress and compaction effects for four tractor types. *J. Terramech.* 33: 223–232.

Bailey A.C., Raper R.L., Way T.R. et al. 1996. Soil stresses under a tractor tire at various loads and inflation pressures. *J. Terramech.* 33: 1–11.

Bekker M.G. 1969. *Introduction to Terrain-Vehicle Systems.* Ann Arbor, MI: Michican Press.

Block W.A., Johnson C.E., Bailey A.C. et al. 1994. Soil stress measurement under rigid wheel loading. *Trans. ASAE* 37: 1753–1756.

Dąbrowski J., Pytka J., Tarkowski P. et al. 2006. Advantages of all-season versus snow tires for off-road traction and soil stresses. *J. Terramech.* 43: 163–175.

Foda M.A. 1991. On the prediction of drawbar pull–normal slip relationship for a pneumatic tire moving on soft ground *J. Terramech.* 28: 383–392.

Gliński J., Domżał H., and Lipiec J. 1991. Soil compaction as a factor determining plant productivity. *Soil Till. Res.* 19: 95–98.

Hakansson I. 1994. Subsoil compaction by high axle load traffic. *Soil Till. Res.* 29: 105–306.

Hetherington J.G. and White J.N. 2002. An investigation of pressure under wheeled vehicles. *J. Terramech.* 39: 85–93.

Hetherington J.G. and Littleton I. 1987. The role of mean maximum pressure in specifying cross-country mobility for armored fighting vehicle design. *J. Terramech.* 24: 263–280.

Horn R., Blackwell P.S., and White R. 1989. The effect of speed of wheeling on soil stresses, rut depth and soil physical properties in an ameliorated transitional red-brown earth. *Soil Till. Res*. 13: 353–364.

Horn R., Way T., and Rostek J. 2000. Soil deformation under repeated wheeling of tractor tires. *Proceedings of 14th ISTRO Conference.*

Horn R. and Rostek J. 2000. Subsoil compaction processes: State of knowledge. *Adv. GeoEcol*. 32: 44–54.

Megson T.H.G. 2010. *An Introduction to Aircraft Structural Analysis.* Burlington, MA: Butterworth-Heinemann.

Muro T. 1993. Tractive performance of a driven rigid wheel on soft ground based on the analysis of soil–wheel interaction. *J. Terramech*. 30: 351–369.

Pacejka H. 2004. *Tire and Vehicle Dynamics*. Amsterdam: Elsevier.

Piechnik L. 1986. Effect of repeated passages of a tractor on infiltration and water erosion of soil. *Proceedings of ISTVS Conference,* Warsaw.

Pytka J. 1997. Investigation of soil stresses and deformation with respect to loading process dynamics. Doctoral thesis, Institute of Agrophysics, Lublin, Poland.

Pytka J. 2005a. A new method for vehicle–terrain interaction research. *SAE Technical Paper Series,* 2005–01–0940.

Pytka J. 2005b. Effects of repeated rolling of agricultural tractors on soil stress and deformation state in sand and loess. *Soil Till. Res.* 82: 77–88.

Pytka J., Dąbrowski J., Zając M. et al. 2006. Effects of reduced inflation pressure and vehicle loading on off-road traction and soil stress and deformation state. *J. Terramech.* 43: 469–485.

Pytka J. 2007. Modelling and system identification of a wheel–soil system. *SAE Technical Paper Series* Paper No. 2007–01–0482

Raper R.L., Bailey A.C., Burt E.C. et al. 1995. The effects of reduced inflation pressure on soil–tire interface stresses and soil strength. *J. Terramech.* 32: 43–51.

Schjonning P., Lamande M., Togersen F.A. et al. 2006. Distribution of vertical stress at the soil–tire interface: Effects of tire inflation pressure and the impact on stress propagation in the soil profile. In *Soil Management for Sustainability: Advances in Geoecology,* 38: 38–46.

Schwanghart H. 1991. Measurement of contact area contact pressure and compaction under tires in soft soil. *J. Terramech*. 28: 309–318.

Shibusawa S. and Sasao A. 1996. Traction data analysis with the traction prediction equation. *J. Terramech.* 33: 21–28.

Shmulevich I. and Osetinsky A. 2003. Traction performance of a pushed/pulled drive wheel. *J. Terramech.* 40: 33–50.

Skwarek W., Krasowski E., and Karczewski T. 1986. Investigations of soil deformations generated by multiple passes of tractors. *Ann. Agric. Sci.* 76: C2.

Upadhyaya S.K., Sime M., Raghuwanshi N. et al. 1997. Semi-empirical traction prediction equations based on relevant soil parameters. *J. Terramech.* 34: 141–154.

Wanjii S., Hiroma T., Ota Y. et al. 1997. Prediction of wheel performance by analysis of normal land tangential stress distribution under the wheel–soil interface. *J. Terramech.* 34: 165–186.

Way T.R., Johnson C.E., Bailey A.C. et al. 1996. Soil stress state orientation beneath a tire at various loads and inflation pressures. *J. Terramech.* 33: 185–194.

Wiermann C., Way T.R., Horn R. et al. 1999. Effects of various dynamic loads on stress behaviour of a Norfolk sandy loam. *Soil Till. Res.* 50: 127–135.

Wulfsohn D. and Upadhyaya S.K. 1992. Prediction of traction and soil compaction using three-dimensional soil-tire contact profile. *J. Terramech*. 29: 541–564.

5

Stress State under Tracked Vehicle Loads

5.1 Introduction

The performance of a tracked vehicle running on soft terrain depends on, among other factors, a dynamic response of soil that may be quantified by soil stress values. Soil stress state under tracks is a function of both soil strength and the ride dynamics parameters of a vehicle. A general advantage of tracked suspension is that vehicle weight is distributed over a greater surface when compared to wheeled vehicles, and the resulting contact pressure is theoretically equal (constant) along the track (Dąbrowski 1997). Analytical methods for soil pressure determination are based on the fundamental equation introduced by Boussinesq (1885). This equation describes the problem of die loading and expresses the relationship between external force F and pressure in soil p:

$$p = \frac{F}{2\pi a\sqrt{\left(a^2 - r^2\right)}} \tag{5.1}$$

where a is the radius of the die and r represents decentration of loading force vector. This model has been modified several times throughout the years. Fröhlich (1934) introduced the stress concentration factor that depends on soil state. This theory was used to create the soil compaction model (SOCOMO) for wheeled agricultural vehicles cited in Chapter 1.

As noted above, tracked suspensions theoretically distribute vehicle weight over a greater surface than do wheeled suspensions. For agricultural engineering, tracked vehicles mean less soil compaction but present drawbacks due to higher fuel consumption and weakened mobility on hard-surfaced roads. For army engineering, the low ground pressure of tracked suspension is critical for mobility in difficult terrain. A number of methods for predicting ground pressure have been suggested. We present two selected methods below.

The first is nominal ground pressure (NGP) expressed as

$$NGP = \frac{W}{2Rmb} \tag{5.2}$$

where m is the number of axles, b indicates tyre width, and R denotes tyre radius.

The second method is mean maximum pressure (MMP) that may be used for both wheeled and tracked vehicles (with the use of different equations). Three methods may be used to calculate MMP.

Rowland's method for wheeled vehicles — A value of MMP is deduced from full-scale pulling tests of a vehicle:

$$MMP = \frac{kW}{2mb^{0.85}d^{1.15}\left(\frac{\delta}{h}\right)^{0.5}} \tag{5.3}$$

where k is a factor depending on vehicle undercarriage type (proportion of axles driven), δ is the tyre deflection on hard ground, and h represents tyre height.

Maclaurin's method for wheeled vehicles —

$$MMP = \frac{1.14W}{2mb^{0.85}d^{1.15}\left(\frac{\delta}{d}\right)^{0.5}} \tag{5.4}$$

where d equals tyre diameter.

Rowland's method for tracked vehicles on fine-grained soils —

$$MMP = \frac{1.26W}{mb\sqrt{ld}} \tag{5.5}$$

where l is track plate length.

These equations consider the effects of averaging peak pressures under the road wheels. Equation (5.5) was developed from a series of full-scale tests using pressure transducers buried at an average depth of 0.23 m. Larmine (1992) discussed numerous factors affecting the MMP system, such as weight, slipperiness, soil depth, axle loading, steering, and others. Hetherington and Littleton (1987) and Hetherington and White (2002) discussed the role of MMP and soil pressure measurements for vehicle design and for prediction of off-road performance. In any vehicle–terrain study

for determining micromechanics of soil compaction or general considerations of go-or-no-go conditions, soil pressure data plays a necessary role.

Many research papers have shown soil stress to be an important measure describing track–soil interactions. When compared to contact pressure, soil stress—especially a complete stress state—gives more precise information on dynamic soil responses to wheel loads. In this chapter, we focus on determining and analysing soil stress and deformation state under loads of tracked vehicles based on (1) loads (vehicle mass), (2) ride velocities, and (3) track slip. We also consider the effects of rubber pads on soil stresses and the resulting vehicle traction. Simultaneous measurements of soil stresses and deformation allow determination of soil stress–strain relationships that can serve as primary input data for further soil strength analysis.

5.2 Experimental Methods

5.2.1 Test Vehicles

Three military tracked vehicles were selected for the tests: 44.3 tonnes (A), 12.13 tonnes (B), and 9.7 tonnes (C) (Tables 5.1 and 5.2). Each track runs around a series of road wheels, causing potential variations in loads as a vehicle moves over a given spot. In a comparison test, the vehicles were driven with a velocity of 5 km/h. In such conditions, dynamic effects are small and the mass distribution through the road wheels is the most significant factor affecting soil stress. The effect of vehicle speed was investigated for vehicle B, which was driven at velocities of 5, 10, and 20 km/h. Vehicle A was used to determine the stress–strain relationship and the effects of rubber pads on soil stress. Vehicle B was used to determine vehicle traction. Vehicle C was used to investigate the effects of track slipping.

TABLE 5.1

Characterisation of Vehicles Used in Experiments

Parameter	Vehicle A	Vehicle B	Vehicle C
Total mass ($kg \times 10^3$)	44.3	12.13	9.7
Total m^2 comparison area (length × width)	5.22 (4.5 × 0.58)	1.830 (3.545 × 0.258)	2.18 (4.22 × 0.25)
Single element m^2 comparison area (length × width)	0.008 (0.138 × 0.58)	0.036 (0.142 × 0.258)	0.043 (0.168 × 0.25)
Mean contact pressure (kPa)	90.2	66.2	44.3

TABLE 5.2

Load Distribution under Individual Wheels of Track Assemblies of Test Vehicles

	Vehicle Load Distribution (kg/kPa)		
Wheel Number	**A (44.3 tonnes)**	**B (12.13 tonnes)**	**C (9.7 tonnes)**
1	3200/392	1211/393	231
2	3637/446	1010/328	286
3	3910/479	1070/347	300
4	3810/467	990/321	307
5	3940/483	896/291	311
6	3643/446	831/270	315

5.2.2 Soil Stress and Deformation Determination

We utilised the same stress state transducer (SST) used in the wheeled vehicle experiments (Chapter 4); the SST has a wide measuring range of 0 to 700 kPa, although we did not expect soil pressures under tracked vehicle loads to be as high as under wheeled trucks. The measuring range was not a problem, but the running gears (tracks) sank so deeply into soft sandy soil that a track element destroyed the SST during an early test ride. We continued the measurements with a backup SST at a depth of about 15 to 20 cm in the centre line of the right track. The installation was simple (Figures 5.1 and 5.2) and involved excavation, positioning of the SST, and refilling the soil. We previously tested this method and found that it does not influence the accuracy of measurements significantly in sandy soil. A portable, industrial-class computer was used for soil pressure data recording. Figure 5.3 shows a test vehicle approaching the measurement point.

5.2.3 Vehicle Traction Determination

Vehicle traction was determined in experiments with rubber pads. A 500-kN range dynamometer installed between the test vehicle and a braking vehicle measured pull force. The braking vehicle was behind the test vehicle and they were joined with a rubber "bungee" rope that allowed us to obtain an almost linear increase in braking force and a resulting 0% to 100% slip for the test vehicle. Steel ropes would have caused sudden braking force peaks, without the possibility of sensitive investigation of the slip range (Dąbrowski 2001).

We used two kinematics measures to determine slip: longitudinal vehicle speed and rotational speed of a driven track. Longitudinal speed was measured with an optical, non-contact sensor, while the rotational speed was measured with an electromagnetic tachometer installed on a driven

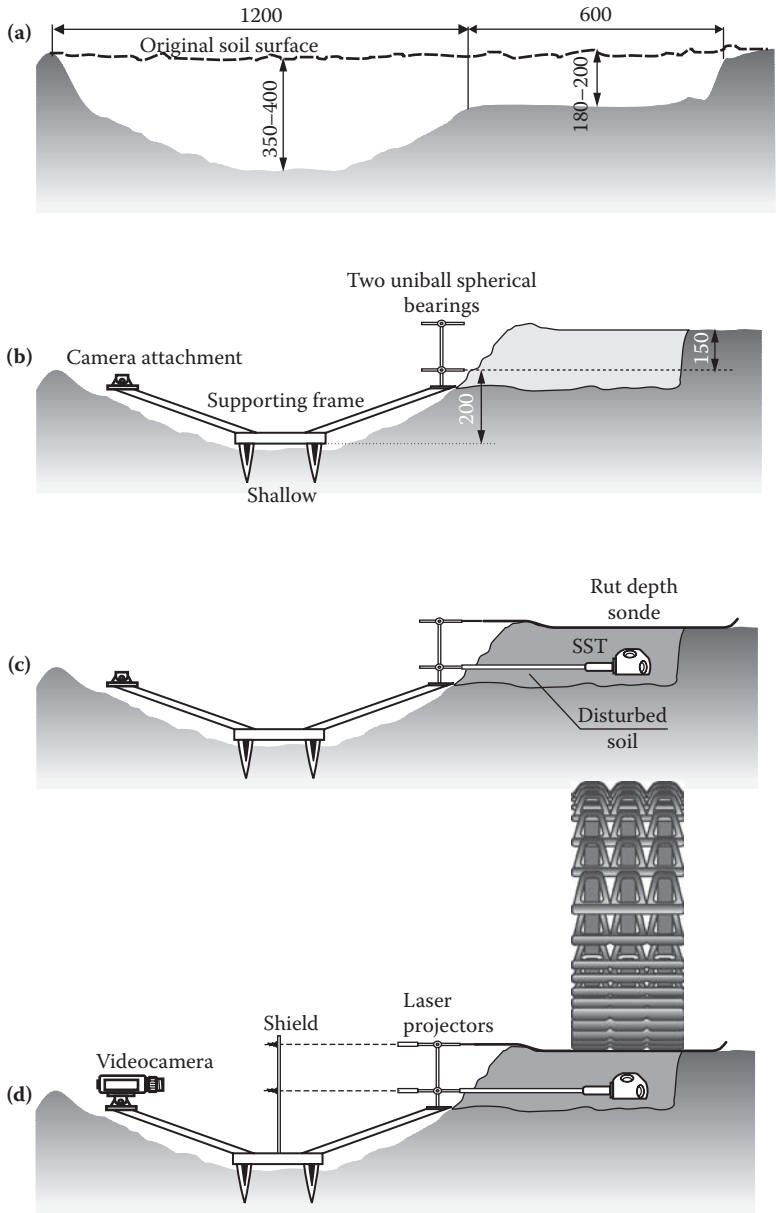

FIGURE 5.1
Installation of the measuring equipment in soil. (a) preparing the site for installation, (b) installing the supporting frame, (c) installing the SST and rut depth sonde, (d) installing the laser projectors, camera, and the shield.

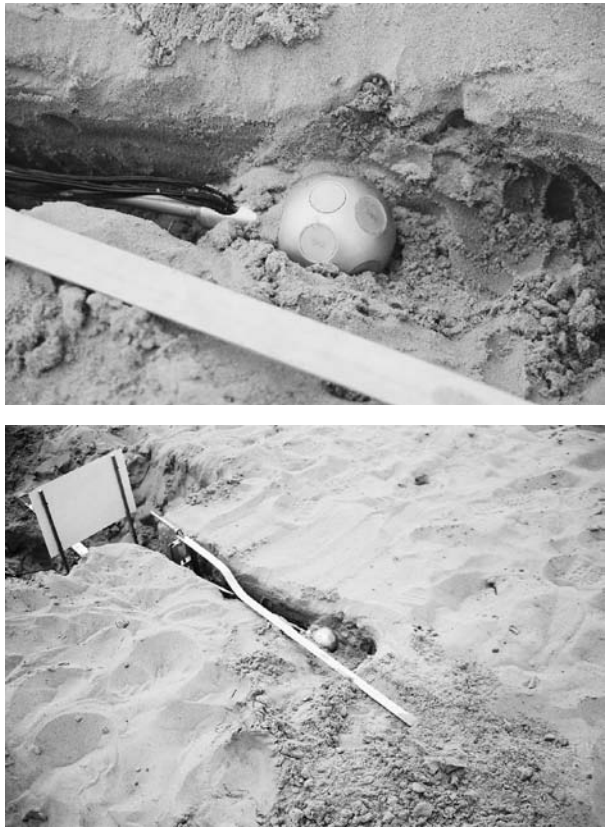

FIGURE 5.2
Stress state transducer (SST) and rut depth sonde during installation in soil.

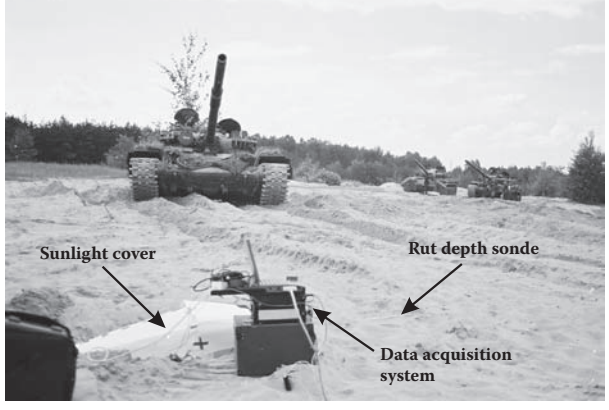

FIGURE 5.3
A test vehicle (main battle tank) approaching the measuring point.

road wheel. For data acquisition, we used a portable computer with a multi-channel digital-to-analogue converter and software.

5.3 Analysis of Soil Stress State under Loading by Tracked Vehicles

5.3.1 Experimental Details

We ran test vehicles A, B, and C over a sandy soil surface. The soil had a bulk density of 1.72 g/cm^3 and a moisture content of 4% to 7%. For each test variant, we performed at least five repetitions (test runs); after each repetition, we replaced the SST and manually homogenised the soil at the measuring point and about 10 metres before and after the point. This let the vehicle run smoothly and allowed us to conduct all the measurements in similar soil conditions. Some skills were required by the drivers and test engineers to ensure that the vehicles ran exactly over the SST. We sprayed chalk over the soil or marked locations with tree branches to guide the drivers. It was especially difficult to perform high-speed test runs at 20 km/h. We used radiofrequency (RF) transceivers to communicate with test engineers and drivers. The soil pressure data were saved to a portable, industrial-class computer, then recalculated into soil stress components via the methods described in Chapter 2. Results of analysis of soil stresses for particular test variants are discussed in the subsequent sections.

5.3.2 Analysis of Principal Stresses

Figure 5.4 shows a set of sample curves of soil stresses. The stress concentration under the wheels may be seen by the peak stresses that represent loading of each road wheel. The stress relaxation between the road wheels that varies from 100% under the wheels to 0% between the wheels suggests non-homogeneous load distribution along the line of track.

With a tracked undercarriage, the total load from the vehicle's weight is theoretically distributed under the total contact area, which is considerably greater than for wheeled vehicles. In the field, however, most of vehicle weight is distributed on the small contact area of a single track element under a road wheel. This causes soil stress concentration under the wheels. This is obviously dependent on track tension force that can be controlled within a limited range and also on surface conditions: the greater the surface strength, the more homogeneous the stress distribution. For sandy soil, stress distribution is non-homogeneous. This is significant and causes

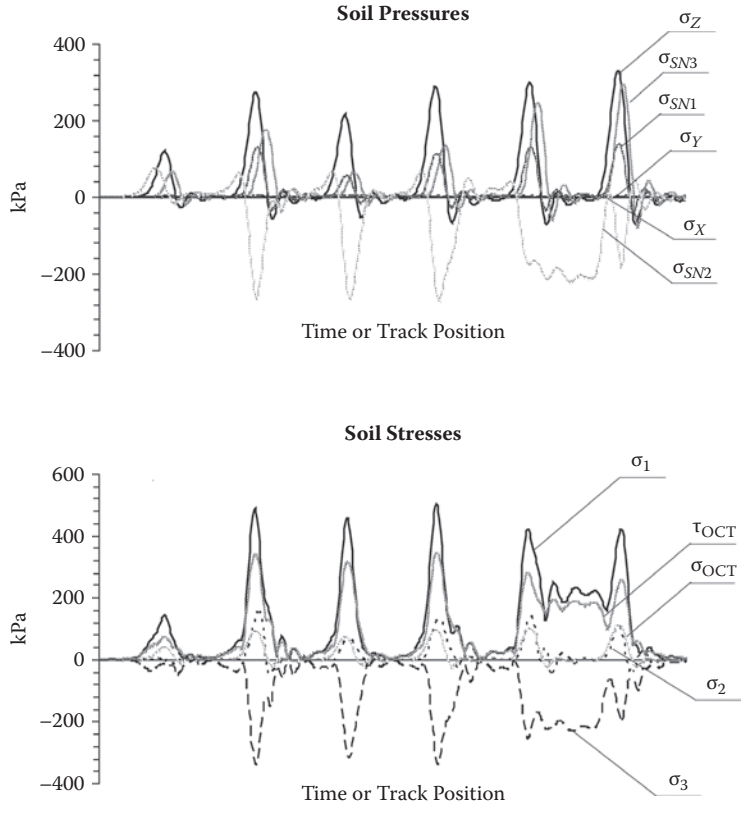

FIGURE 5.4
Sample set of soil pressures and calculated stresses curves.

vibrations in vehicle suspension that were subjectively noticed by the crew members.

The type and quality of a surface may also have significant effects on spatial stress distribution. In soils, including sandy soil, the main direction of stress propagation is almost the same as the vehicle weight vector direction. The σ_1 to σ_2 to σ_3 relationships confirm this statement: the values of minor stresses are no more than 25% of the major stress σ_1. The non-homogeneity of sandy soil does not allow horizontal stress distribution greater than one-quarter of the total external load. One of the consequences of this is a decrease of traction.

5.3.3 Analysis of Octahedral Stresses

From the analysis of the stress plots in Figure 5.4, we conclude that the shear stress is always higher in value than mean normal stress in an

octahedral system. When related to the major σ_1 stress in a three-dimensional stress system, the peak τ_{OCT} is 60% to 70%, while the σ_{OCT} is 30 to 40% of the peak σ_1 stress. The domination of shear over compression would suggest the shearing and structural damage in soil under the wheels are dominant and of more importance than volumetric deformations (soil compaction).

Sandy soil with small cohesion does not create a structure that could be resistant to destruction. The soil volume is deformed, especially in horizontal directions (this is logical as the minor stresses are considerably lower than the major stress). On the other hand, compressibility of sandy soils is relatively small; the volumetric changes are significantly less important. These statements, however, are still hypotheses and require further research of soil deformations as the result of acting stresses.

5.3.4 Effects of Mass Distribution and Dynamic Load

To investigate the effect of vehicle mass distribution on soil stress, peak values of σ_1, σ_{OCT}, and τ_{OCT} were analysed for every road wheel of the three investigated vehicles. Relationships of contact pressure and peak stresses (Figure 5.5) were calculated for each road wheel; wheels were numbered from the front to the rear. The standard deviation for five repetitions analysed for each wheel was smaller for the aft road wheels: the decrease was about 30% to 40% for the last wheel, compared with the first. This was most probably caused by soil consolidation, enabling the stress transducers to function better with the closer contact between membranes and soil.

This is significant, especially when the stress values for rearward road wheels are not higher.

Table 5.3 and Figure 5.6 show relationships between increasing contact pressure and corresponding stresses for the three vehicles. The table includes stresses calculated with the Boussinesq equation. The figure illustrates the relationships between contact pressure and calculated soil stresses as described by logarithmic functions. Calculated soil stress is significantly smaller than measured.

5.3.5 Effects of Vehicle Speed

Karczewski (1978) and Horn et al. (1989) confirmed the inverse influence of deformation speed on stress state in soil: the higher the deformation speed, the lower the soil stress. A decrease in soil stress at increasing speed is explained by the shorter time for wheel–soil interaction and less intensive stress propagation. This is certainly true for smooth soil surfaces that are very rare under real conditions. Surface roughness causes vehicle oscillations in the vertical direction, and the resulting stress may differ from theoretical predictions.

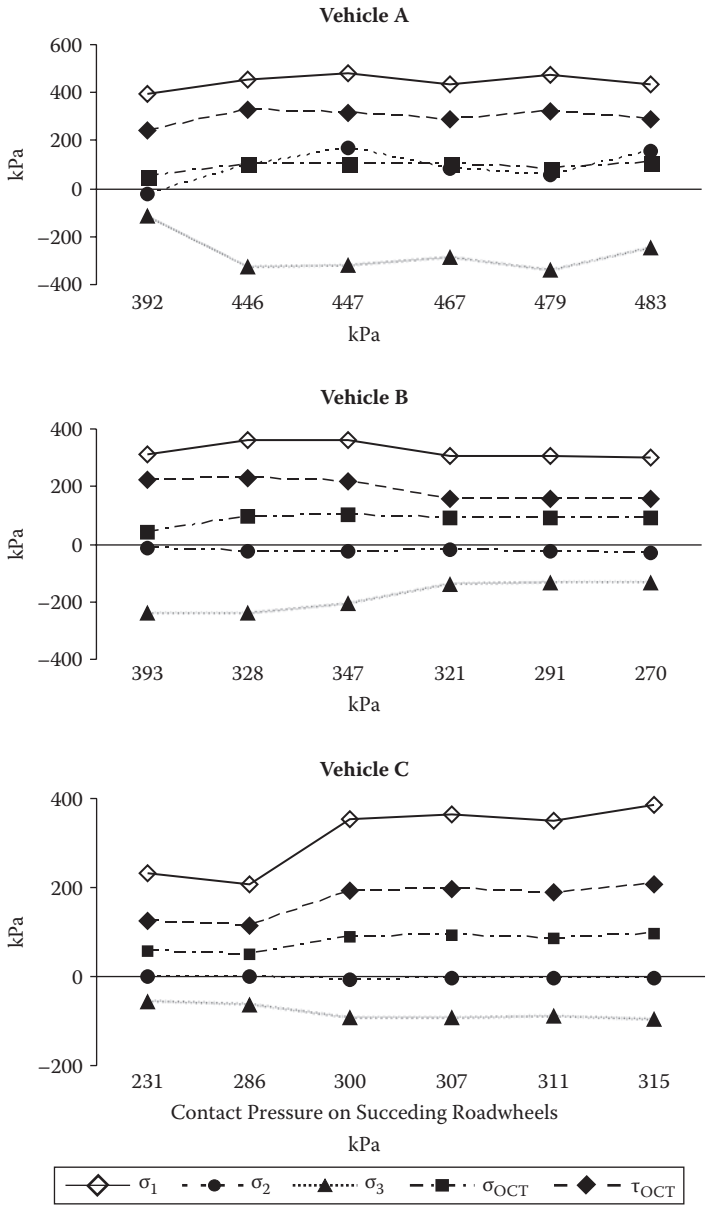

FIGURE 5.5
Effect of mass distribution on soil major principal stress σ_1, octahedral shear stress, and mean normal stress for the three test vehicles A, B, and C.

TABLE 5.3

Measured Peak Maximum Soil Stresses (σ_1, σ_{OCT}, and τ_{OCT}) versus Theoretical Stress Calculated from Boussinesq Equation

Load (kPa)	Indicated Stress (kPa)			Calculated Stress (kPa)
	σ_1	σ_{OCT}	τ_{OCT}	Boussinesq Model
231	232.78	58.78	125.06	110.21
270	302.65	93.67	155.17	128.91
286	208.46	48.36	115.88	136.45
291	307.97	92.42	156.45	138.94
300	353.8	87.63	192.12	143.01
307	364.78	91.21	196.96	146.55
311	348.3	85.97	187.74	148.25
315	384.62	96.78	207.74	150.48
321	305.45	91.73	158.85	153.26
328	359	97.06	231.25	156.60
347	359.7	102.78	217.85	165.68
392	392.3	49.36	244.9	187.16
393	310.3	43.05	223	187.64
446	455.86	103.33	329.6	212.95
447	478.3	104.38	291.3	222.97
467	433.4	104.38	291.3	222.97
479	473.7	85.45	321.9	228.7
483	432.98	107.36	290.7	230.61

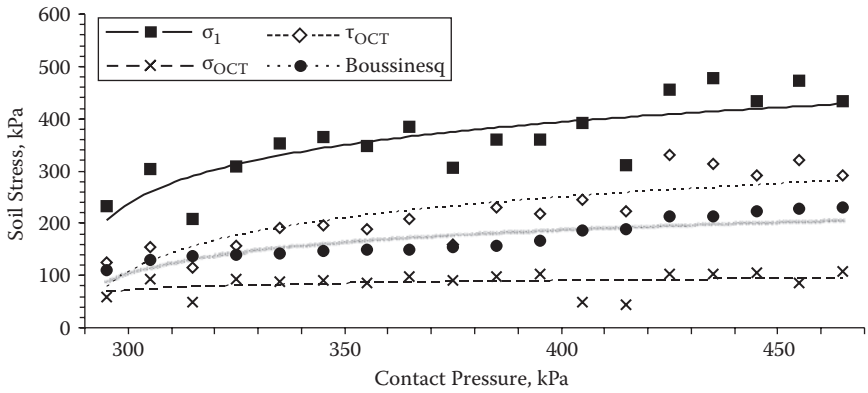

FIGURE 5.6
Comparison of experimental soil stress data (σ_1, σ_{OCT}, and τ_{OCT}) for the three test vehicles A, B, and C with calculated stress (Boussinesq equation).

Figures 5.7 and 5.8 show our results for different vehicle speeds. Stress curves are plotted for three speeds (5, 10, and 20 km/h) for the mid-weight vehicle B (see Table 5.1). The shapes of the curves are interesting. Comparing the three graphs, we can notice smoothing or levelling of the stress curves at higher speeds. Soil stresses do not reach zero values between the road wheels at higher speeds; stress distribution changes and

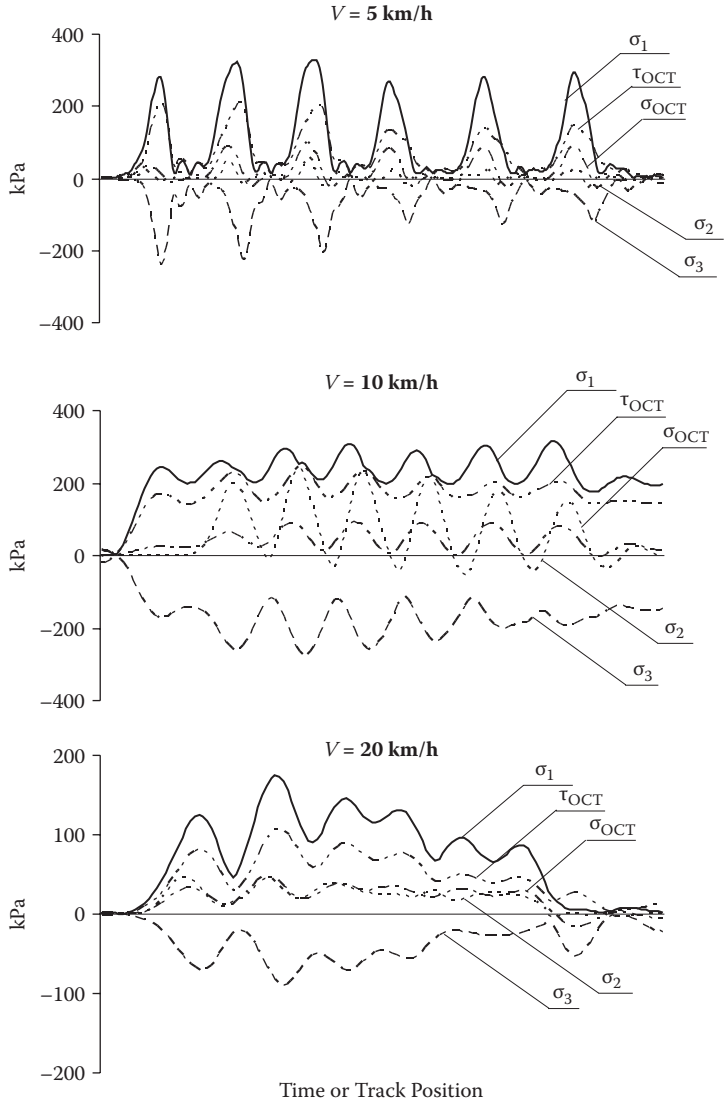

FIGURE 5.7
Soil stress state graphs for the vehicle B running with various speeds: 5, 10, and 20 km/h.

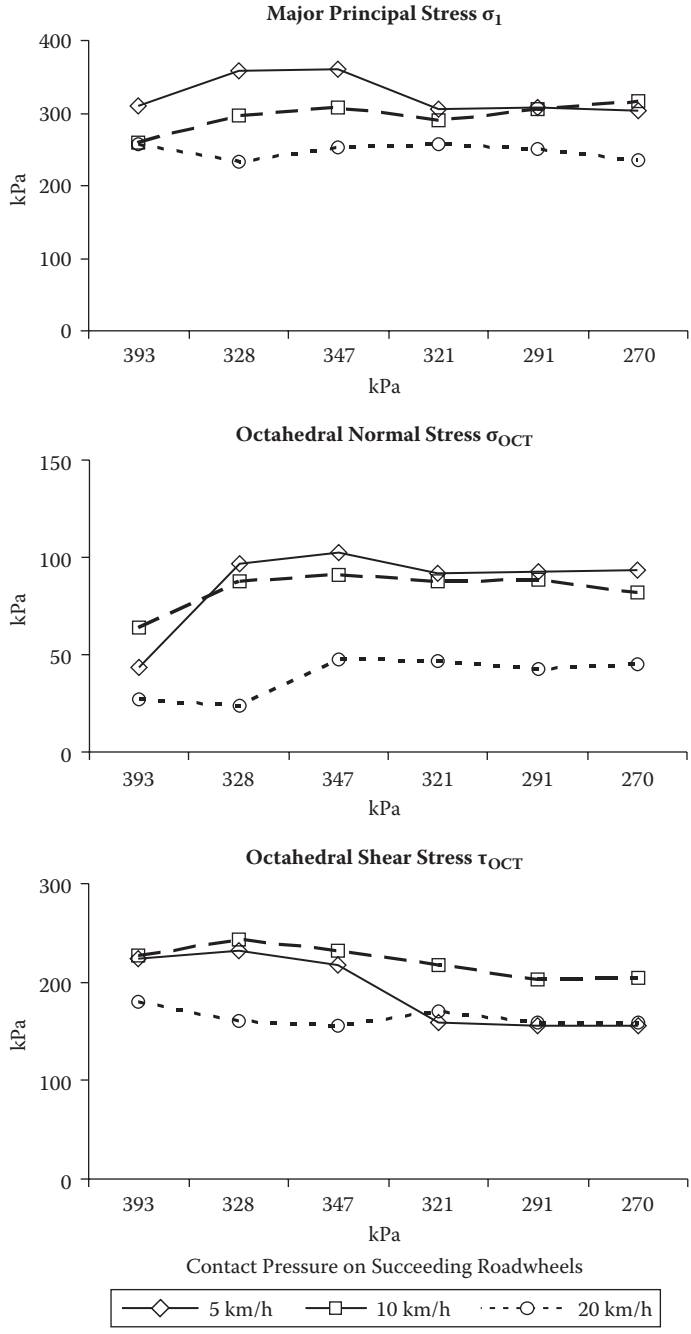

FIGURE 5.8
Effect of vehicle speed (vehicle B) on major stress σ_1 and octahedral stresses σ_{OCT} and τ_{OCT}.

stress relaxation are not as pronounced as they are for lower speeds. We conclude that there are advantageous soil–track interactions and better vehicle performance at higher speeds. Analysing the stress values, we assume that stress decreases at higher vehicle speed. The effect is significant between 10 and 20 km/h and less significant or uncertain between 5 and 10 km/h. Higher deviations in stress values can be explained as surface roughness and dynamics effects (Figure 5.8). At higher speed, surface-induced oscillations are pronounced.

5.3.6 Effects of Slipping

The effect of slipping was investigated for the lighter vehicle C (see Table 5.1). The vehicle was stopped by increasing the braking force on an additional vehicle connected behind the test vehicle as described in Section 5.2.3. This generates a linearly increasing slip from 0% to 100%; a 100% slip occurs for a fully stopped braking vehicle. The graphs in Figure 5.9 show stress state components for test rides with various braking forces leading to increasing track slip. Note that the applied braking force caused changes in the distribution of vehicle mass and contact pressure.

The middle graph in Figure 5.9 shows increasing peak values of stresses (especially σ_1, τ_{OCT}, and σ_{OCT}) for subsequent road wheels. The braking force applied to a point higher than the centre of gravity (CG) caused significant nose-up effect that lightened the road wheels in front of the CG and increased the loading of the road wheels behind the CG. In general, this effect of external braking occurs at a relative low percentage slip (0% to 30%) and influences the interactions between soil and track. Rut depth and rolling resistance both increase, which may cause a significant reduction of tractive performance.

For the higher values of braking force (bottom graph in Figure 5.9), we can see irregular (saw-shaped) stress curves. The local peak stress values may be the effects of intensive vibrations of the vehicle at high braking force when the power was set on maximum. These vibrations were magnified by resonances and transmitted into the soil. The measured stresses, however, are of unpredictable values, not correlated with contact pressure as the vehicle mass distribution was strongly disturbed. This would suggest significant changes in soil–track interactions and vehicle performance.

5.3.7 Discussion

Soil stress state generated under off-road vehicles is dependent on a number of factors and conditions, but it can be used as a precise descriptor for soil reactions to various dynamic loads (Wiermann 1999, Bailey et al. 1996), inflation pressures for wheeled vehicles (Raper et al. 1995, Bailey et al. 1996, Way et al. 1996), and vehicle speeds (Karczewski 1978). Researchers focus

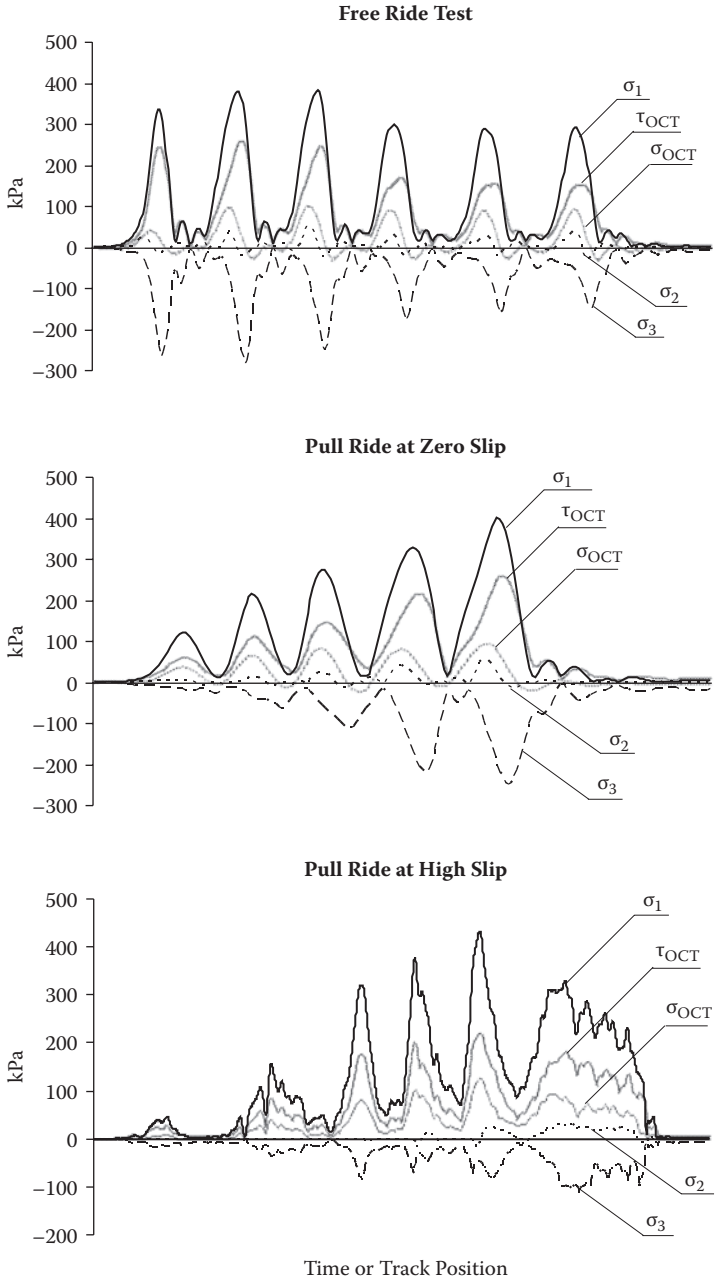

FIGURE 5.9
Stress state graphs for vehicle C driving with increasing drawbar pull force.

on (1) ecological aspects of soil compaction by vehicle traction (Horn and Lebert 1994, Bailey et al. 1996), and (2) mobility problems, important especially for military vehicles (Dąbrowski 2001, Pytka and Dąbrowski 2001, Rowland 1989, Wong 1984 and 1989). They use different instruments and methods that vary in measurement accuracy. The experiments described in this chapter show the complexity and problems of measuring soil stress in real field conditions. Especially for dynamic manoeuvres, it is difficult to measure stress state. On the other hand, replication of field conditions in a laboratory is often impossible.

Results presented here show how the soil stress is affected by changes of mass distribution, vehicle speed, and track slip. Results also show that the measurement device (SST with strain gage pressure sensors) is sensitive enough to capture those effects. This suggests that we can continue these investigations on other soil types and examine other factors.

However, one important methodological aspect must be considered. All the measurements were performed in one soil under nearly constant conditions. A change in soil moisture content or simply a change of soil type would probably affect the values of the measured stress significantly. The effect of soil particle size and distribution on measured stress values is important. To validate the measuring method, we must calibrate the sensors in all investigated materials under various conditions.

The repeatability of the results from field tests is lower than for laboratory experiments, but it is difficult to reproduce real conditions in a soil bin. Our philosophy is to obtain field data that are as accurate as possible and use them to complement laboratory tests results. Unpredictable effects—soil surface roughness, precision of driving, preparation of soil, and SST installation—may influence final results significantly. Therefore, at least five replications are needed and special care must be taken during the preparation.

5.4 Determination of Soil Stress–Strain Relationships

5.4.1 Introduction

The literature describes many research methods for determination of soil mechanical properties. We can summarize measurements of soil strength under laboratory conditions via (1) indirect methods such as the Attenberg test and Proctor test; and (2) direct methods, for example, the uniaxial unconfined and confined tests, triaxial test, and direct shear test.

In the indirect stability tests, neither the homogenised soil material nor the loading process is comparable to in situ soil conditions. Results

from direct tests are highly influenced by compression and drainage conditions and by shearing velocity. Thus, in situ measurements of soil strength, especially the stress–strain relationship, are more sophisticated approaches to the study of soil mechanical properties.

The stress–strain state in soil during a loading process determines the mechanical properties of soil strength limits, energy of deformation, and hysteresis behaviour. There is no theoretical description for the soil stress and deformation state under loading, but we believe this information can be obtained from experimental investigations.

Measurements of stresses and deformations in soil are therefore important for studying soil compactability and trafficability. Most models of soil deformation relate the volume change in soil to the applied stress. If shearing stresses influence the deformation process, the complete soil stress state must be obtained. On the other hand, soil stress and deformation state are dependent on vehicle undercarriage configuration, mass, and load distribution, and vehicle tractive performance. Therefore, examining traction dynamics for various tyres by measuring stresses and deformations in soil may help optimise vehicle design. Special features of the soil material compound the methodological difficulties; new experimental methods are needed.

5.4.2 Field Experiment Details

A main battle tank (vehicle A; see Table 5.1) made five repetitions of a single pass over the investigated soil volume. The vehicle speed was constant at 5 km/h, and the centre line of a right track was exactly (±0.05 m) over the SST. The single track link element measured 0.138×0.580 m. The total length of the track was 4.4 m and the diameter of carrying wheels was 0.735 m. Table 5.2 shows load distribution under the wheels. Mean pressure under the two tracks was 90.2 kPa when the total mass of the vehicle was 44.3 tonnes.

The experiment used the first generation of the optical system for soil determination (see Chapter 2). The SST with a rigid arm for the laser projector was placed horizontally at a depth of 15-cm under the top surface. The remaining volume around the transducer was then filled with excavated soil, with extra care to fill the space of direct contact with the SST. The regular shape of the transducer was specially chosen to obtain optimum conditions of contact between soil and pressure transducers. The rut depth sonde (one of the two soil deformation probes) was put on the soil surface over the SST, then laser projectors were installed with a cover to shield them from the sun. Installation of the elements in soil and the complete system are shown in Figure 5.1; Figure 5.3 shows the test vehicle in front of the experimental set-up.

5.4.3 Analysis of Soil Stresses under Loads

The complete soil stress state during a single vehicle pass is shown in Figure 5.10. Five curves (σ_1, σ_2, σ_3, σ_{OCT}, and τ_{OCT}) are shown as functions of time. Table 5.4 contains the data from the five repetitions, showing maximum values of each stress as well as the average values and standard deviations for each vehicle wheel. For the calculations of the average values, two extremes were omitted. All five stresses reach peak values six times, which is a consequence of six road wheels in the vehicle's undercarriage.

Between the first four peak values, minimum values close to zero are reached because of intense stress relaxation. Stresses were generated under all but the last two road wheels, where the residual stresses are 59% to 80% of the peak values. Some values of the σ_1 major stress in repetitions are under- or over-estimated. This may be caused by gradual soil consolidation and by stress concentration zones. Although wheel loads indicated in Table 5.4 do not exceed 500 kPa, it is possible that the existing load becomes much greater because of the geometry of the single track element. However, average values of the σ_1 soil stress correspond to the contact pressures under the wheels.

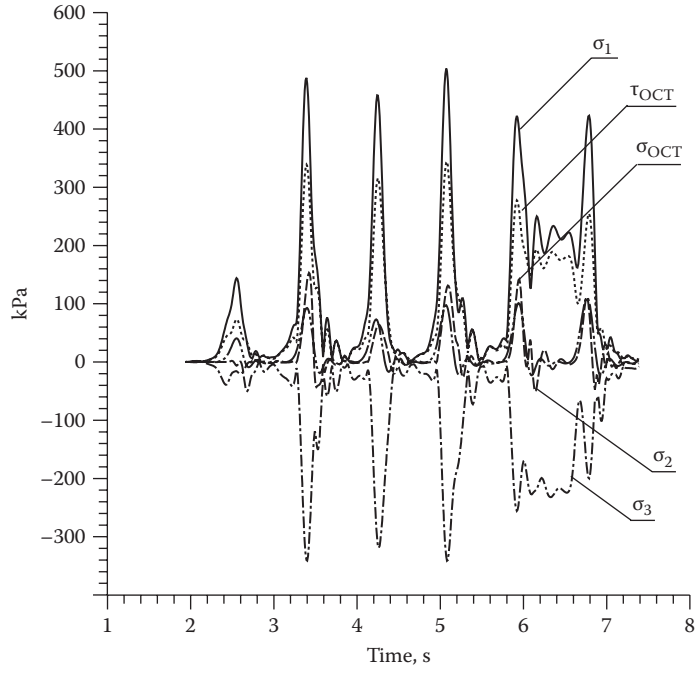

FIGURE 5.10
A sample set of soil stress components curves (for vehicle A).

TABLE 5.4

Soil Stress State Components

Wheel Number and Pressure	Repetition	Stress (kPa)				
		σ_1	σ_2	σ_3	σ_{OCT}	τ_{OCT}
1: 392 kPa	1	362.4	–204.3	–84.01	101.2	185.3
	2	143.9	1.84	–39.22	40.56	73.2
	3	478.2	43.33	–240.4	74.76	309.9
	4	337.9	2.24	–384.9	32.98	239.5
	5	484.8	99.99	–882.2	90.79	565.0
Avg/Std Dev		392.3/61.4	–20.6/54.6	–118.43/89	49.36/18.1	244.9/51.1
2: 446 kPa	1	401.7	218.2	–316.2	105.5	303.5
	2	487.9	153.1	–341.3	92.63	339.1
	3	576.2	44.1	–325.8	95.99	368.6
	4	375.8	–59.58	–459.0	20.33	264.3
	5	478.0	90.14	–377.9	108.5	346.4
Avg/Std Dev		455.86/38.5	95.74/44.6	–327.76/10.3	103.33/5.3	329.6/18.7
3: 479 kPa	1	334.5	–197.8	53.64	105.2	202.0
	2	457.9	63.78	–319.2	73.07	315.5
	3	495.0	49.3	–317.2	80.02	330.1
	4	398.1	–68.28	–469.9	–0.87	320.1
	5	468.2	55.25	–382.0	103.3	343.1
Avg/Std Dev		473.7/15.6	56.11/5.9	–339.46/30.8	85.45/12.9	321.9/6.1
4: 467 kPa	1	397.1	35.42	–245.8	105.1	256.8
	2	503.8	131.2	–341.5	97.44	344.2
	3	399.3	86.55	–269.0	72.09	273.0
	4	540.4	–73.72	–591.3	25.78	466.3
	5	686.4	229.3	–724.1	110.6	579.2
Avg/Std Dev		433.4/49.7	84.39/39.1	–285.43/40.7	104.38/5.4	291.33/37.9
5: 483 kPa	1	487.0	218.3	–219.6	106.6	292.3
	2	422.5	142.1	–232.1	100.9	277.5
	3	442.7	118.0	–297.0	85.94	302.4
	4	433.6	–151.7	–560.4	–13.52	392.7
	5	641.3	238.4	–810.9	114.6	556.0
Avg/Std Dev		432.93/8.2	159.46/42.7	–249.56/33.9	107.36/5.6	290.73/10.2
6: 446 kPa	1	606.2	–242.2	–338.2	239.3	333.4
	2	422.9	111.3	–200.0	110.5	254.5
	3	428.0	125.1	–420.0	96.93	348.3
	4	627.5	–199.3	–543.7	–212.8	519.7
	5	584.0	281.1	–941.0	103.2	657.2
Avg/Std Dev		478.3/74.7	172.5/76.9	–319.33/90.7	103.54/5.5	312.06/41.1

The absolute maximum of the σ_1 major stress was recorded under the last road wheel, whereas load and consequently contact pressure are the highest for the third and the fifth wheels. Such a situation is possible because terrain roughness may cause significant unsteady dynamic forces between vehicle undercarriage and soil surface.

The major stress σ_1 is the highest stress state component, whereas the σ_3 stress reaches negative values: the σ_3 vector is in the opposite direction from traction. The minor σ_2 stress values are 20% of σ_1 on average, which may indicate that the soil stress state is two-dimensional in this case.

The octahedral shear stress is significantly higher than mean normal stress, and it proves that structural damage and not compaction may be a major factor of soil deformation in this case. It proves that structural damage is more important in soil deformation in this case although structural damage and compaction cannot be treated as separate processes.

5.4.4 Analysis of Soil Deformation

Figure 5.11 shows typical video frames for four representative wheel positions. Deformations of soil volume—vertical displacement of the SST a**nd**

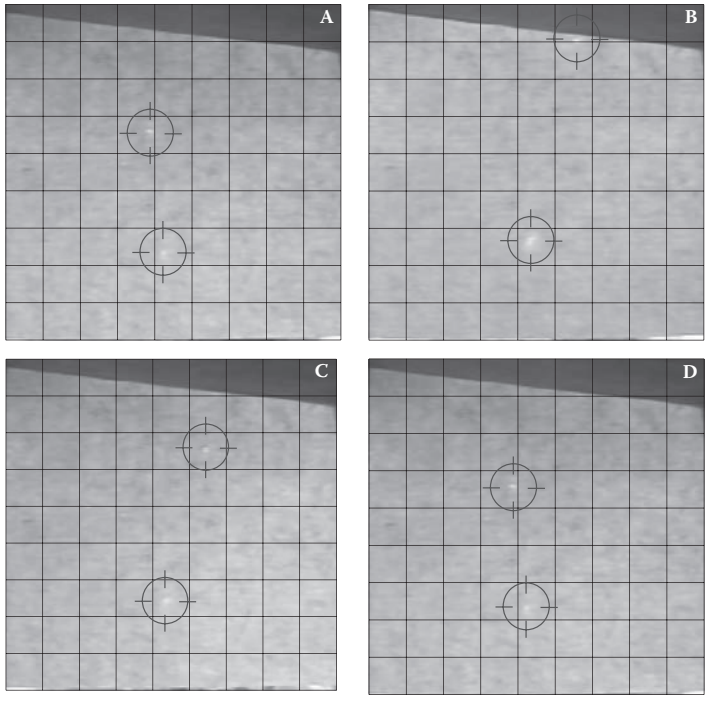

FIGURE 5.11
Typical video grabs for soil deformation analysis.

sinkage—can be calculated from image data. Co-ordinates are read from video data of the time-dependent movement of the lighting points on the shield. Rut depth and displacement of the SST can be determined in both Z and X directions because the laser projectors are supported in spherical bearings. A standard software application analysed the images taken during vehicle passes and quantified the horizontal and vertical co-ordinates of a centre light point as functions of time.

Soil deformation data correspond with stress state: the greatest rut depths and transducer displacement are seen under the road wheels of the vehicle (Figure 5.12). Significant displacements of the SST were recorded only in the vertical direction, whereas the rut depth sonde trajectory is two-dimensional. The absolute maximum vertical movement of the transducer was recorded under the fifth carrying wheel with the highest partial load and contact pressure, but the maximum rut depth was observed under the last road wheel. From the deformation data, soil compaction can be determined by the assumption of a one-dimensional compaction model.

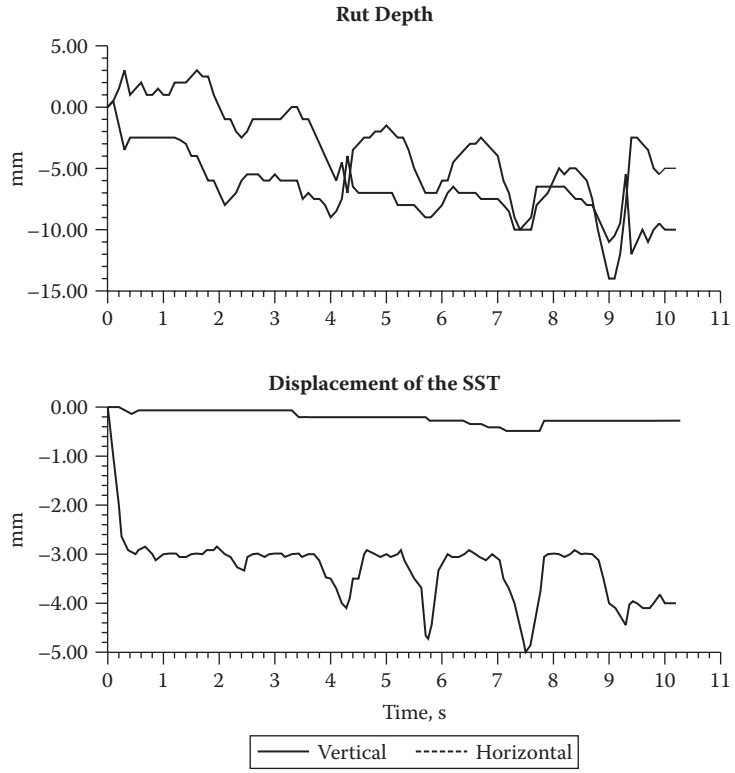

FIGURE 5.12
Soil deformations under loads of the test vehicle A.

5.4.5 Soil Stress–Strain Relationship

Stress–strain curves for the investigated soil may be developed from further analysis of the results. The major normal σ_1 stress is related to vertical strain of soil volume between the rut depth sonde and the SST. The relative deformation of soil volume (vertical soil strain) was determined using the obtained deformation data. The volumetric vertical strain ε_v is calculated as

$$\varepsilon_v = (150 + X_1 + X_2)/150 \times 100\% \tag{5.6}$$

where X_1 and X_2 represent vertical movements of the rut depth sonde and the SST in millimetres, respectively, and 150 is the vertical initial distance in millimetres between rut depth sonde and the SST.

The shapes of such stress–strain curves may describe and quantify mechanical properties of an investigated medium. Soil compactability, trafficability, energy of deformation and hysteresis, and the immediate strength of soil medium can be derived from the relationship. Six stress–strain curves obtained for each road wheel are shown in Figure 5.13. Analysis of the curves shows how the mechanical properties of the investigated soil change during a single pass of a vehicle.

The soil stress–strain curves for the six road wheels are different, and we can assume that the soil compactability changes: the resistance of the soil against volumetric strain increases for the successive wheels. With the exception of the first stress–strain curve, the volumetric strain in the vertical direction decreases from 9.3% for the second loading cycle to 8, 6.5, 6,

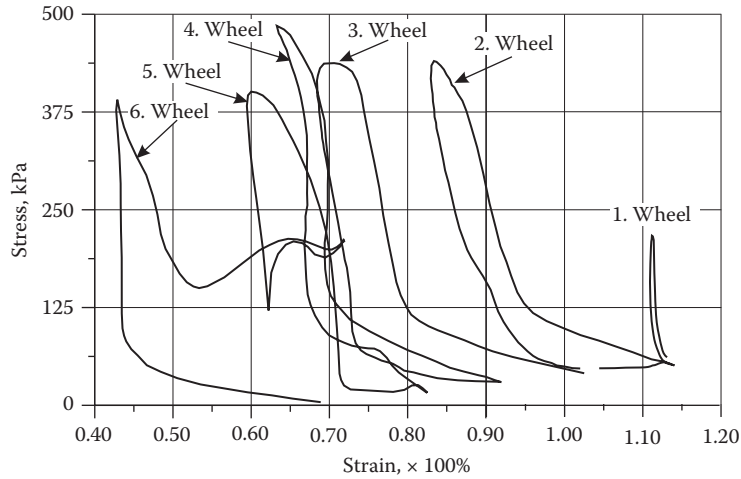

FIGURE 5.13
Soil stress–strain relationship obtained in the field experiment with vehicle A on sand.

and 5%, respectively. This shows that soil compactability decreases for the repeated wheeling events.

Measured negative volumetric strain under the first wheel is caused by the soil wedge in the front of the track that lifts the rut depth sonde. These observed differences in loading–relaxation cycles inform us about the changes in soil strength caused by cyclic loading of the six road wheels.

The width of the loop changes for the subsequent loading cycles under the wheels, indicating how changes in soil structure caused by loads influence the total energy uptake and consumption in the process of soil deformation. We also observe that the pre-compression stress value can be quantified from the stress–strain curve for the initial loading. This stress, defined as the value at the transition of the less declined loosening curve relative to the origin compression line, indicates the strength of the soil at a given water content.

5.5 Effects of Rubber Pads on Soil Stress and Tracked Vehicle Traction

5.5.1 Introduction

Poland's accession to the North Atlantic Treaty Organization (NATO) in 1999 resulted in many new demands for the Polish Army, one of which was the technical and tactical compliance of its armaments. This requirement was especially important if the Polish regiments were to participate in implementation force (IFOR) peacekeeping missions, for example, in Kosovo. In the case of armoured vehicles, the undercarriage systems of Polish military vehicles needed to be adapted to use rubber pads as practised by other NATO armies. This modification was especially required for vehicles that operate on public roads that could be destroyed by undercarriages of tracked vehicles.

Rubber pads for tracked vehicles used by the Polish Army were designed and developed by Polish industry, but the effects of the pads on vehicle performance were uncertain. Some general questions arose about the changes of operational parameters and environment impacts of vehicles equipped with rubber pads. The main objective of this study was to determine the effects of rubber pads on traction and stress state in sandy soil under vehicles.

5.5.2 Experimental Set-Up

Three identical tracked vehicles were used for these experiments: two had rubber pads applied and the third vehicle was left without rubber pads.

Two types of rubber pads were used; one had a flat contact plane and the other was treaded. The two pad types were made of a similar rubber composition. Each of the three vehicles had a total mass of 12.13 tonnes; the load distribution under the road wheels for the vehicles is presented in Table 5.5.

The contact pressures were calculated with an assumption that the wheel load was transmitted through an area of a single track element (142×258 mm for the vehicle without pads) or a single rubber pad. Table 5.6 shows the geometric parameters of a single track element and the two types of rubber pads. The horizontal contact area is the total area of a horizontal cross section of a track element or a pad while a shear area is the total area of a vertical cross section.

5.5.3 Effects on *S*oil Stress State

Soil stress state can be described by means of (1) the three major stresses, $\sigma 1$, $\sigma 2$, and $\sigma 3$, that act along three mutually orthogonal axes and six shear stress components; or (2) by two stresses in the octahedral system: σ_{OCT} and τ_{OCT}. For the analysis of rubber pad effects, it was reasonable to choose stress state components that would provide optimum information without the need to analyse all measures. Since we know that σ_2 and σ_3 are less pronounced and more uncertain and unrepeatable, it is more convenient

TABLE 5.5

Load Distributions and Contact Pressures for B Vehicle at Different Track Configurations

Wheel Number	Load (kg)	Contact Pressure (kPa)		
		No Pads	Flat Pads	Treaded Pads
1	1211	393	632	781
2	1010	328	527	651
3	1070	347	559	690
4	990	321	517	639
5	896	291	468	578
6	831	270	434	536

TABLE 5.6

Geometric Parameters of Track Elements and Rubber Pads

Parameter	Track Element	Flat Rubber Pad	Treaded Rubber Pad
Length × width (mm)	216×140	193×98	195×78
Horizontal contact area (cm^2)	302.4	187.9	152.1
Vertical contact area (cm^2)	78.0	40.5	58.5

to analyse σ_{OCT}—the arithmetic mean value of the three major stresses. On the other hand, the major stress σ_2 was close to 0 for a significant number of trials. This suggests a two-dimensional stress state.

Moreover, the loading pattern—high values of shearing forces employed in the experiment—suggests consideration of the σ_{OCT}. The third chosen measure is the highest compressive stress σ_1 that is significantly affected by load.

The stress curves for the three vehicles for passes at slipping (the percentage slip was nearly constant and of the same value) reveal differences. The rubber pads caused increases of peak stresses, but the effect of pad types was not significant. Higher values of peak stresses result from stress concentration under higher contact pressure.

For the vehicle with treaded pads, the stress curves are jagged or saw-shaped. This may be the effect of the tread and sharp edges. For the vehicles with flat pads and vehicles without pads, those curves are smooth. These differences are significant but difficult to quantify. Here, the higher value of contact pressure may also play an important role.

5.5.4 Relationships of Drawbar Pull Force and Soil Stresses

Off-road performances of vehicles depend on forces in wheel–soil interactions. Especially on deformable surfaces where the mechanical strength of a surface material is weakened, the performance of a vehicle should be investigated for possible surface effects. The soil reaction to applied external loads is stress state, which is non-homogeneous.

We investigated relationships between measured drawbar pull (main traction measure) and soil stress through further analysis of the experimental data. Table 5.7 shows maximum values of drawbar pull force F_{DBP} as related to corresponding peak stresses, σ_1, σ_{OCT}, and τ_{OCT}, for the three investigated vehicles. The soil stress peak values increase with increased drawbar pull, but we noted a range of decrease of ~50 to 60 kN drawbar pull. This may be caused by intensive soil deflection under increasing loads. This was followed by another increase of an exponential character as a result of soil hardening. We performed approximations to obtain analytical descriptions of the relationships. The resulting polynomial functions are

$$\sigma_1 = a_3 \cdot F_{DBP}^3 + a_2 \cdot F_{DBP}^2 + a_1 \cdot F_{DBP} + a_0 \tag{5.7}$$

$$\sigma_{OCT} = a_3 \cdot F_{DBP}^3 + a_2 \cdot F_{DBP}^2 + a_1 \cdot F_{DBP} + a_0 \tag{5.8}$$

$$\tau_{OCT} = a_3 \cdot F_{DBP}^3 + a_2 \cdot F_{DBP}^2 + a_1 \cdot F_{DBP} + a_0 \tag{5.9}$$

where a_1, a_2, and a_3 are the polynomial coefficients whose values were collected in Table 5.8.

TABLE 5.7

Relationship of Peak Drawbar Pull (F_{DBP}) and Stress State Components (σ_1, σ_{OCT}, and τ_{OCT})

F_{DBP} (N)	σ_1 (kPa)	σ_{OCT} (kPa)	τ_{OCT} (kPa)
No pads			
0	388.1	103.5	252.1
18.5	398.2	113.0	258.9
25.9	405.2	104.5	260.9
38.8	401.8	98.4	249.0
62.4	405.8	101.2	254.6
80.1	420.1	100.9	280.5
81.2	428.6	114.0	285.0
Flat rubber pads			
0	305.6	83.2	179.6
19.3	323.0	93.6	163.0
46.6	242.8	57.4	146.5
49.0	231.2	65.2	118.2
55.3	227.8	71.0	113.4
75.2	285.6	76.9	149.4
76.3	400.1	92.5	257.9
76.7	287.6	82.4	152.4
79.6	180.4	51.4	134.8
84.9	234.6	58.4	138.9
99.4	499.2	127.6	301.5
Treaded rubber pads			
0	512.6	130.6	277.9
21.5	550.9	125.4	330.5
28.0	605.7	130.4	345.0
46.1	625.3	135.0	403.6
54.6	500.1	130.4	302.5
58.8	635.8	154.6	454.7
61.5	544.2	156.2	347.9
88.0	570.6	145.2	325.4
92.0	573.0	147.0	400.6
104.7	725.4	195.8	510.2

The drawbar pull–soil stress relationship shows the most significant changes in octahedral shear stress with increasing drawbar pull that may be explained as the effect of soil shearing or structural damage at high values of lateral forces. The effect of rubber pads on the character of these relationships is clearly visible in Figure 5.14. The relationship is quasi-linear for the vehicle without pads; it is polynomial for the two vehicles with

TABLE 5.8

Polynomial Coefficients for Functions Describing Relationships of Drawbar Pull and Stress Components

Equation	a_0	a_1	a_2	a_3	Correlation
No pads					
(5.7)	339.1	4.846	–0.1108	0.0008	0.72
(5.8)	210.69	4.1866	–0.1122	0.0009	0.68
(5.9)	95.62	1.2797	–0.0413	0.0003	0.45
Flat rubber pads					
(5.7)	299.52	3.3734	–0.1635	0.0015	0.73
(5.8)	89.185	0.6391	–0.0401	0.0004	0.76
(5.9)	160.62	1.2242	–0.0736	0.0007	0.75
Treaded rubber pads					
(5.7)	509.10	7.5498	–0.1904	0.0013	0.81
(5.8)	130.83	0.3386	–0.0098	0.0001	0.84
(5.9)	284.07	6.1596	–0.1392	0.0009	0.81

rubber pads. The stress values for drawbar pull of mid-range decrease; this phenomenon may be related to gradual soil compaction and consolidation in active Rankien zones. The stress increases again only after drawbar pull reaches high values of 60 to 70 kN. This effect is most significant for flat rubber pads.

5.5.5 Discussion

The major advantage of the use of rubber pads is the improvement of vehicle characteristics on public roads by reducing noise and preventing surface damage. Rubber pads are not required in off-road operations and may be undesirable because of the possible decreases in vehicle performance. On the other hand, it is not practical to frequently change an undercarriage. Therefore, the rubber pads must meet several requirements.

The tactical usability of military vehicles should not be limited. Rubber pads must install easily on an undercarriage and should work for a number of vehicle types. The pads should also resist intensive mechanical wear. Our investigations focused on the effects on vehicle traction. The two types of rubber pads installed on track elements increased drawbar pull by 22% and 29% (for flat and treaded pads, respectively) over the conventional undercarriage. This could be explained by the increase of contact pressure. Local contact pressure (under rubber pads) increased by 60% (flat) and 98% (treaded). As is well known, the value of drawbar pull F_{DBP} on sand is a function of contact pressure p:

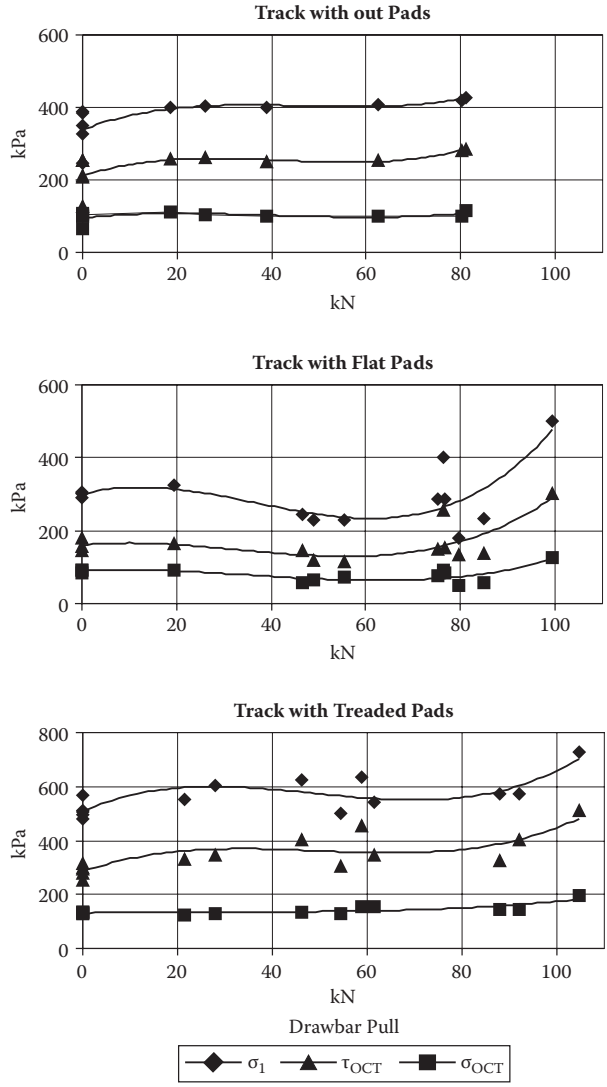

FIGURE 5.14
Soil stress–drawbar pull relationships for the three tested track configurations (flat pads, treaded pads, and no pads on vehicle B).

$$F_{DBP} = Cbl + p \operatorname{tg}\varphi \tag{5.10}$$

where C is cohesion, b and l are the geometrical parameters of a track (wheel), and φ denotes the angle of internal friction of soil. For sand with low water content, we can assume the cohesion to be 0, so only the p tgφ

term in Equation (5.10) describes drawbar pull and the vehicle-dependent parameter is contact pressure. Therefore, it is logical that the rubber pads would exert positive effects on vehicle performance on sand. We must also investigate the effects on other soils.

5.5.6 Conclusions

We observed increases of drawbar pull on sand of about 22% and 29% for the two types of rubber pads. Rubber pads of both types led to significant improvements of vehicle performance on sand. With rubber pads, peak values for soil stress state components increased significantly while the calculated contact pressure was lower. We also saw changes in the character of the drawbar pull–soil stress relationships, especially for flat pads.

5.6 Final Conclusions

Measurements of contact pressures or soil stresses are probably the most important for tracked vehicles, especially fighting tanks and armoured carriers. This is mainly because of the most common mobility models designated NGP and MMP. In this chapter, we show that the SST method of determining soil stress state is practical and sensitive, while the results obtained in the field are logical and comparable with predictions of analytical models.

A general analysis of the soil stress state under tracked vehicle loads reveals similar trends to results for wheeled vehicles. We found pronounced stress concentration under the track's road wheels and significant residual stresses under the track between the wheels. Determination of stress–strain relationship (Section 5.4) is important for research, while the analysis of rubber pads (Section 5.5) provides an immediate practical application.

References

Bailey A.C., Raper R.L., Way T.R. et al. 1996. Soil stresses under a tractor tire at various loads and inflation pressures. *J. Terramech.* 33: 1–11.

Boussinesq J. 1885. Application des potentielles à l'etude de l'equilibre et du movement des solides elastique. Paris: Gauthier-Villars.

Dąbrowski J. 1997. Natural soil as a tractive ground for off-road vehicles. *Tech. Rev. Military* (in Polish).

Dąbrowski J. 2001. Effect of rubber pads on tractive performance of tracked vehicles. PhD dissertation, Military Institute of Automobile and Armaments Technology, Sulejówek.

Fröhlich O.K. 1934. *Druckverteilung im Baugrunde*. Wien: Springer.

Harris H.D. and Bakker D.M. 1994. A soil stress transducer for measuring in situ soil stresses. *Soil Till. Res.* 29: 35–48.

Hetherington J.G. and White J.N. 2002. An investigation of pressure under wheeled vehicles. *J. Terramech.* 39: 85–93.

Hetherington J.G. and Littleton I. 1987. The role of mean maximum pressure in specifying cross-country mobility for armored fighting vehicle design. *J. Terramech.* 24: 263–280.

Horn R., Blackwell P.S., White R. et al. 1989. The effect of speed of wheeling on soil stresses, rut depth, and soil physical properties in an ameliorated transitional red-brown earth. *Soil Till. Res.* 13: 353–364.

Karozewski T. 1978. The influence of speed on soil compaction by the wheels of agricultural machinery. *Zesz. Probl. Posteous Nauk Roln.* 201: 69–74.

Larmine J.C. 1992. Modifications to the mean maximum pressure system. *J. Terramech.* 29: 239–255.

Nichols T.A., Bailey A.C., Johnson C.E. et al. 1987. A stress state transducer for soil. *Trans. ASAE* 30: 1237–-1241.

Pytka J. and Dąbrowski J. 2001. Determination of stress–strain relationship for sandy soil in field experiments. *J. Terramech.* 38: 185–200.

Raper R.L., Bailey A.C., Burt E.C. et al. 1995. The effect of reduced inflation pressure on soil-tire interface stresses and soil strength. *J. Terramech.* 32: 43–51.

Rowland D. 1989. Tracked vehicle ground pressure and its effect on soft ground performance. *Proc. 4th Intl. ISTVS Conference,* pp. 353–384.

Shoop S.A., Affleck R., Collins C. et al. 2005. Maneuver analysis methodology to predict vehicle impacts on training lands. *J. Terramech.* 42: 281–303.

Way T.R., Johnson C.E., Bailey A.C. et al. 1996. Soil stress state orientation beneath a tire at various loads and inflation pressures. *J. Terramech.* 33: 185–194.

Wiermann C., Werner D., Horn R. et al. 2000. Stress–strain processes in a structured unsaturated silty loam Luvisol under different tillage treatments in Germany. *Soil Till. Res*. 53: 117–128.

Wong J.Y. 1984. An improved method for predicting tracked vehicle performance. *J. Terramech.* 21: 35–43.

Wong J.Y. 1989. *Terramechanics and Off-Road Vehicles.* Amsterdam: Elsevier.

6

Wheel–Soil Dynamics for Aircraft Tyres on Unsurfaced Airfields

6.1 Introduction

6.1.1 Airfields and Airstrips

Multipurpose aeroplanes—utilised for transport, search and rescue (SAR), agricultural, or sport purposes—occasionally operate on grass fields that often offer insufficient traction. Bearing capacity and surface friction significantly affect ground handling performance during take-offs and landings and are critical to the safety of flight operations.

Early airfields were not paved. The first aeroplanes had skids instead of wheels and a grassy surface was the only place to take-off or land without causing substantial damage to an undercarriage. The next generation aircraft were equipped with narrow, massive rubber tyres that gave directional stability during rollout but were impractical on soft surfaces. The low-pressure balloon-type tyres now in use are much better for grassy airfields. The biggest aircraft tyres, called "tundra tyres," can have diameters greater than 1 m and are used for flying into the wild where no airports or airfields exist.

The earliest grassy airfields had large rounded areas that enabled pilots to always land into the wind. This practical advantage over fixed-direction runways helped some rounded airfields survive to this day in many parts of the world. Of Poland's 130 airports, 44 are grassy airfields, similar to those from the Golden Age of aviation. They are mainly used by clubs that fly sailplanes or small aircraft. Grass airfields are also very popular in western Europe. In Great Britain, for instance, it is difficult to count the number of grassy airfields or airstrips because many are privately owned. In France, private aviation and tourism benefit from a wide web of grass fields that allow private pilots and their passengers to reach attractive spots on the French Riviera or in the Alps.

The Light Aviation Airports Study Group (LAASG) was formed in the United Kingdom in 2005 as a direct initiative of the Civil Aviation

Authority (CAA)–Industry Joint Review Team (JRT). Its creation was influenced by requests from the general aviation sector for a review of light aviation aerodromes and airfields. According to the LAASG, aerodromes where certain types of flight training and no public transport operations take place must obtain aerodrome licenses. One important issue of licensing is that an aerodrome must maintain its surface throughout the flying season.

Well-conditioned grassy airfields provide obvious benefits. Touchdown and landing rollout are much smoother than on paved runways, and tyre wear is substantially less. Of greatest importance is their availability to serve as valuable emergency landing sites for any pilot experiencing trouble en route.

One major problem with grass airfields is their sensitivity to weather conditions that can affect bearing capacity and traction. After a heavy rainfall, the surface of a grass airfield becomes too soft to accommodate stresses generated by aircraft wheel loads. Even a little rain on a summer day can affect wheel–grass friction significantly. Logically, the dryer the grass surface, the better for aircraft operations, but too little soil moisture harms the vegetation and can lead to a dirt field with no grass. This is a typical situation on many Polish airfields during the hot, dry days of summer.

According to the CAA, about one-third of general aviation accidents in the United Kingdom occur at unlicensed grass airfields during ground operations (take-offs and landings). Although those accidents are believed to mainly result from inexperience or a lack of familiarity with "grass roots flying," all operations on grass fields could be enhanced with knowledge of the effects of wheel–soil dynamics on these fields.

6.1.2 Bearing Capacities of Unsurfaced Airfields

The quality of an airfield's surface differs over time as a result of atmospheric effects and external loads imposed by aeroplane landings and take-offs. Knowledge of the bearing capacity of a surface is important, as it allows us to predict the total contact pressure that can be applied to a surface without damaging it (Shoop et al. 2008)). Bearing capacity depends on the soil type and structure and is pronouncedly greater for grassed surfaces because the root systems increase soil strength. Landing techniques also affect the soft surfaces of an airfield. Short takeoff and landing distances are often critical for aircraft operating from informal, unsurfaced airfields. Touchdown at a high vertical speed causes great pressure on a soil surface; on a soft field it may result in nose-down moments on the aircraft that are especially dangerous for tail-wheel types of undercarriage.

To ensure economical and safe operation, classification systems of airfield bearing capacities are needed. The International Civil Aviation Organization (ICAO) introduced the load classification number (LCN) system in 1950. LCN values were determined for airfields and for aeroplanes and then the values were compared. The LCN value for an airfield was experimentally determined in special fatigue tests. The LCN values for aeroplanes were determined from nomograms provided by manufacturers. This insufficient and inaccurate system was replaced by the ACN-PCN system between 1980 and 1983.

This system uses two values: aircraft classification number (ACN) and pavement classification number (PCN). The ACN value is based on aeroplane mass, centre of gravity location, wheelbase, and tyre inflation pressure (Czarnecki 1987). Various experimental methods can be used to determine PCNs. Generally, rigid and flexible surfaces are considered. For flexible surfaces, a value of bearing capacity designated the California bearing ratio (CBR) is analysed. This measure depends on the mechanical characterisation of homogeneous soil.

Four categories of flexible surfaces were introduced—high, medium, low, and very low—with CBR values of 15, 10, 6, and 3, respectively (Shoop et al. 2008). These classification systems are very approximate. Even the significantly better ACN-PCN system represents only an approximation of real conditions.

In the models and methods described in previous chapters, tyre loading on a soil surface is expressed using the Boussinesq problem. It is significant that, for flexible surfaces, stresses are accommodated in a very small volume, leading to pronounced stress concentration. This leads to a sudden and irreversible deformation of the surface. Therefore, the Boussinesq technique may be insufficient for some cases of dynamic forced landings and for airstrips with hardened surfaces, as the stress concentration factor may vary widely over the short duration of a touchdown.

6.1.3 Traction and Rolling Resistance on Unsurfaced Airfields

Another important concern is traction. Coefficients of rolling and braking friction affect field performance during take-offs and landings. For different surfaces, these coefficients vary through a wide range of values; moreover, on a given surface, tractive performance of a wheel may also vary significantly with meteorological conditions. While the rolling resistance coefficient for a hard, paved surface is about 0.02, the value is 0.05 for short dry grass and 0.13 for long wet grass (Raymer 1989). Similarly, for turf, sand, and clay surfaces, rolling friction is 25% to 30% greater than on a paved surface and even more if the surface is wet. Traction and rolling resistance are important because increased rolling resistance can lengthen the time and distance required for an aircraft to reach take-off velocity.

6.1.4 Performance of Wheels on Grassy Airfields

As noted earlier, about 40% of Poland's airports have unsurfaced runways. Most are club airfields used for sport flying and flight training; the fields are still used extensively and many small and medium aircraft operate from them. No standards exist for classifying the quality of these airfields with respect to the wheel–soil relations and the resulting flight conditions. Operations on these airfields may be performed outside of safety margins, resulting in accidents. Some examples of accidents and causes are shown in the table.

Aircraft	Description of Accident
PA 46 Piper Malibu	Fatal crash on take-off; high rolling resistance of turf surface airfield plus high altitude
PZL 101 Gawron	Rollover on landing; wet surface and high deformation
PZL 104 Wilga	Crash on landing in deep snow
PZL 104 Wilga	Fatal crash on take-off; insufficient airfield length plus high rolling resistance

As cited in the previous subsections, two major factors affect aircraft taking off and landing on unsurfaced airfields: (1) high rolling resistance on take-off, causing a too-long ground roll; and (2) high deformability of the airfield surface at touchdown, causing nose-down moments. Considering the extensive use of unsurfaced airfields, research in this field is vital (Stinton 1998).

A wheel–soil interaction is usually described with terramechanics; additional rolling resistance of a wheel on a soft surface is determined as a function of surface deformation. However, classic terramechanical considerations are valid only for relatively low speeds, (up to ~40 to 50 km/h). Some researchers suggest that the effects of higher speeds during take-offs and landings must be taken into account (van Es 1999, Gibbesch 2003, Shoop et al. 1999), but a complete solution to this problem remains to be found.

Our goals for this chapter are to

1. Determine whether the soil stress state method can be used as a measuring tool for aeroplane landings on unsurfaced airfields by determining the soil stress state and soil deformation under a wheel of a landing aircraft as well as loading force values and orientation at touchdown.
2. Design and perform an airfield experiment that provides sufficient data to identify rolling resistance of aircraft wheels on unsurfaced airfields under various conditions.

3. Calculate ground roll for an aeroplane operating on an unsurfaced airfield to illustrate how the wheel–soil interactions affect its ground performance.

As a final result of this research, we propose a test method project for evaluation of grassy, unsurfaced airfields.

6.2 Soil Stress State under Loading of Landing Aircraft

6.2.1 Analysis of Landing on Airfield

A normal landing can be divided into three phases (Lowry 1999):

- Touchdown
- Acceleration of wheel rotation with slip
- Deceleration of the entire aircraft until stop

The undercarriage wheels are motionless before touchdown and begin to rotate because of frictional force between tyre tread and surface. This frictional force is dependent upon wheel load F_Q that equals the difference between lift and weight. During the ground run, vertical vibrations occur as a result of energy dissipation—the kinetic energy of vertical motion is partially dissipated by shock absorbers and surface deflection, but a portion of the elastic energy is given back to the aeroplane. Then, a quasi-stable decelerating motion begins. Deceleration is caused by aerodynamic drag and rolling friction forces, but the wheel–soil interactions at touchdown also affect ground-roll distance (Currey 1988).

A critical moment of a landing is the touchdown when temporary contact forces act between the surface and the wheel. Both the surface and the wheel deform significantly. A great amount of an aircraft's kinetic energy is dissipated into the energies of soil deformation, shock absorption, and tyre deflection (Prithard 2001). The remaining kinetic energy of the aircraft will be consumed by rolling friction force and aerodynamic drag during ground roll (Raymer 1989). The most important forces acting on aircraft wheels during a touchdown (Figure 6.1) are total load force F_Q that results from aerodynamic lift forces, aircraft weight Q, inertial forces during duration of the touchdown, and soil reaction R.

The total load force F_Q acts along the total contact area between the tyre and soil surface. This force is distributed along the total contact area S and can be determined as an integral:

$$F_Q = \int F_Q^{\alpha}\, d\alpha + \int F_Q^{\beta}\, d\beta \tag{6.1}$$

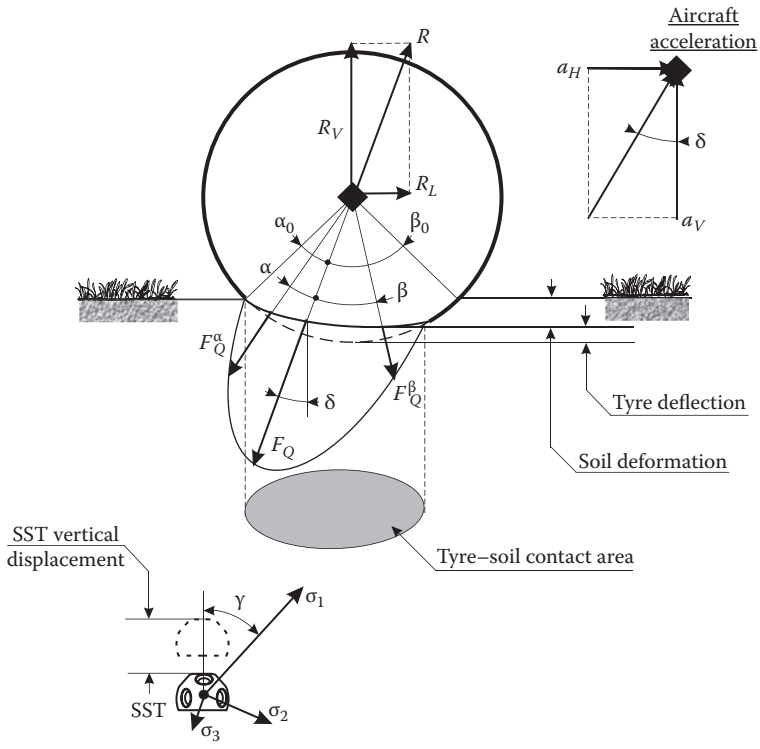

FIGURE 6.1
A schematic of wheel–surface interaction.

The load force distribution is a function of (1) tyre deflection, (2) contact area surface, and (3) soil mechanical strength. The load components are functions of α and β, angles of wheel–surface interaction area:

$$F_Q^\alpha = F_Q \left(\frac{1}{\sin(\alpha)} + \cos(\alpha) \right) \tag{6.2}$$

$$F_Q^\beta = F_Q \left(\frac{1}{\sin(\beta)} + \cos(\beta) \right) \tag{6.3}$$

Aerodynamic forces—lift, drag, and propeller thrust—are functions of air speed of the aircraft. The lift force acts vertically and equals the aircraft's weight at lift-off. This force reduces the vertical load on the undercarriage wheels. These three forces change their values during landing and take-off. Lift decreases as an effect of deceleration. In effect, vertical loads on

the landing surface increase and reach a maximum of Q at $V = 0$. At the moment of touchdown, the aircraft weight is balanced by lift force, so the wheel loads are mainly the temporary inertial forces:

$$F_{AV} = Q\frac{a_V}{g} \tag{6.4}$$

$$F_{AV} = Q\frac{a_V}{g} \tag{6.5}$$

Soil reaction is important as a basic input parameter in the load stress analysis of an aircraft's undercarriage. Forces acting on a soft surface cause deflections; therefore, the vertical loading force is lower. At the moment of touchdown, soil reaction has both vertical and longitudinal components. In a short period after a touchdown, the aerodynamic forces are constant as the velocity does not change significantly. Thus the vertical reaction on an aircraft wheel can be expressed as

$$R_V = b\int \sigma \sin(\phi) d\phi \tag{6.6}$$

and the longitudinal reaction as

$$R_L = b\int \sigma r \sin(\phi) d\phi \tag{6.7}$$

where σ equals stress on a tyre–soil contact surface and b represents tyre width.

6.2.2 Soil Stress State and Soil Deflection under Wheels at Touchdown

6.2.2.1 Soil Stress Measurements

Stress state was determined with an SST similar to the one described in Chapter 2 with the addition of a built-in accelerometer (Figure 6.2). The method is explained in the next section. As noted in Chapter 2, the SST consists of six transducers that measure soil pressures needed for the determination of stress state components: σ_1—major principal stress; σ_2 and σ_3—minor principal stresses; and σ_{OCT} and τ_{OCT}—normal and shear stress invariants in the octahedral stress system. The SST was installed at 15-cm depth by simple excavation of the soil. After the SST was in place, the soil was backfilled and the grass replaced on the surface. The soil over

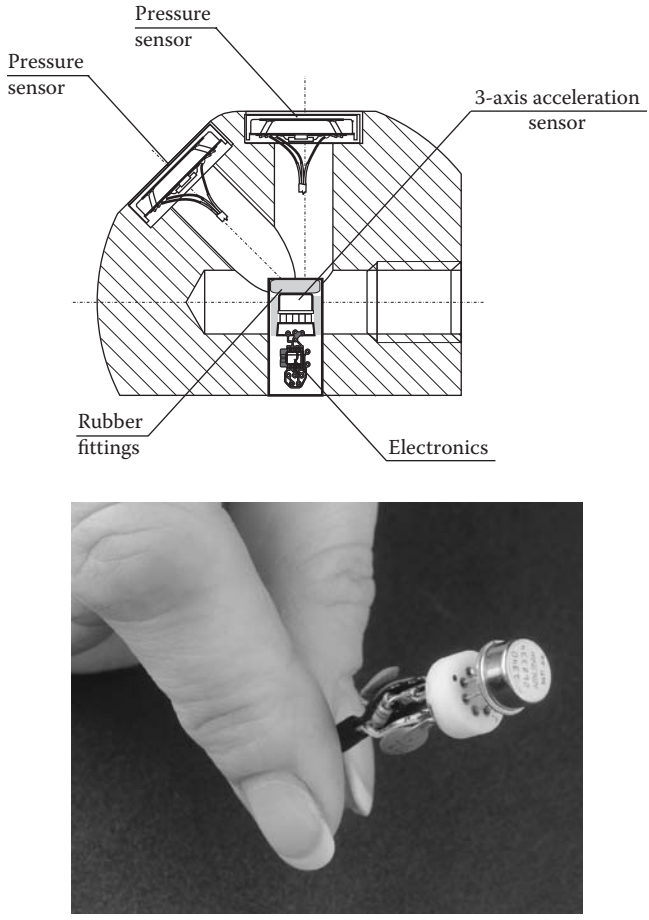

FIGURE 6.2
Details of the SST and accelerometer used in the aircraft landing experiment.

the SST was compacted to obtain the initial bulk density. The transducer remained in place for all landing tests (Pytka et al. 2004).

6.2.2.2 Soil Deflection Measurements

Soil deflection was determined indirectly, using the vertical movement of the SST. The accelerometer installed in the SST measured the vertical acceleration of the SST. The microelectronic–micromechanical (MEMS) accelerometer range was 0 to ±2.5 g. Vertical velocity and vertical movements of the SST were calculated by double integration of the measured acceleration values versus time. Vertical movement of the SST was used

to determine soil deformations. Because of the high level of compaction of the soil in the region of the SST after several preliminary tests, the soil material became quasi-elastic and at each touchdown a typical loading–loosening response with hysteresis occurred. Therefore, we defined the deflection of soil layer as the difference between the initial position (before landing) and the final placement of the SST along the vertical axis.

6.2.2.3 Aeroplane Used in Experiment

A four-passenger, single-engine, multipurpose Wilga aeroplane (Figure 6.3) was used. It is a high-wing unit with a conventional tail and non-retractable, tail-dragger landing gear. The main legs are rocker type with oleo-pneumatic shock absorbers. The main wheels have low-pressure 500 × 200-mm tyres with hydraulic brakes. The wheels are castered and have a positive rake angle of 18°; the axle offset is 400 mm.

The aeroplane is 8.10 m in overall length, with a wingspan of 11.12 m, a wing area of 15.5 m^2, and an empty mass (equipped) of 900 kg. In the landing tests, four persons were on board and the take-off weight was 1150 kg.

A three-axis (X-Y-Z) accelerometer was installed at the centre of gravity in the aeroplane (Figure 6.4) to collect aircraft acceleration data during landing tests. The accelerometer block was mounted to be parallel to the runway when the aeroplane was in tail-down (landing) position. The acceleration data were used to determine wheel loads and angles of loads eigenvectors.

FIGURE 6.3
The Wilga aeroplane used for the tests.

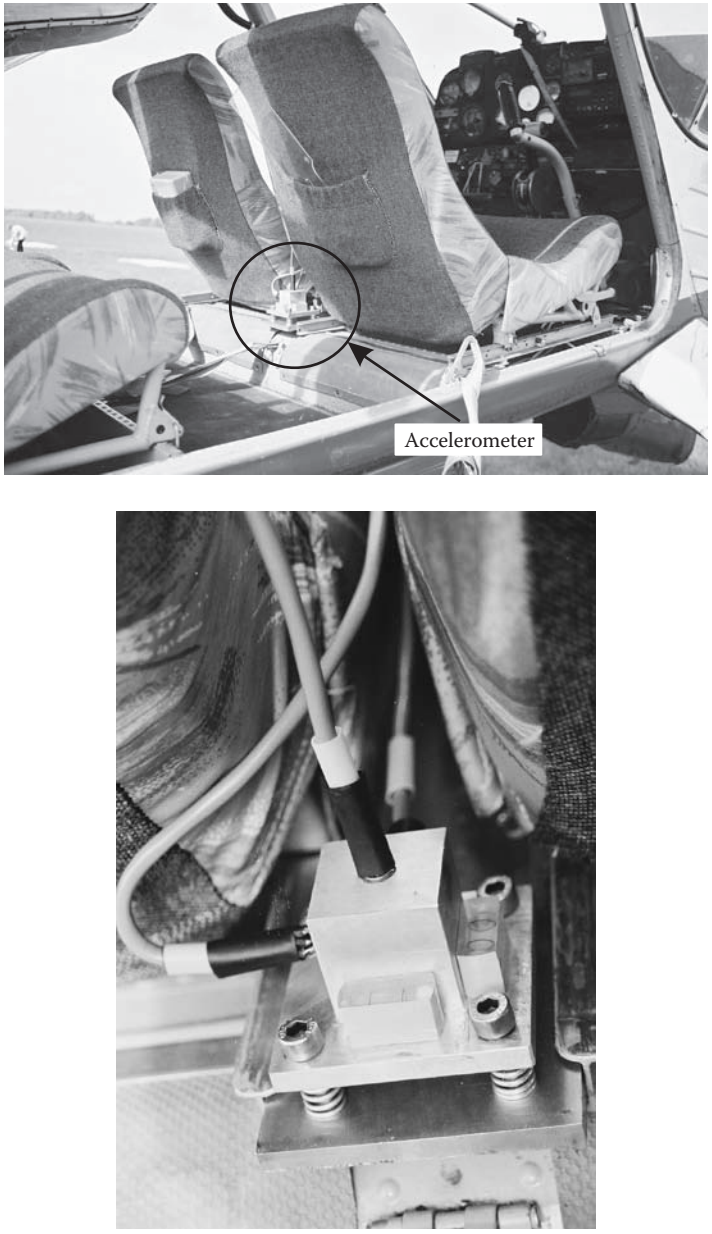

FIGURE 6.4
Installation of the three-axis accelerometer in the Wilga aircraft.

6.2.2.4 Experimental Procedures

Numerous trials were needed to ensure that the results were repeatable. The tests were conducted during a training of contest pilots for the Polish national precision flying championships. Four champion sport pilots took part in the experiment. Each pilot performed conventional approaches and landings (5% gradient of glide slope, 2.5 m/s descent rate, approach speed 100 km/h, power setting 25 to 30%) and emergency zero thrust landings on idle power from an altitude of 300 m above the airstrip. More than a hundred landings were performed and 32 successfully touched ground with the left wheel of the aircraft at the point above the SST. Not all the landings provided satisfactory soil pressure data.

6.2.3 Results

6.2.3.1 Soil Stress State

Soil stress state components—σ_1, σ_2, and σ_3 as well as σ_{OCT} *and* τ_{OCT}—were calculated from the soil pressure data obtained by the SST. For further analysis, we used only tests that exhibited significant values of stress. These results are collected in Table 6.1. To recognize whether a wheel touched the surface exactly over the SST, we analysed the relations of peak values of major stress σ_1 and the acceleration according to the accelerometer. If the peak aircraft acceleration (wheel load) appeared first, it meant that the wheel touched the surface in the sensitive area of the accelerometer before the SST. The area of sensitivity for the SST stress sensors is smaller, so if both peak σ_1 and acceleration appeared simultaneously, the point of touching the surface by the wheel could be estimated more precisely.

Figure 6.5 shows graphs for (a) a zero thrust emergency landing; (b) a conventional landing in which the wheel hit the surface exactly in the centre of the sensitivity area above the SST; and (c) a landing in which the wheel touched the surface before the sensitivity area—the SST was rolled over by the landing aircraft.

The σ_1 is the dominant stress component for all tests. For zero thrust landings, a quasi-two-dimensional stress state ($\sigma_2 = 0$) is present. For normal landings and landings during which the aircraft rolled over the SST, the stress state is three-dimensional. Minor stresses reach 15% to 30% of maximum σ_1 values. Octahedral shear stress is always greater than the mean normal stress.

6.2.3.2 Soil Deflection

The deflection of the soil layer occurs when stress overcomes the soil's strength limit. Because the soil became highly compacted during preliminary tests (the SST was installed once and used for all the landing trials),

TABLE 6.1

Soil Stress State Data for Conventional Landings, Emergency Zero-Thrust Landings, and Rolling over SST

		Stress State Components (kPa)				
Landing Pattern	**Number of Tests**	σ_1	σ_2	σ_3	σ_{OCT}	τ_{OCT}
Zero thrust	48	416.9	283.0*	–347.0*	117.6*	333.1*
	110	375.9	0.3958	–248.2	42.71	256.5
	207	382.0	–0.7585	–253.4	42.63	261.2
	Avg/Std Dev	391.6/18.06	–0.577/0.18	–250.08/2.6	42.67/0.04	258.85/2.35
Conventional	121	526.1	94.62	–219.7	133.7	305.7
	203	506.4	29.66	–4.847	177.1	233.3
	Avg/Std Dev	516.25/9.85	62.14/32.48	–	155.4/21.7	269.5/36.2
Rolling over SST	111	155.5	–0.2112	–42.27	37.67	85.06
	119	165.4	–13.10	–50.09	34.05	94.06
	202	121.0	0.5102	–40.86	26.87	68.64
	Avg/Std Dev	147.3/19.03	–4.26/6.25	–44.38/4.03	32.86/4.48	82.58/10.52

* Over-registered values that were ignored.

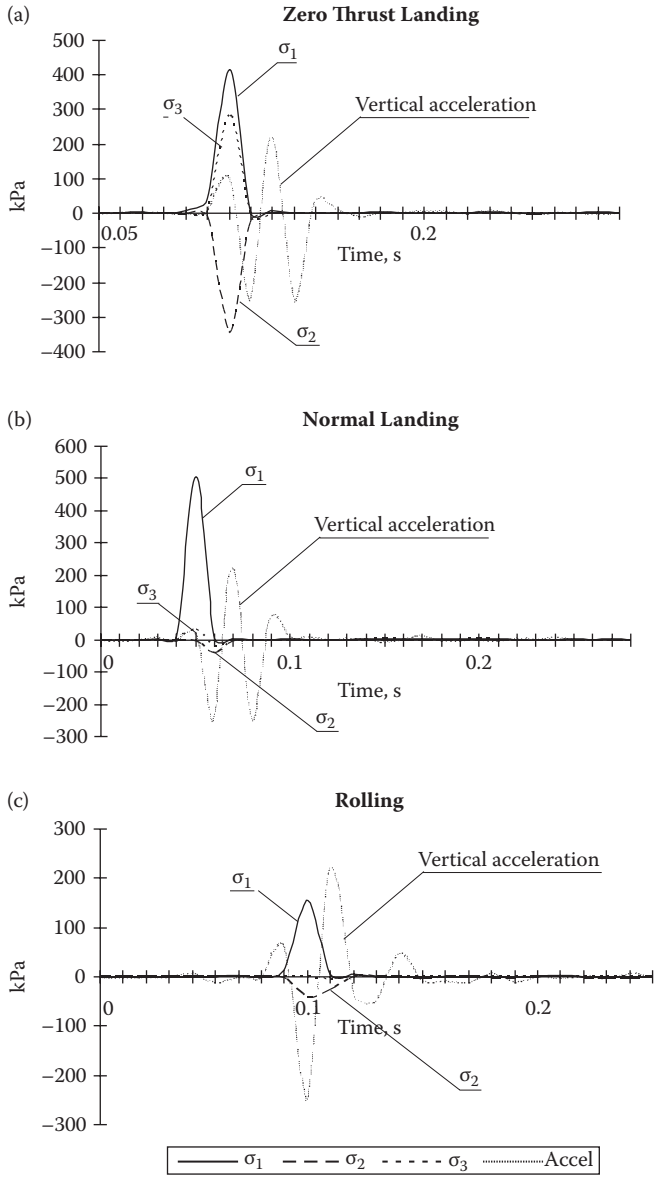

FIGURE 6.5
Stress state components and acceleration. Sample curves for (a) zero-thrust landing, (b) normal landing, (c) rolling over the SST.

TABLE 6.2

Soil Surface Deflection (Average Value/Standard Deviation)

Surface Deflection (mm)		
Zero-Thrust Landing	**Normal Landing**	**Rolling over SST**
–2.777/—	–2.56/0.16	–2.26/0.33

it demonstrated quasi-elastic behaviour. At the moment of touchdown, there was maximum SST displacement, then the soil relaxed and the final deformation was smaller. The difference between these two vertical positions of the SST is called soil deflection. This measure reveals the total amount of vertical deformation (compaction) of the soil at the 15-cm (SST installation) depth after a single landing (Table 6.2).

Multiple landings had no effect on soil deflection after the first several tests. The soil deflection changed for the two landing patterns—normal and zero-thrust—but the changes were not significant. This could be a result of high soil compaction after a number of landings. On the other hand, soil deflection was pronouncedly smaller when the aircraft rolled over the SST after landing.

6.2.3.3 Effect of Landing Pattern

The measured values of the stress state components are significantly higher for normal than for zero-thrust landings; the difference is more than 20% for σ_1. The time during which the stresses are active is longer for zero-thrust landings (0.03 versus 0.02 seconds). In normal landings, the propeller thrust force is a significant component influencing ground reaction and thus the soil stress state components. On final approach, the power setting was about 20% to 30%; at ~1 second before touchdown (flare), the engine was set to idle, causing a sudden sinking such that the aircraft hit the surface with high vertical speed.

The zero-thrust landings were softer as the pilot has no possibility of engine control and the forces acting on the aircraft are stable (only when the landing is technically correct, however). At constant idle, a pilot must use the greatest glide ratio of the aircraft; the flight profile is gentle and the wheels touch the surface softly. The specific landing technique used by the competition pilots in this study also affected the soil stress state in this experiment; the discussion section (6.2.4) examines that factor.

Rolling over the SST with high longitudinal (or landing) velocity generates a soil stress state in which components are significantly smaller (0.3 times) than for a touchdown. The effects of impact and the gravity force are partially balanced by aerodynamic lift force, so the contact pressure and soil stress are smaller.

6.2.3.4 Orientation of Inertial Force and σ_1

The acceleration data of the entire aircraft at the moment of touchdown made it possible to determine both inertial force and orientation. Vertical, longitudinal, and horizontal (i.e. transversal) acceleration data are presented in Table 6.3. Both vertical and horizontal accelerations are significantly greater for normal landings than for zero thrust and this trend corresponds to the σ_1 peak values. The orientation of the acceleration–inertial force vector, however, was not affected by landing method.

The SST measuring method allows determination of both soil stress state components and their direction cosines (Way et al. 1996). The orientation of the stress state components, especially the major stress σ_1, is valuable information, as the character of the loading suggests that the σ_1 is not vertical at the location where it peaked. In such a case, minor stress components are of great importance and the stress state is three- or two-dimensional. Those data can be related to the orientation of the inertial force that is the major generator of stresses in soil.

The results for δ (angle of σ_1 tilt) and γ (angle of inertial force tilt) were obtained for the two types of landings and for the aircraft rolling over the SST after landing (Table 6.4). The vectors are shown in Figure 6.6. The type of landing has a significant effect on the σ_1 orientation: for a maximum value of σ_1, the stress vector is pronouncedly more tilted for normal landings. The σ_1 tilt angle is much smaller for rolling over the SST. In any case, the relatively high values of δ for both landing types suggest that the other stress state components should be analysed as significant. Peak

TABLE 6.3

Vertical a_v, Longitudinal a_l, and Horizontal a_h Accelerations at Moment of Touchdown

	Acceleration ×g (m/s^2)		
Landing Pattern	a_v	a_l	a_h
Zero thrust	1.72/0.37	–0.98/0.18	—
Normal	2.44/0.80	–1.50/0.40	0.20/0.02

TABLE 6.4

Orientation of σ_1 Major Stress, δ, and Orientation of Wheel Load Force γ at Moment of Touchdown for Two Landing Patterns and Wheeling over SST (Average Value/Standard Deviation)

	Angles (degrees)		
Landing Pattern	**Zero Thrust**	**Normal**	**Rolling**
γ	29° 40′	31° 35′	~0°
δ	48° 55′/2° 33′	54° 50′/3° 86′	31° 00′/1° 56′

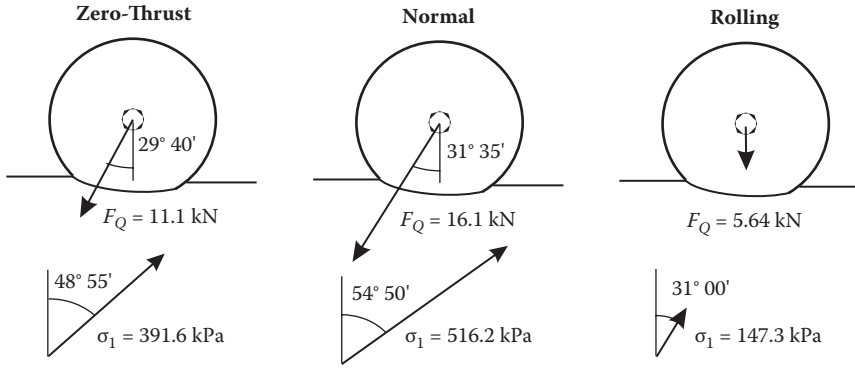

FIGURE 6.6
Orientation of the σ_1 major stress and load force. The vectors are plotted to the scale.

minor principal stresses σ_2 and σ_3 range from almost 0 (σ_2 for zero thrust landings) to –250 kPa (σ_3 for zero thrust landings) and 62 kPa (σ_2 for normal landings). However, we observed no significant trend in σ_2 and σ_3 peaks for the different types of landings.

Apparently, the σ_1 is more tilted than FQ for the both landing types. This may be caused by the kinematics of the undercarriage: the main wheels are castered and supported by an oleo shock absorber, so that vertical movements of the wheels are exaggerated.

6.2.4 Discussion

High inertial forces and elasto-plastic deformations of the surface that are sudden and irreversible must be considered in the analysis of soil–wheel interactions during the unsteady motion of an aircraft. Thus, classic terramechanical methods and traction theory are insufficient. In phenomenological wheel–soil models for high speeds, additional components are needed to express the dynamic behaviours of deformable wheels and surfaces.

Crenshaw (1972) investigated soil reaction forces on a wheel. The values and orientation of total soil reaction are dependent upon vehicle speed and the total contact area. If we recognize that the soil particles under a wheel may also reach high speed and acceleration, an additional component must be considered: soil lift. Hovland (1973) developed a theory to determine which inertial forces of moving (i.e. deforming) soil influence the motion of a wheel. Based on the theory, the soil lift force is predictable. As an example, Hovland presented a theoretical relationship between soil lift force and velocity for a Cessna 150 light aeroplane landing on a soft playa or marsh. It is possible to predict the velocity at which the wheels for the aeroplane landing on such a surface will sink severely and become immobilized.

Stress state analysis for wheel–soil interaction relates wheel loads to dynamic soil response. The conventional models for stress distribution are based on Boussinesq theory, in which normal stress within isotropic and elastic materials is proportional to a force applied to the surface. The most significant problems faced were: (1) soil plasticity and anisotropy and (2) methodological problems with measuring soil stress. Further modifications of the Boussinesq technique add the stress concentration factor that describes stress propagation in a soil volume.

As soil is a non-homogeneous, non-isotropic, visco-elasto-plastic material, the concentration factor accounts for the influence of those characteristics on stress propagation. Several wheel–soil models have been constructed based upon this theory. These critical state theory models differ from Coulomb theory-based models, in which normal and tangential stresses on a contact surface are correlated.

SSTs were designed based upon the elasticity theory. Although the theory has limits for surface materials, especially for soil, it is not erroneous to apply the theory of elasticity to the surface of a grass airfield compacted by repeated high loads.

The stress–strain analysis method seems to be more adequate than critical state theory in cases of unsteady motion. By integrating the stresses on a soil volume randomized by the range of stress propagation, it is possible to determine forces with higher precision. The subject has not yet been investigated sufficiently, but it is promising for further research.

There are also other limitations. First, the assumption of the elasticity theory must be validated. Stress state data obtained for soft and loose soil, fresh snow, and till should be analysed with care. It is insufficient to relate the stress values to deformations without the analysis of nonlinearity. Pukos (1983) investigated stress–strain relationships for sandy and loamy soil for various deformation velocities; a non-linear parametric model gave promising results when compared with the experiments. Other promising methods are stochastic and probabilistic models (Pukos 1983).

The repeatability of the experimental results and the methodology of stress measurements are at issue. The probability of a landing with a touchdown exactly over the SST was below 10% in our experiment. More than a hundred trials were needed to obtain results of scientific value. Moreover, the reliability of the obtained results is below 90%, as we were not completely sure where the wheel hit the surface (a sophisticated photo or video technique would be helpful). It would be reasonable to use a 2×2 or 3×3 matrix of SSTs in a future test.

Another factor is the landing technique. To obtain the highest probability of success, champion pilots were engaged for the experiment. They used a special competition technique in which the precision of the landing is vital. In such landings, abrupt manoeuvres on approach and intensive thrust control lead to semi-forced landings that are not symmetrical.

This landing technique is not a handbook standard and it would be interesting to see how different standard landings would be.

6.2.5 Summary

A literature-based review of methods for estimating the quality of unsurfaced airfields and an analysis of wheel–surface interactions show the need for new methods of studying the unsteady motions of a landing aeroplane. We analysed forces on a wheel of a landing aeroplane at touchdown and conducted a preliminary experiment on soil stress and surface deflection under loading from a landing aeroplane wheel. Soil stress state components were determined with an SST, and surface deflection was measured with an inertial method.

We observed that soil stress and surface deflection were 20% greater for normal than for zero thrust landings. A method based on soil stress–strain appears convenient, but it would be more practical to construct a test rig with a falling wheel to represent the full-scale conditions rather than capturing soil stresses under landing aeroplanes.

6.3 Rolling Resistance Coefficients for Aircraft Tyres on Unsurfaced Airfields

This section examines different methods of determining the rolling resistance coefficients, looks at how they might be useful for aircraft rolling resistance, and then presents results for each method.

6.3.1 Rolling Resistance of Wheel on Deformable Surface

When a wheel rolls over a hard (non-deformable) surface, the components of rolling resistance F_{RR} present are: (1) bearing friction, (2) inertia forces in cases of unsteady motion (acceleration), and (3) rolling resistance caused by local deformation of tyres and wheel slip.

Rolling resistance is expressed as e and indicates a shift of the vertical force acting point caused by the above factors; it is described by a resulting resistance moment M_{RR} against the driving moment on a wheel (see Figure 6.7):

$$M_{RR} = eF_{RR} \tag{6.8}$$

This consideration, although very close to real conditions, is difficult to use for calculations. Therefore, a proportionality coefficient k was introduced and, thus, we obtain

$$F_{RR} = k\,Q \tag{6.9}$$

where Q is the vertical load of the wheel.

In a number of technical papers and books, the rolling resistance coefficient is introduced as the rolling friction coefficient μ. In fact, this is not true, since rolling friction cannot be identified with rolling resistance. We can speak of rolling friction during braking or driving, when a horizontal force is generated on a tyre surface contact patch and this force is physically similar to friction. During rolling, friction exists in wheel suspension (bearings). On the other hand, the major components of rolling resistance are tyre and surface deformations, and therefore we use the rolling resistance coefficient k_{RR} that represents all components of rolling drag. When the wheel brakes are applied during ground roll, the value of the rolling resistance coefficient increases.

The value of the rolling resistance coefficient is dependent upon speed of motion, and this dependency is described (Mitschke and Wallentowitz 2004) as

$$k_{RR} = k_{R0} + k_{R1}\frac{V}{100} + k_{R4}\left(\frac{V}{100}\right)^4 \tag{6.10}$$

where k_{R0}, k_{R1}, and k_{R4} denote coefficients determined experimentally. The k_{R0} coefficient describes rolling resistance of a tyre at speeds near 0. The k_{R1} and k_{R4} represent an increase of rolling resistance of a tyre at higher

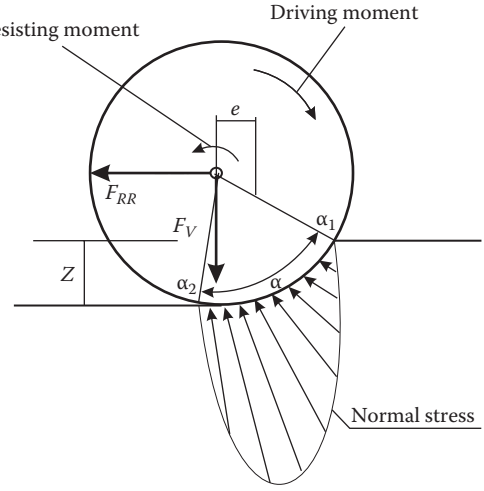

FIGURE 6.7
Forces and moments acting on an aircraft wheel during rolling.

speeds—up to and above 100 km/h, respectively. This approach, however, is applicable only for automotive tyres on hard surfaces. The rolling resistance coefficient of a wheel on a hard surface can be determined experimentally by measuring the rolling resistance in a "coast-down" or tow test.

A typical soft surface (grass, soil, or snow) differs due to an additional resistance component resulting from surface deformation in general. For low speeds, this component can be determined based on Bekker's model (1969), but a more precise solution for high speeds requires other methods. Generally, rolling resistance $F_{RR}{}^{S}$ of a wheel on a soft surface at high speeds consists of three components (Shoop et al. 1999):

$$F_{RR}^{S} = F_{RR}^{H} + F_{LS}^{S} + F_{HS}^{S} \tag{6.11}$$

where $F_{RR}{}^{H}$ is the rolling resistance on hard surface, $F_{LS}{}^{S}$ indicates resistance due to deformation of soil (or other soft surface) at low speed, and $F_{HS}{}^{S}$ equals resistance at higher speeds and consists of the drag of a wheel through the soil and the drag caused by a spray of loose soil (or snow) against the aircraft and landing gear. Some analytical methods for determining these components are included in the cited literature (van Es 1999, Shoop et al. 1999).

Rolling resistance attributable to surface deformation at low speed can be determined in tow tests or by the use of specifically instrumented vehicles. Similarly, resistance at high speed can be determined experimentally. Experimental data document high-speed rolling resistance on contaminated airfields; however, there are no data for rolling resistance on unpaved, grassy airfield under various conditions. Most of the data presented in the literature were determined by measurements with single wheels or ground vehicles. A goal of this study was to apply new and known methods for measuring of rolling resistance components for aircraft tyres on an unsurfaced airfield.

6.3.2 Rolling Resistance Measurements: Review of Test Methods

6.3.2.1 Flight Test Method

This method can identify rolling resistance coefficients at a full range of speeds during a take-off run. An instrumented aircraft was flown on an unsurfaced airfield to gather experimental data needed for further calculations of rolling resistance. The Wilga aircraft used for the flight tests was weighed before the tests, and the results used for k_{RR} calculations (Figure 6.8). During all the tests, four occupants (one pilot, two test engineers, and one observer) were on board. (These are the same flight tests described for the landing stress measurements in Sections 6.2.2.3 and 6.2.2.4, but here we are interested in the ground speed measurements.)

FIGURE 6.8
Weighing the Wilga aircraft before determining the rolling resistance.

The intent was to determine aircraft ground speeds during take-off runs. For this purpose, special instrumentation was needed because the on-board instruments do not capture ground speed. The instrumentation consisted of (1) an optical sensor for ground speed measurements; (2) a multi-channel differential global positioning system (DGPS) for acquiring and measuring several kinematic factors (velocities, accelerations, etc.); and (3) a non-contact optical sensor.

This type of optical sensor is widely used for ground vehicle speed measurements. Its range of measurement (0 to 250 km/h) and resolution (0.1 km/h) made it suitable for our tests. The optical sensor was mounted outside the cockpit on an external rake, as shown in Figure 6.9. For accuracy and the best sensor function, the sensor must be placed 400 mm above the ground. For measurements on an aircraft in which the height of the centre of gravity changes during a take-off roll, it was practical to use a special version of the sensor, with a tolerance of mounting height of ±130 mm. Electronics, power supply, and a data recorder were installed in the cockpit. The DGPS was also installed in the cockpit and connected to a PC notebook. The two test engineers ran the optical sensor and DGPS independently during the tests.

Flight tests were performed on the grassy airfield of the Lublin Aeroclub in Radawiec, Poland. This airfield is about 1×1.5 km in area and its surface is generally rough. Our tests were done on short and long grass areas and on a selected 100×150-m area with a smooth, grassy surface used by aeroplane modelers. The tests were conducted between April and October. A minimum of five replications were done for each case. During all the

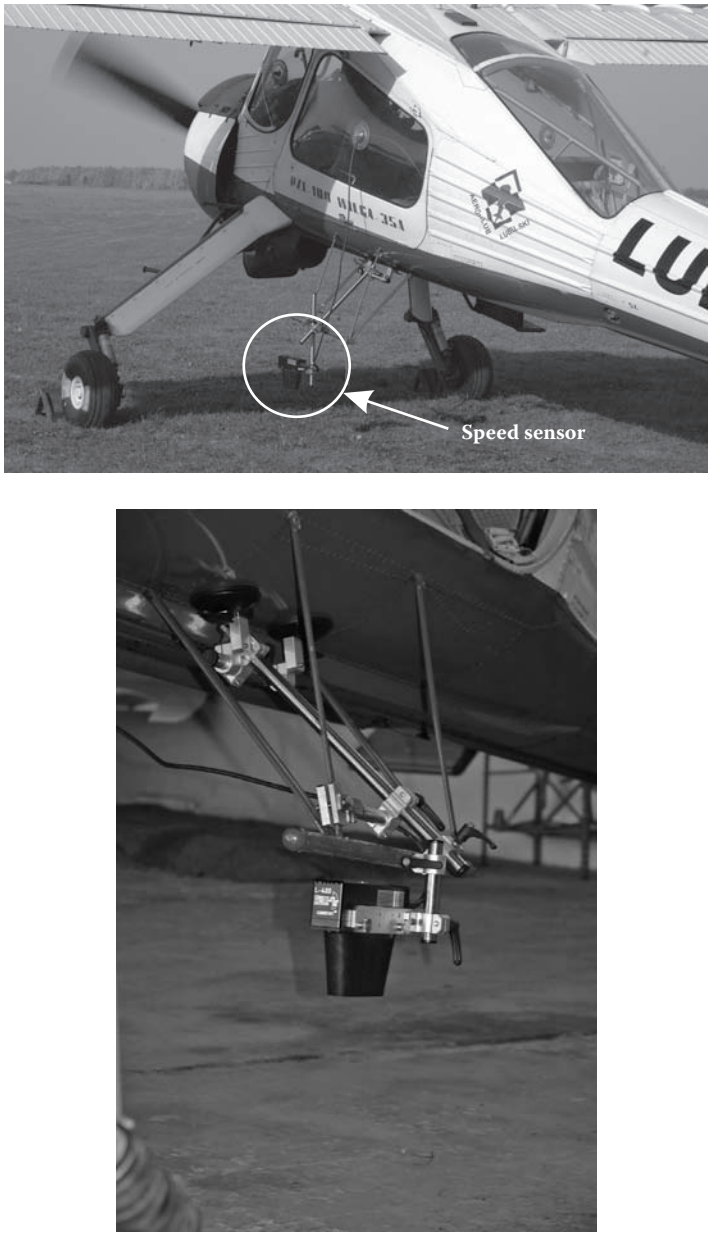

FIGURE 6.9
The non-contact speed sensor mounted on the Wilga aircraft.

tests, the same person piloted the aircraft to achieve consistent piloting technique as closely as possible. Days with no wind were chosen to minimise the effect on take-off speed.

Data from the optical sensor were captured from the DAT recorder to a PC and then evaluated. Each record contained time histories of aircraft ground speed (time intervals of 0.001 second). The data were analysed separately for each replication and final results were averaged. Data captured by the DGPS were use to determine characteristic time points (start of take-off run, lift-off, etc.). The knowledge of these time points helped find the right data series from the optical sensor.

One of the aims of the study was to derive a simple calculation method for identifying the rolling resistance coefficient from speed curves. A sample speed curve is presented in Figure 6.10. The speed curves were analysed for ground speed at the moment of lift-off. The motion resistance was determined by solving a differential equation as below:

$$\frac{dV}{dt} = \frac{g}{W}\ T - D - k_{RR}\left(W - L\right) \tag{6.12}$$

where V is aircraft ground speed, W is aircraft weight, T equals thrust, D is aerodynamic drag, L is aerodynamic lift, and g denotes gravity acceleration, 9.81 m/s^2. This equation includes lift and drag aerodynamic forces and propeller thrust. The aerodynamic forces were calculated with the classic equations. The aerodynamic coefficients were determined from experimental data based on certain assumptions:

First, in the after-liftoff flare, the aerodynamic lift force is equal to aircraft's weight with respect to climb angle:

$$L = \frac{1}{2}\rho V^2 S C_L = Q\cos\beta \tag{6.13}$$

Second, the aerodynamic drag is equal to the propeller thrust force minus the longitudinal acceleration of the entire aircraft (determined from speed data for the after-liftoff flare):

$$D = \frac{1}{2}\rho V^2 S C_D = T - \frac{Q}{g}a_x \tag{6.14}$$

where C_D and C_L are aerodynamic coefficients, S is the reference area, and ρ represents air density.

The aircraft used for the tests was relatively old and the engine substantially worn; thus the actual thrust force may have varied from the manufacturer's data. To determine true engine–propeller thrust, the aircraft

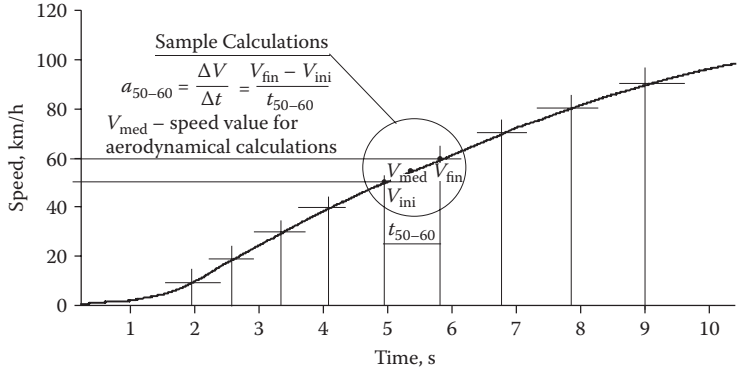

FIGURE 6.10
Sample speed curve of the test aircraft captured during take-off.

was attached to a rigid point by a load cell and a cable, and the thrust was measured at take-off power setting.

The first step in reducing the take-off data is to correct for wind (Kimberlin 2003). The wind correction is made for the observed ground speed:

$$V_t = V_o + V_w \tag{6.15}$$

where V_t is true aircraft ground speed, V_o is observed ground speed, and V_w is the wind speed (plus or minus). To simplify the calculations and to avoid errors, most of the tests were performed at no-wind conditions. After measuring measured true aircraft ground speed and knowing the aerodynamic drag, lift, and thrust forces, the rolling resistance coefficient was calculated using the inverted Euler method.

We assumed that the pitch attitude of the aircraft was constant and consequently the angle of attack and the aerodynamic coefficients C_L and C_D were unchanged during the ground roll. The pilot was asked to perform an "off-three-point" take-off to assure constant pitch. Using the Euler method and Equation (6.12), the take-off speed history was divided into ten small time intervals with the assumption that acceleration was constant during each interval. The rolling resistance coefficients were obtained for the end of each time interval, as shown on a sample speed curve in Figure 6.10. Note that the k_{RR} determined by this method is a summary complex value containing all components: drag due to high speed, drag due to soil and tyre deformation, and drag due to rolling.

6.3.2.2 Instrumented Vehicle Method

In this method, rolling resistance coefficient is determined with an instrumented ground vehicle. The method determines the rolling resistance

coefficient for the instrumented vehicle's tyres, not aircraft tyres. A wheel dynamometer was mounted on the test vehicle along with measuring equipment (data acquisition system, power supply). The wheel dynamometer was mounted between a wheel hub and a modified wheel rim. It was built with strain gage transducers and can measure all forces and moments acting on a wheel: vertical F_Z, horizontal F_X, and transversal F_Y forces as well as moments M_Z, M_X, *and* M_Y. The rolling resistance experiment required measurements of the horizontal force F_X or the moment on the transversal axis M_Y as well as the vertical load F_Z.

A slip ring transducer or telemetry system is usually required to gather data from a dynamometer, but we used an on-board data acquisition system with a semiconductor memory. This system is a microprocessor-based six-channel unit that can collect simultaneous data at a 10-millisecond rate from all six channels. This battery-operated system is installed in the centre of the wheel. Data can be transmitted through an RS 232 port when the vehicle stops or the data are saved on a memory card and can be read via a PC after a test ride.

The dynamometer was installed on a front wheel of a 1.6-tonne SUV (see Chapter 8 for a description of the instrumented vehicle). The vehicle was run over the same surfaces as the flight test at speeds of ~3 to 5 km/h. Higher speeds were not used because of the surface roughness.

For the rolling resistance tests, the vehicle was run in rear-wheel-drive mode (without front drive) so that a resisting moment was the only force acting on the front wheels. A six-element wheel dynamometer measures three forces and three moments acting on a wheel simultaneously. The rolling resistance coefficient is determined with the use of two measures: (1) the M_y moment acting around the transversal axis and (2) the F_z vertical force. The k_{RR} is then calculated as

$$k_{RR} = \frac{M_y}{r_d} \times \frac{1}{F_z} \tag{6.16}$$

where r_d represents the dynamic radius of the tyre (ETRTO 2006, Reimpell and Sponagel 1988). The M_y is calculated by averaging a portion of the measured data. The F_z is an average of maximum values determined simultaneously with the M_y. Sample experimental data are shown in Figure 6.10. This method yields a complex coefficient of resistance that summarises drag due to rolling and drag due to wheel and soil deformation. Note that this method currently provides the rolling resistance coefficient for the instrumented-vehicle tyre, not an aircraft tyre, and does so at low speeds.

6.3.2.3 Soil Stress and Deformation Method

Rolling resistance caused by deformation of an airfield surface at low speed must be determined with respect to soil response to the applied wheel load. In our proposed method, we determine soil stress and deformation under the aircraft wheel and then determine the coefficients of resistance based on the experimental data. A theoretical background for the method lies in Bekker's traction equations (1969) that correlate tractive forces (driving force, rolling resistance, and vertical load) with stresses on a contact surface between a wheel and the terrain. Substituting surface stresses with volume stresses gives a more precise solution of wheel–soil interactions because the wheel loads are distributed into the soil volume in multiple directions.

This soil stress and deformation experimental method has been used primarily for off-road vehicle performance measurements on soft deformable surfaces (Figure 6.11). It determines soil stresses and deformations under a wheel rolling at low speed and can estimate rolling resistance based on the assumption that the energy consumed to deform the soil equals the work of the rolling resistance force.

The soil stress measurements are performed with an SST installed in soil. This device was placed at ~15-cm depth by digging a hole, installing and levelling the SST, and refilling the hole with removed soil. During a test, a vehicle is run over the SST at a low velocity (3 to 5 km/h) and the soil pressures are measured and recorded.

Soil deformation was determined by measuring rut depth and the vertical position of the SST: soil deformation is defined as the change from the initial volume of soil between the surface and the SST to that between the rut and the SST after a wheel pass. In terramechanics, rolling resistance is one of the tractive forces acting on a wheel; the others are the driving force that moves a vehicle forward and the wheel load that acts vertically.

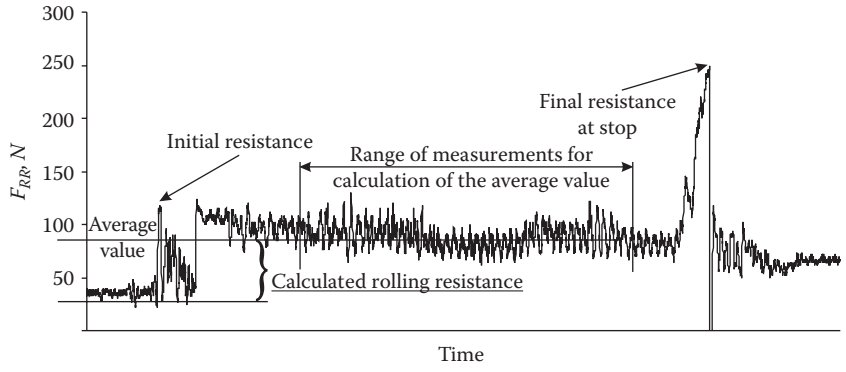

FIGURE 6.11
Sample results from the measuring wheel: Time versus the rolling resistance moment.

The tractive forces can be expressed with soil stresses generated under wheel loads. These calculations assume that the rolling resistance on soft soil is dependent upon soil deformation, so that the rolling resistance can be expressed as

$$F_{RR} = b\int_0^z \sigma\, dz \tag{6.17}$$

where σ represents normal soil stress and z is wheel sinkage (soil deformation). The normal stress is distributed over a soil volume, not just the wheel–soil contact surface. Normal stress distribution along the stress path—determined by the SST—is needed to calculate the rolling resistance. A sample soil stress curve is shown in Figure 6.12a and a sample soil deformation is plotted in Figure 6.12b. Based on the experimental data, a soil deformation–soil stress relationship was constructed.

The next step was integrating the experimental stress–deformation relationship (Figure 6.12c). The result is a separate component of rolling resistance: drag due to soil deformation. We used this method to identify rolling resistance of aircraft tyres on loose loess soil with high moisture content. This soil stress and deformation method is suitable for identification of low-speed rolling resistance coefficients for aircraft wheels.

6.3.2.4 Pull Test Method

This method is often used to determine rolling resistance coefficients in automotive research and testing. A second vehicle tows a test vehicle and the force needed to pull the test vehicle is measured with a load cell. This method allows identification of low-speed components of rolling resistance. In our airfield tests, the Wilga aircraft and a towing vehicle were connected by a load cell and a cable, positioned so that the cable was taut. With the aircraft fully occupied and fueled and the brakes released, the towing vehicle pulled the aircraft at a constant speed of about 3 to 5 km/h for approximately 30 m (Figure 6.13). The average pulling force divided by wheel load produces the coefficient of rolling resistance. The tests were repeated on high grass, low grass, and the smooth model aircraft area.

Calculation of rolling resistance from experimental data obtained in the pull test was simple because the method provides time histories of the tow resistance force, which is equal to rolling resistance. The values were arithmetically averaged. It was important to use data reduction to choose the right range for averaging: this range should not start at the beginning of the recorded test, but at a moment when the measured value of rolling resistance is stable (Figure. 6.14).

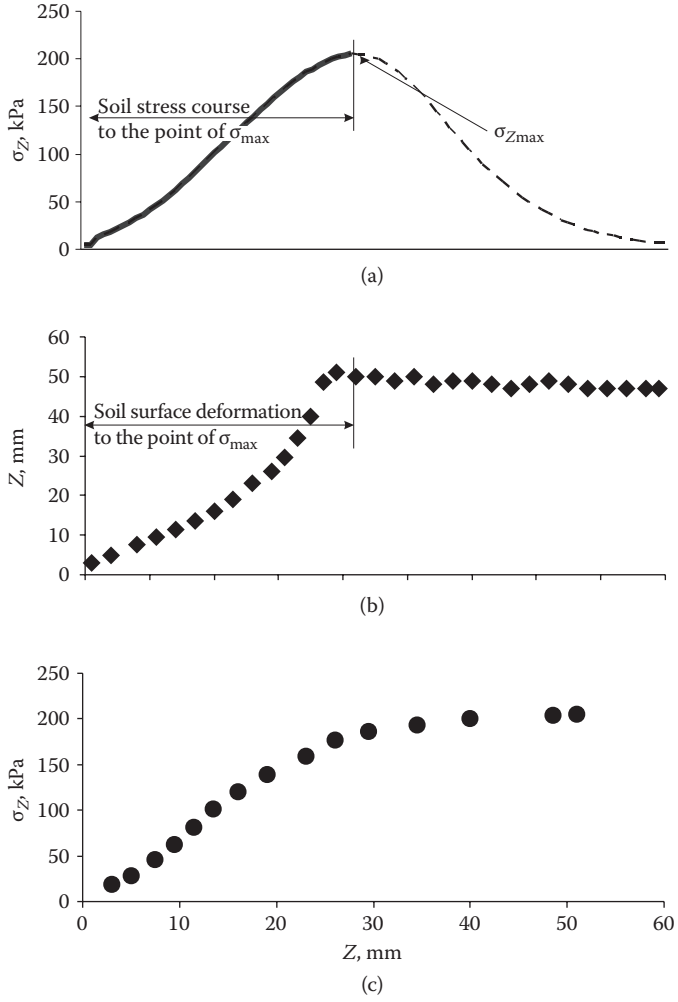

FIGURE 6.12
Soil stresses calculated from the soil pressures measured with the SST (a), soil surface deformation (b), and the relationship soil deformation – soil stress (c).

To calculate the rolling resistance for the entire aircraft, we needed to determine the distribution of the force on all the aircraft wheels. With the assumption that the aircraft was tested on a level surface, the rolling resistance force distribution over the wheels is proportional to the aircraft weight distribution. The weight distributions of the test aircraft were (1) front right wheel, 526 kg; (2) front left wheel, 604 kg; and (3) tail wheel, 230 kg.

FIGURE 6.13
Pull test for determination rolling resistance of aircraft tyres.

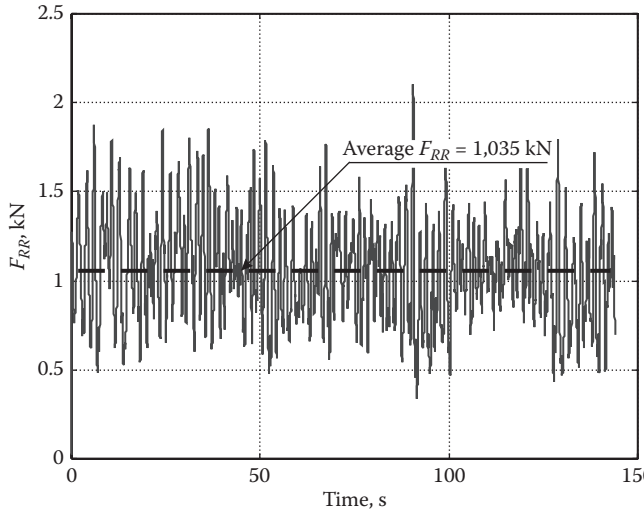

FIGURE 6.14
A typical plot of the rolling resistance obtained in the pull test.

Finally, the rolling resistance was calculated for the front wheels (superscript *F*) and for the tail wheel (*T*) separately, using the equation

$$k_{RR}^{F,T} = \frac{W^{F,T}}{W} \times \frac{F_{RR}^{A}}{W} \tag{6.18}$$

where $W^{F,T}$ is the front or tail wheel load, W equals the total weight of the aircraft, and $F_{RR}{}^{A}$ indicates averaged value of rolling resistance from the tow test. This method provides a complex value of resistance consisting of drag due to soil or surface deformation and drag due to rolling, both at low speeds.

6.3.3 Results and Discussion

6.3.3.1 Rolling Resistance Coefficient as a Function of Aircraft Ground Speed

Figure 6.15 shows results from flight tests (see Section 6.3.2.1) in the form of k_{RR} versus speed relationships for the three investigated surfaces: high

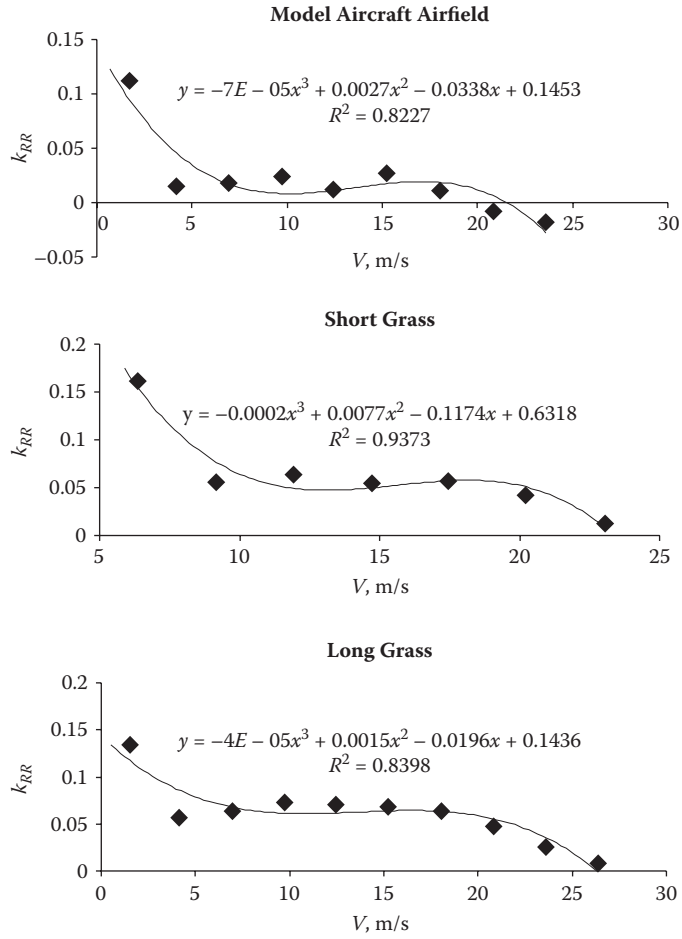

FIGURE 6.15
Effect of ground speed on the rolling resistance coefficient on three different surfaces.

grass, low grass, and the model aircraft field. The general shape of the k_{RR}–V curves is similar for all three cases: decreasing from a relative high k_{RR} at low speeds (0 to 10 m/second) to a local minimum point at ~10m/second, then increasing in the middle range of speed, and finally decreasing at higher speeds. This agrees with Crenshaw's (1972) results.

Results revealed little or no difference between the two grassy surfaces, while the smoother model aircraft field grass differed significantly from the others with a k_{RR} much lower in the full range of ground speeds. Both grassy surfaces were rough, while the model airfield was smooth (this is a subjective estimation; we did not measure the roughnesses of the surfaces). This suggests that the total rolling resistance is more dependent on roughness than on the length of the grass.

The flight test method is complex. The aircraft cannot fly from all investigated surfaces. For example, we were not able to perform flight tests on loess soil because of safety concerns. This method can also suffer from other effects such as wind or piloting technique variations.

6.3.3.2 Results from Instrumented Vehicle

Figure 6.16 presents these results. The values of the k_{RR} range from 0.01 to 0.016. This is much smaller in comparison to the values presented in the previous flight test section and those reported in the literature (Currey 1988, Raymer 1989). However, these values were determined for an automotive tyre inflated to a higher pressure and deformed less than an aircraft tyre. The relationship between the values of the k_{RR} are similar to those obtained in the flight test method.

The method can be modified by performing tests at high speeds and by using aircraft tyres or by utilizing a calibration method to recalculate the results obtained with an automotive tyre. This method can be used on

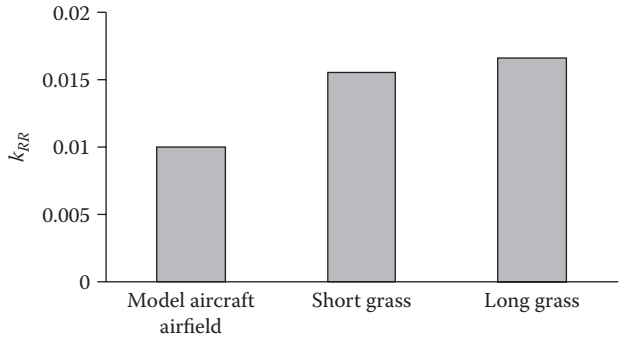

FIGURE 6.16
Rolling resistance coefficients for the investigated surfaces obtained with the instrumented vehicle.

any surface type. Finally, it seems to be the most practical and suitable for determination of rolling resistance coefficients.

6.3.3.3 Soil Deformation Resistance

As noted in Section 6.3.2.3, the soil stress and deformation method was applied to only one surface: loess soil with high moisture (25% to 27%) content. The final calculations are shown in Table 6.5. Note that the first test was performed on an uncompacted soil surface. In the second test, the aircraft wheels rolled over the compacted soil (ruts) from the first test. Two repetitions were performed for each of the two uncompacted and compacted tests.

The final results for the uncompacted soil agree with those from the literature. The value of about 0.2 is typically cited for soft surface or soil generally. Lower values of the k_{RR} obtained in the second test were the result of lower soil deformation and, consequently, decreased rolling resistance force. This method was limited to a very low speed.

This is the only method used in this study that allows determination of a single component of the total rolling resistance: drag due to soil deformation.

6.3.3.4 Results of Pull Test

Pull test results are shown in Figure 6.17. The values of k_{RR} ranged from 0.032 for the model aeroplane airfield to 0.075 to 0.08 for the rough grassy surfaces. The difference between the extreme values is pronounced, but again, the effect of the grass length does not seem to be significant. This corresponds logically with the results obtained in the other presented methods. Comparing the absolute values of the k_{RR}, there is a similarity with the flight test method, in which the k_{RR} measures ~0.02 to 0.1. These values are comparable to those presented by other researchers. The pull test method is suitable for various surfaces with no limitations, but it is not possible to use it at high speeds.

TABLE 6.5

Results of Soil Stress Deformation Analysis

Test Number	Integer σ (z)	b (m)	F_{RR} (N)	k_{RR}
1	5406	0.2	1081.2	0.195
	5390	0.2	1078.01	0.194
2	3265.25	0.2	653.05	0.117
	2770.37	0.2	554.07	0.099

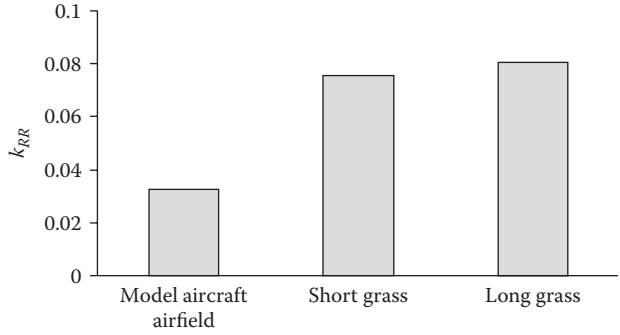

FIGURE 6.17
Results obtained with the pull-test method on the three investigated surfaces.

6.3.4 Concluding Remarks

The literature shows that the total rolling resistance of a tyre on a soft surface is complex and consists of separate components, and various methods are needed to determine those components. The goal of this study was to develop new methods or apply known methods to the problem. Rolling resistance coefficients were determined for aircraft tyres on different surfaces with the use of four different test methods.

The flight test method allows determination of the effects of ground speed on rolling resistance on an unsurfaced airfield. The instrumented vehicle (IV) method and the pull test method are both suitable for performing tests on a variety of surfaces, but only at low speeds. The IV method, after some modifications, may be suitable for high-speed tests as well. The soil stress and deformation method is suitable for separating the drag due to soil deformation—a single component of rolling resistance on soft surfaces.

The analysis of the results showed that the effect of surface roughness on rolling resistance may be more significant than the effect of the length of grass. The methods used in this work, except for the IV method, yielded results comparable with those reported in the cited literature.

6.4 Effect of Grassy Surface on Take-off Distance

6.4.1 Aircraft Take-off and Landing Performance

In take-off analysis, the forces that act on an aircraft are thrust T, aerodynamic drag D, weight W, aerodynamic lift L, and rolling resistance

of the wheels. The aerodynamic forces are functions of aircraft velocity, and they change during take-off (they increase as velocity increases). The thrust generated by the propulsion unit (engine plus propeller or turbine) is the force that acts against aerodynamic drag, rolling resistance, and inertial force. The thrust also changes during take-off as a function of velocity (decreases to approximately 70% of the initial value).

At the start, weight is the only force in the vertical direction, but during ground roll the lift force is generated and it decreases wheel loads. When the lift equals the weight, the aircraft becomes airborne and the thrust is consumed by the aerodynamic drag during climbing or accelerating in the air. The acceleration of the aircraft during a take-off ground roll can be expressed by the following equation:

$$a = \frac{g}{W}\left[T - D - \quad (W - L)\right] = g \quad \frac{T}{W} - \quad + \frac{\rho}{2W/S}\left(-C_{D0} - KC_L^2 + \quad C_L\right)V^2 \qquad (6.19)$$

where C_{D0} is the drag coefficient, K is the ground effect coefficient, C_L indicates lift coefficient, and V represents velocity. The ground roll distance is determined by integrating velocity divided by acceleration:

$$S_G = \int_{V1}^{V2} \frac{V}{a}\,dV = \frac{1}{2g}\int_{V1}^{V2} \frac{d(V^2)}{K_T + K_A V^2} = \quad \frac{1}{2gK_A} \quad \ln \quad \frac{K_T + K_A V_f^2}{K_T + K_A V_i^2} \qquad (6.20)$$

$$K_T = \quad \frac{T}{W} \quad - \qquad (6.21)$$

$$K_A = \frac{\rho}{2(W/S)}\left(\quad C_L - C_{D0} - KC_L^2\right) \qquad (6.22)$$

Landing is much like taking off, but in reverse. Equation (6.20) can be used to calculate ground roll during landing *related* change of velocity. The thrust force during landing is called the idle thrust for conventional aircraft. When an aircraft is equipped with a thrust reverser or reversible propellers, the resulting thrust will be negative. Also, the aerodynamic drag may be increased by spoilers, speed brakes, or drag chutes. There are often obstacles around airfields, so it is practical to determine *both* the ground roll *and* the total take-off distance from the start to the point where the aircraft is 15 m above the ground (Figure 6.18).

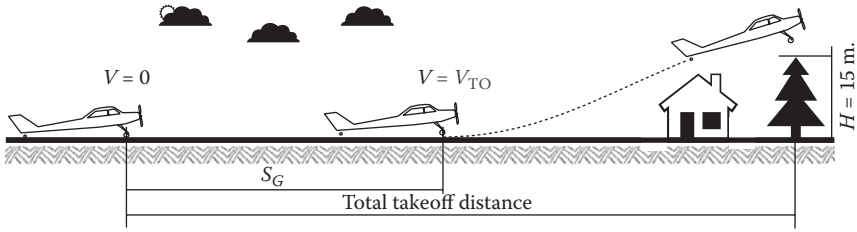

FIGURE 6.18
A schematic of a typical take-off.

6.4.2 Airfield Experiment

The Wilga aircraft with four persons on board was used for the tests. The take-off weight with 125 litres of fuel was 1150 kg. The kinematic details of aircraft motion were determined with a combined DGPS–inertial navigation system that consisted of a main unit installed in the aircraft with a 12-V power supply, remote base station, and portable computer for data acquisition and storage. The system must be initiated before the tests by moving at a constant velocity of approximately 10 km/hour. The initiation was done in a ground vehicle because of the high vibration levels in the aircraft. The base station was an option that was used to enhance the precision of the positioning.

The acquisition time of the system is 10 milliseconds and positioning resolution is 20 cm. The system contains an inertial navigation unit that can measure 39 kinematics parameters of aircraft motion. The measuring system was maintained by two people on board. The tests were conducted on the same sport airfield as the other flight tests described in this chapter (Radawiec, near Lublin, Poland). Tests were conducted on low (10 cm) and mid-high (20 cm) grass. For both grass conditions a total of ten flights were performed, five with flaps in take-off position and five with no flaps during take-off. On landings, flaps were extended to normal landing position for all ten flights. The wind was 5 m/second and the aircraft was flown facing the wind.

6.4.3 Data Reduction Methods

Data from the DGPS–inertial system collected numerous kinematics measures of aircraft motion, but only a few were used and evaluated: (1) height (altitude) above the ground, (2) ground speed, and (3) take-off or landing ground roll. For the precision of the analysis, it is important to determine the exact moments when the aircraft lifts off and touches down. This was done on altitude graphs (Figure 6.19). From the time co-ordinates, we

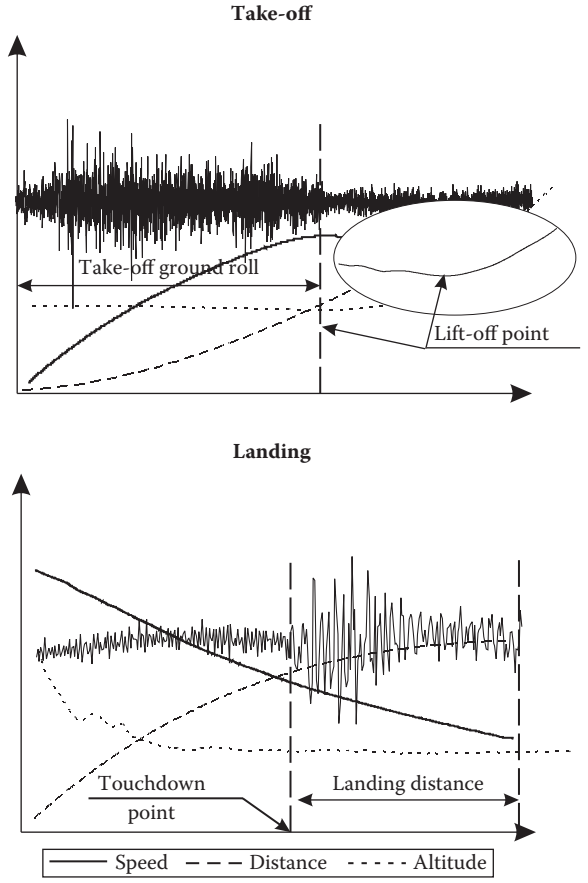

FIGURE 6.19
Example sets of flight data for a take-off and a landing.

could analyse the altitude, speed, and ground roll and find a lift-off time point.

6.4.4 Results

Figure 6.20 graphs the take-offs and landings and shows speeds with and without flaps. Table 6.6 also shows the results with and without flaps. The values for the no-flaps mode are higher. Also for no-flap take-offs, the difference between V_{TO} and V_{TD} is higher (Figure 6.20) because a landing is always performed with extended flaps (flap landing configuration for this aircraft is 44°).

The effect of flaps on the take-off and landing profile of the aircraft is clearly visible in Figure 6.21 showing a sample ground roll distance curve

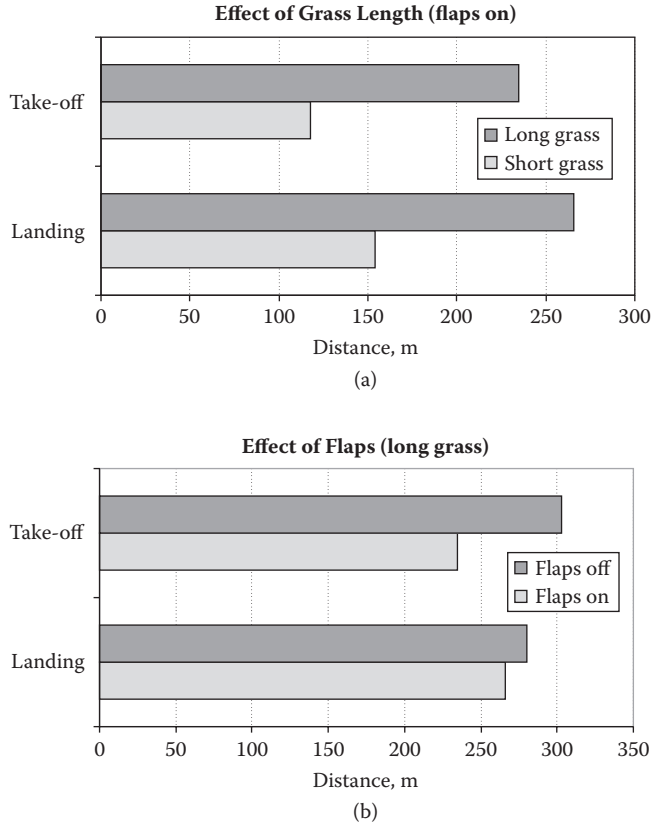

FIGURE 6.20
Take-off and landing ground roll distances as determined in the tests.

TABLE 6.6

Average Values of Ground Roll Distance and Ground Speed for Low and High Grass

Manoeuvre	Landing Ground Roll	Take-off Ground Roll
Short grass, flaps on		
Take-off	117.4 (10)	73.06 (6.3)
Landing	154.1 (7)	71.2 (5.7)
Long grass, flaps on		
Take-off	234.5 (13.6)	98.3 (3.6)
Landing	265.8 (6.5)	92.7 (4.5)
Long grass, flaps off		
Take-off	303.2 (5.7)	113.2 (2)
Landing	280.2 (7.7)	95.7 (4)

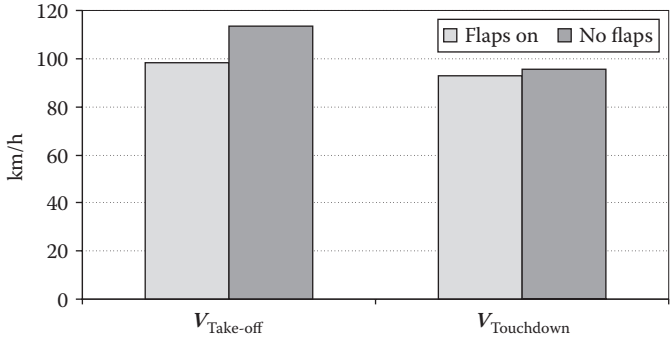

FIGURE 6.21
Effect of the flaps on take-off and landing profile and ground roll distance of the Wilga aircraft on a grassy airfield.

along with altitude profiles for the two operational modes. The effective ground roll at take-off is much longer without extended flaps. Similarly, the total take-off distance (up to 15 m altitude) with extended flaps is shorter than in a clean, no-flap configuration (495 versus 577 m).

Long grass compared to short grass increased the take-off distance almost double and increased landing distance by 1.7 times. The effect is significant and the grass could be taller. Problems occur for Wilga aircraft, however, when grass is so tall that it collides with the rotating propeller during take-off.

6.5 Proposed Method for Airfield Surface Evaluation and Classification

It is clear that aircraft ground performance on grassy airfields is weakened and depends upon a number of factors that we are unable to control. Safe take-offs and landings on an airfield require that the pilot know how the actual conditions may affect take-off and landing distances. As a result of what we learned from the research presented in this chapter, we proposed a test method for evaluating and classifying unsurfaced airfields. We are still developing the idea and propose the following project to complete the method.

The project will test a method to evaluate unsurfaced airfields based on each airfield's mechanical properties that affect aircraft field performance during take-off, touchdown, and landing roll. Aircraft operations could be more effective at many unsurfaced airfields in the European Union

(EU) and elsewhere if surface conditions and their impacts on field performance are known. The proposed method could provide this information.

An advantage of the new method over the existing methods [cone index (CI), aircraft index (AI), LCN, CBR, etc.] is that it would determine (1) bearing capacity of a given surface, (2) wheel–surface traction (friction), (3) rolling resistance, (4) surface roughness, and (5) soil moisture. All these parameters are essential for analysis of wheel–soil interactions and airfield performance. The parameters would be determined with a tester built from the methods presented in this book. The completed test method would include procedures, instructions, comparison charts, and other documentation.

The test method is based upon the analysis of (1) wheel–soil interactions with respect to dynamic loads caused by aircraft tyres, (2) aviation regulations and safety requirements (ICAO Annex 14), and (3) expectations and needs of potential end users (aeroclubs, airport administration, private users of aircraft, etc.). We plan to present the complete test method for certification so that it will be widely by the general aviation community.

As background for developing the method, we would perform a thorough analysis of wheel–soil (wheel–grassy surface) interactions with a special caution related to loads on aircraft tyres. We also need an analysis of aircraft dynamics during take-offs and landings. An analysis of aircraft wheel loads on unsurfaced airfields and dynamic responses of the surfaces would provide a basis for developing a primary test method. At this stage, we must also consider legal requirements and safety standards and answer fundamental questions about what will be measured and when and how those measurements will be evaluated.

The next stage would be construction. We already have a wheel dynamometer and its equipment for measuring wheel traction, rolling resistance, vertical loads, and surface roughness. The devices are included in a wheel tester that can be attached to an SUV or similar vehicle. Our wheel tester, shown in Figure 6.22, can gradually load or unload a wheel and control wheel slip with an electro-hydraulic brake. These two features together are new for wheel testers, but our idea is to replicate the ground roll as fully as possible by rolling with increasing and decreasing vertical loads and with the use of brakes.

After we have completed the wheel tester, we will perform early tests with the new measuring equipment. Our goal at this stage will be primarily to verify the method with airfield tests using sample aircraft. The final test method would need to undergo multiple tests on chosen airfields to evaluate and examine the tester and the instrumentation.

We plan two approaches to applying the completed method. If an airfield operator purchases a complete tester (it would probably be costly), the surface could be tested at any time and the results would be the most accurate. If a tester is not available, the surface could be evaluated based on conversion tables calculated from experimental results obtained on some

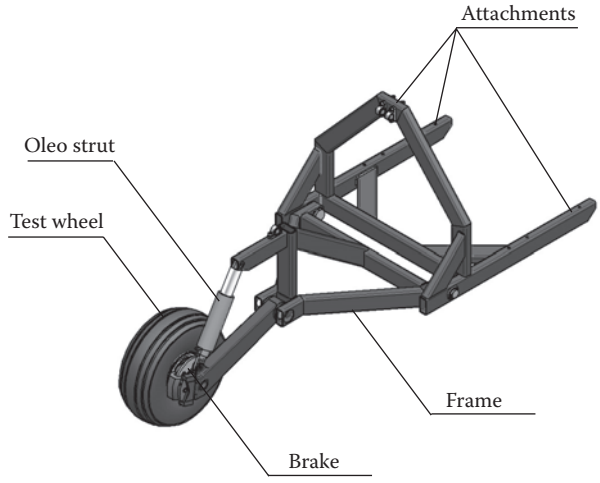

FIGURE 6.22
Design of a single-wheel tester with controlled vertical load and wheel slip.

typical airfields. These tables could be prepared in hard copy form or as electronic media—preferably compatible with today's portable devices. A simplified version of the method would assume the soil moisture and grass length as basic information for a pilot's decisions to fly or not to fly. This would be especially useful, for example, when an aircraft is sent to retrieve a sailplane that has landed off field.

When we have completed the method (test equipment, methodology, procedures, instructions, handbook, software, conversion tables, etc.), we will present it to the potential users. A prototype tester with procedures will be shared with an airfield operator for practical testing. Some training activities will probably be needed: an end user will benefit from a short course and on-site training. Comments and feedback from users will help to improve the method.

One of the final tasks will be presentation of the method to the aviation authorities for certification. Regardless of the practical use of the whole method, the wheel tester will be applied to future research in the fields of wheel–soil and wheel–grass interaction analysis.

6.6 Summary

For determination of soil stress state under a wheel of a landing aircraft, we developed an improved version of the SST that contains a three-axis

accelerometer to identify the moment of touchdown. The concept performed well and we were able to capture real values of soil pressures at touchdown. This method seems impractical, however, for obtaining experimental data of scientific importance. Therefore we propose to develop a test rig for future research.

In this chapter, we also examined four experimental methods for determining the rolling resistance coefficients for aircraft tyres on grassy ground and soft soil. Any method used to analyse aircraft wheel interactions with unimproved surfaces must consider dynamics effects, especially at high speeds.

References

Bekker M.G. 1969. *Theory of Land Locomotion*. Ann Arbor: University of Michigan Press.

Crenshaw B.M. 1972. Soil–wheel interaction for high speed. *J. Terramech*. 8: 97–104.

Currey N. 1988. *Aircraft Landing Gear Design: Principles and Practices*. Reston, VA: AIAA Publishing

Czarnecki K. 1987a. Classification of bearing capacity for airfield pavements in ACN-PCN method I. *Technik.Lotnicza i Astron.* 1: 19–21.

Czarnecki K. 1987b. Classification of bearing capacity for airfield pavements in ACN-PCN method II. *Technik. Lotnicza Astron.* 2: 19–21.

Czarnecki K. 1987c. Classification of bearing capacity for airfield pavements in ACN-PCN method III. *Technik. Lotnicza Astron.* 3: 18–20.

ETRTO (European Tyre and Rim Technical Organization). 2006. *Standards Manual*. Brussels.

van Es G.H.W. 1999. Method for predicting the rolling resistance of aircraft tires in dry snow. *J. Aircraft* 36: 762–768.

Gibbesch A. 2003. Reifen-Boden Interaktion von Flugzeugen auf Nachgiebigen Landebahnen bei hohen Geschwindigkeiten. *Proc. DLR Luft und Raumfahrtkongress*.

Hovland H.J. 1973. Soil inertia in wheel–soil interaction. *J. Terramech*. 10: 47–65.

Kimberlin R. 2003. *Flight Testing of Fixed-Wing Aircraft*. Reston, VA: AIAA Publishing

Lowry J. 1999. *Performance of Light Aircraft*. Reston, VA: AIAA Publishing.

Mitschke M. and Wallentowitz H. 2004. *Dynamik der Kraftfahrzeuge*. Heidelberg: Springer.

Prithard J. 2001. Overview of landing gear dynamics. *J. Aircraft* 38:130–137.

Pukos A. 1983. Thermodynamic interpretation of soil medium deformation. *Zesz. Probl. Postepow Nauk Roln.* 220: 367–389.

Pytka J., Tarkowski P., Dąbrowski J. et al. 2004. Soil stress and deformation determination under a landing airplane on an unsurfaced airfield. *J. Terramech*. 40: 255–269.

Raymer D. 1989. *Aircraft Design: A Conceptual Approach*. Reston, VA: AIAA Publishing.

Reimpell J. and Sponagel P. 1988. *Fahrwerktechnik: Reifen und Räder*. Wurzburg: Vogel.

Shoop S.A., Diemand D., Wieder W.L. et al. 2008. Predicting California Bearing Ratio from Trafficability Cone Index Values. ERDC/CRREL Technical Report TR-08-17.
Shoop S.A., Richmond P.W., and Eaton R.A. 1999. Estimating rolling friction of loose till for aircraft takeoff on dirt runways. *Proc. 13th Int. ISTVS Conference*, Munich.
Stinton D. 1998. *Flying Qualities and Flight Testing of the Aeroplane*. London: Blackwell.
Way T.R., Johnson C.E., Bailey A.C. et al. 1996. Soil stress state orientation beneath a tire at various loads and inflation pressures. *J. Terramech.* 33: 185–194.

7

Snow Stress State under Ground Vehicle Loads

7.1 Introduction

7.1.1 Basic Snow Mechanics

Snow is a three-phase medium of ice, water, and air. It is built of crystals that form by sublimation or freezing. The properties of snow vary, depending on how it was formed and at what temperature. Generally, a more dense snow forms at higher temperature. Even when undisturbed, snow undergoes a natural transformation. Dry snow can undergo constructive or destructive metamorphism; wet snow is subject to melt or freeze metamorphism. Metamorphism occurs intensively at higher temperature gradients and changes the crystal formation and size. Important snow properties are

- Grain size and formation; grains of newly fallen snow may be 0.2 to 5 mm in size; sizes for machine-prepared snow range from 0.1 to 0.8 mm.
- Density may vary from 10 to 50 kg/m^3 for a light powder snow, 100 for an average fresh snow, 200 to 450 for old settled snow, and 400 to 600 for groomed snow on a piste.
- Temperature may vary from –45°C to 0°C and is mainly affected by air temperature and snow depth.
- Liquid water content increases rapidly when snow temperature reaches 0°C.

Mechanical properties of snow are important for snowmaking by machines. The properties that should be considered include snow strength, visco-elasto-plastic characteristics, hardness, deformability and compressibility, and mechanical stress propagation in snow under loading.

7.1.1.1 Snow Strength

Snow strength is affected mainly by the numbers and types of bonds between grains. Certain distinct processes affect final strength:

- Sintering via an exchange of matter at temperatures around zero; natural sintering is a major source of snow strength.
- Interlocking in irregular crystals.
- Capillarity occurring at moisture levels of 5% to 20%; the process is driven by capillary forces between snow crystals and water between them.
- Freezing; water in snow refreezes and enhances the bonds and strength of snow.

7.1.1.2 Constitutive Properties

Snow is a visco-elasto-plastic material and the proportions of the three properties depend on the basic condition of the snow. The reaction of snow to mechanical input can be different and is based on the velocity of deformation. A slow load rate results in near-plastic deformations while rapid inputs will cause almost elastic processes. Density plays a major role in mechanical properties of snow. Generally, the higher the density, the greater the mechanical strength of the snow.

7.1.1.3 Hardness

Snow hardness can be expressed as a force of resistance to penetration, as measured with snow penetrometers (Fauve et al. 2002). Fresh, settled, processed, and machine-made snow exhibit many differences. Snow temperature also influences its hardness. In general, snow hardness varies from 0.1 to 35 N.

7.1.1.4 Other Mechanics Factors

The general physical conditions and mechanical properties of snow depend strongly on environmental factors such as sun radiation, wind, air humidity, and precipitation (rain, haze, snow). Moreover, snow properties vary over time, sometimes rapidly. Snow is a natural material of great instability. All these factors must be considered for preparing and maintaining a ski piste or route. Improvements to known methods of snow processing may require further investigations.

7.1.2 Winter Traction

Winter traction can be compared with performance of a vehicle on a soft soil surface. The general trends are identical: compared to hard surfaces, traction on snow is weaker because of surface deformations that increase motion resistance and because of low shear resistance of soft surface materials. There are some differences, however, between snow and soft soil. Snow, especially when fresh, is generally more compactable and compressible than any kind of soil. The range of compactability is much wider for snow than for soils. On the other hand, shear resistance and strength for snow vary widely, but maximum values are higher for soils. The lower shear resistance of the snow–wheel combination is caused by low friction. Keep in mind that rapidly varying snow properties, sometimes within a day, can cause a wide variation in vehicle traction parameters.

In the analysis of winter traction, snow-related measures and snow stress state must be determined. Few publications describe experimental snow stress state determination (Jamieson, 2003, Johnson et al. 1993, Johnson 2004), and none consider vehicle loading on snow. Several analytical works consider winter traction (Abele 1990, Shapiro et al. 1997, Shoop 2001 and Shoop et al. 2006), but a lack of sufficient experimental results makes it difficult to validate the models and verify predictions.

7.1.3 Preparation of Ski Routes

Preparation and maintenance of ski routes and pistes play significant roles in sports. To meet the wide popularity of alpine and Nordic skiing, ski areas attempt to keep ski routes and pistes in good condition as long as possible—even longer than natural conditions might allow. Grooming machines are used for most snow preparation at ski areas. They may use other methods such as snow making or hardening by chemical additives, but most snow processing is mechanical. Therefore, it is plausible to focus on snow mechanics. Processes that occur during snow preparation are of two main types:

- Mechanical processes that happen immediately: compaction, shearing, and grain-pore size redistribution
- Mechanical and thermal processes of long duration: sintering and metamorphism

Basic snow grooming loads and deforms the surface under the machine tracks. This compacts the snow and increases its normal density from 80 to 200 kg/m^3 to a far denser 230 to 330 kg/m^3. The contact pressure exerted by a typical grooming machine is about 3 to 5 kPa (average of total contact area of tracks and snow). Therefore the effect of the machine alone may be reduced and unsatisfactory. Additional implements that can increase

the compaction of the snow are described below. Proper timing of snow grooming is essential. Sintering is time dependent and such operations should be finished at least 10 hours before pistes are opened. For example, snow hardness only 3 hours after treatment can be as low as 30 N and reach 80 N after 13 hours of sintering (Fauve et al. 2002). This effect happens naturally with overnight drops in temperature.

Snow temperature and initial snow density also influence the final state of a ski route or piste. Snow grooming is especially efficient at temperatures near 0°C, as natural sintering is most intensive and the hardening effect is high. At low snow temperatures (<20°C), final results are minimal; grooming work should be postponed or performed at a very low velocity. In such conditions, vehicle traction is also worse, mainly because of weakened snow structure and strength.

Grooming machines are usually tracked vehicles, powered by diesel engines of ~200 to 300 HP. The tracks are very wide to maintain low contact pressure for good traction on loose fresh snow. Preparation and maintenance of ski areas are performed by machine traffic and specialized implements:

- Clearing front blades shift snow, level and smooth bumps, and accumulate snow for construction of fun park structures (half pipes, rail slides, jumps, fun boxes, etc.).
- Rear snow tillers are the main implements for piste preparation. They homogenize snow, make snow grains smaller, improve grain distribution, compact and level the surface, and allow snow density to exceed 500 kg/m^3.
- Rear finishers are combined with tillers to create a visually attractive surface with a good grip.
- Front snow buckets mounted in place of front blades transport and move snow.
- Front snow blowers blow large volumes of snow aside.
- Front renovators mix the top layers of the surface to make them more homogeneous.
- Sail winches help compact snow by reducing the need for shear resistance on slopes.

7.2 Snow Stress Measurement Methods

One of our first tasks was to prepare instrumentation suitable for snow measurements. We considered modifying measuring devices used in

previous studies and creating totally new measuring equipment (based on SST methods) to engineer them specifically for winter conditions.

Pilot tests are practical starting points because the choice of instrumentation is so critical for a long-term, costly experiment. Experiences from pilot studies can be valuable for future research. This chapter therefore contains more methodological information and practical comments rather than results from multiple repetitions. Our experiences from previous tests with tracked and wheeled vehicles on different soils were applicable to our snow-related studies.

7.2.1 Use of Soil Stress Measurement Equipment

The measurement equipment used for soil consists of several SSTs with different measuring ranges, data acquisition systems, and a deformation measurement system. We chose SSTs with low and medium measuring ranges for snow. The main practical difference between soil and snow measurements is the temperature that may affect the results. Strain gage stress transducers were installed in the SSTs; it is well known that strain gage results are affected by temperature. We therefore examined how the transducers and the data acquisition system functioned at low temperatures.

A hermetic calibration chamber was placed in a low-temperature box and a complete SST, data acquisition system, and laptop were installed in the box. Air tubing, signal cables, and power supply cables lead outside the box (Figure 7.1). The transducers were loaded by air pressure applied through a rubber coat to the stress transducers of the SST. Trials were conducted from 0°C to –10°C. Loading characteristics of the SST transducers were determined at various temperatures. We found that temperature

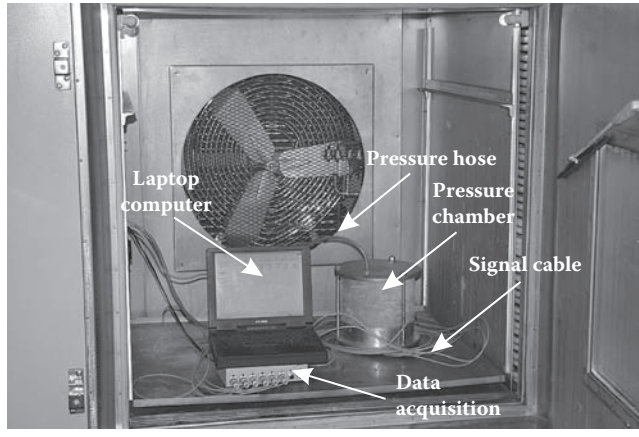

FIGURE 7.1
Soil pressure instrumentation being tested in low-temperature box.

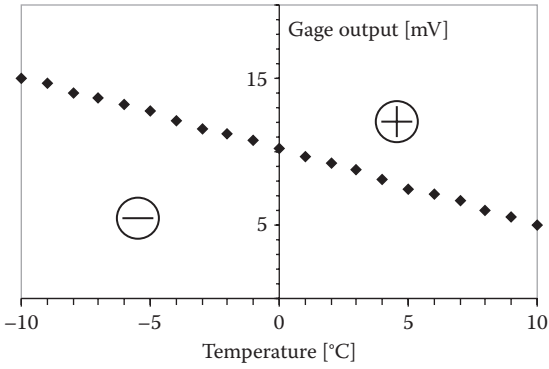

FIGURE 7.2
Effect of temperature on pressure sensor bias value.

had little or no effect on transducer characteristics (inclination to X-axis), but exerted a significant effect on readings (Figure 7.2).

The complete measuring system (SST, data acquisition system, laptop computer) was found unsuitable below –10°C. A typical laptop is temperature sensitive and its display fails at freezing temperatures. We noted fluctuations of the measured data, probably caused by computer malfunction. The transducer, when tested separately, showed no such effects. As a result, we decided not to use the laptop in outdoor winter tests. Instead, we chose an industrial, PC-compatible computer that could operate at low temperature according to the manufacturer's recommendations. We could not study this computer because it was too large to fit into the low-temperature box.

7.2.2 New Measuring Devices for Outdoor Snow Stress Experiments

7.2.2.1 Low Pressure Transducer

Despite the modified soil measuring system, we wanted to build a completely new transducer for snow measurements. The lowest measuring range for a soil SST is 200 kPa. To measure snow stresses under a grooming machine, the range of stress transducers should be as low as 30 kPa because the calculated contact pressure for a grooming machine is about 5 kPa. Based on the strain gage measuring method, the resulting thickness of a membrane for a 30-kPa load is 0.3 mm. Chapter 2 describes the design and fabrication of such a thin membrane.

The strain gage transducers were encapsulated in a low-profile case (see Figure 7.3) to facilitate easy installation into snow. Each sensor was built of a thin aluminum membrane with a strain gage glued to the bottom. An instrumentation amplifier was installed near the strain gage of each

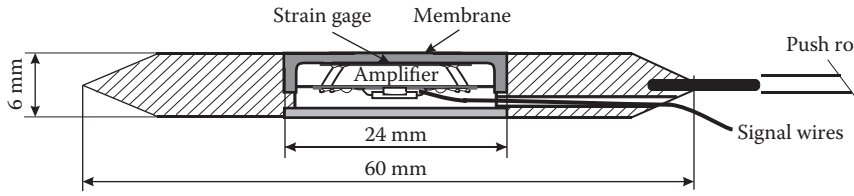

FIGURE 7.3
A membrane for a snow pressure sensor.

FIGURE 7.4
A schematic and a view of a low-profile pressure sensor for snow measurements.

sensor, so that the sensors could be supplied by a +5-V battery to simplify their use in field conditions. One of the four low-profile sensors is shown in Figure 7.4

7.2.2.2 Portable Data Acquisition System

A data acquisition device is an integral part of a typical measuring system. It can be a computer-based system or a data logger. At low outdoor temperatures, a data acquisition system must be weather resistant. After our test in the low-temperature box (Section 7.2.1), we decided not to use a computer-based system. Instead, we developed a new, processor-controlled system that would support data acquisition for the six-transducer SST in various weather conditions. To ensure resistance against low temperatures, we (1) designed the system to be as small as possible and (2) encapsulated it into a hermetic box.

The system is a processor-based, eight-channel data logger. Its major features are

- Simultaneous acquisition of eight channels (six for the six transducers of the SST)
- Data sampling rate of 100 Hz per channel
- Data storage on internal RAM
- Transfer of data after a single test to a 32-MB flash memory card or external computer via RS 232 port
- Visual Basic software for controlling and handling the system
- LCD display for user interface
- Small size, battery powered

The main board of the system with the LCD display is shown in Figure 7.5. For field use, the system was enclosed in hard foam to protect it against low temperature and moisture. The SST could be electrically connected directly to the data acquisition system. The complete measuring system was battery operated and small enough to fit into a pocket—an important feature for snow stress measurements in mountains.

7.3 Determining Snow Stress under Loading of Grooming Machine

7.3.1 Introduction

Snow packing is the major task of a grooming machine. The surface of a good ski piste should have enough mechanical strength to bear skier loads. Multiple passes over a snow surface with a grooming machine can produce the desired surface. As discussed in Chapter 1, soil compaction can be modelled on soil stress state analysis. Similarly, we can assume that snow can also be modelled with snow stress data. In this section, we apply the soil stress measurement method to snow.

7.3.2 Experimental Set-Up

The experiment with a grooming machine was performed in a mountainous area at approximately 1700 m above sea level (Figure 7.6). The region inside Tatra National Park is extensively used by alpine skiers. On the day of the tests, the sky was 8/8 clouded, snow was falling, and the air

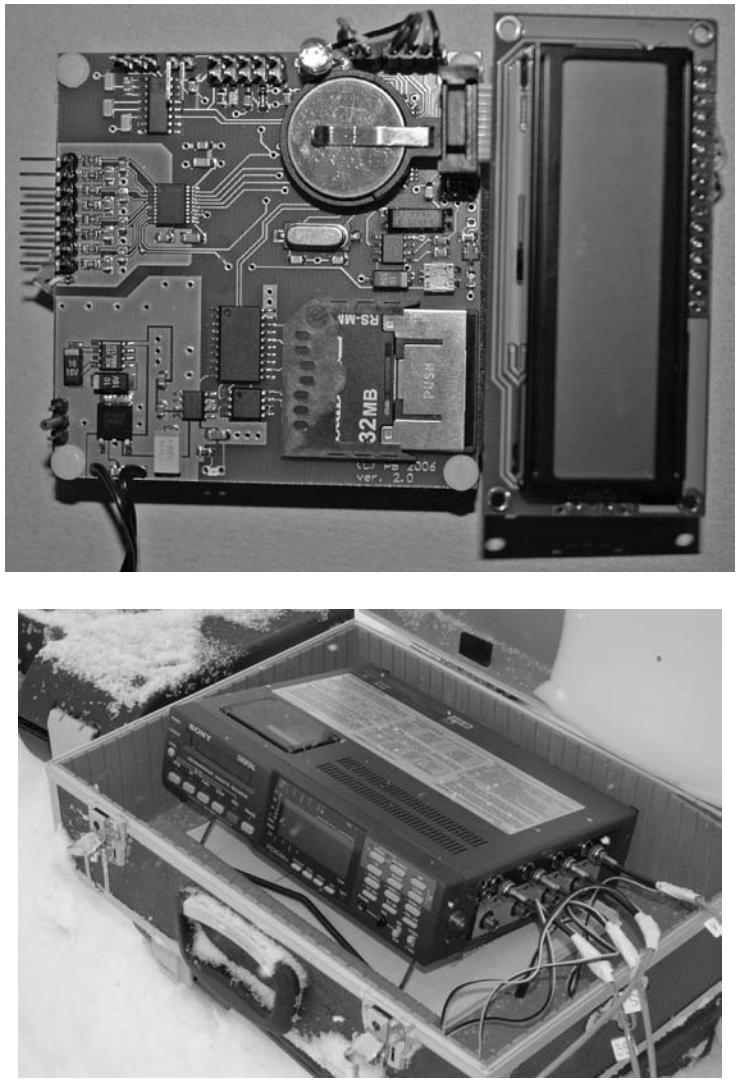

FIGURE 7.5
Portable data acquisition system (top) and a digital tape recorder (bottom) for use with snow pressure sensors.

temperature was –6°C. The snow temperature where the tests took place was –1.9°C, snow depth was 170 cm with a 7- to 10-cm layer of freshly fallen snow.

Snow density was determined by a time domain reflectometry (TDR) method using a portable TDR-meter produced by The Institute of Agrophysics, Lublin, Poland. Based on measured values of electrical

FIGURE 7.6
Experimental site in the Tatra Mountains.

permittivity of snow at four different depths, snow density was obtained from Looyenga's formulae with an assumption of ice permittivity equal to 3.15 (Stacheder 2005):

$$\varepsilon_{snow} = \left(W\varepsilon_w^{\alpha} + I\varepsilon_{ice}^{\alpha} + A\varepsilon_{air}^{\alpha}\right)^{\frac{1}{\alpha}} \tag{7.1}$$

where W indicates water content, I is the ice fraction, A is air in snow, ε_w is water permittivity, ε_{ice} is ice permittivity, ε_{air} is air permittivity, and α equals 0.3. Snow density was calculated knowing that

$$W + I + A = 1 \tag{7.2}$$

and assuming that W equals 0. Table 7.1 includes final values for snow density at four different depths before test rides; the use of the TDR-meter is shown in Figure 7.7.

Snow stress measurements were carried out on a flat, horizontal surface. We used four of the low-profile transducers that we developed for snow (Section 7.2.2.1). Four 2-m long Kevlar push rods installed the sensors in the side of the snow profile at four depths (10, 20, 30, and 40 cm), as pictured in Figure 7.8. This method was used instead of coring, to allow

TABLE 7.1
TDR Readings and Snow Density Data

Depth	0 to 10 cm	10 to 20 cm	20 to 30 cm	30 to 40 cm
TDR (ε)	1.07	1.17	1.25	1.46
Density (kg/m^3)	129	311	447	778

FIGURE 7.7
Measuring electrical permittivity of snow with the TDR-meter.

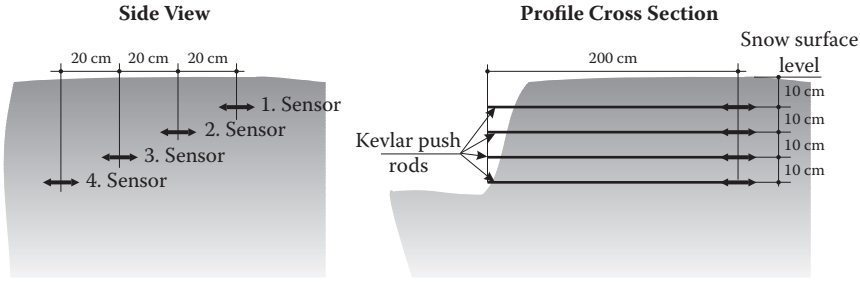

FIGURE 7.8
Installation of the low-profile sensors in snow for the grooming-machine tests.

TABLE 7.2

Technical Data for Vehicles Used in Experiments

Vehicle	Tyre Track (m)	Total Mass (kg)	Wheel Load (kN)/ Contact Pressure (kPa)	
			Front	Rear
4 × 4 Truck	12.00 × 20	5.560	16.90	10.1
Grooming machine	2 × 1.318 × 4.140	8.411	7.7	

minimum disturbance of the snow structure before measurements. The portable data collector described above (Section 7.2.2.2) was used without PC support. Data acquisition is possible at 1 or 2 kHz frequency. The whole system was extensively tested before the experiment because repairs and technical support were not available at the remote field location.

The snow-grooming machine used in this experiment is shown in Figure 7.6; Table 7.2 lists basic technical data. The vehicle was driven at a speed of ~3 to 5 km/h. The experiment consisted of six forward and reverse passes to describe the effects of multiple tracking.

7.3.3 Results

Figure 7.9 shows a sample set of snow stress curves from the tracked vehicle. We can see indicated snow stresses versus time or track position for the first pass through fresh snow and the third pass. The time curves of snow stresses exhibit six peaks due to the road wheels of the vehicle, indicating that stresses magnify under road wheels. This result does not agree with some theoretical predictions stating that stress distribution under a tracked vehicle should be more evenly distributed, but it agrees with most experimental data.

We can also notice a significant increase of stress values indicated by sensor 1 (10-cm depth) for the third pass. Table 7.3 shows peak values of snow stresses for each sensor for the six successive passes of the six road wheels. The effect of successive passes is significant for the snow stresses measured by sensor 1 (10-cm depth), especially within the first four passes, while for the other three sensors (at depths of 20, 30, and 40 cm), changes in stress values are pronounced only between the first and the second passes.

For the third through sixth passes, snow stresses decrease, but not much. This can be explained as a result of multiple shearing of snow that leads to weakening, but this explanation requires knowledge of snow deformation along with the stresses.

We calculated the average stress, which is a mathematical mean of all readings within a range when a sensor gives non-zero signals. This average stress can be identified with a theoretically predicted stress by an

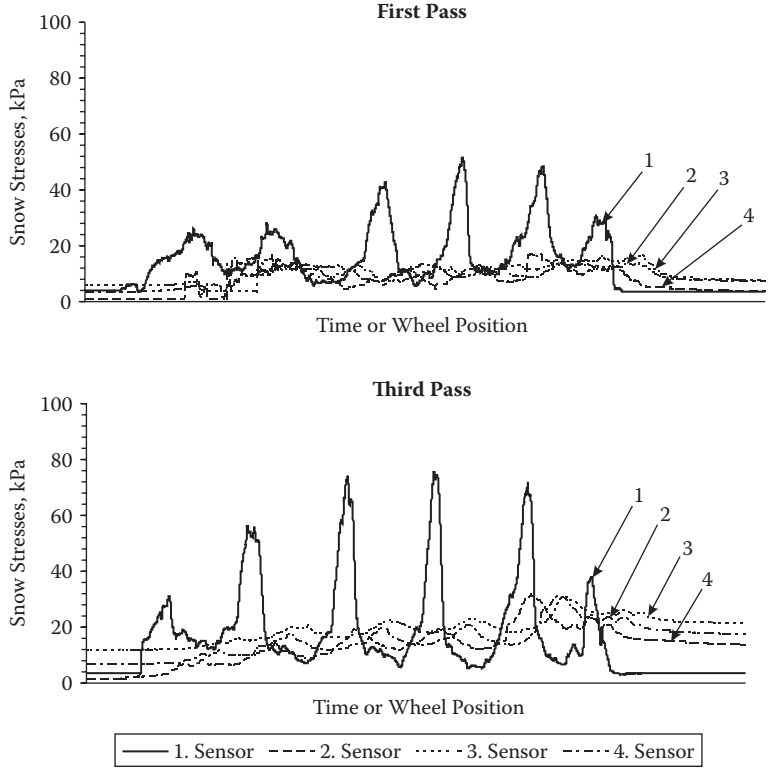

FIGURE 7.9
Sample snow stress curves determined under the tracked grooming machine.

assumption of a flat pressure distribution under a track. Figure 7.10 presents values of average snow stresses for the six passes and four sensors; they are much lower than peak values (about 30% to 40% of the peak value of sensor 1 and 50% for the other sensors). The average stress may provide an additional measure of the impact of a vehicle on a surface, similar to the MMP concept (see Chapter 5).

We then used the calculated values of average stresses for further analysis that introduced a stress concentration coefficient. This measure was defined by a simple relationship of a maximum peak stress value to average stress value; Figure 7.11 illustrates this. Note that successive passes and the depth of the snow affect the concentration of snow stresses under the road wheels of a machine. Data from sensor 1 at 10-cm depth shows the concentration is more intensive for the successive passes, ranging from about 2.85 (first pass) to 5.65 (sixth and final pass).

This effect for the other deeper sensors is not as significant, and the values of concentration coefficient ranged from 1.12 to 2.56. This suggests

TABLE 7.3

Peak Values of Snow Stresses (kPa) under Loading (Wheels I through VI) of Grooming Machine

Sensor (Depth)	I	II	III	IV	V	VI
First pass						
1 (10 cm)	25.6	27.7	42.2	51.3	47.4	30.1
2 (20 cm)	10.1	15.2	10.9	12.7	17.3	12.5
3 (30 cm)	16.3	12.7	12.2	13	14.7	16.2
4 (40 cm)	15.8	12.6	13	11.9	13	13.5
Second pass						
1	42.8	45.2	43.3	53.2	58	68.3
2	14.4	23.2	27.1	33.1	34.6	0
3	12.9	22.3	23.8	35.1	24.5	0
4	10.7	12.6	15.7	27.4	52.8	45.3
Third pass						
1	29.8	56.5	73.4	74.8	71.6	36.7
2	7.81	16.4	18.9	19.4	31.5	25.4
3	15.8	19.6	22.4	23	29.8	25.5
4	1.1	17.8	19.6	20.6	30.9	23.5
Fourth pass						
1	56	62.4	64.5	88.9	92.8	35.4
2	15	19	18.5	24.3	25	20.7
3	19	21.7	24	26.5	23.8	19.9
4	14.3	16	17.4	20.7	22.5	22.8
Fifth pass						
1	48.6	60.9	70.6	43.8	30.2	24.8
2	10.3	18.8	25.7	24.8	25.8	18.2
3	16.2	19.6	20.9	22	22.7	18.5
4	13.1	18.2	21.3	22.6	22.3	16.3
Sixth pass						
1	16	21.2	83.8	56.2	44.8	24.4
2	10	12.8	17.6	17.9	22.8	17.7
3	12	16.2	19.8	21.4	21.1	21.7
4	9	12.5	18	19.8	25.1	22.4

that stress concentration under road wheels occurs mainly in the upper layers of a snow pack, where the snow is highly compacted and hardened by machine-generated high stresses. Lower layers, on the other hand, are less compacted, resulting in lower concentration of stresses. It would be worthwhile to support these stress measurements with simultaneous measurements of snow deformations.

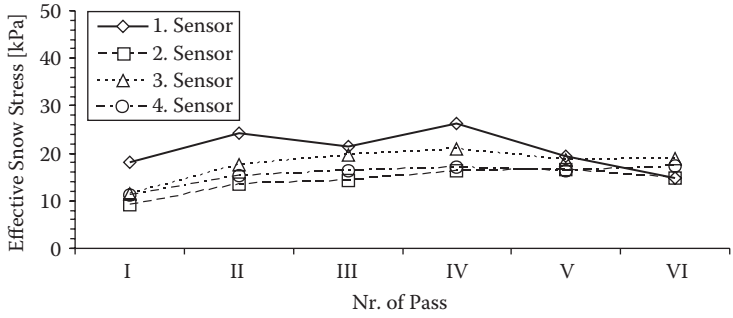

FIGURE 7.10
Average snow stresses for the six passes and four sensors under the tracked grooming machine.

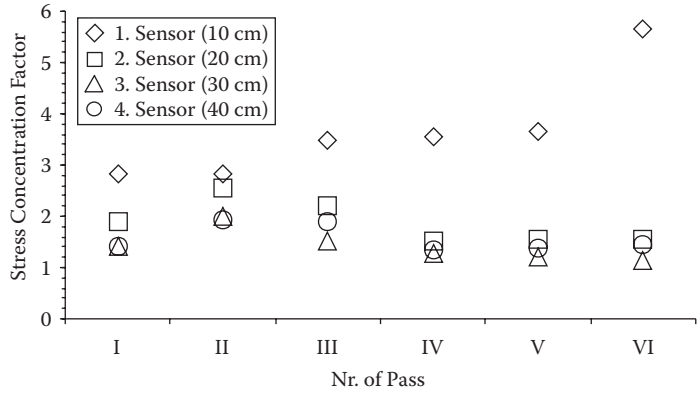

FIGURE 7.11
Relationship of maximum peak stress values to average stress values under the tracked grooming machine.

7.3.4 Summary

Vertical snow stresses under the grooming machine were measured at four depths (10, 20, 30, and 40 cm) in natural deep snow. Typical strain gage type pressure sensors were used in the experiment, but we developed a special low-profile sensor case for easy installation in snow. A major difference between fresh, loose snow and soil is that snow disturbed during transducer installation cannot return to its initial conditions (density, structure). This characteristic requires a reliable installation method.

7.4 Determination of Winter Traction and Snow Stresses under Military Truck Loading

7.4.1 Introduction

A classic analysis of off-road vehicle mobility and traction uses the soil pressures generated by a vehicle. This measure is well correlated with traction forces (drawbar pull, vertical reaction, and side forces), so a number of off-road mobility models are based on soil pressures. We completed several experimental studies on soil stress determination under loads different vehicles; these are documented in previous chapters and in the literature.

A main purpose of this section is to describe instrumentation for winter tests and measure snow stresses under vehicle loads along with winter traction. One objective was to implement the methods of stress measurements for winter experiments by measuring stresses in shallow snow under wheeled vehicles. This study is a preliminary work intended to answer the following questions:

- Are the methods used previously for soil surfaces good for snow?
- How will the SST and stress transducers function in snow?
- How will all soil stress instrumentation work in winter conditions?
- What are the actual values of snow stresses under loads of vehicles?

7.4.2 Experimental Set-Up

Field experiments with military vehicles were performed at the WITPIS Sulejówek proving grounds near Warsaw, Poland. These tests were carried out in late winter (March) on shallow frozen snow.

A modified SST was used for the experiment. The six pressure sensors were installed in an SST body with water-resistant silicone glue. No additional insulation was applied. The tests were conducted on settled shallow snow, 30 to 35 cm deep. Snow temperature was approximately –0.5°C, and density about 0.6 g/cm^3. Before installation, the SST was exposed to the outdoor temperature for 1 hour. It was installed in snow by a simple method: digging a hole to 30 cm deep, levelling an installation surface, placing the SST, and then filling with the remaining snow, taking care to obtain good contacts between the snow and all six transducers on the SST. The SST, installed at approximately 30-cm depth, was in fact placed on the ground.

Figure 7.12 shows a schematic of the installation, while Figure 7.13 shows the SST placed at depth. Such an installation method was possible thanks to the relatively high strength of the settled and frozen snow. To minimise any effect of transducer installation on the results, the measurements were

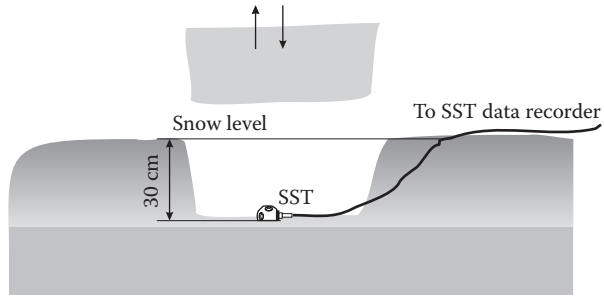

FIGURE 7.12
A schematic of SST installation in snow at a depth for the truck tests.

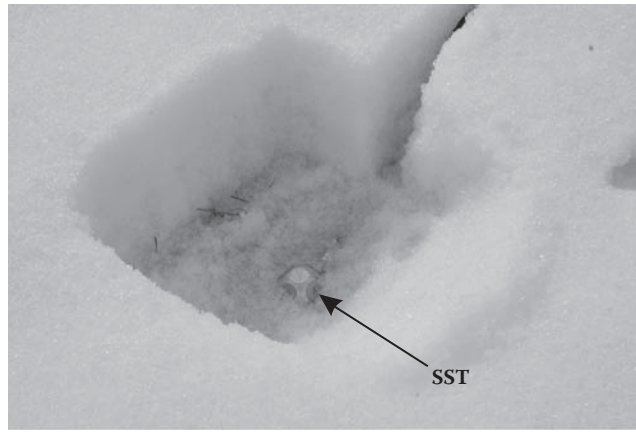

FIGURE 7.13
The SST emplaced in the measuring point for the truck tests.

postponed for 1 to 3 hours to allow for sintering processes to reconstruct the snow structure. After each test of two runs (driving and rolling), the SST was reinstalled in a new location. The SST installation was based on experience with soil stress measurements. The method of transducer installation is still a concern.

Snow pressures were captured with an industrial portable computer with a multi-channel data acquisition card. The computer could be stored in a vehicle to prevent freezing during operation.

The vehicle used for the test was a 5.6-tonne 4×4 military truck (Figure 7.14) used for experiments described in Chapter 4. The vehicle was equipped with all-season tyres inflated to 500 kPa. The tests were carried out at low speed, approximately 5 to 8 km/h.

We determined snow stresses for two driving (wheel slip) and rolling modes. In the driving mode, the test vehicle pulled an additional braking

FIGURE 7.14
A 5.6-T 4 × 4 military truck used as a test vehicle.

vehicle to generate high drawbar pull and wheel slip that were also measured. In the rolling test, the vehicle was pulled backward by the braking vehicle, also at low speed. One test consisted of two runs—one driving and one rolling—on the same track. After each test, the vehicle was moved to another track where the snow cover was undisturbed.

To determine winter traction, the test vehicle was instrumented with a load cell for drawbar pull force measurements, an optical sensor for speed monitoring, and a tachometer to measure road wheel rotations. Traction curves were created from the measured vehicle data for each test ride. Dąbrowski et al. (2006) developed the procedure and methodology for the traction curves. In brief, a full slip range of 0% to 100% was divided into twenty 5% sub-ranges and a maximum F_{DBP} found in each sub-range. A typical traction curve therefore consists of twenty points in s–F_{DBP} coordinates. Also, rolling resistance of the test vehicle was measured with the load cell when the test vehicle was towed by the braking vehicle.

7.4.3 Results and Discussion

7.4.3.1 Snow Stress Curves

Figures 7.15 and 7.16 plot stress state components and continuous functions of time (or wheel position) for the driving and rolling modes. Two groups of peak values correspond to two wheels of the vehicle. From left to right in Figure 7.15, stresses under front wheels first appear first, then those under the rear wheels. The order is reversed in Figure 7.16; the vehicle was pulled backward for the rolling run.

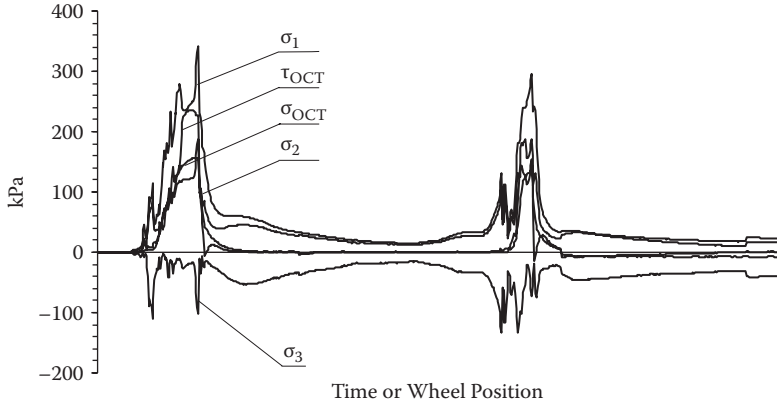

FIGURE 7.15
Snow stresses under wheel loads at driving for a 5.6-T 4 × 4 truck.

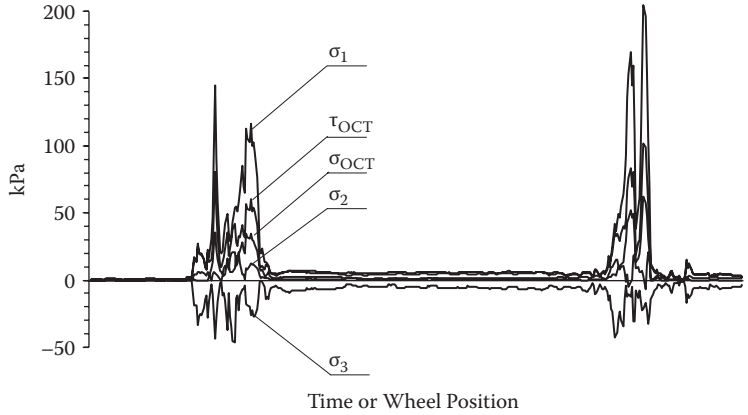

FIGURE 7.16
Snow stresses under wheel loads at rolling for a 5.6-T 4 × 4 truck.

The highest indicated stress is the major principal stress σ_1. All other stresses showed similar trends, but reached markedly lower values. Stress relaxation between the wheels is noticeable, although the stresses do not reach 0. Especially during rolling, the resting stresses after the pass of the front wheel are high and decrease slowly.

7.4.3.2 Analysis of Peak Snow Stresses

Table 7.4 contains numerical data of peak stress values from five driving and two rolling tests chosen for the analysis. We performed more tests,

TABLE 7.4

Peak Values of Snow Stresses under Loads of 5.6-Tonne 4 × 4 Truck Wheels

Wheel	Pass	σ_1	σ_2	σ_3	σ_{OCT}	τ_{OCT}
Driving						
First	1	337.2	94.3	–112	96.78	174.2
	2	296.3	85.41	–87.4	93.72	161
	3	116.7	20.47	–46.38	34.62	60.32
	4	291.3	49.38	–106.4	78.42	156.9
	5	257.8	162.6	–122.7	30.5	174.2
	Mean	259.86	82.432	–94.976	66.808	145.324
Last	1	336.9	168.6	–249.7	85.88	202.4
	2	279.9	115.3	–104.7	88.28	146.8
	3	204.4	20.62	–42.95	61.89	101.3
	4	337.2	176.6	–110.9	93.56	189.3
	5	272.1	96.77	–74.3	40.12	129.7
	Mean	286.1	115.578	–116.51	73.946	153.9
Rolling						
First	1	341.5	234.3	–101.4	156.1	187.7
	2	318.4	223.4	–122	150.6	174.4
	Mean	329.95	228.85	–111.7	153.35	181.05
Last	1	295.4	186.7	–132.4	136.8	154.2
	2	288.3	183.9	–222.7	84.21	189.8
	Mean	291.85	185.3	–177.55	110.505	172

but some of them failed. Generally, peak snow stresses under wheel loads were higher at rolling than at driving. This can be caused by the effect of snow compaction in the first driving pass; rolling passes followed back along the same track for each test run. Stresses in compacted snow are higher, especially when the snow is shallow. The relationship of peak values under front and rear (first and last) wheels between driving and rolling also changed: snow stresses under last wheels are higher than under first wheels at driving, while stresses under first wheels are higher at rolling.

7.4.3.3 Snow Stresses versus Soil Stresses

Figure 7.17 compares peak stress values in snow and in some soil surfaces. The soil data were obtained with the use of the 5.6-tonne 4 × 4 truck, so the wheel loads are identical. The results show that stresses generated in settled shallow snow are between the levels of stress for sandy soil and turf surfaces. Snow is much more deformable and its deformations are much larger than deformations of soils. Thus stress results alone, without

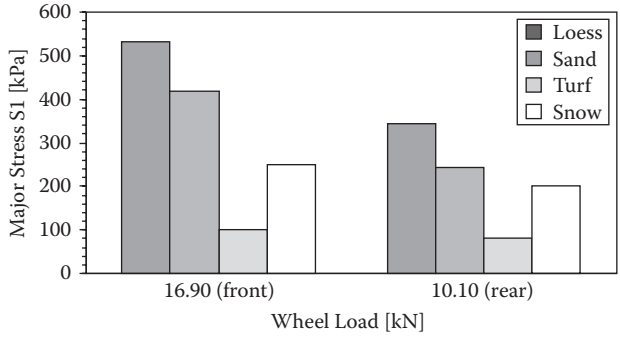

FIGURE 7.17
A comparison between snow and soil surfaces for a 5.6-T 4 × 4 truck: peak values of the major principal stress σ_1.

information about resulting deformations, cannot give complete information on mechanical characteristics and traction of a given surface.

7.4.3.4 Winter Traction

Figure 7.18 presents an example set of winter traction results obtained for the 5.6-tonne 4 × 4 truck. These are (1) raw vehicle data (pull force, forward velocity, and wheel rotation as functions of time); (b) drawbar pull; and (c) traction curve. The figure summarises the captured data. The curve is typical for snow traction: a maximum at approximately 20% to 40% slip, then dropping to 0 pull at higher slip values.

7.4.4 Conclusion

Snow stress state under loads of a 5.6-tonne 4 × 4 military truck was determined with the use of a stress state transducer (SST) at 30-cm depth. The stresses were determined in settled shallow snow at driving and rolling. The instrumentation was examined and modified for low temperatures before the tests. The most significant findings were

- Standard soil measurement instrumentation (SST, data acquisition system, PC notebook) is not suitable for winter measurements, mainly because of the effect of low temperature on the computer systems.
- SST measurements conducted after some improvements indicated that snow stress magnitude after one pass of a vehicle lies between sandy soil and turf surfaces.

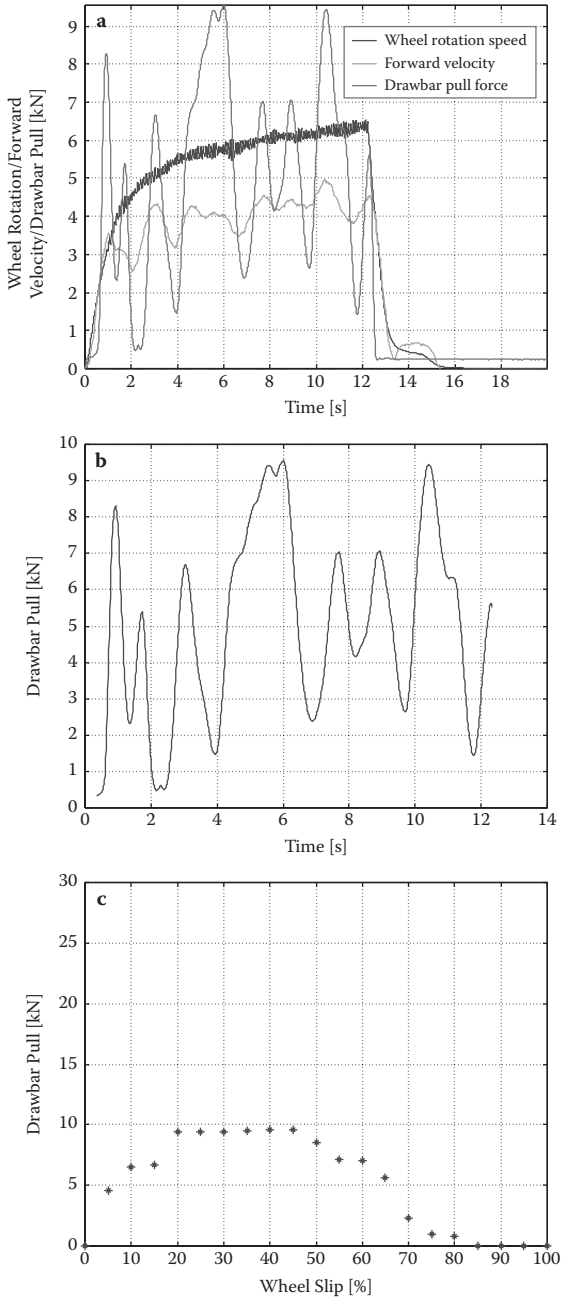

FIGURE 7.18
Traction data obtained in the tests with a 5.6-T 4 × 4 truck: (a) raw vehicle data, (b) drawbar pull as a function of wheel slip, (c) a final traction curve.

- Snow deformations must be determined together with stresses because of the high level of compressibility of snow.

Further research should focus on various snow conditions; our study was done on relatively hard, settled snow.

7.5 Effects of Snow Skis on Snow Stresses and Aircraft Ground Performance

Skis in the place of wheels improve ground performance of an aircraft on a snow-packed airfield or on deep, fresh snow. As in soft soil, intensive surface deflection causes high resisting moments on the wheels and may create a dangerous nose-down action for the aircraft. A major advantage of a ski is that its contact area is several times that of a typical aircraft tyre so the contact pressure is significantly lower. A typical ski design—a slender rectangular shape with straight grooves or a keel strip along centre of the bottom—also helps provide longitudinal stability during ground roll.

Aircraft with skis are widely used in northern regions including Canada, the United States, Scandinavia, and mountain regions in Europe such as the Alps. In Poland and other European countries, skis are used mainly on multipurpose aircraft but they are also popular for sport aircraft used for sailplane towing, especially in mountain regions. In northern territories with year-round snow cover, skis are permanently installed. Skis can also be mounted with the wheels and the pilot can retract the skis via a mechanical system; this optional use of skis is especially good for areas with irregular snow cover.

We expect that lower contact pressure would improve stress distribution in snow under ski loading in comparison to wheels. Consequently, motion drag should also be lower for an aircraft equipped with skis. The purpose of this study was to measure the effects of skis on snow stresses under loads and on sliding drag of the Wilga aircraft.

7.5.1 Experimental Methods

The Wilga aircraft was used (see Chapter 6) with a combined ski and wheel system. Skis for this aircraft measure 1.75×0.50 m (length $\times$ width) and are mounted to the wheel axle, as shown in Figure 7.19. A pneumatic system powered by an on-board high-pressure system raises or lowers the skis remotely. Additionally, a small 0.75×0.26-m ski was installed along

FIGURE 7.19
Skis mounted on the Wilga aircraft.

with the tail wheel. We measured resistance and snow pressure for two options: the aircraft on wheels and on skis.

For towing resistance measurements, a tractor vehicle with on-board instrumentation (load cell, A/D converter, and data acquisition system) towed the Wilga aircraft with four persons on board at 3 to 5 km/h forward speed (Figure 7.20) about 500 m over undisturbed snow. Four tests were completed: two with wheels and two with skis. Figure 7.21 shows

FIGURE 7.20
Measuring towing resistance of the Wilga with and without skis on snow.

FIGURE 7.21
Placing the snow stress transducers in the depth for the Wilga test.

preparation for snow pressure measurements performed with the use of one low-profile pressure cell installed at 10-cm depth. To measure snow pressure, the aircraft was pulled so that the right ski (or wheel) slid over the sensor.

On the day of the test, the air temperature was 0°C and an active cold front produced occasional snowfalls. There was a 25- to 30-cm cover of fresh, wet, partially frozen snow. Snow density was 450 kg/m^3.

7.5.2 Results

Figure 7.22 shows time curves of snow stresses under loading of the wheels and skis. The difference is significant. Peak maximum stress under the wheel was almost six times greater than stress under the ski. The snow stress curve under the wheel is typical and similar to those we obtained in tests with wheeled vehicles. The curve indicates slow stress relaxation that may have been caused by wet, partially frozen snow. During compaction, the structure and crystals of wet snow are damaged by destructive metamorphism. Air is pressed out and water from melting fills thin pores. The resulting capillary action adds to snow viscosity.

Mechanical processes, deformation, and stress distribution are therefore significantly affected by time. The snow stress curve under ski loading (lower graph of Figure 7.22) has an almost rectangular shape. Such a stress distribution is better for traction. Calculated mean contact pressure was approximately 7 kPa, and the mean value of indicated snow

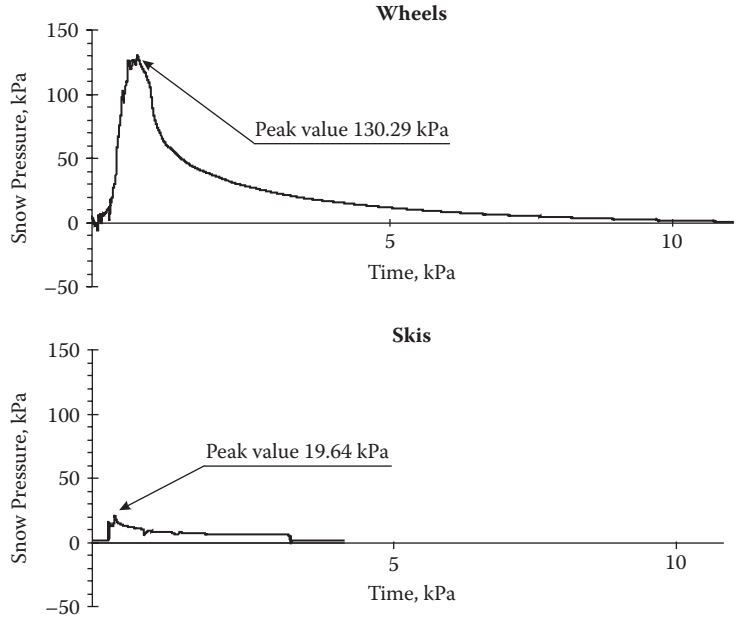

FIGURE 7.22
Snow stress under loads of the Wilga on the wheels (top) and with skis (bottom).

stress (average from all measuring points) was 7.93. The ski helped stress distribution in snow.

We also determined motion resistance (drag). Figure 7.23 presents the results. The upper graph shows a time curve of rolling resistance of the aircraft on wheels and the lower graph depicts the curve for skis. The difference in resistance between the two gear types is not significant: 158.06 N on skis versus 150.87 N on the wheels. We expected lower sliding resistance with the skis, but the effect of the ski may have been weakened by shallow and wet snow.

Analysis of the shapes of the time curves indicates that skis may improve the longitudinal dynamics of motion. The standard deviation of drag values is significantly lower for skis compared to the wheels. The amplitude of indicated forces is much smaller for the ski-equipped aircraft. That may be a result of the effects of ground surface roughness on the wheels. Wheels generate high contact pressures and are affected by surface unevenness. This results in fluctuations of rolling resistance. On the other hand, the skis slide smoothly and provide an important advantage during winter flying.

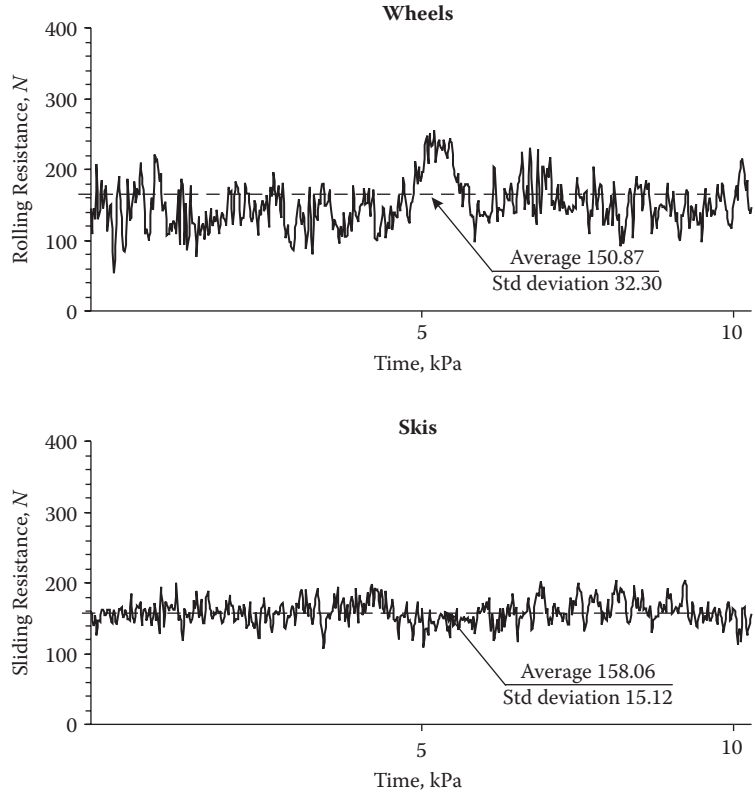

FIGURE 7.23
Motion drag for two variants: on the wheels (top) and with skis (bottom).

7.6 Summary

We have shown that soil mechanics methods are suitable also for snow measurements. Snow stress state can be determined with the use soil pressure instrumentation after minor modification (adding water-resistant insulation). Similarly, we successfully examined winter traction with a typical load cell, velocity sensor, and tachometer combination. The main problems that arose were the effects of low temperatures on power supplies in portable systems. Dry batteries and accumulators are extremely sensitive to temperature drops and it is practical to carry spares.

We obtained results for deep snow stresses under loading of the grooming machine; these values were between 10 and 25 kPa. Peak snow stresses

depend on depth of measurement points: the deeper measurement, the lower the stress. We also saw a significant effect of successive passes.

At 10-cm depth, snow stresses increased especially within the first four passes. For the other sensors at depths of 20, 30, and 40 cm, changes in stress values were pronounced only between the first and the second passes. The absolute peak value recorded for snow stress was 90.2 kPa. For comparison, boot–soil contact pressure is about 40 to 120 kPa and wheel–soil contact pressure can be 150 to 700 kPa. We introduced an average stress term to describe the impact of the machine on the snow surface more precisely than simple peak stresses. We also introduced the stress concentration coefficient. This measure was defined as a simple relationship of a maximum peak stress value to average stress value (Pytka 2010).

We determined snow stress state under loading of a military truck in shallow, compacted snow in freezing and melting conditions for both rolling and driving modes. Generally, snow stress values were comparable to those in previous sandy soil experiments. We also determined vehicle traction, drawbar pull as a function of wheel slip, and rolling resistance. Those results were also similar to those obtained on a sandy soil surface. We studied the effects of skis on snow stress and motion drag of a Wilga aircraft on a shallow snow surface.

In conclusion, we found that the application of the classic terramechanical method of soil stress determination to snow stress measurements can produce good results. Additional research of this issue would be reasonable. The results presented here may be useful in designing parameters for models and validating simulations.

References

Abele G. 1990. *Snow Roads and Runways*. CRREL Monograph 90-3. Hanover, NH: U.S. Army Cold Regions Research and Engineering Laboratory.

Dąbrowski J., Pytka J., Tarkowski P. et al. 2006. Advantages of all-season versus snow tyres for off-road traction and soil stresses. *J. Terramech.* 43: 163–175.

Fauve M., Rhyner H., and Schneebeli M. 2002. *Preparation and Maintenance of Pistes: Handbook for Practitioners*. Davos: Swiss Federal Institute for Snow and Avalanche Research.

Jamieson B. 1999. Skier triggering of slab avalanches: Concepts and research. *The Aval. Rev.* 18(2): 8–10.

Johnson J.B. 2004. A theory of pressure sensor performance in snow. *Hydrol. Proc.* 18: 53–64.

Johnson J.B., Solie D.J., Brown J.A., Gaffney E.S. 1983. Shock response of snow. *J. Appl. Phys.* 73(10): 4852–4861.

Pytka J. 2010. Determination of snow stresses under vehicle loads. *Cold Reg. Sci. Technol.* 60: 137–145.

Shapiro L., Johnson J., Sturm M. et al. 1997. *Snow Mechanics: Review of the State of Knowledge and Applications.* CRREL Report 97-3. Hanover, NH: U.S. Army Cold Regions Research and Engineering Laboratory.

Shoop S.A. 2001. *Finite Element Modeling of Tire–Terrain Interactions.* CRREL Technical Report 01-16. Hanover, NH: U.S. Army Cold Regions Research and Engineering Laboratory.

Shoop S.A., Richmond P.W., and Lacombe J. 2006: Overview of cold regions mobility modeling at CRREL. *J. Terramech.* 43: 1–26.

Stacheder M. 2005. TDR and low-frequency measurements for continuous monitoring of moisture and density in a snow pack. *Int. Agrophys.* 19: 75–78.

8

Modelling of Wheel–Soil System Based on Soil Stress and Deformation State Analysis

8.1 Introduction

Off-road vehicle performance differs from normal performance on paved roads mainly due to soil deformability. Vertical deformation of the soil surface (compression) under a running device increases motion resistance. The cause is a loss of driving energy due to greater rolling drag. Similarly, longitudinal deformation (shearing) weakens driving action as a result of wheel slip and a loss of friction between tyre and soil surface. These effects depend on surface type and condition, and off-road performance results for a given vehicle may vary over a wide range.

There are many methods for predicting off-road performance. An archetypical solution to the problem of wheel action on a deformable surface was derived from Coulomb's yield criterion and Bekker's pressure–sinkage model. Coulomb's yield criterion determines shear resistance of a plane in a granular body (such as soil), and this shear resistance is a function of both internal friction and cohesion:

$$\tau = C + p\,tg(\phi) \tag{8.1}$$

where τ is shear stress, C is soil cohesion, p equals contact pressure, and φ denotes angle of internal friction. Bekker's pressure–sinkage model is

$$p = \left(\frac{k_c}{b} + k_\phi\right) z^n \tag{8.2}$$

where k_c and k_φ indicate soil deformation moduli, b represents tyre (or track) width, z is the rut depth, and n is the soil state exponent. These two basic equations have been extensively modified and applied to wheel– or track–soil systems through the years. The wheel–soil models have performed well, with sufficient efficiency and accuracy for typical engineering applications.

Additional models have been developed from the two basic ones to predict the driving force and the rolling resistance of a wheel on a soil surface; some of these are still in use.

Bekker (1969) devised a set of equations expressing the traction forces, FDR, FRR, and FDBP, that were mentioned in Chapter 4. These forces are functions of stresses in the contact path; it is therefore important to know the distribution of shear and normal stresses over the contact path. Janosi and Hanamoto (1962) modelled the shear stress distribution as a function of longitudinal deformation of soil:

$$\tau = \tau_{\max} \quad e^{-\frac{j}{K}} \tag{8.3}$$

where j is the horizontal deformation of soil and K is the deformation modulus.

The above models are based on physical attributes and can yield good results. The major problem is obtaining the accurate soil stresses needed to calculate the forces. Wulfsohn and Upadhyaya (1992) predicted traction in the soil profile on the basis of two-dimensional (2-D) and three-dimensional (3-D) representations of the dynamic soil–tyre contact area. They assumed a semi-logarithmic porosity–stress relationship for the determination of pressure distribution along the contact path. Muro (1993) presented an analytical method for predicting traction of a rigid wheel on soft ground. In that method, the normal stress and shear resistance applied around the peripheral contact part of the wheel were calculated from a dynamic pressure–sinkage curve obtained in plate loading and unloading tests.

A traction prediction equation introduced by Godbole et al. (1993) used the soil deformation modulus and physical properties of tyres as input parameters. It assumed a non-linear shear stress distribution and change in the values of soil deformation modulus with normal stress. This method, however, requires complex calculations of contact path area.

Wanjii et al. (1997) developed an algorithm for calculation of tractive forces with respect to soil stress distribution derived from Maxwell's model. Soil material parameters needed for calculations are soil elasticity moduli that can be determined in penetration tests with a standard loading plate. The only unknown terms required in this algorithm are horizontal distances from the centre point of the bottom of wheel to the initial and final wheel–soil contact points. A good correlation between model and experimental results was obtained for a sandy–loamy soil.

In this chapter, we use several examples to show how soil stress state data can be used in wheel–soil system modelling. We propose that models or their parameters should be developed based on experimental data. This is an alternative to the classic modelling algorithm, in which experimental

data verifies models only at a final stage of the modelling process. Our approach starts with analysing experimental data for the purpose of creating models. Our aim in this chapter is not to describe complete, ready-to-use models, but to provide ideas on how to derive algorithms from soil stress data.

8.2 Modelling Off-Road Traction

8.2.1 General Description of Model

The above examples of traction prediction methods are relatively simple but they have limitations and uncertainties may appear. Their results are only as good as the precision of stress distribution predictions used for the model calculations. Our idea was to incorporate precise soil stress distribution data into modelling of off-road traction. The traction forces, F_{DR} and F_{RR} (driving force and rolling resistance), can be expressed with soil stresses as arguments:

$$F_{RR} = \int \sigma_{OCT}(\alpha)\, d\alpha \tag{8.4}$$

$$F_{DR} = \int \tau_{OCT}(\beta)\, d\beta \tag{8.5}$$

where α and β are angles of normal and tangential stresses, respectively (Figure 8.1). It is difficult to determine α and β, but for a case of constant speed motion, we can substitute time co-ordinates for these angles.

The two soil stresses—shear and normal—are distributed over a soil volume, not only at the wheel–soil contact surface (as assumed in previous models); therefore, a model that takes that into account is expected to perform better. The first step to create the model is to obtain shear and normal stress distributions that will be used for traction calculations.

8.2.1.1 Shear Stress Distribution

We assume that the total value of shear stress τ consists of two components:

$$\tau = \tau^{I} + \tau^{II} \tag{8.6}$$

where τ^{I} is the shear stress on the contact path and τ^{II} is the shear stress in the soil volume. The first component is determined with the Coulomb equation:

$$\tau^{I} = C + p\ tg(\varphi) \tag{8.7}$$

where C is the soil cohesion, φ represents the angle of internal friction, and p indicates contact pressure. The second shear stress in Equation (8.6) is τ_{OCT} acting along the longitudinal (wheeling) axis:

$$\tau^{II} = \tau_{OCT}\ sin(\beta) \tag{8.8}$$

β represents the angle of the octahedral shear stress (Figure 8.1).

8.2.1.2 Normal Stress Distribution

To calculate rolling resistance, we need to know the normal stress distribution along the vertical axis. In the present method, major normal stress σ_1 and mean normal stress in the octahedral stress system were taken as input data for the calculations. The σ_1 was related to rut depth and the σ_{OCT} represented soil deformations. They were determined together with soil stresses at depths of 15 and 30 cm. The next step was integrating shear and normal stresses; the results were values of drawbar pull. Traction curves $F_{DBP}(s)$ were obtained as below:

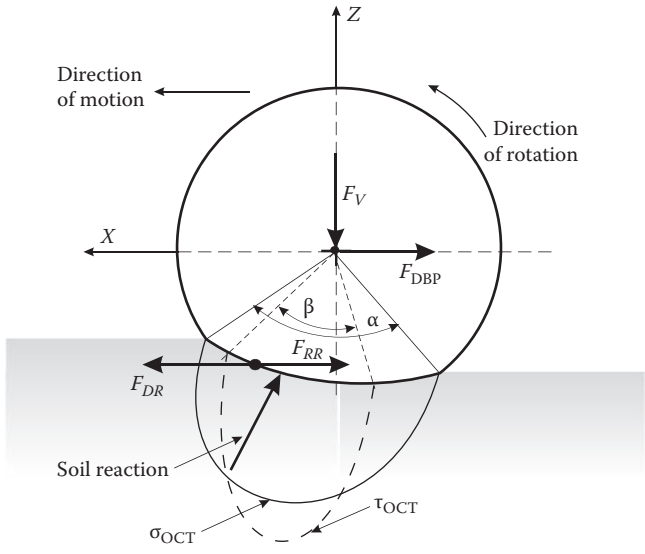

FIGURE 8.1
Traction force diagram as a basis for wheel–soil modelling.

$$F_{DBP}(s) = F_{DBP}^{Peak} \quad 1 - e^{-\frac{j}{K}} \tag{8.9}$$

where j represents soil displacement and K is the soil deformation modulus. All the stress data needed for the calculations (σ_1, τ_{OCT}, $\sigma_{OCT,}$ and β) are determined experimentally with the methods presented in Chapter 2. The next section presents a brief description of field procedures.

8.2.2 Experimental Methods

We measured two groups of data simultaneously: vehicle-related data (drawbar pull, rolling resistance, wheel slip) and soil-related data (soil pressures). These data were captured by two computer systems: one installed in the research vehicle to collect traction-related data, the other in the field to collect soil data. The computers were automatically triggered to collect real-time data. Two military trucks were used (see Chapter 4 and Table 4.1). A 14-tonne 6×6 truck was driven at three loads (empty, 60%, and 100% of total weight) and a 5.6-tonne 4×4 vehicle was driven at empty weight only. The 6×6 truck was equipped with snow tyres and driven over sand and loess soil surfaces. The 4×4 truck had all-season tyres and was driven over sand, loess, and turf surfaces.

The SSTs were placed at the prescribed depths in the centre line of the path of the vehicles' right wheels. Stresses were measured for (1) driving, when F_{DBP} was determined; and (2) rolling, when F_{RR} was determined. Chapter 4 describes the installation of the SSTs in the soil.

A pull test can measure drawbar pull and rolling resistance forces of a vehicle. The idea is simple. In driving mode, an investigated vehicle pulls a braking vehicle for measuring $F_{DBP.}$ In rolling mode, the test vehicle is pulled by the braking vehicle to measure F_{RR}. Forces acting on the entire vehicle (not on separate wheels) can be measured. To determine traction curves [$F_{DBP}(s)$ relationships], wheel slip was determined from the velocity measurement taken simultaneously.

8.2.2.1 Instrumentation

Drawbar pull force F_{DBP} was measured via a load cell mounted to the rear of the investigated vehicle, as shown in Figure 8.2. In addition, the braking vehicle generated a reacting (F_{DBP}) force. The vehicles were connected via an elastic rope, to avoid sudden increases (peaks) of force. Wheel slip was determined from kinematics measurements. An optical sensor mounted to the front of the vehicle measured longitudinal velocity, and a tachometer mounted in the centre of one road wheel (all the axles were locked) counted wheel rotations.

(a)

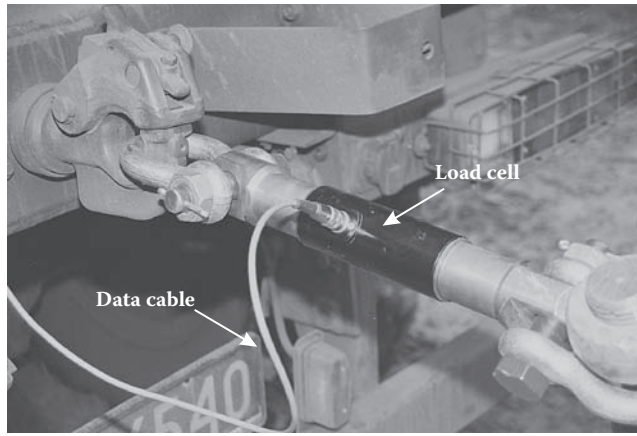

(b)

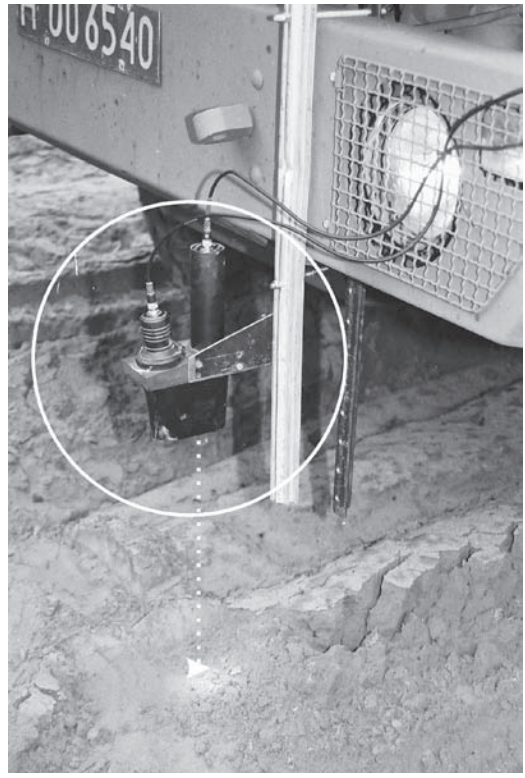

FIGURE 8.2
Instrumentation for the measurement of drawbar pull force: (a) a load cell, (b) a tachometer installed in the centre of a wheel.

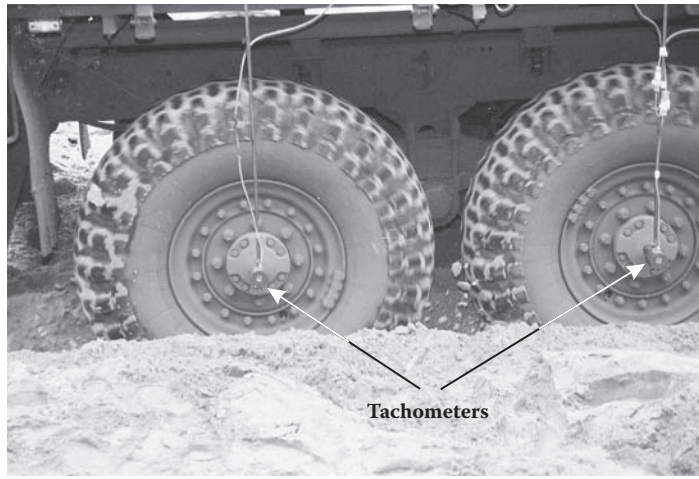

FIGURE 8.2 (continued)
Instrumentation for the measurement of drawbar pull force: the opto-electronic system.

The measurements were performed at low speed, ~5 to 10 km/h. Rolling resistance was measured when the research vehicle was towed by the braking vehicle with a low velocity of ~5 km/h. Experimental data were saved to a mobile computer installed in the investigated vehicle; a portable data recorder (DAT) was used in parallel to provide backup. A 24-V 50-Ah battery provided the power supply for the instrumentation.

8.2.2.2 Procedures

Five to six repetitions were carried out for each truck and driving mode on two soil surfaces. The two connected vehicles started to move approximately 20 m in front of the test point (where the soil instrumentation was installed). At a speed of 5 to 8 km/h, the towed vehicle started to brake, smoothly increasing the braking force. Simultaneously, the test vehicle was controlled to keep constant speed (F_{DBP} increased). When the towed vehicle reached maximum braking force (wheels locked), full power was applied in the test vehicle and the column moved slowly over the test point.

8.2.2.3 Data Reduction

Generally, traction curves are constructed to analyse traction over a given surface. This is a relationship between drawbar pull force F_{DBP} or net traction μ and percentage of wheel slip s. Here we constructed a final traction curve from averaged values of F_{DBP} for the repetitions of all the experiments together. The full wheel slip range of 0% to 100% is divided into 20

sub-ranges of 5%, and the average value of F_{DBP} at each wheel slip range from all repetitions is noted on the graph. A general example is presented at the top Figure 8.3. The raw graph shows F_{DBP} readings for all repetitions and after the averaging process. The final state of the traction curve is presented in the bottom graph.

To obtain optimum traction conditions, the data were further reduced. Shoop et al. (1994) compared traction determination techniques and

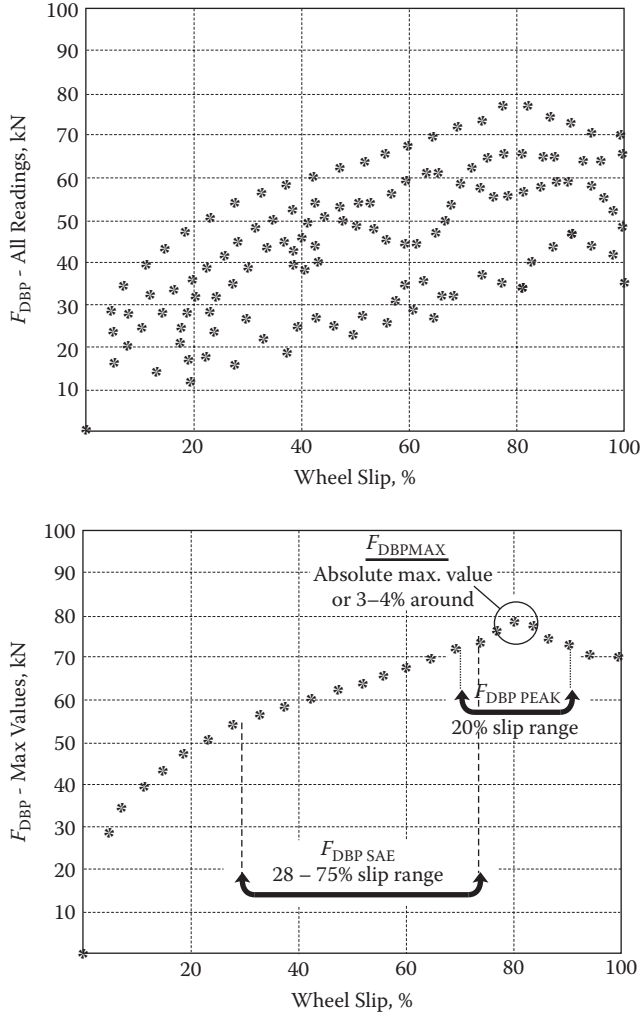

FIGURE 8.3
A set of typical traction data: a raw graph with all FDBP readings for all repetitions and after the averaging process (top graph) and the final state of the traction curve (bottom).

methods to derive traction curves from experimental data and analyse traction data. Several methods can determine optimum traction from a typical traction curve:

μ_{max} = Absolute maximum value of net traction on a curve throughout a full slip range

μ_{peak} = Peak maximum value averaged from a 3% range around the absolute maximum

$\mu_{12\%}$ = Net traction at 12% slip

μ_{sae} = Average net traction from a slip range of 28% to 75%

From these methods, a traction coefficient F_{peak}/W was chosen as the most suitable for terrain traction applications. In this method, traction is determined by averaging the peak F_{DBP} values. Those average values divided by vehicle weight W yield the traction coefficient μ_{peak}. We also analysed peak maximum values of F_{DBP}/W or μ_{max}. Towed motion resistance was averaged from peak maximum values.

8.2.3 Results

Traction curves calculated for the 14-tonne 6×6 truck running on loess (left column) and sand (right column) are shown in Figures 8.4 and 8.5. The experimental results are also depicted to compare and verify the model. Figure 8.6 presents a comparison between measured and predicted F_{DBP} values for the 5.6-tonne 4×4 truck.

Predicted traction data are similar to experimental data, but differences exist. *T*he model underestimates traction at the lower slip range for sandy and loess soil surfaces and at the full slip range for turf. The reason may be the soil coefficients (*C*, *K*, and φ) *t*aken from the literature for similar soils.

8.2.4 Reconstruction of Model Based on Soil Stress State Data

An alternative method uses stress state data to reconstruct and identify parameters for the model. The second shear stress in Equation (8.6) can be determined based on Boussinesq's model:

$$\tau^{II} = \nu F_V (2\pi r^2)^{-1} \cos^{\nu-1}(\beta)\sin(\beta) \tag{8.10}$$

where β is the angle of shear stress (Figure 8.1), ν is the stress concentration factor, and F_V denotes vertical load on a wheel.

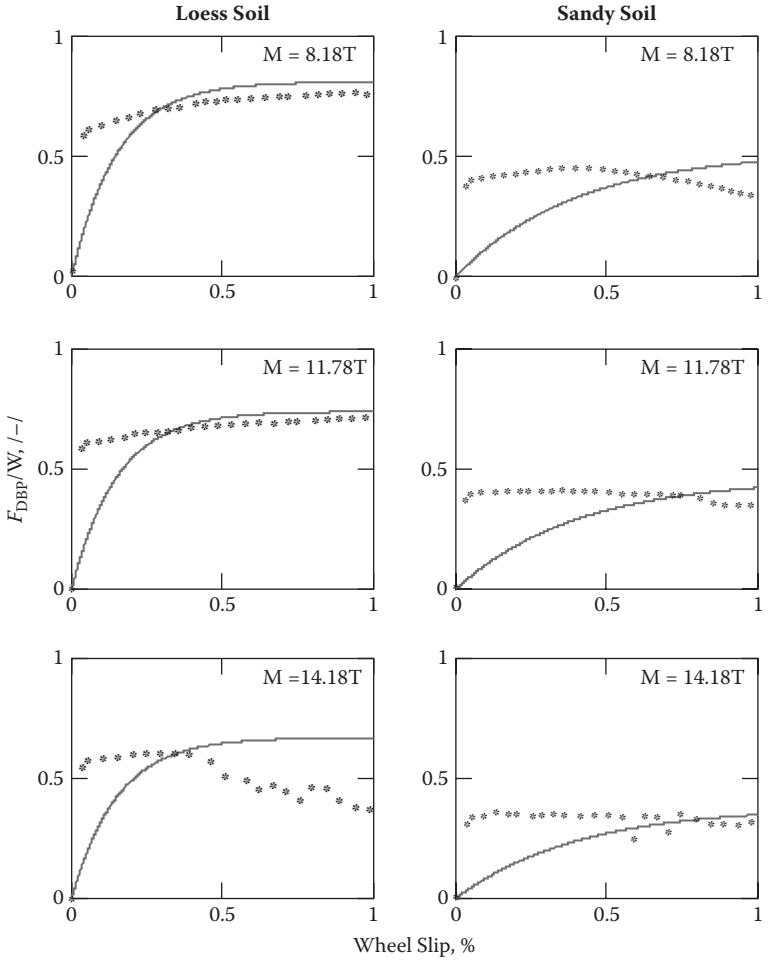

FIGURE 8.4
Predicted (lines) and measured (stars) traction curves for the 14-T 6 × 6 truck running on loess soil (left column) and sandy soil (right column). The graphs from the top down are for increasing vehicle weight (8.18 T, 11.78T, and 14.18T). The vehicle was equipped with all-season tyres.

8.2.4.1 Normal Stress Distribution

To calculate the rolling resistance, normal stress distribution along the stress path is needed. This measure can be calculated from Boussinesq's model:

$$p = \nu F_V (2\pi r^2)^{-1} \cos^{\nu}(\beta) \tag{8.11}$$

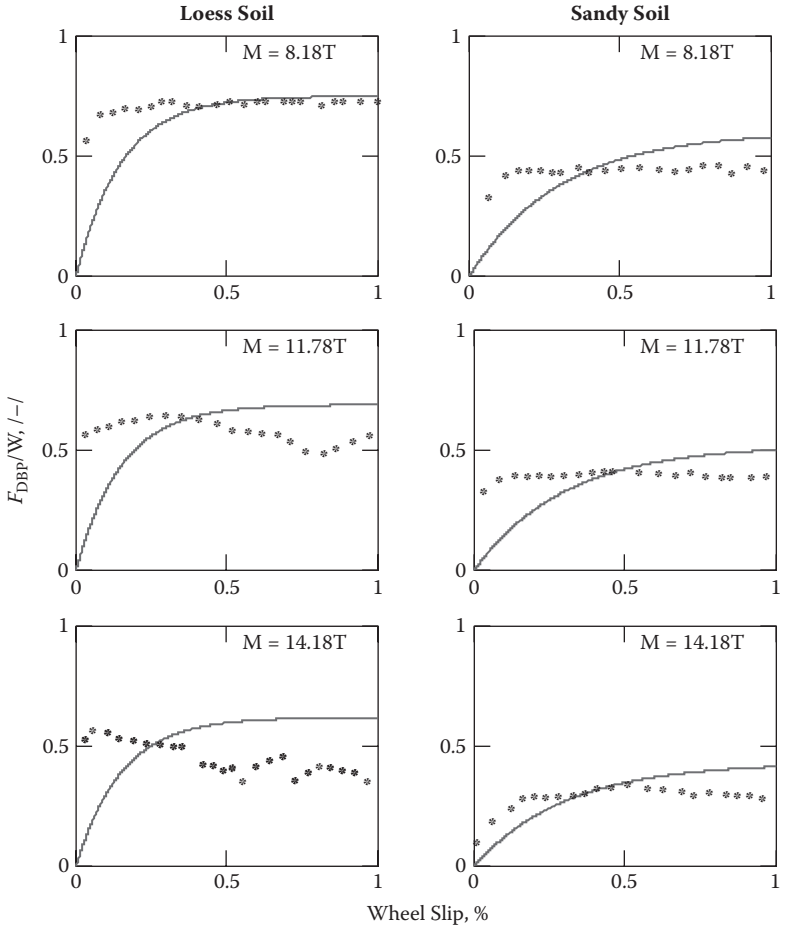

FIGURE 8.5
Predicted (lines) and measured (stars) traction curves for the 14-T 6 × 6 truck running on loess soil (left column) and sandy soil (right column). The graphs from the top down are for increasing vehicle weight (8.18 T, 11.78T, and 14.18T). The vehicle was equipped with snow tyres.

The problem here is to determine stress distribution in a semi-infinite body subjected to an external force acting on a point on the body surface. Equations (8.10) and (8.11) are Boussinesq's solution to the case for wheel–soil interaction for which this model is often used. In the analysis of stresses in soil in Chapter 4, we assumed that the normal pressure can be replaced by octahedral normal stress σ_{OCT}. The two measures tend the same way and have very similar values. The next step was integrating

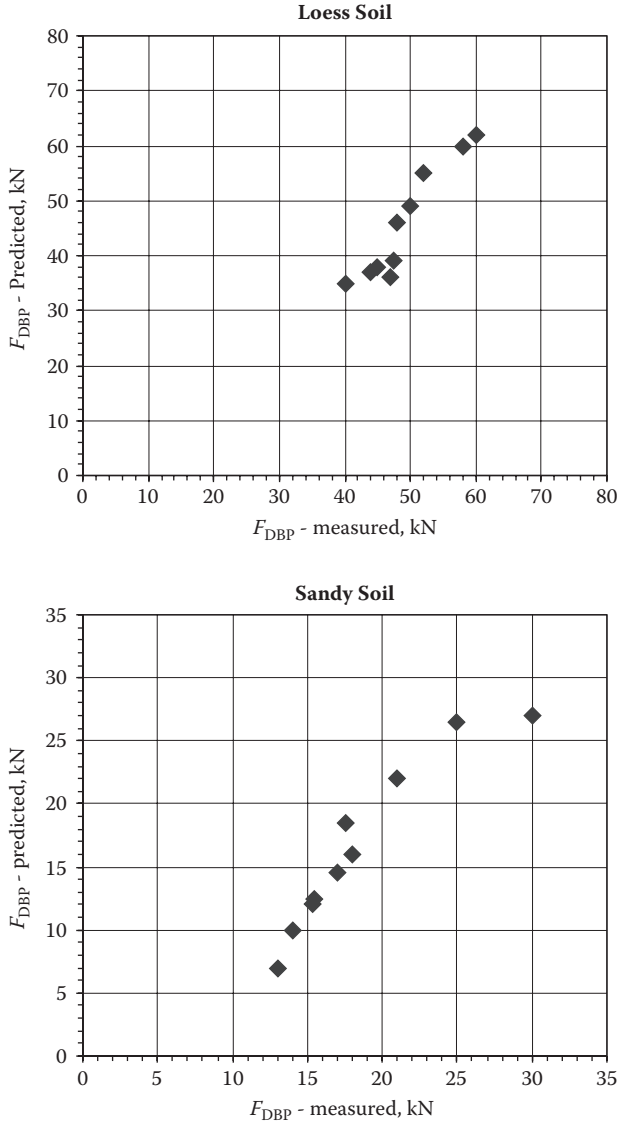

FIGURE 8.6
A comparison between predicted and measured values of drawbar pull for the 5.6-T 4 × 4 truck running on sandy and loess soil.

shear and normal stresses to produce values of traction forces. Finally, traction curves $F_{DR}(s)$ can be obtained as below:

$$F_{DR}(s) = F_{DR}^{Peak} \quad 1 - e^{-\frac{j}{K}} \tag{8.12}$$

where j represents soil displacement and K is the soil deformation modulus. Parameterisation of the models normally uses estimates of soil constants (C, φ, K, k_c, k_α, n). These parameters can be obtained from shear and compression tests performed on small soil samples or from a bevameter. Our current idea, however, is to reconstruct the model with the soil stress state data obtained in field experiments.

8.2.4.2 Experimental Methods

The experimental set-up is identical to that of the previous approach (Section 8.2.2) except for determination of (1) soil surface deformation and (2) soil stress state for two directions: compaction and traction. Two SSTs are installed to obtain sufficient data to reconstruct the proposed model (Figure 8.7). One SST is placed to obtain traction data; it is rotated about

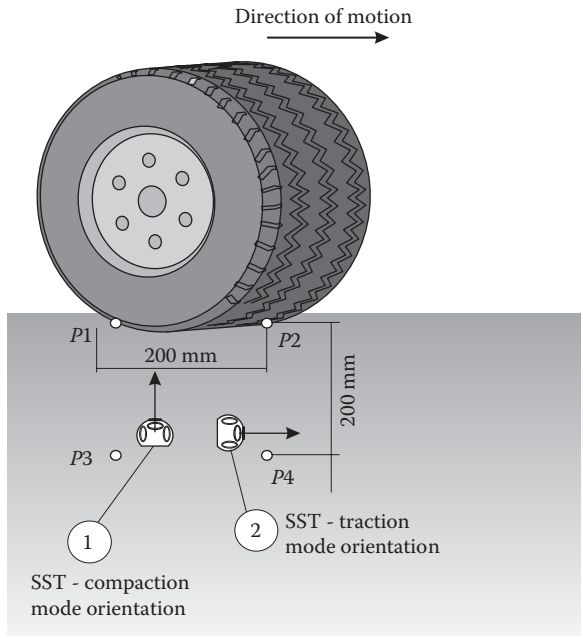

FIGURE 8.7
A schematic of the SST installation in soil.

90° (complying with the model equation expressing the driving force). The second SST is placed to obtain compaction data. This is a typical installation (complying with the model equation describing rolling resistance). The model equations are described in subsequent sections.

Four long probes are installed in the soil to enclose a soil volume that will be deformed by wheels during the tests. Two probes are installed at the depth of SST emplacement; two others are set on the surface or inserted 3 to 5 cm under the soil surface. The soil deformation probes should be installed close to the SST installation points. Laser projectors are installed on the opposite ends of the probes and the light points are visible on a shield. When wheel loads deform the soil, the probes move together with the deforming soil. The light points show soil deformation history on the shield and the history is recorded by a camera. Chapter 2 presents a more detailed description of this method.

8.2.4.3 Test Program

We performed the experiments on three soil surfaces (loess, sand, and turf) and on a snow surface. We decided not to change any vehicle factors (wheel loading, inflation pressure, or tyre tread pattern). Five replications of both driving and rolling modes were aimed at obtaining statistically valuable data. In driving mode, data are captured for the identification of the first model equation (expressing the driving force F_{DR}), while rolling rides provide data for the second model equation (rolling resistance F_{RR}). Those equations will appear in the subsequent section.

Field tests were carried out at different sites between March and June 2006. Tests on the snow cover and on sandy and turf surfaces were performed at a military test facility; tests on loess soil were carried out on private property. The soils were initially investigated "as is" without special conditioning routines. Soil moisture content was measured with a hand TDR-meter. After each replication of test rides, soils were conditioned by hand homogenisation and repacking to rebuild their initial bulk density.

8.2.4.4 Field Procedures

We performed typical pull tests for driving and rolling as described in Section 8.2.2. In the driving tests, the vehicle had to pass the point at highest possible wheel slip (for sandy soil) or at highest possible F_{DBP} (loess soil, and snow). Good coordination among the drivers in the test and braking vehicles was a concern, and the procedure was first tested for several runs. Figure 8.8 photographs show sample test runs on loess and turf soil.

FIGURE 8.8
Experimental set-up for the reconstruction of the traction model.

When the vehicle passed over the SSTs and soil probes, data recording systems captured a complete data set of

- Drawbar pull generated by the vehicle
- Forward vehicle velocity and wheel rotation speed (all road wheels were locked)
- Soil pressures to determine soil stress state (from two SSTs)
- Soil deformation as a video clip

8.2.5 Results

Typical plots of soil pressures and calculated soil stresses are shown in Figure 8.9. This figure also presents traction force curves. Such data sets for all test rides were analysed and the results determined included

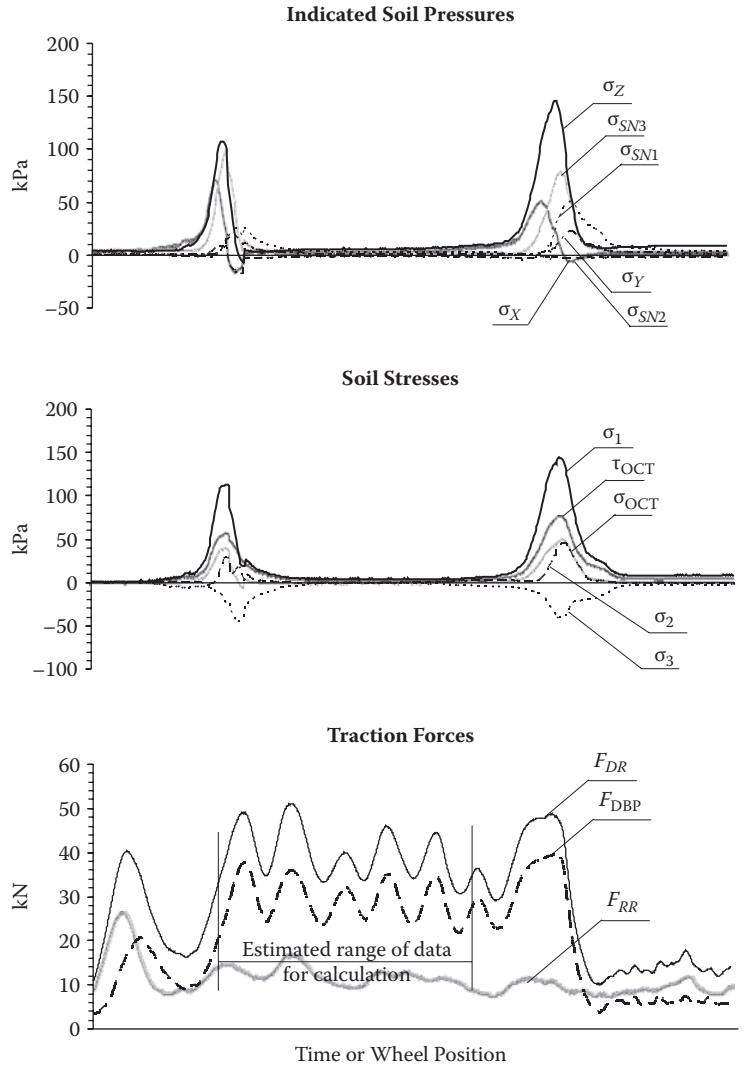

FIGURE 8.9
Typical plots of the indicated soil pressures and calculated soil stresses as well as vehicle traction data.

- Peak values of octahedral shear and normal stresses for the front and rear wheels
- Integer values of τ_{OCT} and σ_{OCT}
- Average values of traction forces: drawbar pull, rolling resistance, and driving force
- Values of experimental coefficients *A* and *B* that represent proportional factors in the relationships

$$F_{DR} = A\tau_{OCT}^{Intgr}, \quad F_{RR} = B\sigma_{OCT}^{Intgr} \tag{8.13}$$

Table 8.1 shows the results from the field tests including stresses for the front and rear wheels—three values for each repetition. The *A* and *B* coefficients can be called "imaginary surfaces of stresses" in soil since they are shown as square metres. It is interesting that the calculated stresses reached their highest values in sandy soil and their lowest in loess soil.

This contradicts our other results (Pytka 2005 and 2009) where the highest values were observed in loess. The reason may be the soil moisture that was relatively high at the time of the tests. Soil moisture was low in our earlier tests. This suggests the need for an experiment on the effects of moisture content on soil stresses (and vehicle traction). Peak values of octahedral shear stress are higher than mean normal stress in loess and turf, while the relationship is the opposite on sand and snow surfaces.

Both sand and snow deformed very intensively, so the normal stress related to compaction was high. Vehicle traction depends on the surface: the best performances were observed on loess and sandy soil surfaces, but the net drawbar pull was higher on loess due to the very high rolling resistance on sand (F_{RR} on loess was greater than F_{DBP} on sand). The lowest traction on snow was expected due to low rubber–snow friction conditions.

8.2.5.1 Model Reconstruction

The algorithm of model reconstruction was as follows:

1. Estimation of parameter correlating the integers of soil stresses with traction forces. This was already done and the *A* and *B* value results are included in Table 8.1.
2. Determination of soil stress values with the Boussinesq formulae [Equations (8.5) and (8.6)] and their correlation with experimental results (τ_{OCT} and σ_{OCT} curves).
3. Estimation of correlation parameters for the stress components: *C* and *D* for shear stress of front and rear wheels, respectively, and *E* and *F* for normal stress.

TABLE 8.1

Soil Stress and Vehicle Traction Data for Four Investigated Surfaces

Loess soil							
τ_{OCT}	Peak	56.52	60.20	59.47	74.63	75.09	72.84
	Integer	22.14	31.48	36.89	35.87	29.58	41.91
σ_{OCT}	Peak	50.76	41.12	46.94	24.54	27.28	37.94
	Integer	11.54	12.23	17.17	7.89	9.44	12.20
F_{DBP}	30.29	29.82	28.85				
F_{RR}	9.59	10.36	9.35				
F_{DR}	39.88	40.18	38.02				
A	3.437	3.290	2.420				
B	2.467	2.390	1.592				
Sandy soil							
τ_{OCT}	Peak	308.2	389.5	339.6	347.9	299.8	296.0
	Integer	32.13	41.87	38.88	52.23	77.22	67.53
σ_{OCT}	Peak	558.9	304.6	301.5	459.1	237.4	210.7
	Integer	83.9	35.23	57.01	29.38	45.27	38.60
F_{DBP}	14.99	24.80	25.25				
F_{RR}	30.68	23.06	25.51				
F_{DR}	45.67	47.86	50.76				
A	2.706	2.009	2.385				
B	1.353	1.432	1.348				
Turf							
τ_{OCT}	Peak	127.9	219.9	223.5	107.1	103.6	160.6
	Integer	62.33	90.09	61.16	120.06	47.35	57.52
σ_{OCT}	Peak	57.17	9.47	42.52	74.00	27.30	33.48
	Integer	3.33	3.01	6.71	11.90	5.45	7.15
F_{DBP}	22.01	19.79	19.06				
F_{RR}	6.58	5.77	5.83				
F_{DR}	28.59	25.56	24.89				
A	0.783	0.929	1.037				
B	2.162	3.414	2.080				
Snow							
τ_{OCT}	Peak	104.7	174.2	159.6	232.29	202.4	201.0
	Integer	34.23	38.59	43.24	32.30	56.04	44.99
σ_{OCT}	Peak	155.7	150.6	78.42	136.8	84.21	93.56
	Integer	64.36	48.06	18.05	27.01	9.04	18.25
F_{DBP}	6.24	7.26	7.28				
F_{RR}	9.39	10.64	10.51				
F_{DR}	15.63	17.90	17.74				
A	1.174	0.945	0.999				
B	0.513	0.931	1.47				

TABLE 8.2

Values of Parameters for Model Reconstruction

Parameter		Surface			
		Loess Soil	**Sandy Soil**	**Turf**	**Snow**
A	F + R	3.049	2.366	0.916	1.039
B	F + R	2.149	1.377	2.552	0.971
C	Front	0.491	2.891	1.592	1.223
	Rear	1.039	4.401	1.731	2.964
D	Front	0.257	0.054	0.187	0.132
	Rear	0.244	0.104	0.304	0.105
E	Front	0.193	1.623	0.208	0.536
	Rear	0.209	2.115	0.314	0.733
F	Front	0.187	0.096	0.055	0.215
	Rear	0.210	0.079	0.115	0.109

The values of the estimated parameters *A* through *F* are included in Table 8.2. Based on Jakliński (1999), the final model equations are

$$F_{DR} = 2A \;\; C\int \frac{F_V^F \cos^2(\alpha)\sin(\alpha)}{2\pi r^2}\,d\alpha + D\int \frac{F_V^R \cos^2(\alpha)\sin(\alpha)}{2\pi r^2}\,d\alpha \qquad (8.14)$$

$$F_{RR} = 2B \;\; E\int \frac{F_V^F \cos^2(\alpha)}{2\pi r^2}\,d\alpha + F\int \frac{F_V^R \cos^2(\alpha)}{2\pi r^2}\,d\alpha \qquad (8.15)$$

8.2.5.2 Model Validation

The model was validated with another set of experimental data: traction data for a 14-tonne 6 × 6 military truck driven on both loess and sandy soil surfaces (the same soils as in the experiment for model reconstruction) and for a 4.6-tonne 4 × 4 high mobility multi-purpose wheeled vehicle (HMMWV or Hummer) driven on the sandy soil surface only. The 14-tonne truck was driven with three loads: empty, with 3.6-tonne payload, and with 6-tonne payload (maximum weight). For the two vehicles, traction forces were calculated from Equations (8.14) and (8.15). A sample comparison of experimental and predicted values of F_{DBP} is included in Table 8.3 and shown graphically in Figure 8.10.

The prediction ability of the model was good or satisfactory. The differences between experimental and predicted values were 3% to 47%. The differences are greater for the sandy soil surface in the case of the 14-tonne truck and they increase as wheel loading increases. We noted a substantial difference in water content (WC) of the sandy soil during the

TABLE 8.3

Comparison of Measured and Predicted Drawbar Pull Values for Two Vehicles

	Drawbar Pull Force (kN)					
	Loess Soil			Sandy Soil		
Load/Weight	**Measured**	**Predicted**	**% Difference**	**Measured**	**Predicted**	**% Difference**
14-tonne 6 × 6 truck						
Load						
Empty	59.60	52.72	11.53	38.22	45.08	15.21
+3.6 tonnes	79.15	81.63	3.04	49.47	77.44	36.12
+6.0 tonnes	83.90	101.90	17.66	52.58	99.21	47.00
4.6-tonne 4 × 4 HMMWV						
Weight						
4.665 kg	No data	26.77	—	7.50	7.25	3.3

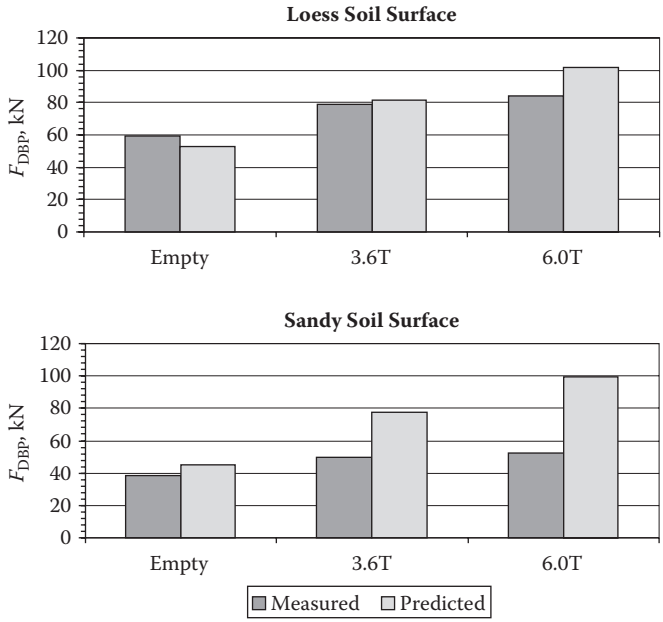

FIGURE 8.10

Measured versus predicted values of F_{DBP} for the 14-T 6 × 6 truck on loess and sandy soil surfaces.

two experiments. During the tests with the 14 tonne truck, the WC was between 3% and 7%, and in the experiment for model reconstruction with the 5.6-tonne 4 × 4 truck, the WC was 15% to 22%. This could have caused the differences mentioned above since no parameter in the model structure describes soil sensitivity based on changes in water content. The test runs of the HMMWV were done at a WC of 12% to 15%, so the difference is very small. Further research is needed so that the model can be reconstructed to accommodate fluctuations in the soil water content.

8.3 Modelling Soil Stress State by System Identification (SI)

8.3.1 Introduction

A wheel–soil system can be described by forces acting on a wheel and stresses generated in soil. From the view of mechanics, wheel forces are actions and soil stresses are reactions, and Newton's third law can be applied to this system. However, soils and rubber in tyres are not elastic bodies, so a relationship between wheel forces and soil stresses is not as simple. First, soil deformability causes the relationships to be strongly non-linear. Both tyres and soil partly transmit and absorb the energy in the system. Important tyre factors are

- Type (radial, diagonal, winter, all-season) and load index
- Inflation pressure
- Dynamic aspects (rates of deformation)

Likewise, a selection of soil-related factors that affect the system includes

- Soil type and structure
- State, especially water content and porosity
- Deformation rate

It is obvious that a typical analytical model should take into account as many factors as possible by means of functions or parameters. Only six factors are listed above, but it would be reasonable to consider others to improve model predictability. We can expect the final model to be very complicated, time consuming to apply in practice, and expensive.

The objective of this study was to overcome these disadvantages by inferring a model (or set of models) of the wheel–soil system by the system identification method. In many applications, it is more important to obtain

a very precise mathematical model. Development of ride simulators is one example. In aerospace engineering, system identification is often used to reconstruct models of aircraft dynamics from flight test data, and such models are used to build and master computer codes in simulators. Such models consider all factors affecting a system's dynamics.

8.3.2 Structure of Model

Figure 8.11 shows a schematic of the wheel–soil system with acting forces and generated stresses in soil. The system is described by the following measures:

Wheel forces:

F_v = Vertical load

F_x = Driving force

F_y = Steering force

Soil stresses:

σ_v = Vertical stress

σ_x = Longitudinal stress

σ_y = Transversal stresses

τ_{zy}, τ_{zx}, τ_{xy} = Shear stresses

Soil deformations:

ε_z, ε_x, ε_y = Volumetric deformations (compaction)

ε_z^τ, ε_x^τ, ε_x^τ, ε_z^α, ε_x^α, ε_x^α = Other deformations (shearing and rotation)

The wheel–soil system will be described analytically with input and output variables and the relationships between them.

8.3.2.1 Input Variables

The following measures will be treated as input variables in the model:

$u_1(t) = F_v(t)$ = Vertical load acting on a wheel

$u_2(t) = F_x(t)$ = Longitudinal horizontal force on a wheel

$u_3(t) = F_y(t)$ = Transversal horizontal force on a wheel

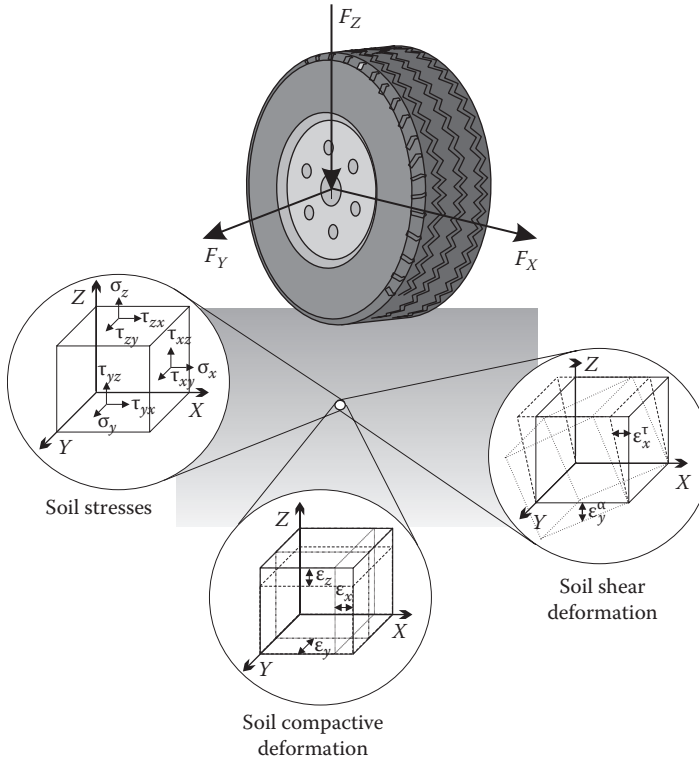

FIGURE 8.11
A model of the wheel–soil system based on wheel forces and soil stress and deformation state.

8.3.2.2 Output Variables

Similarly, output variables may be defined for the system as follows:

$y_1(t) = \sigma_z(t)$ = Vertical stress in soil measured at given depth during pass of a vehicle wheel

$y_2(t) = \sigma_x(t)$ = Horizontal longitudinal stress in soil

$y_3(t) = \sigma_y(t)$ = Horizontal transversal stress in soil

$y_4(t) = \tau_{xy}(t)$ = Shear stress acting in XY plane

$y_5(t) = \tau_{zx}(t)$ = Shear stress acting in ZX plane

$y_6(t) = \tau_{zy}(t)$ = Shear stress acting in ZY plane

$y_7(t) = \varepsilon_z(t)$ = Vertical deformation of soil volume between soil stress measuring point and soil surface

$y_8(t) = \varepsilon_x(t)$ = Volumetric deformation of soil in OX direction
$y_9(t) = \varepsilon_y(t)$ = Volumetric deformation of soil in OY direction
$y_{10}(t) = \varepsilon_{xy}{}^{\tau}(t)$ = Shape deformation of soil; shearing in XY plane
$y_{11}(t) = \varepsilon_{zx}{}^{\tau}(t)$ = Shape deformation of soil; shearing in ZX plane
$y_{12}(t) = \varepsilon_{zy}{}^{\tau}(t)$ = Shape deformation of soil; shearing in ZY plane
$y_{13}(t) = \omega_z{}^{\alpha}(t)$ = Rotation around OZ axis
$y_{14}(t) = \omega_x{}^{\alpha}(t)$ = Rotation around OX axis
$y_{15}(t) = \omega_y{}^{\alpha}(t)$ = Rotation around OY axis

8.3.2.3 Relationships of Input and Output Variables

The following relationships are defined:

Coupling normal stresses and wheel forces —

$$y_1(t) = f(u_1) = A F_z \tag{8.16}$$

$$y_2(t) = f(u_2) = B F_x \tag{8.17}$$

$$y_3(t) = f(u_3) = C F_z \tag{8.18}$$

Coupling shear stresses and wheel forces —

$$y_4(t) = f(u_2, u_3) = DF_x + EF_y \tag{8.19}$$

$$y_5(t) = f(u_2, u_1) = F F_z + GF_x \tag{8.20}$$

$$y_6(t) = f(u_1, u_3) = H F_z + I F_y \tag{8.21}$$

Coupling volumetric deformation of soil and soil normal stresses —

$$y_7(t) = f(y_1) \tag{8.22}$$

$$y_8(t) = f(y_2) \tag{8.23}$$

$$y_9(t) = f(y_3) \tag{8.24}$$

Coupling shearing deformations and soil stresses (normal and shear) —

$$y_{10}(t) = f(y_1, y_2) \tag{8.25}$$

$$y_{11}(t) = f(y_2, y_1) \tag{8.26}$$

$$y_{12}(t) = f(y_3, y_1) \tag{8.27}$$

Coupling rotations and soil stresses —

$$y_{13}(t) = f(u_2, u_3) \tag{8.28}$$

$$y_{14}(t) = f(u_1, u_3) \tag{8.29}$$

$$y_{15}(t) = f(u_2, u_1) \tag{8.30}$$

To simplify, vectors and matrix notation will be introduced and we obtain a

General relationship between wheel forces and normal and shear stresses [Equations (8.16) through (8.21)] —

$$\begin{matrix} A & 0 & 0 \\ 0 & B & 0 \\ 0 & 0 & C \\ 0 & D & E \\ G & F & 0 \\ H & 0 & I \end{matrix} \times \begin{matrix} F_z \\ F_x \\ F_y \end{matrix} = \begin{matrix} \sigma_z \\ \sigma_x \\ \sigma_y \\ \tau_{xy} \\ \tau_{zx} \\ \tau_{zy} \end{matrix} \tag{8.31}$$

General relationship between soil stresses and volumetric and shape deformations [Equations (8.22) through (8.27)] —

$$\begin{matrix} \sigma_z & \tau_{zx} & \tau_{zy} \\ \tau_{xz} & \sigma_x & \tau_{xy} \\ \tau_{yz} & \tau_{yx} & \sigma_y \end{matrix} \times C_{ijkl} = \begin{matrix} \varepsilon_z & \varepsilon_{zx}^{\tau} & \varepsilon_{zy}^{\tau} \\ \varepsilon_{xz}^{\tau} & \varepsilon_x & \varepsilon_{xy}^{\tau} \\ \varepsilon_{yz}^{\tau} & \varepsilon_{yx}^{\tau} & \varepsilon_y \end{matrix} \tag{8.32}$$

Using tensor notation, we write Equation (8.32) as

$$\sigma_{ij} = C_{ijkl}\, \varepsilon_{kl},\ (i,j,k,l = z, x, y) \tag{8.33}$$

Stress tensor components, τ_{xy}, τ_{xz}, and τ_{yz}, are symmetrical, so only three of them are given in Equation (8.31). Similarly, in Equation (8.32), the deformation tensor is symmetrical and has only six independent components. The factors of proportionality, $A, B, \ldots, I$ are based on the Boussinesq model and can be expressed as

$$\frac{\cos^2(\alpha)}{2\pi r^2}$$

for the equations involving normal stresses and

$$\frac{\cos(\alpha)\sin(\alpha)}{2\pi r^2}$$

for the equations involving shear stresses.

8.3.3 System Identification Method

System identification (SI) is a process by which a model and its parameters are reconstructed from experimental data. SI methods range widely from simple approximations to complex statistical analyses (Ljung 1999, James 2002, Klein and Morelli 2006). In general, SI processes follow the following steps and the steps are described briefly below:

- Model postulation
- Experiment design
- Data compatibility analysis
- State and parameter estimation
- Model structure determination
- Model validation

Model postulation — Model postulation is influenced by a system and its primary dynamics characterisation. In the case of wheel–soil systems, basic input variables are wheel load, driving torque, and soil stress and deformation relationship to external loads. Output variables can be of the first order: time histories of soil stresses and deformation, time histories of tyre deflections. One output variable of the second order can be drawbar pull as a function of wheel slip.

Experiment design — An experiment must be designed and performed to yield measured data for model reconstruction. Experiment design is primarily based on model postulation. In this step of SI, it is important to select the correct input forms. The shape of an input signal can influence the accuracy of estimated parameters from measurements.

Data compatibility analysis — A successful SI process depends primarily on the accuracy and precision of the measurements. The measured response data can contain bias and scale factor errors due to the characteristics of sensors or measurement conditions. It is important to apply careful data handling, filtering, and checking procedures. Moreover, a compatibility check can also be applied to the data.

State and parameter estimation — State estimation is usually reduced to integration of vehicle equations of motion, provided that these equations represent a deterministic system that includes no process noise or random parameters in the equations.

Model structure determination — A major problem in SI development is the selection of an adequate model that should have a structure sufficient to characterize the data and estimate unknown parameters; it should also have good prediction capabilities.

Model validation — The last step is model validation. The identified model must demonstrate that its parameters have physically reasonable values with adequate accuracy and prediction capabilities. Model validation can be performed by comparing output data with experimental data or with output data from other models of known performance. Its prediction capabilities can be checked on a set of data not used for the SI of this model.

8.3.4 Experiment Design

According to the SI scheme, a wheel–soil system has to be represented by both input and output variables. We chose wheel forces (input) and soil stresses (output). Based on our studies (Pytka 2005, 2008, and 2009), these variables remain closely correlated and may be used to create a good model. Thus, one of the most important objectives was to develop methods and measuring equipment for these variables.

8.3.4.1 Rotating Wheel Dynamometer (RWD)

The purpose of a dynamometer is to measure all three forces and moments acting on a wheel that are to be used as input data for the SI method. The dynamometer was designed as an autonomous measuring device, with an on-board data acquisition system and power supply. Application of a dynamometer for testing requires only minor modifications of a wheel rim and the use of a wheel hub adapter. The device was designed for wheeled vehicle weights ranging from 1.5 to 6 tonnes. The complete rotating wheel dynamometer (RWD) system consists of four sub-systems (Figure 8.12):

- Sensor
- Modified wheel rim
- Mounting sub-system (wheel hub adapter, mounting screws)
- Autonomous data recording system (ADRS) with power supply

The ADRS converts the signals from analogue to digital and then records them in an on-board memory. The system is a microcontroller-based device with custom software to manage all needed functions. The data can be transmitted when the vehicle stops, and it should be saved after each test run on a micromemory card (MMC) or external PC via an RS 232 connection. The electronics, display, control switches, and power supply

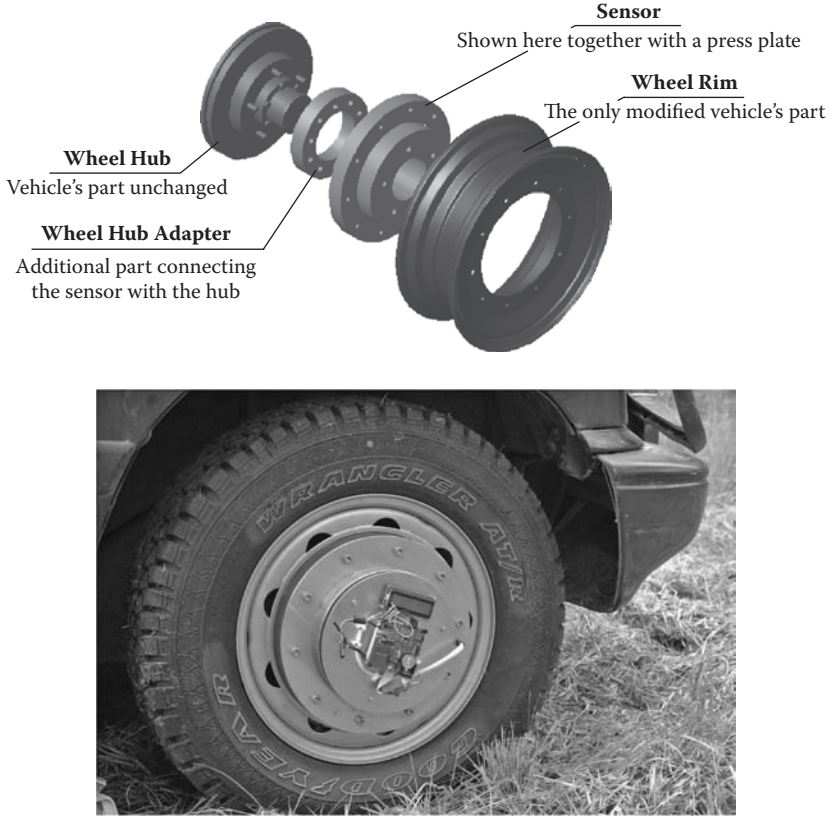

FIGURE 8.12
A schematic of the rotating wheel dynamometer and the dynamometer installed on a test vehicle (the electronics are shown without a housing).

are grouped on a circular plate attached to the sensor and encapsulated with an electromagnetically resistant cover.

The power supply for both the sensor and ADRS is a lithium–polymer rechargeable battery that adds ~300 g to the total weight and is located in the centre of the wheel to minimise vibrations from rotation. More details can be found in Pytka (2008). Figure 8.12 shows the RWD installed in a test vehicle.

8.3.4.2 Soil Stress Determination

A stress state transducer (SST) was used to determine a complete state of stress at a point in the soil under wheel loads. The SST was installed at 10- to 15-cm depth, beneath the centre lines of the right wheels of the vehicles. Various installation methods were used to place the SST at the

depths in loess, sand, turf, and snow cover (see Chapters 2 and 4). Briefly, simple excavation was used in the sandy and loess soils and in snow. In the loess soil that contains structural bonds between particles, the SST was installed 3 to 6 hours before the tests to let the aging effect rebuild the damaged soil structure. In the sandy soil that lacks structural bonds and in snow cover, tests were done immediately after the SSTs were placed. In the turf that contained growing plants (grass), the SSTs were installed by cutting away a piece of upper surface with plants and roots, placing the SST at depth, and then replacing the removed piece of the surface.

8.3.4.3 Test Program

A 5-tonne 4 × 4 personnel carrier vehicle was used to obtain data suitable for SI analysis. The vehicle shown in Figure 8.13 was equipped with the RWD mounted on the right front wheel.

The tests were conducted on three different types of soil surfaces: loess soil, sandy soil, and turf (forest soil). After installation of the SST in soil at a depth of ~10 to 15 cm, the vehicle was positioned to pass exactly over the SST with the right wheels.

The recording systems (ADRS and SST data logger) were activated and the vehicle was driven at a low speed of 5 to 8 km/h with no wheel slip. After a single pass of the vehicle, the SST was replaced and installed again in a new spot before the next pass. The procedure was repeated a minimum of five times for each soil.

FIGURE 8.13
An armoured personnel carrier as a test vehicle with the rotating wheel dynamometer installed in the right front wheel, here during test runs on sandy soil surface.

8.3.5 Results

The first step after testing was data reduction, consisting mainly of simply checking the time curves of wheel force and soil stress for completeness and integrity. Segments of the data were chosen for filtering to enhance fit and ultimately derive models of high correlation between the simulated and measured outputs. A fifth-order high-pass (HP) Butterworth filter was used for the data.

8.3.5.1 Reconstruction of Mathematical Models from Data

This section focuses on practical use and examination of the method. For the identification procedures, we chose two data sets for the loess soil surface: (1) vertical load F_v and longitudinal force F_x as input variables, and (2) vertical soil stress σ_v and longitudinal soil stress σ_x as output variables. Models of the wheel–soil system were generated based on these data. After filtering, the sets of data were used for inferring different models. In general, the types of models considered were (1) linear parametric models, (2) non-linear models, and (3) process models.

The family of linear parametric models consists of 32 sets. The most frequently used are the ARX (auto regression with eXtra inputs), ARMAX (auto regression moving average with eXtra inputs), OE (output error), BJ (box Jenkins), and state space (N4S).

The ARX is the simplest structure and is often a first choice. Parameterisation of such models can be performed by means of the least-squares method. The different ARX models will be referred to as ARX(n_a, n_b, n_k), where n_a and n_b are integers defining the model structure, n_a is the number of poles, n_{b+1} is the number of zeros, and n_k is the pure time delay (dead time) in the system. For multi-input systems, n_b and n_k are row vectors, where the ith element gives the order or delay associated with the ith input.

The family of non-linear models includes two types: (1) the non-linear ARX model (NLARX), and (2) the non-linear Hammerstein–Wiener model (NLHW). The NLARX represents a parallel form of non-linearity in which simple transformations of measured inputs and outputs (regressors) are used in parallel linear and non-linear blocks to describe the observed phenomenon. A Hammerstein–Wiener model represents a series of non-linear forms in which inputs and outputs to an OE linear model are distorted by static non-linearities.

Process models are simple continuous-time models described in terms of main time constants, static gain, possible dead time, and a possible process zero (non-constant) numerator. Multi-input models can be handled and noise descriptions of certain structures can be added. The model structure acronym (see legend in Figure 8.14) uses P to denote a number

of poles, *D* to indicate delay, *I* to represent an integrator, *Z* for zero, and *U* for underdamped. A typical such model is the transfer function:

$$G(q) = \sum_{k=1}^{\infty} g(k) q^{-k} \tag{8.34}$$

Figures 8.14 and 8.15 show sample results of simulations performed with the three model families described above for loess and sand soils. The output from these simulations is soil stress under loading of a wheel, for which we know (i.e. we measured) the input value, the vertical load. A thick black line represents the measured stress (experimental data), while the thin colored lines denote simulated output for the system. In the figures, fits for every model are included in the legend box; the higher the value, the better the fit. Note that the maximum theoretical (best) fit value is 100.

8.3.5.2 Effect of Soil Surface

An important concern in modelling of wheel–soil systems is inclusion of the type of soil surface because the surface affects a number of physical and mechanical processes (compaction, traction, etc.). Having measured input and output variables for three soils—loess, sand, and turf—we inferred models of a wheel–soil system for these surfaces. Loess and sand possess opposite mechanical properties. Loess has low internal friction and high cohesion, while typical sand has high internal friction and less cohesion. Turf is an organic soil. At this stage of our research, we considered two input and output variables: (1) vertical load F_v and longitudinal force F_x, and (2) vertical and longitudinal soil stresses σ_z, and σ_x.

The previous section examined a selection of three groups of models for better fits but only for the loess soil surface. Considering the results as determinants for further analysis, we tested the chosen models with results from the other soil surfaces. SI software-derived models of the system and other models were examined for the best fit of simulated and measured outputs. Table 8.4 includes results from a comparison of the models for the best fit.

Models chosen for this comparison provided very good fits for the loess soil surface. A question arises, however, whether those models would be also suitable to represent the two other soil surfaces.

Significantly, the worst fits were models inferred from data captured on turf surface; fit results for the sandy soil surface fall between loess and turf. The results agree with earlier statistical analysis of soil stress data (Pytka 2009) indicating that standard deviations for stress results are the highest for turf surfaces, thus explaining why it is difficult to infer a good model from experimental data obtained from this soil surface.

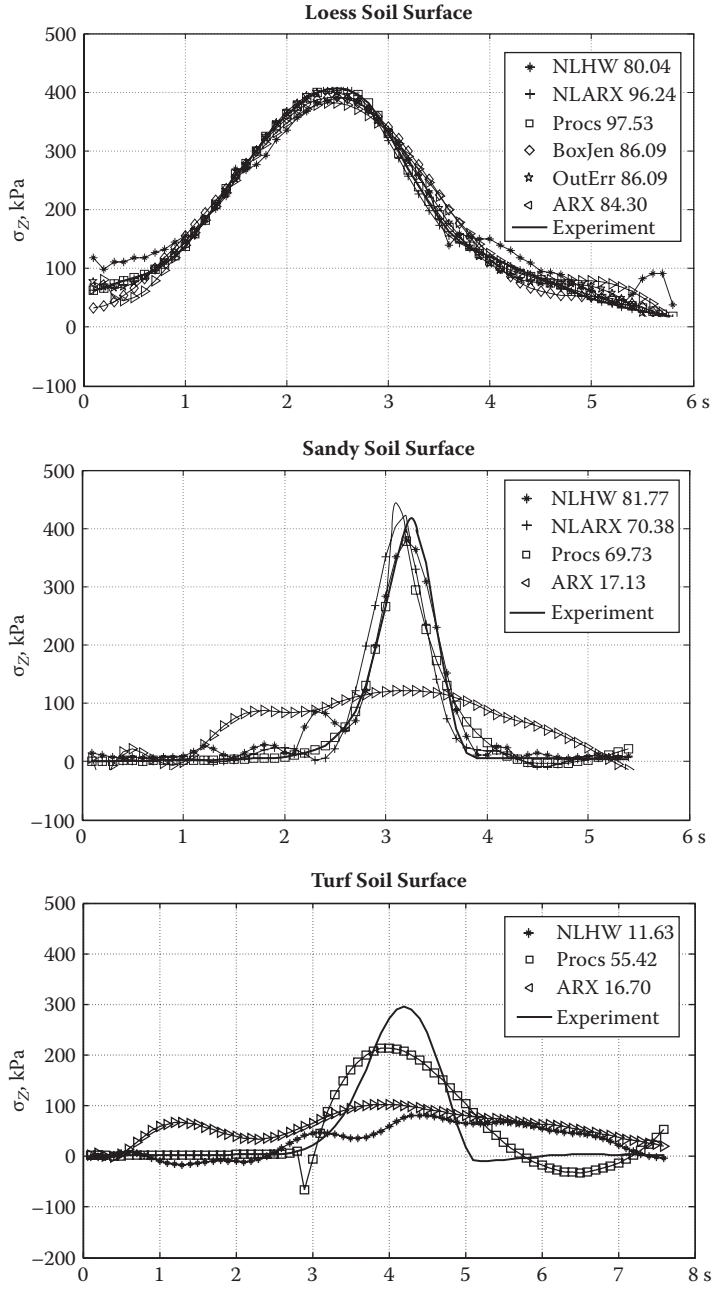

FIGURE 8.14
Simulation results for a selection of models for the F_v – σ_z sub-system on loess, sandy, and turf soil surfaces.

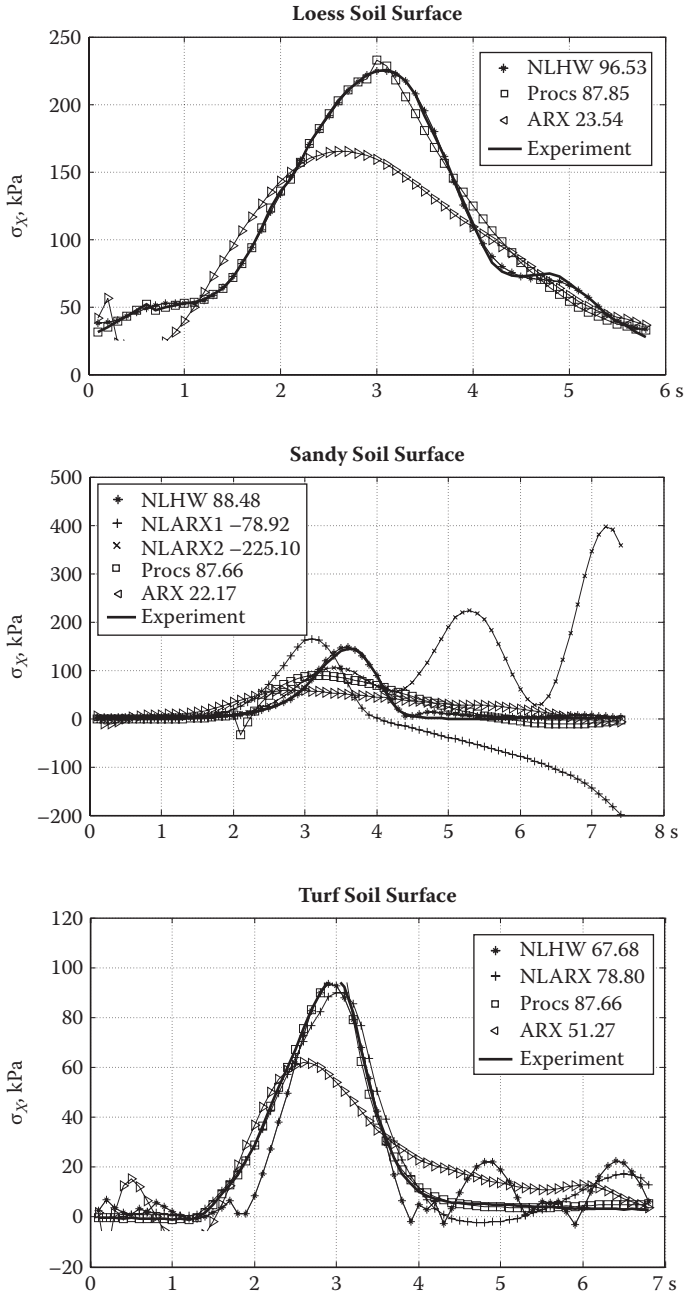

FIGURE 8.15
Simulation results for a selection of models for the $F_x - \sigma_x$ sub-system on loess, sandy, and turf soil surfaces.

TABLE 8.4
Comparison of Models of Wheel–Soil Systems for Three Soil Surfaces

Model Structure	Loess	Sand	Turf
F_z–σ_z sub-system			
ARX 441	84.30	17.13	16.70
NLHW	80.04	81.77	11.63
NLARX	96.24	70.38	—
P1DZ/DIZ	97.53	69.73	55.42
F_x–σ_x sub-system			
ARX 441	65.24	22.17	51.27
NLHW	96.53	88.48	67.60
NLARX	—	–78.92	78.90
P1DZ/DIZ	87.85	44.27	94.53

The best fit obtained was 97.53 for the F_v–σ_v sub-system on loess; this fit was for one of the process models. ARX models performed well only with data from loess soil and for the F_v–σ_v. Non-linear Hammerstein–Wiener models are in general good choices, with an exception of turf surface data for the F_v–σ_v sub-system. This type of model performed well for most surface and sub-system combinations and would be the first choice. NLARX models yielded good or very good fits in some cases (best fit was at 96.24 for loess, F_v–σ_v), but in other cases the quality of results was unsatisfactory. For this type of model, a negative fit of –78.92 was obtained for the F_x–σ_x from data on sandy soil. Finally, process models of different structures gave only good or satisfactory fit to both sub-systems.

The comparison of models in Table 8.4 shows an effect of soil surface on model quality. This effect may be caused by data uncertainty for turf or sandy soils. Also, models used to describe vertical and longitudinal subsystems performed differently.

8.3.6 Conclusions

In this section, we examined a method for obtaining mathematical models of soil stress propagation. The method is based on the analysis of experimental data of input and output variables (wheel forces and soil stresses) describing the system. Based on experimental data from tests of three soil surfaces, mathematical models of vertical load (vertical soil stress, driving force) and horizontal soil stress sub-systems were inferred. Generally, methods based on SI yielded good results and several model structures were examined. We included a preliminary comparison of the models for the best fit between simulated and measured values of output values. Effects of soil surface significantly impact the quality of model predictions that also depend on the analysed sub-systems (vertical or longitudinal).

8.4 Modelling Dynamic Effects of Wheel–Soil System

8.4.1 Introduction

Soil is a three-phase, granular material containing particles that may be bound in aggregates. The structure of a typical aggregated soil is porous, with spaces filled with air and water. Exposure to atmospheric and environmental factors causes dynamic fluctuations in water content and soil mechanical strength—important aspects of terramechanics and off-road vehicle performance.

Natural soils possess all three mechanical properties of matter: elasticity, plasticity, and viscosity. The latter is strictly connected with the fluid phase and is responsible for time effects in stress–strain behaviours of soil. Introducing rheology into soil mechanics opened new possibilities by including time effects. Pukos (1983, Pukos 1985) and Wulfsohn and Upadhyaya (1992) described sample applications of rheology models in terramechanics.

Pukos (1987) also investigated effects of dynamical loading on soil at various deformation rates, similar to the effects caused by agricultural and off-road vehicles. He proved that the widely used rheological models were not suitable for describing soil stress–strain processes at high deformation rates and proposed a new model that considers time effects on soil elasticity and viscosity. The model was experimentally examined and a new theory in statistical mechanics was created based on Eyring's assumption that soil is partially a Newtonian fluid in which viscosity is temperature dependent. We used some of Pukos' results in this study to create a model of tyre lateral force generation on a deformable surface.

8.4.2 Sample Model: Steered Wheel on Soil Surface

We assume that the mechanics of tyre lateral force generation consist of two phenomena: (1) shearing of soil by turning (steering) the tyre, and (2) soil reaction force generated laterally on the sidewall when a tyre is turned at sideslip angle and sinks into soil. The first action is dynamic and active only when the wheel is turning. Shearing depends on wheel turning rate and is the major parameter influencing soil viscosity. The second action is static, dependent on sideslip angle and wheel sinkage. After the wheel sideslip angle is set to a given value, the first (dynamic) effect vanishes and soil reaction is the result of tyre lateral force.

Most studies (Schwanghart 1968, Coutermarsh and Shoop 2009) investigated tyre lateral force under static conditions. We may expect that the effect of dynamic wheel turning also causes a small reduction of tyre lateral force when the wheel stops turning, as an effect of soil stress relaxation. We mathematically described our model with partial use of Pukos'

model and used our experimental results from soil stress measurements to verify the model.

8.4.3 Mathematical Model

A classic theory of stress–strain behaviours of three-phase, deformable materials like soils is called rheology (Kisiel and Lisiak 1966). Among many models used to describe wheel–soil systems, the Poynting-Thomson model takes into account all the rheological effects while utilizing simple mathematical notation. The following equation

$$E_1E_2e(t) + (E_1 + E_2)\,\nu\frac{de}{dt} \quad = \quad E_1\,F(t) + \nu\frac{dF}{dt} \tag{8.35}$$

relates soil stress F and strain e along with their derivatives (E_1 and E_2 are soil moduli of elasticity and ν is soil viscosity).

As noted earlier, Pukos (1987) showed that rheological models failed to describe soil mechanics at high deformation rates mainly because of the linearity of the models. Also, linking of models did not provide good results. Dynamics of soil mechanical properties during deformation do not work with a linear visco-elasticity theory. An adaptation by Pukos of a statistical Eyring theory for viscosity and elasticity led to the following expressions to account for the effect of time:

$$\nu = \frac{A\,F(t)}{\sinh(B(t))} \tag{8.36}$$

$$E = \frac{CF(t)}{\arcsin h(D(F(t))} \tag{8.37}$$

where A, B, C, and D are soil constants. The base equation was proposed by Mitchell (1976) to express viscosity of wet loam in terms of temperature:

$$\nu = \frac{Fl_1h\exp\ \dfrac{E_s}{kT}}{2l_0\,kT\sinh\ \dfrac{Fl_0l_2l_3}{2kT}} \tag{8.38}$$

where l_0 is distance between two points of equilibrium of a loam molecule in fluid (water); l_1,l_2, and l_3 represent distances between loam molecules in three mutually orthogonal directions; E_s is the energy of water molecules; k is Boltzmann's constant; h is Planck's constant; F is stress; and T

is temperature. *A*, *B*, *C*, and *D* were introduced to replace the above terms by soil constants that could be determined experimentally. We simplified the model and use only *A* and *B*.

Assuming that soil deformation rate may affect viscosity, we can simplify this description and set the moduli of elasticity as constants. Equation (8.35) is set into (8.36), resulting in the following differential equation:

$$E_1E_2\,e(t) + (E_1 + E_2)\frac{AF(t)}{\sinh(BF(t))}\frac{de}{dt} = E_1F(t) + \frac{AF(t)}{\sinh(B(t))}\frac{dF}{dt} \tag{8.39}$$

Equation (8.39) is solved numerically since *sinh* is a non-elementary function. Soil deformation function *e(t)* is described for two modes of wheel turning: a trapezoid (or ramp change) input and a sine wave input. For the trapezoid steering input, the soil deformation function is as follows:

$$e_{T1}(t) = \dot{\delta}\cdot t \tag{8.40}$$

for the ramp and

$$e_{T2}(t) = \delta \tag{8.41}$$

for the saturation of steer angle.

For the sine wave steering input, soil deformation is related to steer angle:

$$e(t) = l\sin(\dot{\delta}t) \tag{8.42}$$

where l is the length of wheel–soil contact path and $\dot{\delta}$ is the steer angle rate. To simplify the proposed model, the value of l was determined by a measurement made during the field tests (Pytka et al. 2011, Pytka 2011), not by model calculation, and then input as a constant for a given soil surface. In a more sophisticated approach, l could be determined with Bekker's model. The values of l for two different soil surfaces were determined experimentally by measuring rut depth.

The final model equation for the effects of deformation rate (Eyring-Pukos stress viscosity) for sine wave steer input is

$$E_1E_2\,l\sin(\dot{\delta}t) + (E_1 + E_2)\frac{AF(t)}{\sinh(BF(t))}l\dot{\delta}\cos(\dot{\delta}t) = E_1F(t) + \frac{AF(t)}{\sinh(B(t))}\frac{dF}{dt} \tag{8.43}$$

The final model for the trapezoid steering input consists of two equations:

$$\frac{dF}{dt} + AE_1 \cdot \sinh(F(t)) - \frac{E_1 E_2 \delta \sinh(F(t))}{AF(t)} \cdot t = (E_1 + E_2) \cdot \frac{AF(t)}{\sinh(F(t))} \tag{8.44}$$

$$E_1 E_2 = E_1 F(t) + \frac{F(t)}{\sinh(AF(t))} \cdot \frac{dF(t)}{dt} \tag{8.45}$$

Equation (8.43) describes tyre lateral force in two processes—soil shearing and soil reaction—and is valid for the moment when the wheel is turned. Equation (8.45) is for the saturation of steer angle δ. Changing the sign in the third term of Equation (8.44) from minus to plus yields another equation describing the wheel–soil interactions during a drawback movement of the wheel.

Elasticity moduli E_1 and E_2 for the sandy soil were set based on the literature (Wanjii et al. 1997). All parameters needed for calculations are in Table 8.5. We used Computer Algebra System (CAS) software for numerical calculations.

8.4.4 Results of Sample Simulations

Figures 8.16 and 8.17 contain sample results of model simulations. They show time versus soil shear stress caused by a turning (steered) wheel for two trapezoid and sine wave inputs. Figure 8.16 consists of two curves. The first (increasing) curve is for loading when the wheel is turned. The decreasing curve describes stress relaxation when the wheel stops turning and remains at the resulting steer angle. Based on the results in Figure 8.16, tyre lateral force on sandy soil was calculated for a trapezoid steering action at a steering angle rate of 500°/s. The calculations accounted for the dynamic effect during steering action and the soil reaction to steered wheel loading and stress relaxation.

8.4.5 Experimental Verification

8.4.5.1 Instrumented Vehicle

To verify the model in which soil deformation rate is a parameter, we needed to include deformation rate in the experiment design. We used

TABLE 8.5

Constants for Sample Model

Soil	E_1 (MPa/m)	E_2 (MPa/m)	A, B	δ,°/s
Sand	0.071	1.072	1	100 500 1500

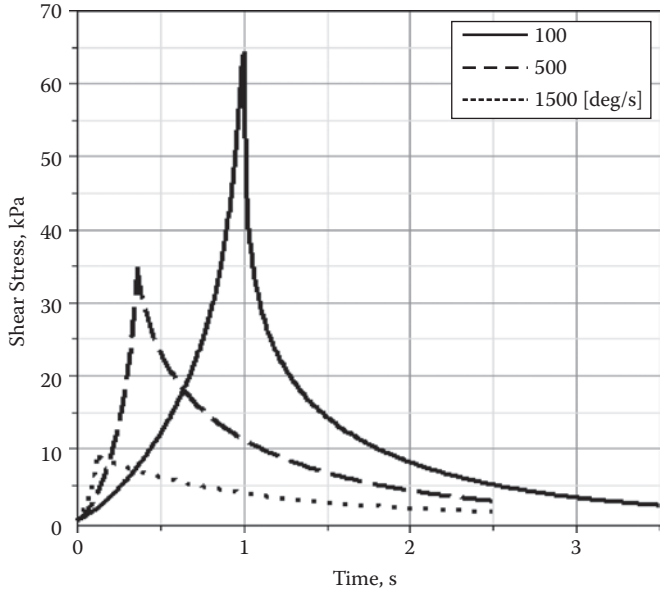

FIGURE 8.16
Shear stress in sandy soil during turning with trapezoid steering input at three different angle rates.

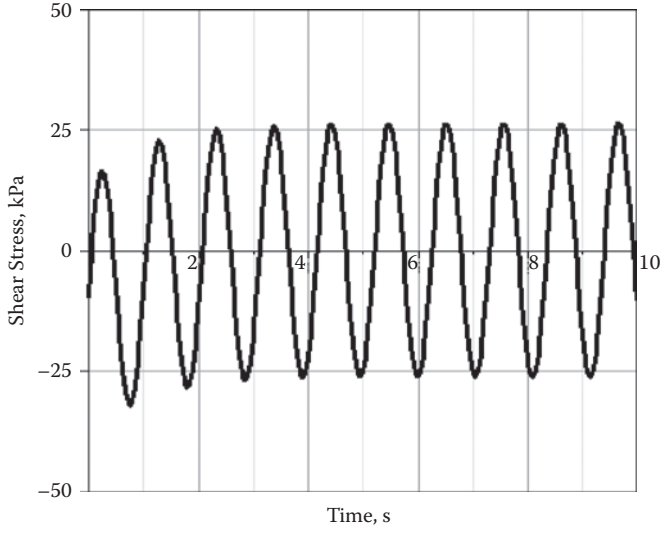

FIGURE 8.17
Shear stress in sandy soil during turning with sine wave steer input at 1 Hz frequency.

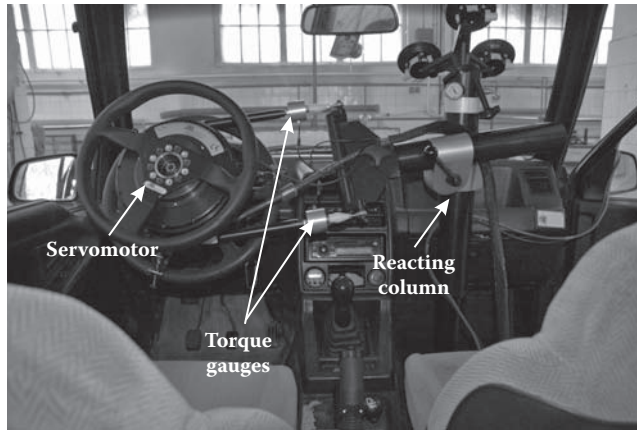

FIGURE 8.18
Steering robot installed in the instrumented vehicle.

a test vehicle equipped with instrumentation that could (1) set the wheel turning modes and rates and (2) measure tyre lateral force. The base vehicle, a 4 × 4 SUV, was equipped with two wheel dynamometers, a steering robot, and an on-board computer with software to control the devices and collect experimental data.

The two wheel dynamometers measure six elements: three orthogonal forces and three moments. The steering robot (Figure 8.18) can control the steering wheel of the vehicle at a variety of excitation modes; it can carry out typical vehicle dynamics tests (ISO 7401, ISO 4138, ISO/TR3888, etc.) and perform custom-engineered tests at a wide range of setting parameters (steer angle rate up to 1600 deg/second).

8.4.5.2 Field Procedures

We used a heavy tractor vehicle pulling the instrumented vehicle that served as a towed sensor. This method is similar to that used by Coutermarsh and Shoop (2009), with the substantial difference of using a steering robot to set the steered (front) wheel angles. The experiment was designed as an open-loop test. Sampling rate was 0.01 s for both steering wheel angle and tyre lateral force. The two measuring systems, wheel dynamometers, and steering robot were activated simultaneously with one common trigger.

8.4.5.3 Comparing Model and Experimental Results

Figure 8.19 represents this sample calculation and for comparison includes tyre lateral force versus time as determined in a full-scale experiment.

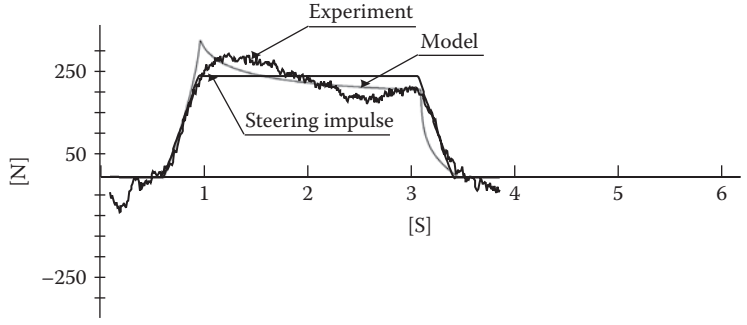

FIGURE 8.19
Tyre lateral force on sandy soil during a trapezoid steering action—a comparison of results obtained in the experiment and with the use of the model.

The figure also includes a non-dimensioned steering input. The sample of tyre lateral force was obtained by connecting the three legs for the following steering angle: an increase from 0 up to saturation as described by Equation (8.9); constant value of steering angle, Equation (8.10); and finally, decrease of steering angle, Equation (8.9) with plus sign between the terms. A similar trend can be noted between the model tyre lateral forces and those obtained in the experiment.

In the first leg at increasing steering angle (loading), both model and experimental curves exhibit a progressive character of tyre lateral force. For the flat saturation leg, asymptotically decreasing curves were obtained from the model and from the experiment. Similarly, the character of the last leg obtained by decreasing steering angle (unloading) is regressive and is comparable for both model and experimental results.

8.4.6 Conclusion

Time effects and dynamics of a system are both aspects of the soil stress state approach in wheel–soil modelling. We developed a non-linear dynamic model of the wheel–soil system based on Eyring-Pukos viscosity for soils. It produced satisfactory results for soil stresses from a turning wheel on a sandy soil surface. The characters of tyre lateral force curves from the model were similar to those obtained in the experiment.

The model also gave good results for different velocities of deformation. Stresses under wheels of the agricultural tractor simulated by the model were similar to the results from measurements. Dynamics effects in a wheel–soil system for a landing aircraft were also modelled. We compared simulation results with the experiment and this comparison looks good or satisfactory, although sandy soil data were used to identify the parameters

of the model. As with other models, identification of parameters plays a significant role.

We performed simulations for sandy soils. A further application of the model to other soil surfaces or snow requires that we gather experimental data of soil elasticity moduli and parameters. One solution to this problem can be identification of those parameters by experiments or by using the system identification method to derive mathematical models of a system and identify required parameters.

8.5 Summary

This chapter models the wheel–soil system based on experimental data for soil stress and deformation state. We used results obtained in the experiments described in the previous chapters and data from new experiments to create new models or calibrate existing ones. Identification of parameters for Boussinesq's equation resulted in a model with satisfactory predictability, but the system identification method is suggested as the best choice when considering empirical models.

System identification created models with very good predictability. The model for a turning (steering) wheel uses a different approach. Here, we started with a physical insight into the soil mechanics based on the Eyring-Pukos theory for deformation rate effects on soil elasticity and viscosity. The model was formulated with differential equations solved with CAS software. Simulation results based on the model compare well with experimental results, proving the quality of the model. Although wheel–soil systems have been investigated extensively, there is potential for new approaches to modelling. One approach is to apply the results presented in this book to create typical empirical models.

References

Bekker M.G. 1969. *Introduction to Terrain–Vehicle System.* Ann Arbor: University of Michigan Press.

Coutermarsh B. and Shoop S.A. 2009. Tire slip-angle force measurements on winter surfaces. *J. Terramech.* 46: 157–163.

Godbole R., Alcock R., and Hettiaratchi D. 1993. The prediction of tractive performance on soil surface. *J. Terramech.* 30: 443–459.

Jakliński L. 1999. *Models of Soil-–Pneumatic Tire Interactions*. Mechanics Research Work 175. Warsaw: Technical University (in Polish with English summary).
James S.R. 2002. Lateral dynamics of an off-road motorcycle by system identification. *Veh. Syst. Dynam.* 38: 1–22.
Janosi J. and Hanamoto B. 1961. The analytical determination of drawbar pull as a function of slip for tracked vehicles in deformable soils. *Proc. First ISTVS Conference,* Turin, Italy.
Kisiel I. and Lisiak B. 1966. *Zarys reologii gruntów*. Warsaw: Arkady Publishing.
Klein V. and Morelli E.A. 2006. *Aircraft System Identification: Theory and Practice*. Reston, VA: AIAA Press.
Ljung L. 1999. *System Identification:. A Theory for the User.* New York: Prentice Hall.
Mitchell J.K. 1976. *Fundamentals of Soil Behavior.* New York: John Wiley and Sons.
Muro T. 1993. Tractive performance of a driven rigid wheel on soft ground based on the analysis of soil–wheel interaction. *J. Terramech.* 30: 351–369.
Pukos A. 1983. Thermodynamic interpretation of soil medium deformation. *Zesz. Probl. Postepow Nauk Roln.* 220: 367–389.
Pukos A. 1991. Soil deformation as affected by pore size solid phase particles distribution. *Probl. Agrophys.* No 61, Institute of Agrophysics PAS, Lublin, Poland.
Pytka J. 2005. Effects of repeated rolling of agricultural tractors on soil stress and deformation state in sand and loess. *Soil Till. Res.* 82: 77–88.
Pytka J. 2008. *A Wheel Dynamometer for Off-Road Vehicle Testing*. SAE Technical Paper 2008-01-0783.
Pytka J. 2009. Determining and analyzing the stress state under wheeled vehicle loads. *J. Auto. Eng.* 223: 233–253.
Pytka J. Tarkowski P., Fijalkowski S., Budzyński P., Dąbrowski J., Kupicz W. Pytke P. 2011. An instrumental vehicle for off road dynamics testing. *J. Terramech.* 48: 384–395.
Pytka J. 2011. Soil stress state under loads of commercial vehicles. SAE Papers. Warrendale: Society of Automotive Engineers, 2011-01-2173.
Schwanghart H. 1968. Lateral forces on steered tires in loose soil. *J. Terramech.* 15: 9–29.
Shoop S., Young B., Alger R., Davis J. 1994. Effect of test method on winter traction measurements. *J. Terramech.* 31: 153–161.
Wanjii S., Hiroma T., Ota Y. et al. 1997. Prediction of wheel performance by analysis of normal and tangential stress distributions under the wheel–soil interface. *J. Terramech.* 34: 165–186.
Wulfsohn D. and Upadhyaya S. 1992. Prediction of traction and soil compaction using three-dimensional soil–tyre contact profile. *J. Terramech.* 29: 541–553.

9

Summary

Our intent was to complement the state of the art in wheel–soil mechanics by introducing some new methods and their applications and analysing the results of soil stress and deformation state under loads generated by ground vehicles. Our approach was an experimental one focused on full-scale field tests. Our goals can be summarized into three categories.

First, we developed new or modified the existing methods of soil stress and deformation measurement. Here, we aimed to increase the precision of the measurements with the intent of obtaining more reliable data. Since the indicated soil pressure is affected by transducer–soil interactions, we considered soil type and moisture content in calibration of the transducers before measurements. An important contribution was the non-contact, opto-electronic method for soil surface deformation.

Second, we performed several field experiments in which soil stress and deformation state was determined under loads of different vehicles: agricultural tractors; military fighting, logistic, and multifunction vehicles; SUVs; a grooming machine; and a general aviation aircraft. These tests were performed on different surfaces: arable soils, loess, sand, turf, and snow. We applied various parameters such as wheel load, vehicle speed, wheel slip, and wheel function modes (driving versus rolling), repeated rolling, and reduced inflation pressure. By introducing specific methods for installing transducer systems into each type of soil, we also improved the accuracy of final results by minimizing the effects of soil disturbances around the transducers.

Third, we applied the obtained experimental data to cast new or recreate existing models of wheel–soil interactions. We utilised three different strategies of model construction: calibration of known models with the use of experimental data, reconstruction of models based on input–output signals describing the wheel–soil system, and a classical physical modelling of the system. We found that the system identification method applied to the wheel–soil interactions produced very good results.

Although most of the results of the experiments presented in this book are of a general character, we can find some practical applications. Results may help optimise vehicle undercarriage concepts and designs with respect to maximum performance and minimum soil degradation (compaction). Similarly, off-road vehicle ride parameters (velocity, tyre inflation pressure, loading, etc.) may be optimised for performance and minimise

low soil compaction and degradation. Moreover, methods, transducers, and procedures presented here are also of practical importance for planning field experiments.

Further experimental research in these areas may focus on investigation of factors not considered here, on deeper analysis of dynamics effects in wheel–soil systems, and on additional applications such as preventing soil environment degradation and improving the safety and comfort of off-road vehicle handling.

Automotive Engineering

Dynamics of Wheel–Soil Systems

A Soil Stress and Deformation-Based Approach

Why is knowledge of a soil stress and deformation state important for off-road locomotion? How do you measure soil stress and deformation under wheel loads? What are the actual values of stresses and deformation in soil or snow under a passing wheel? Providing answers to these questions and more, **Dynamics of Wheel–Soil Systems: A Soil Stress and Deformation-Based Approach** is a practical reference for anyone who works with experiment design and data analysis of soil stress and deformation measurements under vehicle load.

Based on the author's 15 years of experience in field experimentation on wheel–soil dynamics, the book describes methods and devices for soil stress and deformation measurements and presents numerical data from full-scale field experiments. These methods offer practical solutions to methodological problems that may arise during the design and preparation of field experiments.

- Provides technical information on measuring, modeling, and optimizing off-road vehicle traction—including a novel method for describing off-road traction
- Provides rare experimental data on soil stress and deformation under a variety of wheeled and tracked vehicles
- Supplies solutions for designing, building, and using soil or snow pressure transducers and sensors
- Compiles original experimental data on soil degradation due to agricultural machinery traffic and soil compaction
- Explains how to create dynamic models of wheel–soil systems based on experimental data

A valuable reference on an important area of terramechanics, this book shows how to analyze and model wheel–soil interactions to create more effective designs for a range of vehicle types.

K15037

CRC Press
Taylor & Francis Group
an **informa** business
www.crcpress.com

6000 Broken Sound Parkway, NW
Suite 300, Boca Raton, FL 33487
711 Third Avenue
New York, NY 10017
2 Park Square, Milton Park
Abingdon, Oxon OX14 4RN, UK

ISBN: 978-1-4665-1527-7
90000
9 781466 515277